NOTICE

The quality of this microform is heavily dependent upon the quality of the original thesis submitted for microfilming. Every effort has been made to ensure the highest quality of reproduction possible.

If pages are missing, contact the university which granted the degree.

Some pages may have indistinct print especially if the original pages were typed with a poor typewriter ribbon or if the university sent us an inferior photocopy.

Reproduction in full or in part of this microform is governed by the Canadian Copyright Act, R.S.C. 1970, c. C-30, and subsequent amendments.

AVIS

La qualité de cette microforme dépend grandement de la qualité de la thèse soumise au microfilmage. Nous avons tout fait pour assurer une qualité supérieure de reproduction.

S'il manque des pages, veuillez communiquer avec l'université qui a conféré le grade.

La qualité d'impression de certaines pages peut laisser à désirer, surtout si les pages originales ont été dactylographiées à l'aide d'un ruban usé ou si l'université nous a fait parvenir une photocopie de qualité inférieure.

La reproduction, même partielle, de cette microforme est soumise à la Loi canadienne sur le droit d'auteur, SRC 1970, c. C-30, et ses amendements subséquents.

MEASUREMENT AND ANALYSIS OF MnS PRECIPITATION IN ELECTRICAL STEELS

by

Wei Ping Sun

A Thesis Submitted to the Faculty of Graduate Studies
and Research in Partial Fulfilment of the Requirements
for the Degree of Doctor of Philosophy

Department of Mining and Metallurgical Engineering
McGill University
Montreal, Canada

January 1991

ISBN 0-315-67821-6

ABSTRACT

A newly developed creep method is described for following the kinetics of manganese sulfide precipitation in four electrical steels. The technique was also applied to a Ti steel, in which the precipitation kinetics were previously determined using a stress relaxation method. Prior to loading, the specimens are solution treated for half an hour and then cooled to the test temperature. A constant stress is applied to the sample by means of a computerized MTS machine and the strain is recorded continuously during testing. The resulting creep rate is sensitive to the occurrence of precipitation; thus the slope of the true strain-log(time) curve decreases immediately after the initiation and increases on the completion of precipitation. The precipitation-time-temperature diagrams determined in this way are of classical C shape on all of the tested materials. Because higher dislocation densities and internal stress levels are maintained, the present technique is more effective for monitoring the precipitation events occurring in the ferritic phases and at high temperatures than the previously developed stress relaxation method.

The nucleation sites for precipitation during creep testing were investigated with the aid of electron microscopy. It was concluded that the progress of MnS precipitation can be divided into three stages: nucleation, growth and coarsening. By a detailed analysis of the nucleation thermodynamics and kinetics, it is demonstrated that there exists a strong tendency for the nuclei to be formed on dislocations at lower temperatures. However, nucleation at grain boundaries is preferred as the temperature is increased. It was also shown quantitatively that the classical diffusion-controlled growth theory is not satisfactory for strain-induced MnS precipitation. Thus, a modification was made in such a dynamic case by taking the effects of deformation vacancies into account. As regards the coarsening of MnS particles, it was found that the kinetics during this stage are controlled by both bulk and grain boundary diffusion.

The microstructural examinations revealed that both grain deformation and grain boundary sliding take place in the electrical steels at hot working temperatures. Quantitative evaluations showed that the latter process contributes about one-sixth to one-tenth the total strain under the current experimental conditions. The strong retardation of grain deformation after the occurrence of precipitation is explained in terms of the interfacial pinning of mobile dislocations by these incoherent particles. It is also demonstrated that the finely-dispersed precipitates slow down the boundary sliding rate. On the basis of these observations, the relationship between the rate of sliding of a particle-free and of a precipitate-containing boundary is derived.

RESUME

Une nouvelle méthode de fluage a eté développée pour décrire la cinétique de précipitation du sulfure de manganèse dans quatre aciers électriques. La technique a été aussi appliquée à un acier au titane, dans lequel la cinétique de précipitation a été déterminée auparavant en utilisant une méthode de relaxation de contrainte. Avant d'être mis sous charge, les échantillons subissent un traitement de mise en solution d'une demi-heure, puis ils sont refroidis jusqu'à la température du test. Une contrainte constante est appliquée à l'échantillon par le biais d'une machine MTS controllée par ordinateur et la déformation est enregistrée durant le test. Le taux de fluage résultant est sensible à l'apparition de précipités; de ce fait la pente de la courbe de déformation vraie en fonction du logarithme du temps décroît immédiatement après le début de la précipitation et augmente dés la fin de la précipitation. Les diagrammes de précipitation, temps, température déterminés de cette manière présentent une forme classique en C pour tous les matériaux testés. Puisqu'une densité de dislocation et une contrainte interne plus importantes sont maintenues, cette technique est plus adaptée au suivi des événements de précipitation intervenant dans les phases ferritiques à hautes températures, que la méthode de relaxation de contrainte développée auparavant.

Les sites de germination des précipités durant les tests de fluage ont été étudiés à l'aide de la microscopie électronique. Il a été conclu que la précipitation du sulfure de manganèse peut être divisée en trois étapes: la nucléation, la croissance et le grossissement. Par une analyse détaillée des cinétiques et de la thermodynamique de germination, il a été montré qu'il existe des sites de germination préférentiels sur les dislocations à basses températures. Cependant la germination aux joints de grain devient prédominante au fur et à mesure que la température est augmentée. Il a été aussi montré quantitativement que la théorie classique de croissance controllée par la diffusion n'est pas verifiée de manière satisfaisante pour la précipitation induite par la déformation. Donc, une modification a été faite dans le cas dynamique, en tenant compte des effets des lacunes de déformation.

En ce qui concerne le grossissement des particles de MnS, il a été trouvé que la cinétique durant cette étape est gouvernée par la diffusion aux joints de grain et la diffusion volumique.

Les examens de microstructure ont révélé qu'à la fois la déformation des grains et le glissement des joints de grains ont lieu dans les aciers électriques aux températures de déformation à chaud. Les évaluations quantitatives ont montré que le dernier procédé contribue pour un sixième à un dixième de la déformation totale dans les conditions expérimentales présentes. Le fort retard de la déformation des grains après l'apparition des précipités est expliqué en terme d'ancrage interfacial des dislocations mobiles par les particules incohérentes. Il a été aussi montré que la dispersion de petits précipités ralentit le taux de glissement des joints. A partir de ces observations, une relation entre le taux de glissement d'un joint de grains libre de particule et d'un joint contenant une particule a été obtenue.

ACKNOWLEDGMENTS

First and foremost, my deepest gratitude goes to my thesis supervisor, Professor John J. Jonas, for his continuous attention and intellectual inspiration throughout the course of this work. His insight and experience in the fields of mechanical and physical metallurgy laid the foundations for the success of this research. Besides, his kind nature and unique scientific approach towards many of the problems encountered during my Ph. D. studies have been of themselves an example which I will try and emulate in the future.

Of importance also were the cooperation and assistance received from Drs. X.L. He, W.J. Liu, M. Militzer and S. Yue. The genuine interest they took in my work and the beneficial suggestions they provided were invaluable and are greatly appreciated.

Many thanks are extended to my fellow graduate students, in particular to M.P. Butrón-Guillén, D. Daniel, M. Djahazi, A. Laasraoui, S.H. Park, C.C. Roucoules, E.A. Simielli and G.L. Wang, for not only sharing the facilities of the "CSIRA" laboratory in a friendly manner, but also readily sharing their knowledge.

Special appreciation must be expressed here to E. Fernandez, L. Mello and C. Rousseau, whose help in various forms greatly aided the completion of this investigation. Similar thanks are also due to Dr. G.E. Ruddle of CANMET, P. Nestico and A. Pether of Dofasco Inc. for their personal interest and for their assistance in supplying the experimental steels, and to M. Knoepfel and B. Grondin for machining these materials into test specimens.

The financial support received from the Faculty of Graduate Studies and Research, in the form of a Differential Fee Waiver, and from the Natural Sciences and Engineering Research Council of Canada, the Canadian Steel

Industry Research Association, the Ministry of Education of Quebec, and Dofasco Inc. is acknowledged with gratitude.

Last, but not least, I would like to express my sincere gratitude to my wife, Xunxiang Liu, for her selfless patience, unfailing encouragement and assistance in typing this document. In addition, the unconditional support, emotional and financial, received from all my family and friends in China, the United States and Canada cannot go unmentioned. As a result of this support, I have been continuously stimulated to pursue what is considered as our mutual goal. I am, thus, much indebted to all of them for their love and understanding.

TABLE OF CONTENTS

LIST OF FIGURES

LIST OF TABLES

CHAPTER 1

INTRODUCTION

Electrical steels, or silicon steels, are used in electric power applications, typically as magnetic core materials for transformers, electric motors and generators. High permeability is required, but the principal requirements are high induction for moderate driving fields and low power loss. With the advancement of electrical engineering and the thrust for energy conservation, electrical steels have been rapidly developed in response to demands for higher quality.

Broadly speaking, electrical steels can be classified into two categories, one of them being grain-oriented and the other non-oriented. A better quality of non-oriented electrical steel is generally obtained by carefully controlling all the possible factors that give rise to power loss, which is related to the presence of small quantities of carbide-forming elements, such as Ti and Zr. As for the grain-oriented electrical steels, the highly oriented texture is developed through a process called secondary recrystallization. The basic metallurgical principle causing oriented secondary recrystallization is the

retardation of normal grain growth by the second phase particles present during primary recrystallization.

As is well known, manganese sulfide (MnS) has been extensively used as an elementary "inhibitor" in commercial silicon steels. The morphology of MnS is of considerable importance in improving the final texture and, therefore, the magnetic properties of these steels. Since it has been found that large particles only exhibit a very small pinning effect on grain boundaries, it is important to know how to produce a fine dispersion of MnS precipitates during hot rolling. Thus, the nucleation and growth behavior of MnS precipitates at high temperatures is of great interest and requires a detailed and clear description.

The kinetics of MnS precipitation during the hot deformation of electrical steels is not only of practical concern for industry, but also involves fundamental questions in physical and mechanical metallurgy. As is well known, a large number of studies have dealt with the precipitation of carbides or nitrides. By contrast, there has been little research related to the precipitation of sulfides. Furthermore, metallurgists often concentrate on the hot working of steels in the austenite range. However, the hot deformation and heat treatment of 3 percent silicon steels in industrial practice are carried out within the ferrite range, and thus the events occurring during these processes are particularly interesting and less familiar.

Although some scientists and engineers are aware of the usefulness and importance of information regarding MnS precipitation during hot deformation, they are still far from their goal of a clear understanding of the topic. Among the problems faced by these investigators are the notorious difficulties and appreciable times involved in detecting such precipitation at high temperatures. Such experimental difficulties constitute a real barrier to the use of precipitation kinetics in the design of rational rolling schedules and the selection of reasonable annealing parameters. The present investigation was therefore designed with two objectives in view, namely:

1) to develop a new technique, which is easier, more accurate and more efficient than the current methods, for detecting precipitation in ferrite; and

2) to determine systematically the thermodynamics and kinetics of MnS precipitation in electrical steels during hot deformation.

The present thesis includes the following chapters:

Chapter 2 is a summary of the literature reviewed. The development of electrical steels is first described and then some of the results obtained by previous researchers in the fields of precipitation and creep are given.

In Chapter 3, the experimental materials and equipment are described.

Chapter 4 introduces a creep technique --- the new method developed in the present study --- for following precipitation during hot deformation.

Chapter 5 presents the main experimental results obtained by the new technique and by optical and electron microscopy.

Chapter 6 deals with the nucleation thermodynamics and kinetics of MnS precipitation in electrical steels.

Chapter 7 contains two parts: the growth of MnS precipitates is analyzed in the first and the coarsening of such particles is illustrated in the second.

Chapter 8 investigates the microstructural evolution of electrical steels during creep testing to clarify the influence of MnS precipitation on the deformation process; it also includes a discussion of the applicability and sensitivity of the new technique.

Chapter 9, finally, summarizes the general conclusions of the present investigation.

CHAPTER 2

LITERATURE REVIEW

2.1 DEVELOPMENT OF ELECTRICAL STEELS

In order to understand present and future trends in the production, properties and utilization of electrical steels, it is first necessary to review recent progress in the metallurgy of these materials.

2.1.1 PROCESSING OF ELECTRICAL STEELS

In the last century, iron and low carbon steels were used as transformer core materials. The history of silicon steel began at the turn of the century when the beneficial results of adding silicon to low carbon steels were discovered.[1] The addition of silicon to iron or low carbon steels results in an increase in permeability, causing a decrease in hysteresis, and an increase in the electrical resistivity, thereby causing a reduction in the eddy current losses.[2] The presence of silicon as an alloying element also stabilizes the steel

with respect to the deterioration over time of the magnetic properties (magnetic aging). More importantly, silicon modifies the phase changes in steel so that the Fe-Si system shows a much more narrow austenite loop. At silicon contents in excess of 1.9% in weight, the binary alloy, as shown in Figure 2.1, is a single bcc ferrite phase at all temperatures up to the melting point;[3] this makes it possible to carry out the high temperature heat treatments necessary to develop the texture, and prevents the preferred orientation from being destroyed by transformation during the later cooling stage. The disadvantage of silicon addition is that it has a tendency to make the alloy brittle, so that it becomes difficult to roll it into sheets when the silicon content is 5% or higher.[4] The silicon concentration is therefore limited to 3% because of these considerations.[5]

In the early 1930's, electrical steels were improved by means of better hot rolling and cold rolling technologies. By a suitable program of hot rolling, annealing, cold rolling and final primary recrystallization, Goss[6] obtained a polycrystalline silicon steel sheet which had strong anisotropic properties. The breakthrough of the Goss method led to revolutionary reductions in power loss for 3% silicon steels largely through the strengthening of the (110) [001] texture.[7, 8] In this texture, the crystals tend to be oriented with their (110) planes parallel to the surface of the sheet and their [001] directions parallel to the rolling direction, as illustrated in Figure 2.2a. The first grain oriented silicon steel produced by Goss undoubtedly had the required inhibitors present by chance, and it was not until later that the role of the inhibitor was noted and the relationship to the primary recrystallization texture was appreciated.[9-11] The advantages of crystal orientation led to intensive studies of the composition and processing steps associated with improving the degree of preferred orientation.[12-17]

"Modern" Goss materials originated around 1940, when it was found that the degree of orientation could be increased by secondary recrystallization. This grain-oriented silicon steel was produced using manganese sulfide (MnS) as the inhibitor (referred to as the Armco method), a process which was used world-wide until recently.[18-20] By 1950, with the addition of rapid strip decarburization in wet hydrogen, the two stage process practiced today had come to maturity.[21-23]

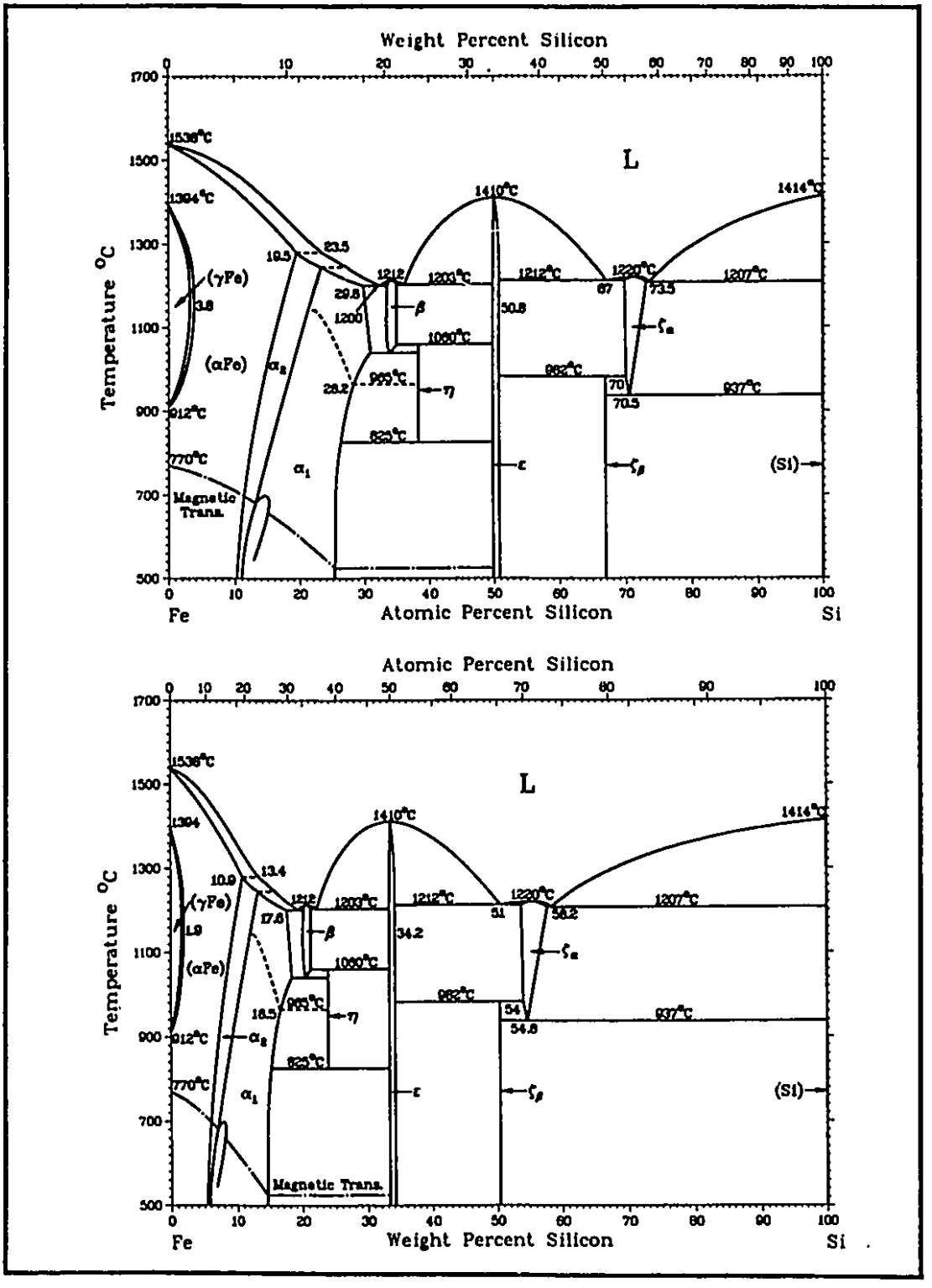

Fig. 2.1 Fe-Si phase diagram.[3]

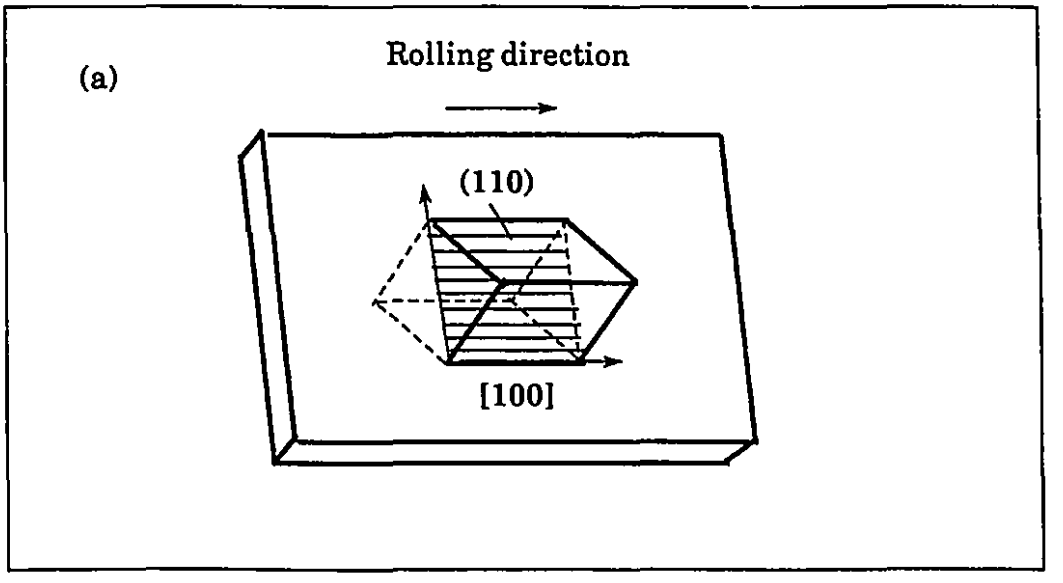

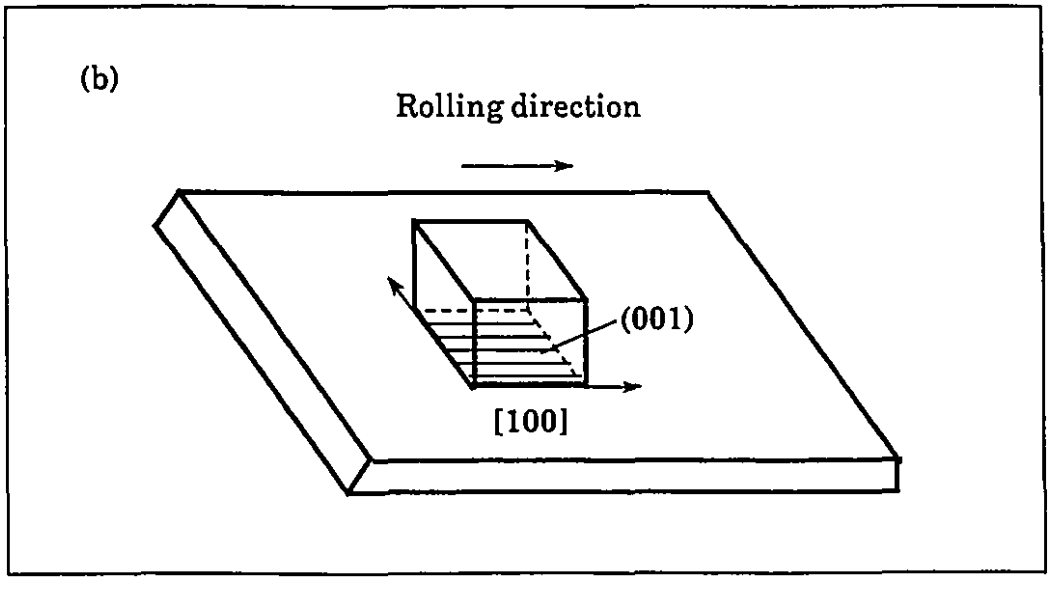

Fig. 2.2 Electrical steel sheets containing the (a) Goss and (b) cube textures.

The disadvantage of the "Goss" orientation involves its highly anisotropic properties. In 1957, silicon steel sheet with a (100) [001] texture was produced.[24] This texture, described in Figure 2.2b, has the grains oriented with their [001] directions parallel to the rolling direction, and their (100) planes parallel to the rolling plane. Thus the material has almost equal magnetic properties along two directions at right angles in the plane of the sheet (i.e. the rolling and transverse directions), and so is less anisotropic. At present, this "cube" material is not produced commercially as it has not proved to have sufficient advantages over the conventional "Goss" material to offset the higher production cost.

In 1966, a new type of grain-oriented electrical steel, commonly known as HI-B, was announced by the Nippon Steel Corporation.[25, 26] The Nippon process is essentially based on the inhibiting effect of fine particles of AlN assisted by MnS precipitates in order to produce the highly oriented (110)[001] texture.[27, 28] In 1973, the Kawasaki Steel Corporation developed a similar grain-oriented silicon steel called RG-H.[29, 30] In the Kawasaki process, a small quantity of Sb is added to the steel, which supplements the inhibiting action of MnS and AlN.[31, 32] At a later date, Jackson[33], Grenoble[34] and Fiedler[12, 35] demonstrated other means of improving grain-oriented silicon steels by the use of boron and nitrogen.

The "highly oriented" silicon steels, such as HI-B and RG-H, have higher permeabilities and lower power losses, particularly at high flux densities, than conventional Goss oriented silicon steels with MnS as the "inhibitor", but are more expensive and only economical for devices operating at high flux densities. The use of these materials is thus restricted to high flux applications. In addition, although these materials are easier to magnetize along the rolling direction than conventional Goss steels, the improved orientation makes it more difficult to magnetize them at right angles to the rolling direction. In a transformer, the flux is not always flowing along the rolling direction (easy direction of magnetization), particularly at joints and corners, and hence in these cases, the use of highly oriented electrical steels does not necessarily produce any beneficial effects.[36] It is due to these disadvantages that the highly oriented silicon steels have not completely supplanted the conventional grades.

In the last decade, the efficiency of electrical steels has undergone considerable improvement. Much of this improvement has been brought about by an increased understanding of the physical metallurgy of these materials.[37,38] One thread of investigation during this period has concerned the origin of the Goss texture. Beginning with the hot-rolled band, the texture at different sheet depths has been studied in successive production stages; for this purpose, both pole figure determinations and crystallite orientation distribution functions (ODF analysis) have been employed.[14,39-41] It has been shown that the Goss-oriented grains (which are the potential nuclei for secondary recrystallization) are formed in the intermediate layers of the hot-rolled sheet.[42] These are produced by the shear deformation introduced by friction between the rolls and the sheet. They then grow by the process of subgrain coalescence, generally during the intermediate to later rolling passes in the finishing stands. Another interesting direction of investigation has been focussed on inhibitors for secondary recrystallization, a topic which will be reviewed in more detail in the next subsection.

The earlier work on improving the properties of electrical steels is summarized in chronological order in Table 2.1. Even though silicon steels have been used for 90 years, further improvements in their properties are still possible and thus the production of more efficient electrical equipment.

2.1.2 EFFECTS OF MnS PRECIPITATION

In the manufacture of grain-oriented 3% Si steels containing the (110)[001] Goss texture, two essential requirements must be met to foster the process of secondary grain growth. First, a grain growth inhibitor in the form of small, dispersed particles is needed to retard primary grain growth in the early portion of the final anneal; the resulting fine grains provide the driving force for secondary recrystallization. The main types of the inhibitors used in industry are MnS, MnS + AlN, MnS + B, and MnS + AlN + B. Second, a suitable structure of completely recrystallized grains containing a cube-on-edge component must be present prior to the final anneal.[11,43,44] These two factors are in turn affected by the slab reheating and hot rolling processes.[44]

Table 2.1
Chronological Development of Electrical Steels

Years	Developments
1890 - 1900	Iron and low carbon steel
1900 - 1920	3% silicon steel
1920 - 1934	Laminated silicon steel
1934 - 1940	Original Goss-oriented 3% silicon steel
1940 - 1956	Modern Goss steel using MnS as an inhibitor
1957 - 1960	Cube-oriented 3% silicon steel
1960 - 1966	Improvements in both oriented and non-oriented steels
1966 - 1973	Highly oriented HI-B steel (MnS + AlN)
1973 - 1975	Highly oriented RG-H steel (MnS + AlN + Sb)
1975 - 1978	Other highly oriented steels (MnS + AlN + B, Se, Sn, etc.)
1978 - 1990	Further improvements in Goss steels as a result of inhibitor and texture studies

Slabs or ingots are usually reheated at high temperatures prior to roughing and finishing. By such treatments, the grain growth inhibitors are dissolved during reheating and subsequently reprecipitated as a fine dispersion of particles during hot rolling. After hot rolling is completed, the basic size distribution of the inhibiting particles has been established, although it can still be modified by subsequent heat treatments.

Regarding the influence of the dispersed particles on texture formation, there has been progress, in recent years, in exploring this phenomenon.[45-49] It has been suggested that MnS precipitates restrain grain growth in a fine-grained recrystallized matrix, resulting in the storage of considerable grain

boundary energy. This is necessary to provide the driving force for (110)[001] secondary recrystallization.[18,50] The growth kinetics of the secondary grains are also influenced by variations in the size distribution of the MnS particles present before the beginning of secondary recrystallization.[51] The retarding force exerted by such particles on the migration of grain boundaries during primary recrystallization follows Zener's criterion.[52, 53] For a given volume fraction, smaller particles have much greater hindering effects on grain growth than larger ones. Even a small volume fraction of MnS precipitates can be effective, if they are finely dispersed in the matrix.

TEM work on the coprecipitation of MnS and AlN has shown that MnS particles act as nucleation sites for AlN precipitation.[54] This means that MnS precipitation must occur prior to AlN precipitation. Thus, the nucleation and distribution of MnS particles play decisive roles in forming the texture of electrical steels even when both MnS and AlN are employed as inhibitors. Further studies have revealed that the combined presence of MnS, AlN and B lead to still stronger grain growth inhibition due to the segregation of boron atoms to grain boundaries.[12,55]

Some other investigations have indicated that individual boundaries with high grain boundary mobilities free themselves spontaneously from the restraining influence of the particles, thereby making the corresponding grains grow.[51, 56] It has been established that dispersed MnS and/or AlN particles restrain slowly moving boundaries more effectively than rapidly moving boundaries.[57, 58] It seems reasonable to conclude that such selective inhibition assists the development of the crystallites with the highly mobile boundaries, leaving them to become the nuclei for secondary recrystallization.[52, 58] As the temperature is high enough to cause the dissolution and coalescence of the dispersed phase during the later stages of secondary recrystallization, the total breakdown of grain boundary inhibition results in abnormal grain growth.[2, 51] The (110)[001] texture is produced in this way with the direction of preferred magnetization along the strip rolling direction.[59]

As described above, electrical steel textures can be manufactured by controlling grain growth during primary and secondary recrystallization with

suitably dispersed precipitate particles. The final electromagnetic properties of these grain-oriented steels depend on the size distribution of such dispersed phases, most frequently MnS precipitates. In contrast to the *effects* of MnS precipitates in these steels, their nucleation and growth behaviors during hot deformation are still relatively unknown. As a deeper understanding of the latter subject is acquired, it will become possible to optimize the distribution and morphology of the MnS particles. Before describing the research carried out on this project in the present investigation, the achievements and contributions of previous investigators in the field of precipitation will be reviewed, particularly in the area of sulfide precipitation.

2.2 GENERAL FEATURES OF PRECIPITATION

The first step in strengthening a pure metal by alloying is to form a solid solution. The second step is to supersaturate the solid solution, and by suitable heat treatment to cause the excess solute to be precipitated as a second phase.[60] This can be carried out in a large number of alloy systems, but the detailed behavior varies from alloy to alloy. This is particularly true of the kinetics of the process as well as of the morphology, distribution and coherency of the precipitated particles. However, it is still possible to generalize the essential features of the process. In this section, we will first consider the formation free energy, solubility and morphology of sulfides, then provide an overview of their nucleation sites, coherency properties and general precipitation kinetics. Finally, the existing methods for detecting precipitation will be described.

2.2.1 FREE ENERGY OF FORMATION OF SULFIDES

In the course of investigations into precipitation, the following question recurs: why is a particular phase precipitated from the supersaturated solid solution under certain conditions? To answer this question, we must determine the equilibrium configuration. From a thermodynamic point of view, a particular precipitate forms when its formation free energy is negative. Since it is impossible in the space available to this section to cover all the

results published for various kinds of precipitates, only the research on the standard free energy of sulfide formation will now be reviewed.

As is well known, sulfur is soluble in molten steel, but its solubility in solid steel is very low and decreases rapidly as the temperature is decreased. It is precipitated in the form of metal sulfides during solidification and, depending on the reheating temperature, reprecipitated during hot rolling.[61] The relative stabilities of the different metal sulfides are indicated by the curves for their standard free energies of formation against temperature. A graph showing this for a number of sulfides important in the steel industry is presented in Figure 2.3, taken from Muan and Osborn.[62] It can be concluded from this diagram that the tendency for the pure metals to form sulfides increases in the approximate sequence Ni→Fe, Si, Cu→Ti, Mn, Al→Mg, Na, K→Ca. The relative stabilities of the different sulfides are, however, dependent on temperature and sulfur partial pressure, as can be seen from the figure.

It should be noted that Figure 2.3 gives the values for the standard states, i.e. when the activities of the elements are equal to 1. This assumption is not valid under industrial conditions because the activities may be decreased or increased when other elements are dissolved in iron. The activity of sulfur, for instance, is strongly influenced by the presence of carbon and silicon.[61] Figure 2.3, therefore, can only be used with great care. If possible, the values of formation free energy should be calculated in each special case from the standard values with the corrections necessary for the actual concentrations and activity coefficients.[63] In practice, solubility products are often used as an additional equilibrium criterion; this subject will be reviewed in the next subsection.

2.2.2 SOLUBILITY PRODUCT OF MnS IN ELECTRICAL STEELS

The solubility product is useful for predicting solution temperatures and calculating the equilibrium amounts of precipitates expected to be present at certain temperatures according to the initial concentrations of the precipitate-forming elements.

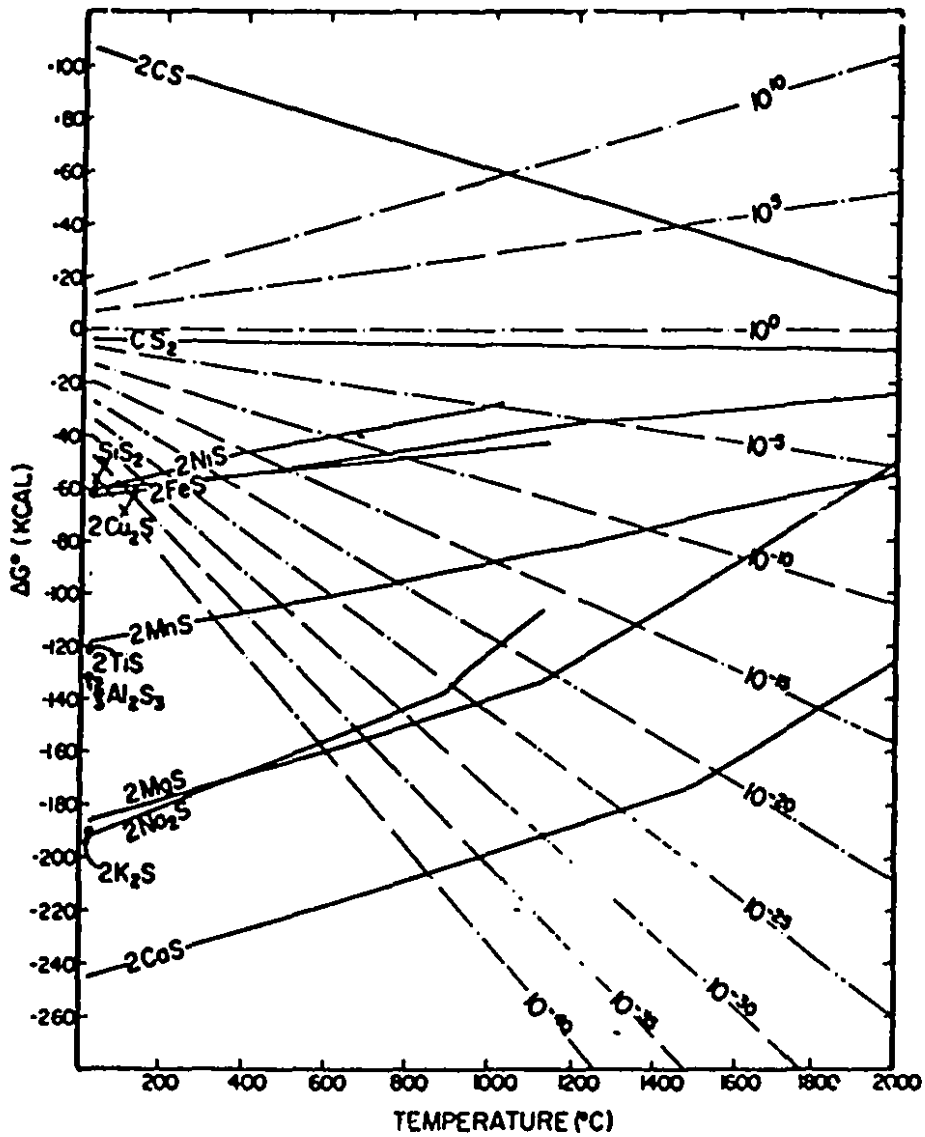

Fig. 2.3 Standard free energies of formation of various sulfides.[62] The broken lines indicate the sulfur partial pressures (in atmospheres) in equilibrium with each compound over the temperature range of the diagram.

For manganese sulfide in steels, the law of mass action indicates that the relationship between the concentrations of Mn and S in equilibrium can be described by the following equation:

$$[Mn][S] = L_{MnS} \tag{2.1}$$

where the factors in parentheses are the concentrations expressed in weight percent, and L_{MnS} is a temperature dependent quantity known as the solubility product. As the temperature is increased, the value of L_{MnS} increases in accordance with the equation

$$log\ (L_{MnS}) = -\frac{\Delta H_{MnS}}{4.575T} + B \tag{2.2}$$

Here ΔH_{MnS} is the change in enthalpy during the passage of 1 g-mol of MnS into solid solution, T is the absolute temperature and B is a constant. Normally, the solubility product of MnS takes the form:

$$log\ (L_{MnS}) = -\frac{A}{T} + B \tag{2.3}$$

Several values of the A and B coefficients for electrical steels have been reported,[64-70] but the results are not in agreement. This may be due to the differences in the experimental methods employed, but most likely different electrical steels were used as well.

Ainslie and Seybolt[64] examined the reaction of an electrical steel containing 3.3% Si and 0.13% Mn with H_2-H_2S mixtures of various compositions. After reaching equilibrium in a closed circulation apparatus, they determined the sulfur concentrations by measuring the radioactivity. On the basis of their experimental results, they derived the equation:

$$log\ (L_{MnS}) = -\frac{5{,}560}{T} + 0.72 \tag{2.4}$$

In a later investigation,[65] the solubility product of MnS in an electrical steel with 3.1% Si and 0.01-0.02% Mn was studied by determining the temperatures of formation and disappearance of the sulfide precipitates. The specimens were sealed in silica ampules filled with argon, annealed at a series of constant temperatures, and quenched. The results were described by the following equation:

$$log\ (L_{MnS}) = -\frac{14{,}000}{T} + 6.30 \qquad (2.5)$$

In a subsequent analysis, the solubility product of MnS in 3% silicon steels was measured by transmission and scanning electron microscopy, and chemical analysis.[67] The experimental results were fitted with a single line represented by an equation applicable to steels with about 0.1% Mn and valid from 1000 °C to 1400 °C:

$$log\ (L_{MnS}) = -\frac{10{,}590}{T} + 4.092 \qquad (2.6)$$

Iwayama and Haratani[69] investigated the dissolution behavior of MnS in an electrical steel containing 3% Si, 0.08% Mn and 0.025% S. The samples were heat treated at various temperatures for half an hour and then quenched in water. The solubility product of MnS obtained in this way was represented as follows:

$$log\ (L_{MnS}) = -\frac{14{,}855}{T} + 6.82 \qquad (2.7)$$

In contrast to the earlier investigations, a wider range of sulfur and manganese concentration was employed by Petrova et al.[70] Their experimental results showed that the calculated values of L_{MnS} remain almost constant as the proportions of [Mn] and [S] are varied at constant temperature. The following equation was used satisfactorily:

$$log\ (L_{MnS}) = -\frac{9{,}800}{T} + 3.74 \qquad (2.8)$$

The above results regarding the solubility product for MnS are summarized graphically in Figure 2.4, in which the straight lines a, b, c, d and, e, plotted in terms of $\log(L_{MnS})$ versus 1/T, correspond to equations (2.4), (2.5), (2.6), (2.7) and (2.8), respectively.

2.2.3 MORPHOLOGY OF MnS PRECIPITATES

The morphology of MnS in steels depends on the steel making and steel rolling practices. Based on the observation that the solubility of sulfur in steel increases as the equilibrium oxygen concentration is decreased, the sulfide phase was classified into three types by Sims and Dahle.[71]

Type I is globular with a wide range of sizes, often found in duplex form with oxygen compounds, and with an apparently random distribution. This type is most common in rimmed or semi-killed steel, where the oxygen content is high and the sulfur solubility low, resulting in the precipitation of the sulfide at comparatively high temperatures. Sulfide precipitation takes place in parallel with the deoxidization process, so that sulfur and oxygen are precipitated at the same time. In alloyed steels, alloying elements are present in high concentrations which may also be present in the MnS phase; e.g. (Mn,Cr)S in high chromium steels.[61]

MnS of type II has a dendritic structure and is often distributed as a thin precipitate. This type of sulfide is formed in killed steels that are thoroughly deoxidized with Al and where the oxygen content is low. Consequently, these steels have high sulfur solubilities and MnS precipitates late in the final stages of ingot solidification. The type II sulfide is sometimes found on primary grain boundaries in a dendritic pattern.[61]

There is no marked shape difference between the type III and type I sulfides. However, type III always forms a monophase, whereas type I is

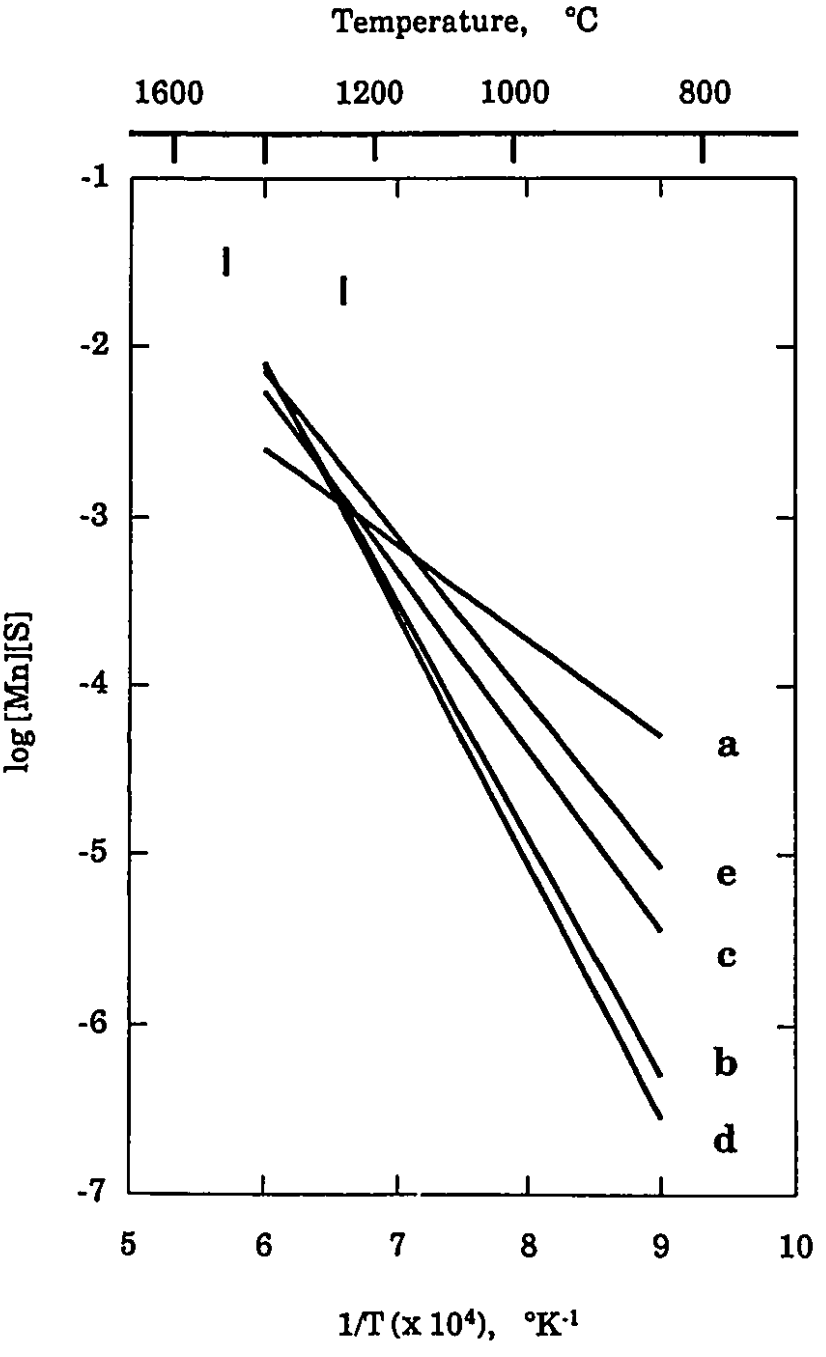

Fig. 2.4 Variation of the logarithm of L_{MnS} in electrical steels with the reciprocal of temperature.

usually present in multiphase form. Type III is most frequently found in steels which have been highly deoxidized. The oxygen content of such steels is low, but the sulfur solubility is also low compared to the steels that form type II sulfides, due to the presence of Al in solution in these steels. This sulfide type is thus precipitated earlier than type II and at higher temperatures. There is no precipitation of oxides in this case due to the low oxygen concentration of the steel, and the sulfide is also free of other metals in solid solution.[72]

2.2.4 NUCLEATION SITES FOR PRECIPITATION

As described earlier in this section, the precipitation of sulfides, carbides and nitrides takes place in supersaturated solid solutions so as to reduce the free energy of the alloy system. Considerable experimental evidence[73,74] supports the view that these precipitates nucleate preferentially at lattice defects. The reason for this phenomenon is that the misfit between precipitates and the parent metal can be best accommodated when nucleation occurs in high energy locations such as dislocations and grain boundaries.[75,76] In this way, the strain energy introduced by nucleation can be released most easily. Nucleation sites for precipitation have often been observed by electron microscopy, principally on dislocations and dislocation substructures, but also at grain boundaries, on stacking faults and in the matrix.

2.2.4.1 Nucleation on Dislocations and Dislocation Substructures

It has frequently been reported that dislocations and dislocation substructures are important sites for the nucleation of second phase particles, especially when the steel is undergoing deformation.[77-79] When precipitation takes place along dislocation lines, a chain-like distribution is often displayed, while precipitates that distribute themselves on dislocation substructures form in a cell-like pattern. Experimental evidence for the former type of precipitation was obtained by Naybour[80] and Silcock.[81] With the help of TEM, the latter kind of precipitate distribution was observed by Davenport et al.[82-84]

There have been two models dealing with the mechanisms of precipitation on dislocations, one of them being the dislocation climb and the other the moving dislocation model. The first was originally proposed by Silcock and Tunstall[85] and modified later by Nes.[86] Based on the fact that a significant volume increase is involved in the formation of precipitates, this model suggests that a vacancy flux to the precipitates is required to reduce the local internal stresses. As a consequence, the nucleation and growth of precipitates are assumed to be controlled by the supply of vacancies provided by the climbing dislocations.

Somewhat later, the dislocation climb model was reviewed critically by Kesternich,[87] resulting in the conclusion that sufficient vacancies are available for the volume relaxation of the precipitates and that the lack of vacancies for balancing the lattice mismatch is unlikely to be the limiting factor controlling precipitation. In addition, he pointed out that the dislocation climb model neglects the long range diffusion of precipitate-forming atoms to the precipitation sites. A different, moving dislocation model, was thus developed by him. In this model, it is assumed that there exists an interfacial reaction barrier which prevents nucleus growth unless another mechanism becomes operative which either reduces the interfacial energy barrier or increases the driving force. Such a facilitating mechanism is supplied by the annealing of pre-existing dislocations. The moving dislocations sweep solute atoms along and locally increase the concentration of the precipitate-forming elements in this way. Particularly at locations where two dislocations react with or annihilate each other, Cottrell atmospheres are united and a locally enhanced supersaturation is created. Significant growth takes place only as long as it is assisted by the arrival of mobile dislocations. Once the precipitates have grown to sufficient size so as to pin the dislocation effectively, the dislocation annealing process ceases.

2.2.4.2 Nucleation at Grain Boundaries

The presence of precipitates at grain boundaries has been widely observed in both deformed and undeformed steels.[88-91] The nucleation of such precipitates occurs mainly on two types of defect:[77, 92] on grain boundary

topographical defects such as steps, ledges and discontinuities, and on the extrinsic grain boundary dislocations introduced by the interaction between dislocations and boundaries during deformation. The first type of defect is prevalent in aged materials, while the second is often present in quenched or deformed steels.

The effects of grain boundary precipitation on mechanical properties such as strength, toughness and hot ductility have been repeatedly investigated by many researchers.[93-96] A frequent observation is that grain boundary precipitation significantly increases the creep resistance.[97, 98] Even a small number of second phase particles at grain boundaries can give rise to a dramatic decrease in the creep rate, particularly at low stresses.[99]

With regard to the morphology of precipitation at grain boundaries, it has been found that such precipitates often have a cube-cube orientation relationship with one of the grains. Usually a precipitate grows preferentially into the grain whose crystal structure is coplanar with the particle.[87]

2.2.4.3 Nucleation on Stacking Faults

This nucleation mode has also been investigated again and again.[81, 85, 86, 100, 101] With the help of vacancies from stacking faults, the nucleation of precipitation at these sites becomes easier due to the lower local internal stresses. Considerable experimental evidence reveals the presence of planar arrays of precipitates in the stacking fault plane. This is largely explained in terms of repeated precipitation on partial dislocations by the dislocation climb mechanism. However, it has been concluded that stacking faults are less favored sites for nucleation than undissociated dislocations because the creation of stacking faults requires additional energy and therefore a higher minimum supersaturation of the solute for nucleation.[77]

2.2.4.4 Nucleation in the Matrix

Random matrix precipitation has occasionally been observed in metals.[81, 101-103] By comparison with the other nucleation modes, however, nucleation in the matrix is believed to be the most difficult. It has been shown that this type of nucleation can only take place when the supersaturation of solutes is very high or when very high concentrations of vacancies are present, which may have been introduced by quenching or by some other means.[102]

2.2.5 INTERFACE STRUCTURES BETWEEN PRECIPITATES AND THE MATRIX

A marked feature of the nucleation of second phase particles is the accommodation of the misfit between the nuclei and the surrounding matrix. As stated above, this increases the probability of nucleation at lattice defects, and thus is of importance to the kinetics of precipitation. In general, the lattice misfit can be described by the relative difference parameter[104]

$$\delta = 2\frac{a_P - a_M}{a_P + a_M} \tag{2.9}$$

where a_P and a_M are the precipitate and matrix lattice parameters, respectively. According to the values of the relative lattice misfit and the crystallographic relationships between the particle and the matrix, the interface structure can be classified into three types: coherent, semi-coherent and incoherent.

2.2.5.1 Coherent Precipitates

The interfaces associated with this type of precipitate are either strictly coherent or quasi-coherent. In the strictly coherent interface, the two lattice parameters are equal and the equivalent lattice directions are aligned. In the quasi-coherent interface, described by Figure 2.5a, the lattice parameters

differ slightly.[104] It can be seen from this figure that the misfit parameter δ is positive, which usually applies to coherent precipitation from supersaturated solid solutions.[105]

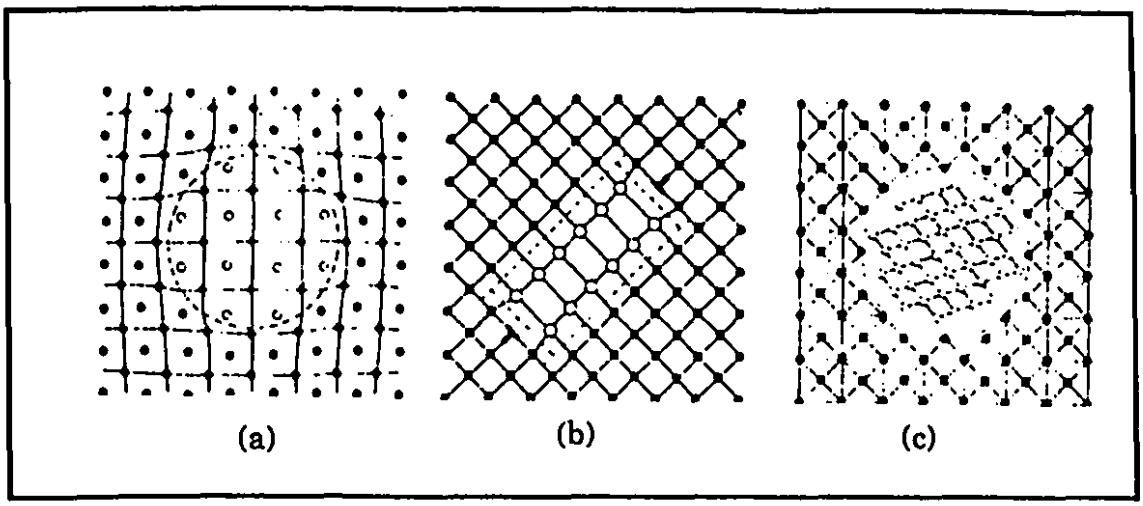

Fig. 2.5 Coherency of a precipitate: (a) quasi-coherent or coherent with a positive misfit; (b) semi-coherent; (c) non-coherent.[104,105]

The first electron micrographs of spherical, or almost spherical, coherent precipitates were obtained by Phillips and Livingston[106] and Bonar and Kelly.[107] The most striking feature of the images of coherent precipitates is a line of no contrast. This line passes through the center of the particle and is parallel to the diffracting planes. It is absent if the precipitate breaks away from the matrix and eliminates the coherency strain. Thus, the presence or absence of the line of no contrast can be used to decide whether precipitates are coherent or not.[108]

2.2.5.2 Semi-coherent Precipitates

As shown in Figure 2.5b, the precipitate and matrix lattices in this case coincide along one set of crystallographic directions where both parameters are closely similar. But along another direction, dislocations are needed in order to accommodate the large difference in the lattice parameters.[104]

Semi-coherent interfaces have been reported for many types of precipitates,[109] such as Ti(CN)[77] and Nb(CN)[78] in microalloyed steels. Many of these have been investigated by TEM but only a few have been observed to have regular arrays of misfit dislocations around them. The most regular examples have been found by Weatherly and Nicholson.[110] They indicated that interface dislocations relieve the misfit stress in a complicated way. For example, the misfit dislocations around lath-shaped precipitates in aged Al-Cu-Mg alloys reduce the misfit strain along two axes in the lath lattice but increase it along the third.[110]

2.2.5.3 Incoherent Precipitates

In this case, the lattice of the particle has nothing in common with the lattice of the matrix,[104] as shown schematically in Figure 2.5c. Clear examples of interface dislocations around incoherent precipitates have been found in a number of materials.[109] For instance, a commercial cast of Nimonic 80 A alloy (Ni 20.0%-Cr 2.32%-Ti 1.48%-Al) which had been aged for 250 hours at 930°C was examined by Weatherly and Nicholson.[110] It was found that the precipitates were enclosed by hexagonal networks of dislocation lines. Although all the dislocations had large edge components, they were not in pure edge orientation.

2.2.6 KINETICS OF PRECIPITATION

2.2.6.1 Overall Kinetics

Having considered the two possibilities of a constant nucleation rate and of a fixed density of nucleation sites, Avrami[111] suggested that isothermal transformation can be represented by the general equation

$$f_v(t) = 1 - \exp(-K_0 t^n) \qquad (2.10)$$

where $f_v(t)$ is the volume fraction transformed, K_0 is a constant which depends on the degree of supersaturation and the temperature, t is the elapsed time, and n is an experimental constant. This equation is often used in the analysis of experimental data representing the overall kinetics, and is generally known as the Johnson-Mehl or Avrami equation.

Experimental results are frequently treated by fitting curves of $loglog[1 - f_v(t)]^{-1}$ against $log(t)$, giving straight lines of slope n when the Johnson-Mehl equation is valid. For example, Harris and Nag[112] investigated the overall kinetics of NbC precipitation in this way. They reported that "n" decreases with an increase in either temperature or the volume fraction precipitated. It varied from 2.6 to 3.3 as the temperature decreased from 750 °C to 650 °C when the precipitated fraction was 10%. Above 10%, "n" ranged from 0.9 to 2. When the steel was deformed at 700 °C, they found that the nucleation of precipitates occurred mainly on dislocations and stacking faults. In that case, the "n" value was about 1 if the precipitate fraction was below 10% and was around 1.2 for more than 10% precipitation. The formal treatment of the nucleation of precipitation at grain boundaries is due to Cahn.[113] His results indicate that the value of "n" is between 1 and 4/3 for such precipitation. The values of the exponent "n" observed under different experimental conditions were summarized by Christian in 1975,[114] and are presented in Table 2.2. From these studies, it seems clear that the time exponent "n" depends on a series of factors such as the temperature, the degree of deformation, the chemical compositions of the steels tested, the types of nucleation site, and the nucleation and growth mechanisms. In what follows, we will first describe the previous researches on nucleation and growth in more detail, and then summarize the influence of other factors on the precipitation kinetics.

2.2.6.2 Classical Nucleation Theory

As described above, when a new phase nucleates within a parent phase, an interface is formed between the two phases. This notion serves as the basis of the theory of nucleation. The interface creates a local increase in the free energy when the first few atoms assemble in the new structure. The theory of this process, which describes the interfacial energy barrier to nucleation, was

Table 2.2

Values of n in the Kinetic Law $f_v(t) = 1-\exp(-K_0 t^n)$ [114]

Conditions	n
Interface Controlled Growth	
Increasing nucleation rate	> 4
Constant nucleation rate	4
Decreasing nucleation rate	3-4
Zero nucleation rate (saturation of point sites)	3
Grain edge nucleation after saturation	2
Grain boundary nucleation after saturation	1
Diffusion Controlled Growth	
Growth from small dimensions, increasing nucleation rate	> 2.5
Growth from small dimensions, constant nucleation rate	2.5
Growth from small dimensions, decreasing nucleation rate	1.5-2.5
Growth from small dimensions, zero nucleation rate	1.5
Growth of particles of appreciable initial volume	1-1.5
Needles and plates of finite long dimensions, small in comparison with their separations	1
Thickening of long cylinders (needles), e.g. after complete edge impingement	1
Thickening of very large plates, e.g. after complete edge impingement	0.5
Segregation to dislocations (very early stage only)	2/3

originally developed for vapor to liquid condensation by Volmer and Flood.[115] The model was applied by Turnbull to the solidification of metals and subsequently to solid-to-solid metallic phase transformations in the late 1940's. Since that date it has been fundamental to the qualitative and quantitative understanding of structural changes in physical metallurgy. The subject of solid-state nucleation has been reviewed on many occasions, for example by Christian,[114] Russell,[116] and Aaronson and Lee.[117] All arrived at expressions of the following form for steady state nucleation:

$$J = Z\beta^* N \exp(-\Delta G^*/kT) \qquad (2.11)$$

Here Z is the Zeldovich non-equilibrium factor, β* the rate at which atoms are added to the critical nucleus, N is the number of nucleation sites per unit volume, ΔG* the critical free energy for nucleation, k the Boltzmann constant, and T the absolute temperature.

There are many problems associated with the use of the above equation to predict experimentally measurable quantities such as the precipitation start times. These include the usual lack of knowledge of the interfacial energy and nucleation site density and the difficulties involved in calculating the strain energy term and in determining the driving force for precipitation of the species of interest. By dealing with these problems in different ways, Dutta and Sellars,[118] Xiao and Haasen,[119] and Liu and Jonas[120] have recently modified this theory for the nucleation of carbides on dislocations, with the conclusion that the theory is in good agreement with a large amount of experimental data for both carbide and carbonitride nucleation. However, there does not seem to be any work to date in which sulfide precipitation is investigated in terms of the classical nucleation theory.

2.2.6.3 Growth and Coarsening Theories

Various researchers, Lifshitz and Slyozov[121] and Wagner[122] in particular, have examined the growth and coarsening of an assembly of second phase particles by considering the different rate-limiting mechanisms. It has

been demonstrated that the theories developed by these researchers can be adequately described by the following relation:

$$\bar{r}^n - \bar{r}_0^n = K_n t \tag{2.12}$$

where $\bar{r}$ and $\bar{r}_0$ are the mean radii of the particles at time t and at t=0, respectively. The value of "n" and the factors incorporated into the constant K_n depend on the mechanisms controlling particle growth or coarsening.

There are two general equations for the growth rate of precipitates.[115, 123] When long-range diffusion is rapid and atom transport across the interface is slow, the resultant condition is usually described as interface controlled growth. In this case, the value of "n" in Eq. (2.12) is equal to 1 and

$$K_1 = M^\circ \Omega \tag{2.13}$$

If the interface reaction is much faster than the diffusion process, the opposite extreme arises, i.e. the situation of diffusion controlled growth. Then, n=2 and

$$K_2 = \alpha_2 D_m \Omega \tag{2.14}$$

In Eqs. (2.13) and (2.14), M°is the modified mobility of the interphase boundary, α_2 is a constant, D_m the effective diffusion coefficient of the slowest precipitate-forming element in the matrix, and Ω the dimensionless supersaturation.

Coarsening is the process during which the competitive growth of particles takes place. This means that the total volume fraction of the precipitates remains constant and the larger particles grow continuously by consuming the smaller ones. In such a process, the kinetics are often controlled by diffusion and the "n" value generally increases. If the coarsening is controlled by a bulk diffusion process,[121, 122, 124, 125] then n=3, and

$$K_3 = a_3 \frac{D_m C \gamma V_m^2}{RT} \tag{2.15}$$

On the condition that grain boundary diffusion is controlling during coarsening,[126-128] n = 4 and

$$K_4 = a_4 \frac{D_{gb} C \gamma \delta V_m^2}{RT} \tag{2.16}$$

Finally, if coarsening is rate limited by pipe diffusion,[129, 130] then n = 5 and

$$K_5 = a_5 \frac{D_{dis} C \gamma N q V_m^2}{RT} \tag{2.17}$$

In the above three formulas,

a_3, a_4, a_5 = constants,
D_m, D_{gb}, D_{dis} = solute diffusion coefficients in the matrix (m), along grain boundaries (gb), and along dislocations (dis),
C = concentration of the rate controlling element,
γ = interfacial energy between the precipitate and the matrix,
V_m = molar volume of the particle,
δ = grain boundary thickness,
N = number of dislocations intersecting each particle,
q = the effective cross-sectional area of the pipe diffusion path,
R = gas constant, and
T = absolute temperature.

2.2.6.4 Precipitation-Time-Temperature Relationships

The design of rational rolling schedules and of reasonable annealing parameters requires knowledge of the precipitation start (P_s) and finish (P_f) times. For practical reasons, most of the results are plotted in the form of

precipitation-time-temperature (PTT) diagrams. Some of the important factors that influence these diagrams will now be summarized.

(a) Temperature

The P_s and P_f times are strong functions of temperature, and are usually associated with C-curve kinetics. This indicates that the precipitation kinetics are controlled by supersaturation at the higher temperatures and by the diffusivity of the precipitate-forming elements at the lower temperatures. The precipitation rate is slow at high temperatures due to the weak supersaturation and is gradually accelerated as the temperature is decreased. When the temperature is decreased still further, the diffusion of the metallic elements becomes difficult and, as a result, the precipitation rate slows down again.[77, 78] The competition between supersaturation and diffusivity is responsible for the "nose" of the PTT curve.

(b) Alloying Elements

By changing either the activity or the diffusivity of the rate controlling element, alloying additions exert a significant effect on the position of PTT diagrams. For instance, Wang[131] found that Al addition shifted the Nb(CN) PTT curve to the right. This was interpreted as being due to a complex interaction between Al and N, as a result of which the effective availability of N in the matrix was reduced. In this way, the solubility of Nb(CN) was increased and the chemical driving force for such precipitation was decreased. The effect of B on the kinetics of Nb(CN) precipitation in HSLA steels, reported by Djahazi, Hé and Jonas,[78, 132] may be taken as another example. According to their observations, the PTT curves for Nb(CN) precipitation on dislocations were shifted to higher temperatures and shorter times when B was added to their steels. These authors explained their observations by stating that "the segregation of B and the presence of Nb-B complexes at dislocations lead to higher concentrations of the precipitating elements at these sites and supply a flux of vacancies which is useful for both the diffusion of atoms and the relief of the strain energy created during precipitation."

(c) Deformation

In general, the PTT curves obtained for deformed steels are located at *shorter* times than those pertaining to undeformed steels.[84, 88, 133] The acceleration of the kinetics by the increase in either the strain or the strain rate is attributed to the presence of strain induced dislocations and vacancies, which increase the nucleation site density as well as the diffusion rate.

(d) Recrystallization

The interaction between recrystallization and precipitation is always an interesting subject for metallurgists. Because of the drastic destruction of dislocations by recrystallization, some investigators believe that precipitation kinetics can be retarded if recrystallization begins before precipitation.[78, 132, 134, 135] However, other researchers have either reported that recrystallization has little influence on the precipitation kinetics[133] or that it even accelerates precipitation because of the grain refinement caused by recrystallization.[136]

2.2.7 METHODS FOR DETECTING PRECIPITATION

The existing approaches to the detection of precipitation are based on one of the following four techniques:

(1) electron microscopy;
(2) chemical or electrochemical extraction;
(3) the measurement of electrical resistivity; and
(4) the analysis of mechanical properties.

2.2.7.1 Electron Microscopy

Electron microscopy has been extensively used for investigating the presence of second phase particles due to its high sensitivity and its ability to provide crystallographic information.[79, 85, 134, 136-140] When using this technique, either thin foils or extraction replicas are employed. For examining small precipitates, the sensitivity of the thin foil method is higher than that of

the extraction replica method. However, the latter method has been shown to be suitable for measuring the mean size and distribution of precipitates. In contrast to the former method, the extraction replica method is easier to perform and more accurate when the mean particle size is comparable with or greater than the foil thickness.

2.2.7.2 Chemical or Electrochemical Extraction

In addition to its time consuming nature, another great disadvantage of electron microscopy is the large "sampling error": only a minute proportion of each specimen can be examined when this technique alone is employed. In order to obtain further information about the specimen, chemical or electrochemical extraction methods have been used to study the kinetics of precipitation.[69, 82, 133] The key step of this method involves the extraction of the precipitates from the quenched specimens either chemically or electrolytically, followed by a means of weight measurement, such as spectrophotometry, X-ray diffraction, or electron microscopy to examine the residues. This method can provide some useful parameters pertaining to precipitation, such as the volume fraction and mean particle size, as well as information about the composition and structure of the precipitates. The well-known shortcoming of this method, on the other hand, is its relatively low sensitivity to the occurrence of precipitation. As pointed out by Davenport et al.,[82] the use of this method will most likely result in missing particles that are less than 10 nm in diameter.

2.2.7.3 Measurement of Electrical Resistivity

This technique depends on the change in electrical residual resistivity with solid solution content.[138, 139, 141-143] The residual resistivity, ρ_r, consists of three terms:

$$\rho_r = \rho_r^i + \rho_r^p + \rho_r^d \qquad (2.18)$$

where ρ_r^i is the resistivity attributable to the impurities (e.g. Al, Si or Cr), ρ_r^p to the precipitate-forming elements left in solid solution and ρ_r^d to the dislocation density. Since ρ_r^d can be evaluated by an X-ray diffraction line broadening technique, the corrected residual resistivity, ρ_c , can be obtained from:

$$\rho_c = \rho_r - \rho_r^d = \rho_r^i + \rho_r^p \tag{2.19}$$

so that

$$\rho_c = A + B[M]_s \tag{2.20}$$

This is a unique function of the amount of the precipitate-forming element left in solid solution, $[M]_S$.

The electrical resistivity technique is, in theory, very sensitive to the occurrence of precipitation. However, many other physical phenomena affect the electrical resistivity, so that its accuracy relies on careful interpretation.[143]

2.2.7.4 Mechanical Methods

Although all the above techniques can be employed for investigating precipitation kinetics, not one of them is entirely satisfactory. The use of electron microscopy alone is often restricted by its significant sampling error and time consuming nature. Chemical or electrochemical extraction is the only technique which can provide complete information about the whole specimen, but its sensitivity is, unfortunately, too low to detect the small precipitates occurring in the early stages of precipitation. It has also been proved[144] that the sensitivity of the electrical resistivity method is, in practice, very low when it is employed on complex alloy systems. The precipitation start times determined by this method have been shown to be much longer than those measured by other techniques. Furthermore, all these

techniques can only be used at room temperature on quenched samples. However, the direct measurement of precipitation kinetics at high temperatures is possible through analysis of the mechanical properties of the specimens.

In view of the effect of precipitation on the microhardness of metals, as well as on dynamic recrystallization and stress relaxation, three mechanical methods have been devised to date to follow the progress of precipitation in austenite: these are flow curve analysis,[144, 145] secondary hardening,[135, 146] and stress relaxation.[77, 147] Compared with the other methods, these mechanical techniques are preferred by plant engineers and laboratory researchers for three reasons.[144-147] First, mechanical testing can be performed directly at the temperature at which precipitation takes place; thus the technique is ideally suited to studying precipitation behavior in phases which are unstable at room temperature. Second, mechanical testing effectively "samples" the entire specimen; and third, the experimental time and effort required to determine PTT relationships are much less than those required for the other methods.

Among the current mechanical methods, the stress relaxation technique is of particular interest due to its relatively high sensitivity, small sampling error, and experimental ease.[77] However, this technique (and the other two mechanical methods) have, up to now, been employed only for monitoring the precipitation events occurring in austenite.[147] An initial attempt by the present author to use the stress relaxation method to detect MnS precipitation in ferritic steels (*e.g.* electrical steels) was unsuccessful,[148] as will be reported in Chapter 4. Thus, it was necessary to find a better mechanical method suitable for measuring precipitation kinetics in both ferrite and austenite. For this practical reason, a creep technique was developed in the present investigation. In order to put this new technique into context, the main principles of creep testing and the results obtained by this means will be reviewed briefly below.

2.3 OVERVIEW OF METAL AND ALLOY CREEP

2.3.1 A SCHEMATIC DESCRIPTION OF THE CREEP CURVE

Creep may be defined as the time dependent deformation which occurs under an applied stress.[149,150] In general, creep tests on metals are carried out by keeping either the applied stress or the load constant and noting the strain of the specimen as a function of time (or log(time)).

The essential features of the creep curve exhibited by metals under constant load conditions are shown schematically in Figure 2.6.[150] On

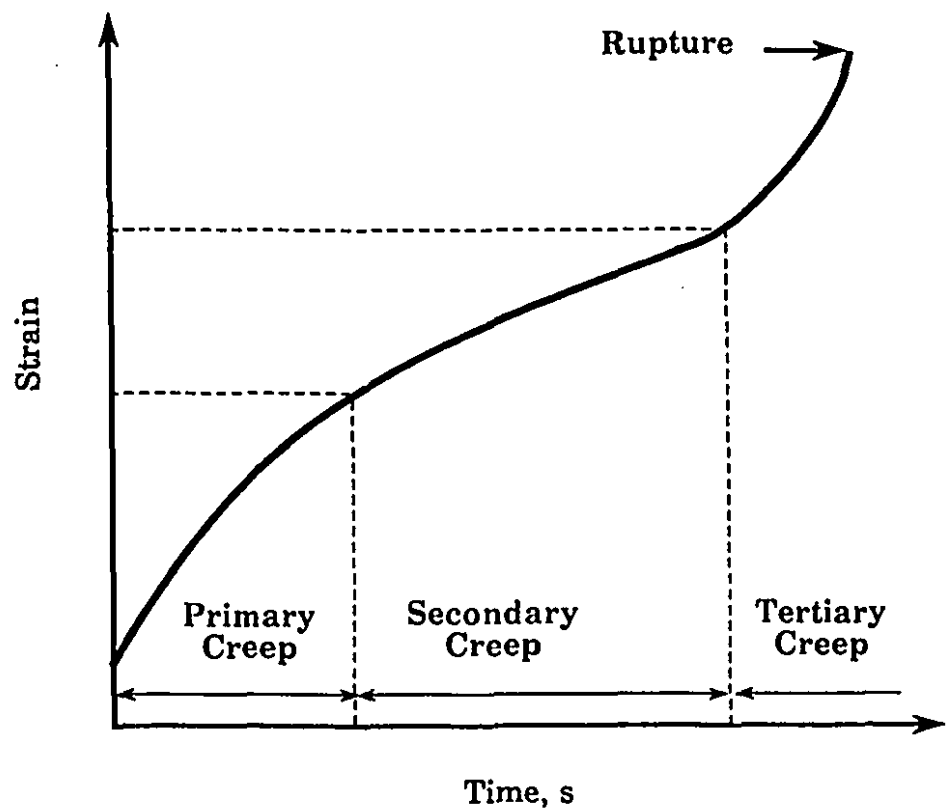

Fig. 2.6 Schematic creep curve.[150]

loading, an initial strain occurs. This is followed by a stage in which the creep rate decreases with time, called the transient or primary stage of creep. During the secondary stage, the creep rate remains constant; it begins to accelerate during the tertiary stage. Finally, fracture takes place when the rupture strain and time are reached.

A large number of empirical equations have been proposed[149, 151, 152] which can express the strain-time relation at a constant temperature and stress. Regardless of their differences, they may be classified as belonging to one of four main types, each of which is described below.

2.3.2 TYPES OF CREEP

The type of creep depends on the test temperature and the applied stress. The temperature-stress diagram of Figure 2.7 indicates the region in which each of these types is to be found.[151] In such a creep diagram, the temperature and stress are usually plotted as T/T_m and σ_a/μ rather than simply as T and σ_a. Here T is the test temperature, T_m the melting point, σ_a the applied stress, and μ the shear modulus.

2.3.2.1 Anelastic Creep or Recoverable Creep

According to the creep diagram presented in Figure 2.7, anelastic creep will be observed below the *critical shear stress* σ_{css}. In this case, the strain ε in a stressed specimen is well described by the following time-dependent equation:[151]

$$\varepsilon = \varepsilon_e + \varepsilon_o[1 - exp^{(-\frac{t}{\tau})}] \qquad (2.21)$$

where ε_e is the purely elastic strain, t is time after loading, and ε_0 and τ are constants. The last term on the right-hand side of Eq. (2.21) gives the non-

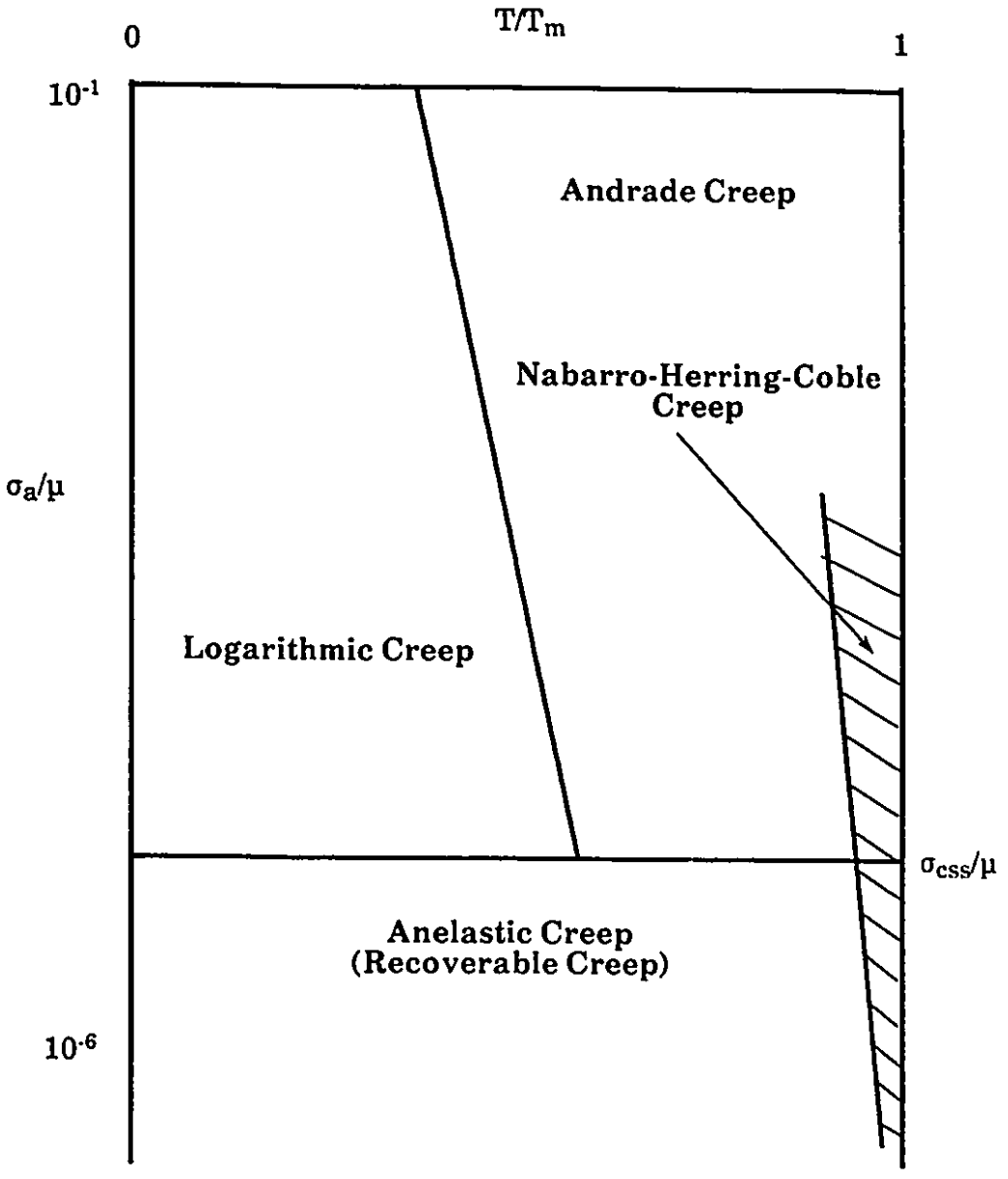

Fig. 2.7 Creep mechanism map.[151]

elastic, time-dependent strain. It can be seen that this strain increases with time and exponentially approaches the limiting value ε_o.

The anelastic creep strain is recoverable. Should the applied load be removed after the strain ε' is reached, the strain at any time t after removal of the load is given by:

$$\varepsilon = (\varepsilon' - \varepsilon_e)\, exp^{(-\frac{t}{\tau})} \tag{2.22}$$

where ε_e is the elastic strain present just prior to the removal of the load. The strain given by this equation closely approaches zero at times which are long compared to the decay time τ.

2.3.2.2 Logarithmic Creep

When a sample is deformed at a stress above the critical resolved shear stress and at a relatively low temperature, the creep is generally observed to be of the type:[77,78,151]

$$\varepsilon = \varepsilon_e + \varepsilon_p + \varepsilon_o log(1 + vt) \tag{2.23}$$

which gives a creep rate

$$\dot{\varepsilon} = \frac{\varepsilon_o v}{1 + vt} \tag{2.24}$$

In the two equations, ε_e is the elastic strain, ε_p is the instantaneous plastic strain, and ε_o and v are constants. The creep strain depends logarithmically on time and is of a transient nature, since the creep rate decreases to zero with the inverse of the time.

2.3.2.3 Andrade Creep

Around 1910, Andrade carried out a series of creep tests on metals in the region of the creep diagram which corresponds to high temperatures and moderate to high stresses.[149, 153, 154] He established that, in this region, creep under constant stress and temperature follows the law:

$$\varepsilon = \varepsilon_e + \varepsilon_p + \beta t^n + Kt \tag{2.25}$$

where ε_e and ε_p have the same meanings as before, and n, β and K are constants. Indeed, the schematic plot of the strain shown in Figure 2.6 is predicted by Andrade's equation, except for the accelerating stage at the end of the test. If a time derivative is taken of Eq. (2.25), the following creep rate is found

$$\dot{\varepsilon} = n\beta t^{n-1} + K \tag{2.26}$$

The first term on the right-hand side of this equation represents transient creep, since it approaches zero after a certain time (note that n is less than 1). The second term on the right gives rise to a constant or steady state creep rate.

2.3.2.4 Nabarro-Herring-Coble Creep

A special kind of steady state creep is labeled "Nabarro-Herring-Coble creep" in Figure 2.7. This type of creep can occur in specimens which are either very small or consist of very fine grains. The dimensions of the grains or of the sample have to be approximately 0.1-0.01 mm or less.[150, 155, 156]

It can be concluded from the above that the occurrence of one of the four well-defined types of creep shown in Figure 2.7 is a function of the stress, temperature and material structure. To obtain a full understanding of the creep behavior, it is necessary to review the mechanisms of creep deformation that have been proposed to date.

2.3.3 MECHANISMS OF CREEP DEFORMATION

The literature concerning the mechanisms of creep deformation is vast,[149, 151, 157-159] thus only the well-established mechanisms will be reviewed in this subsection.

2.3.3.1 Motion of Point Defects

The motion of point defects, such as vacancies and interstitials, always takes place during any kind of creep in metals and alloys. Although, macroscopically, only relatively small deformations can be produced in this way, this mechanism can still dominate the creep process under some very specific conditions, one of which is considered here.

The stress-assisted diffusion of vacancies and atoms

The diffusion of vacancies and atoms is thought to be rate controlling in Nabarro-Herring-Coble creep.[156, 160] At high temperatures, the energy required to form a vacancy at the top or bottom surface of the grain pictured in Figure 2.8a is different from that required at the side surfaces if a vertical stress is applied to the grain. A gradient in the vacancy concentration is thus set up and gives rise to a vacancy flux from the tensile-stressed to the compression boundaries within the grain, as shown in this figure. If there is a net flow of vacancies in one direction, there must be an equal net flow of atoms in the opposite direction. Atoms are removed from the side surfaces of the grain in this way and deposited on the top and bottom surfaces, leading to the change in shape attributable to this kind of mass motion (see Figure 2.8b). A detailed analysis of diffusion creep has been made by Raj and Ashby.[161] It can be concluded from their results that diffusion creep becomes the controlling process at very high temperatures and relatively low stresses.

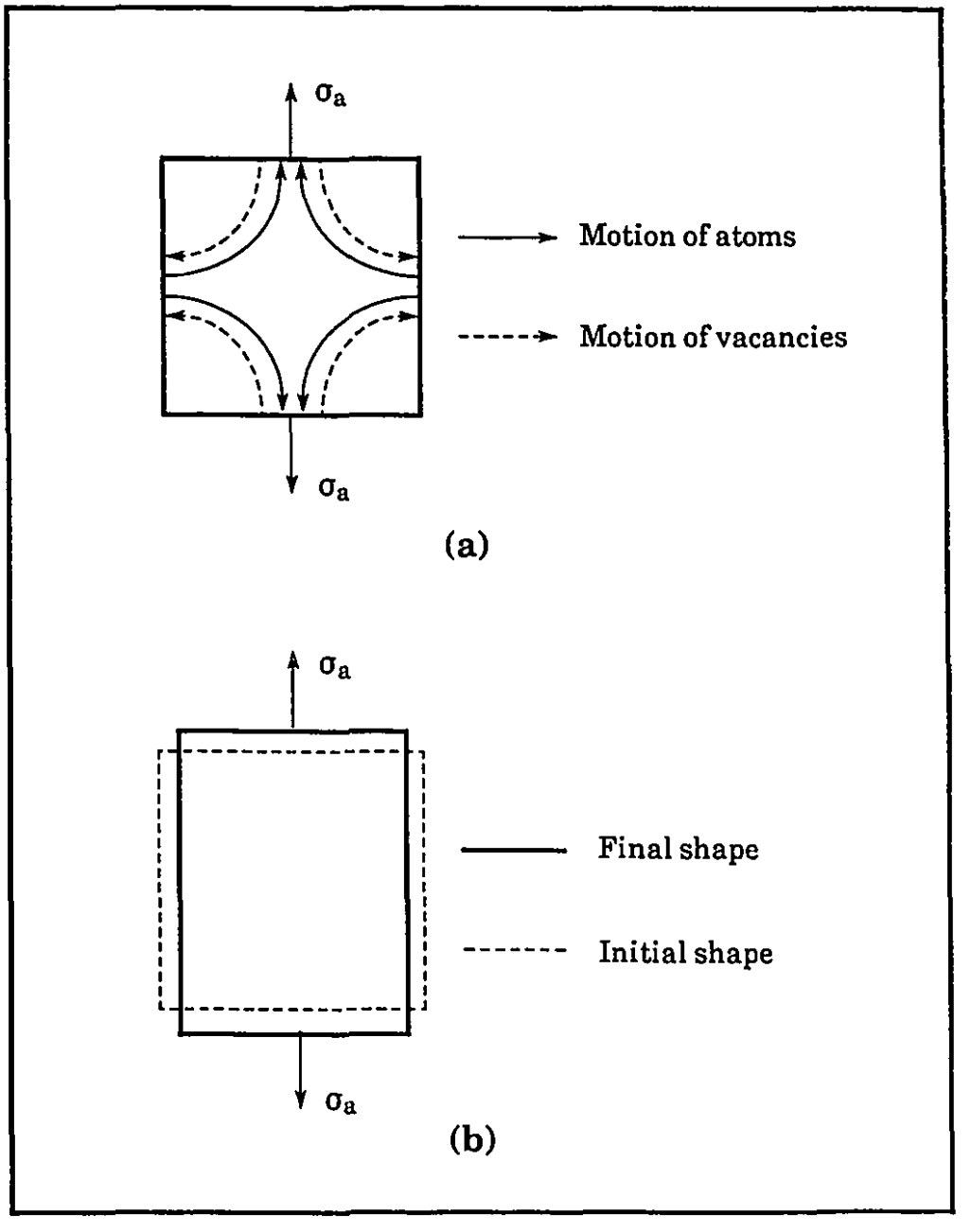

Fig. 2.8 (a) Mass motion of vacancies and atoms across a small grain at a high temperature. (b) Change in the shape of the grain as a result of the mass motion shown in (a).[151,156]

2.3.3.2 Motion of Line Defects --- Dislocation Movement

Particular attention is generally given to the motion of line defects, mainly dislocations, during creep,[150, 162, 163] as this is the mechanism responsible for most of the practical conditions. The dislocation theories have been developed to such an extent that they can predict the deformation with a considerable degree of success.[151, 164] These theories are similar in the sense that a dislocation pinned by a barrier is slow moving. Some of the more familiar theories are reviewed briefly below.

(a) Glide

Creep deformation by dislocation glide occurs at stress levels which are high relative to those normally considered for creep deformation.[150] The movement of a dislocation in this case is impeded by obstacles such as solute atoms, other dislocations, grain boundaries and precipitates. The resultant strain rate, $\dot{\varepsilon}$, may be written as[165]

$$\dot{\varepsilon} = \dot{\varepsilon}_o exp[(-bA_a(\frac{\mu b}{\lambda} - \sigma_a)/kT] \qquad (2.27)$$

on the basis that the creep rate due to dislocation glide depends on temperature in accordance with Boltzmann statistics. In the above equation, b is the Burgers vector, λ the interobstacle spacing, μ the shear modulus, A_a the activation area, σ_a the applied stress, k is Boltzmann's constant, T the absolute temperature, and $\dot{\varepsilon} = \dot{\varepsilon}_0$ when $\sigma_a \approx \mu b/\lambda$.

(b) Cross slip

Cross slip is one of the few processes taking place during creep that is associated with reasonably low activation energies.[166] The ease of cross slip depends primarily on the stacking fault energy; the higher the stacking fault energy, the narrower the stacking fault, and the greater the ease of cross slip.[150] The activation energy associated with cross slip is well below 1 ev for fcc metals which have high fault energies such as aluminum, but it rises

sharply with decreasing values of the fault energy.[167] In bcc metals, cross slip takes place very easily because of the availability of many slip planes.

(c) Jog dragging

An offset in a dislocation line which has a component normal to the glide plane is called a jog. A jog in an edge dislocation is generally mobile and so will not impede the dislocation mobility. However, a jog on a screw dislocation, which may for example be produced by the intersection of two screw dislocations, is sessile since the jog itself has an edge character. When it is to be moved, it must be dragged through the lattice creating a row of point defects, as its Burgers vector does not lie in a suitable slip plane.[150] Thus, such a jog must climb from one slip plane to the next by non-conservative (non-glide) motion.

Experimental support for the operation of the jogged screw dislocation mechanism was recently provided by Liu[77] and by Djahazi[78] in terms of the creep and stress relaxation data they obtained on Ti and Nb steels. They found that a logarithmic dependence of creep strain on the stress relaxation time is displayed when the motion of jogged screw dislocations is likely to be rate controlling:

$$\varepsilon = \frac{\alpha}{E} ln(1 + \nu t) \tag{2.28}$$

The creep rate exhibited by this mechanism was expressed by them as

$$\dot{\varepsilon} = \frac{\alpha \nu}{E} exp(-\frac{\sigma_o}{\alpha}) \; exp(\frac{\sigma_a}{\alpha}) \tag{2.29}$$

In the above two equations, E indicates the elastic modulus of the specimen, σ_0 the initial stress during stress relaxation, and α and ν are constants for a given material under isothermal test conditions.

(e) Climb

It is logical to postulate that the rate-controlling process in the high temperature creep of metals is often the climb of dislocations having an edge component. This suggestion was first made by Mott[168] and was later considered in more detail by J. Weertman and J.R. Weertman.[151] Since vacancies are commonly generated during straining at high temperatures, the climb motion of edge and mixed dislocations is certainly assisted by vacancy diffusion.

The rate of vacancy flow between dislocations, and thus the velocity of dislocation climb, depends on the actual arrangement of the dislocations in a crystal. Weertman estimated the average climb velocity for a group of N straight dislocations, all of which have the same sign and are climbing in the same direction.[151] Let L represent the average distance which a dislocation moves in a direction parallel to its slip plane between the time it is created and the time it is annihilated, d the average distance a dislocation climbs in a direction normal to its slip plane before it is annihilated, and X_v^θ is the equilibrium number of vacancies per unit volume of the crystal in an unstrained metal. Such an average climb velocity can be expressed approximately by the formula:

$$V_c = \frac{D_v X_v^0 \sigma_a b^5 L}{NdkT} \tag{2.30}$$

where D_v indicates the coefficient of diffusion for vacancies, and σ_a, b, k and T have the same meanings as in Eq. (2.27

In general, if dislocation climb is rate limiting, the stress dependence of the steady state creep rate can be described by the empirical power law:[150,154]

$$\dot{\epsilon} = B\sigma_a^n \tag{2.31}$$

where B is a constant and n is the stress exponent, the value of which depends on the temperature and the properties of the material being tested.

2.3.3.3 Motion of Plane Defects --- Grain Boundary Sliding

Grain boundary sliding is another possible creep mechanism for stressed metals at high temperatures.[169, 170] There has been evidence that such gliding is not necessarily restricted to the boundary plane itself, but that, at high temperatures and stresses, a considerable layer may be involved in the deformation.[149] The thickness of the layer increases as the misorientation between the grains is decreased, and such a thickening results in a slower rate of creep. Gibbs, after investigating the role of grain boundary sliding in high temperature creep, pointed out that the grain coherency conditions require grain boundary sliding to be accompanied by other grain deformation processes and that the latter generally determine the rate laws for creep.[171] In a subsequent analysis, it was suggested by LeMay[150] that the accommodation takes place by means of dislocation climb.

The occurrence of grain boundary sliding has been evaluated in detail by Ashby et al.[172-174] The models developed to account for this process lead to equations of the type:[161, 175]

$$U_{gb} = C_{gb}\sigma_a^n \tag{2.32}$$

where U_{gb} is the average grain boundary sliding rate, C_{gb} a proportionality factor, and $n \geqq 1$ the GBS (grain boundary sliding) stress exponent. If grain boundary sliding is controlled by diffusional accommodation at asperities in the grain boundaries, or by the climb of a constant number density of dislocations close to, or in the grain boundaries, we have $n = 1$. If the dislocation density is proportional to the stress, then the sliding rates are no longer linear with stress and the exponent n increases to 2. Finally, if grain boundary sliding is controlled primarily by dislocation movement in the vicinity of the grain boundaries, a stress exponent $n = 3$ to 5 similar to that observed in power law dislocation creep can be expected.[175]

2.3.4 CREEP IN PRECIPITATION-HARDENED MATERIALS

Although the metallurgical changes which take place during the deformation of dispersion-strengthened materials have been repeatedly studied because of their practical importance, a great many remain unidentified. When the creep of precipitate-hardened materials takes place at high temperatures, the dislocations must attempt to cut through the precipitates,[176] to bow out between neighboring particles,[177] or to surmount the particles by climb or cross slip.[151] The manner in which the dislocations by-pass the particles under any specified creep condition then depends on the ease of deformation of the particles, their volume fraction, size and spacing. When dislocations can cut through small precipitates, the strength increases with increasing particle size to a maximum value determined by the interparticle spacing, which just allows the dislocations to bow out between adjacent particles on the slip plane. The strength then decreases as the particle size and spacing increase further. When the volume fraction and size distribution of the particles is such that the creep stress is insufficient to allow the dislocations to cut through or bow out between the particles, creep in a precipitate-strengthened metal can only occur by the dislocations surmounting the obstacles by climb or cross slip. Indeed, a sufficient volume fraction of closely-spaced particles can inhibit creep, irrespective of whether deformation occurs by dislocation movement or by grain boundary sliding or by the diffusion of vacancies and interstitials.[178]

Conventionally, creep testing is frequently carried out on materials which contain a certain amount of precipitates. The volume fraction and distribution of these second phase particles often remain unchanged during deformation. But, sometimes steels are creep tested in the solution treated state. It has generally been accepted that in this case creep enhances the kinetics of precipitation by providing nucleation sites at the freshly generated dislocations which are then surrounded by a Cottrell cloud.[179] A hump in the creep curve of solution treated steels has also been observed and first interpreted as being due to strain-induced precipitation by Saha et al.[180] Subsequent research has further demonstrated the effects of strain-induced

precipitation on the departure of the creep curve from its conventional behavior.[181, 77, 78] After an initial strain, precipitation sets in and the creep rate drops to a minimum. When coarsening of the particles begins, creep is resumed again.[180] The precipitation hardening effect decreases with a decrease in the initial supersaturation of the precipitate-forming elements in this dynamic case.[179]

Enlightened by these existing theories and experimental observations, a new mechanical method for detecting precipitation start and finish times was developed in the present investigation. This technique is based on the analysis of creep behavior at hot working temperatures. As this study demonstrates, it is very sensitive, is not time consuming, and is more effective in ferrite and at high temperatures than the previous methods. Moreover, since the specimen continues to strain in the course of precipitation, industrial rolling operations are more closely simulated when this technique is employed. This method will now be described, together with the results obtained on four Si steels and a Ti steel.

CHAPTER 3

MATERIALS AND EQUIPMENT

3.1 EXPERIMENTAL MATERIALS

3.1.1 STEEL COMPOSITION

Four S-bearing electrical steels were used in the present work for investigating the MnS precipitation behavior during hot deformation. These steels, in the form of 13mm thick hot rolled plates, were provided by Dofasco Incorporated, Hamilton, and the Metals Technology Laboratories of the Department of Energy, Mines and Resources, Ottawa. Their chemical compositions are listed in Table 3.1. The sulfur concentrations ranged from 0.004 to 0.028 in weight percent, with the manganese content varying from 0.042% to 0.125%. The silicon level in the family of materials under study was approximately 3%, which causes these steels to remain ferritic at all temperatures up to the melting point.[3] A Ti steel, which was used in a previous investigation,[77, 120] was also employed for the purpose of comparing the sensitivity of the present technique with that of the stress relaxation

Table 3.1

Chemical Composition in Weight. Percent of the Steels Tested

Steel	C	Si	Ti	Al	Mn	N	P	S
Si Steel A	0.025	3.13	-	0.003	0.070	0.006	0.006	0.021
Si Steel B	0.030	3.04	-	0.004	0.085	0.004	0.003	0.028
Si Steel C	0.029	3.00	-	0.007	0.125	0.003	0.003	0.015
Si Steel D	0.029	3.06	-	0.003	0.042	0.005	0.005	0.004
Ti Steel	0.050	0.27	0.25	0.01	1.43	0.007	0.005	-

method. This steel had a titanium level of 0.25%, with a base composition typical of microalloyed plate steels.

3.1.2 SPECIMEN PREPARATION

Compression samples 12.0 mm in height and 8.0 mm in diameter were machined from the as-received plates, with their longitudinal axes parallel to the rolling direction. The aspect ratio (height-to-diameter) was selected as 1.5 to promote homogeneous deformation.[182, 183] In order to reduce the friction present at the sample/anvil interface during testing, concentric flat-bottomed grooves 0.15 mm deep, 0.36 mm wide and spaced at 0.46 mm intervals were cut into the end faces of these specimens to accumulate the powdered glass lubricants.[184] The lubricants employed in the present work were manufactured by the Corning Glass Co. Ltd. A viscosity of about 10^4 poise at the testing temperature was chosen, according to the suggestions offered by Alder and Phillips.[185] Figure 3.1 illustrates the sample dimensions and groove geometries in detail.

3.2 EXPERIMENTAL EQUIPMENT

The experiments were performed on a computerized materials testing machine set up for hot compression/tension testing. This machine is basically made up of an automated MTS testing system and a Centorr high temperature, high vacuum furnace. An external view of the experimental apparatus is shown in Figure 3.2.

3.2.1 AUTOMATED TESTING SYSTEM

This system is of the single control channel type. It consists of a load frame, a hydraulic power supply, an analog control loop and a computer subsystem.

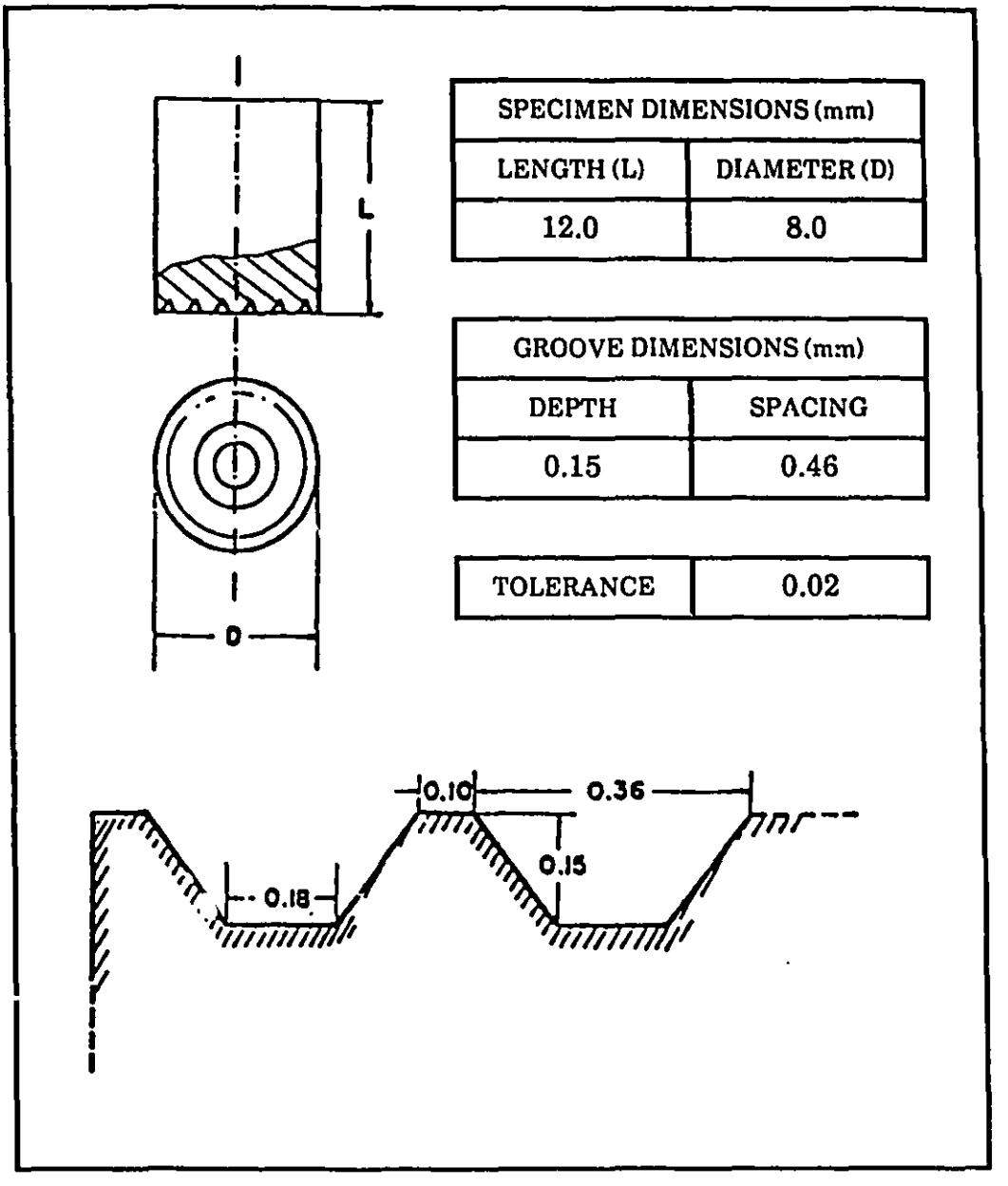

SPECIMEN DIMENSIONS (mm)	
LENGTH (L)	DIAMETER (D)
12.0	8.0

GROOVE DIMENSIONS (mm)	
DEPTH	SPACING
0.15	0.46

TOLERANCE	0.02

Fig. 3.1 Specimen geometry and groove design.

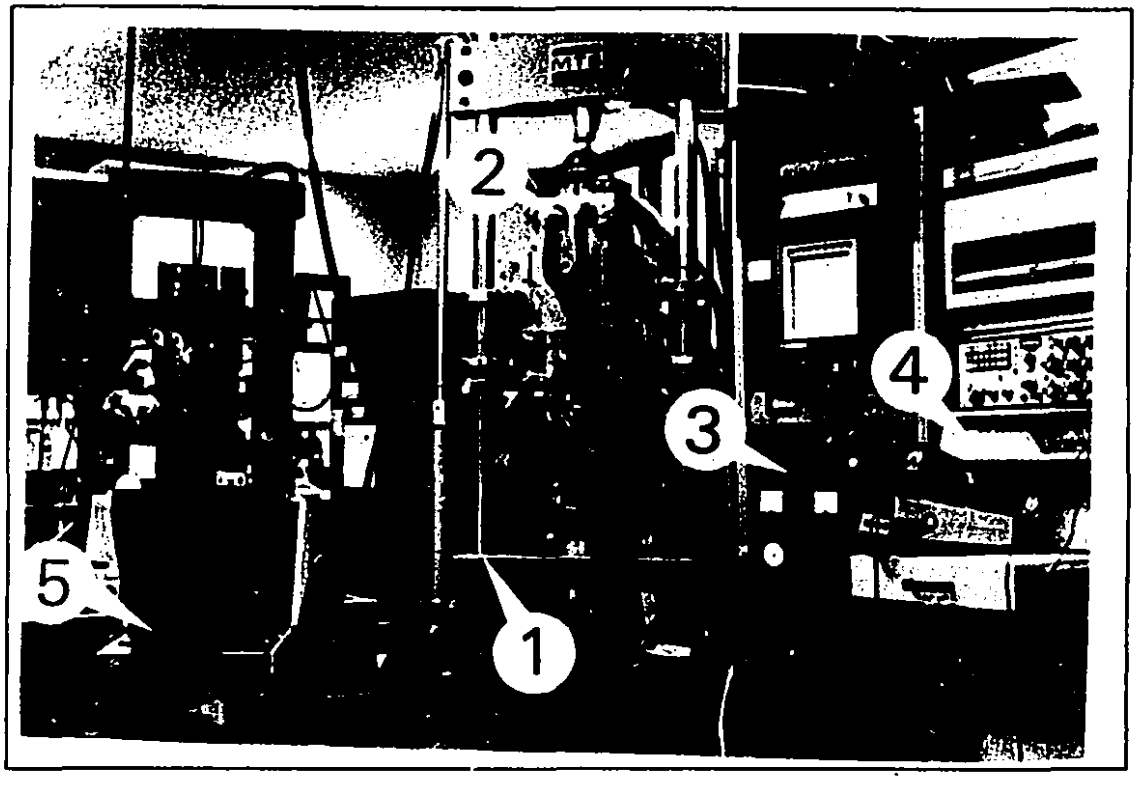

Fig. 3.2 An external view of th· ·ligh temperature compression testing system: (1) MTS load frame; (2) Centc acuum furnace; (3) temperature and vacuum control console; (4) PDP 11/04 computer; and (5) Tektronix terminal.

3.2.1.1 Load Frame and Hydraulic Power Supply

The load frame is rated at 100 kN under static loading conditions. It serves as the mount for the hydraulic actuator, load cell, servovalve, transducers and hydraulic service connections. The hydraulic power supply (HPS) provides a source of hydraulic fluid at a pressure of 3000 psi to the servovalve and the hydraulic service manifold (HSM) for actuator operation. The output flow was adjusted to 38 liters/min.

3.2.1.2 Analog Control Loop

The analog control loop or "test controller closed loop", shown in Figure 3.3 in its simplest form, is a continuous path of interacting elements. As illustrated in this figure, closed loop control compares a command signal (what the actuator is supposed to do) with a feedback signal (what the actuator is actually doing). The polarity and magnitude of the DC error signal derived from this comparison causes the servovalve spool to open in a direction and by an amount necessary to cause a suitable actuator response. As the actuator responds, the feedback approaches the command. When the command and feedback are equal, the DC error is reduced to zero and the servovalve spool closes.

In the MTS servohydraulic system, the command signal for the test system is generated by an MTS function generator. A valve controller converts the DC error signal to the servovalve control signal that causes a force, stress or displacement to be applied to the specimen. To generate the control mode feedback, this quantity is measured by the associated transducers; i.e. the load cell and the linear variable differential transformer (LVDT). The two transducers are linked to their respective conditioners which supply excitation voltages to them and condition the transducer output to generate the control mode feedback signal. The control mode feedback is compared with the input command at the summing junction in the servo controller. The resultant DC error output of the servo controller is applied to

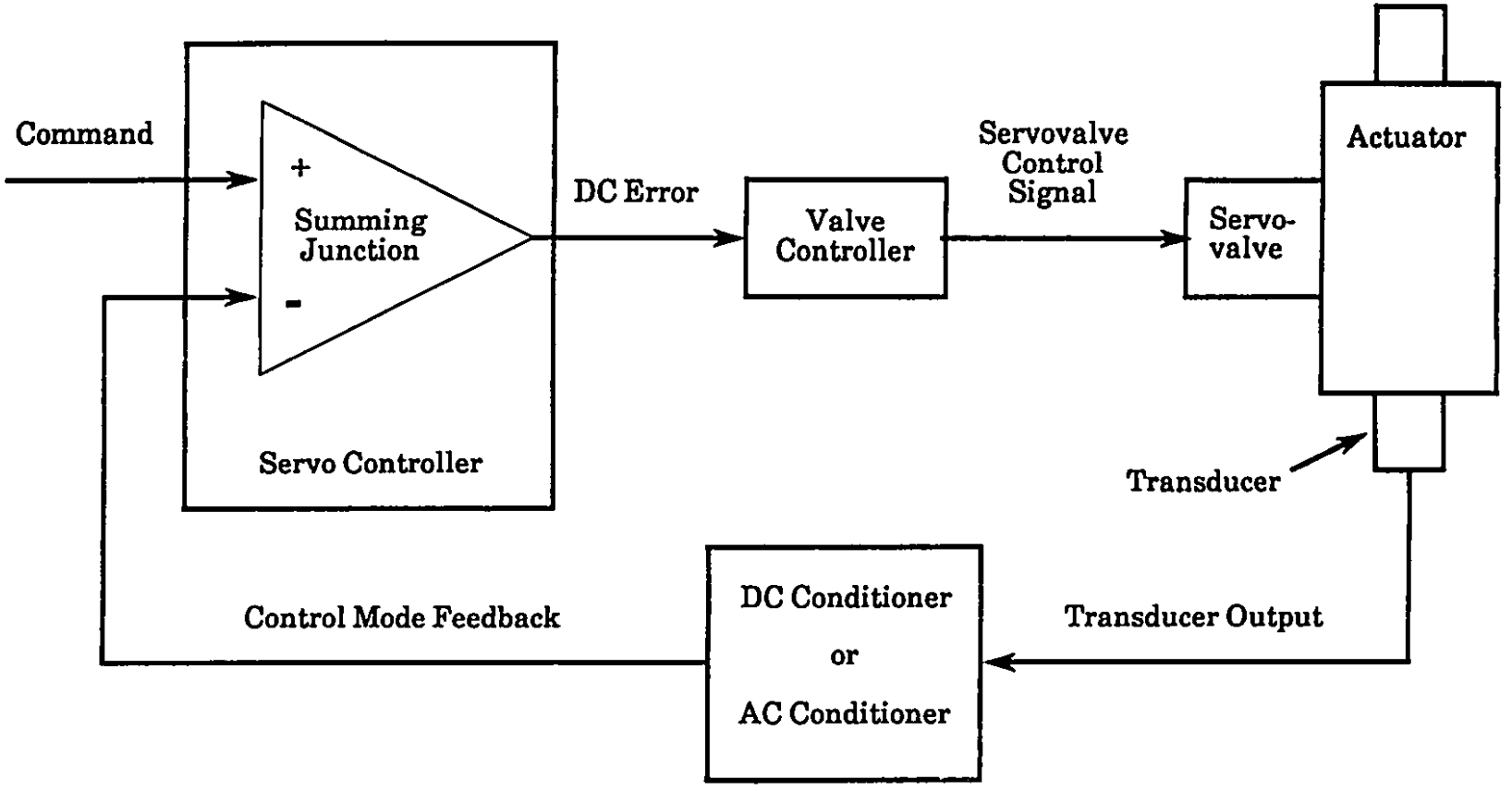

Fig. 3.3 Test controller closed loop control functional.

the valve controller where it is amplified to become the servovalve control signal that drives the servovalve and causes the actuator to respond.

To select the operating range most suitable for an individual test, range selector switches on the transducer conditioners offer the four available ranges; 100, 50, 20, and 10% of the capacity of the transducer. In the present tests, the capacity of the load cell employed was 1000 lbs and the range selected for it was 100%. The gauge length of the LVDT was 100 mm and the range selected for it was 10%.

3.2.1.3 Computer Subsystem

The "automation" in the MTS automated testing system is made possible by the computer/433 subsystem which forms an outer, supervisory loop around the analog control loop. This subsystem performs the functions of command generation, data acquisition, real time decision making and other various system control functions (run/stop, mode switching, etc.). In order to accomplish these functions, there must be communication between the user and the subsystem. This communication is achieved by means of the Digital Equipment Corporation PDP-11/04 minicomputer which has a core memory of 32 k in 16 bit words, the Tektronix 4631 hard copy device, the series 433 processor interface unit, the DEC RX11 disk system with RX02 floppy disk drives, and the system software known as MTS-BASIC/RT-11.

MTS has implemented a number of real-time routines written in assembly language which interface the MTS 433 hardware interface unit and the Tektronix graphics terminal with the MTS BASIC-11 programming language, and other special devices. These routines take the form of external function calls from a mainline BASIC-11 application program using the following format:

10 CALL "function name" (argument 1, argument 2, etc.)

Once initiated by BASIC-11, the Hardware Segment Generator and Data Acquisition functions are driven.

3.2.2 CENTORR HIGH TEMPERATURE VACUUM FURNACE

For high temperature operation in vacuo or a controlled atmosphere, the MTS system is equipped with a 17 kVA Centorr model M60 front loading furnace. This facility consists of the furnace chamber, the Centorr control console, the semi-automatic vacuum pumping system, temperature instrumentation and a helium quenching device. The entire furnace, including the diffusion pump, is mounted on the pillars of the MTS load frame after proper positioning of the furnace and alignment of the tooling.

3.2.2.1 Furnace Chamber

An interior view of the test chamber of the furnace is shown in Figure 3.4. Water flow between the double walls of the furnace chamber assures uniform cooling. A split, vertically oriented, cylindrically-shaped hot zone within the chamber is resistance heated and is surrounded concentrically by the multilayer tungsten and molybdenum radiation shields. The top and bottom ends of the furnace are similarly shielded.

The upper and lower anvils, which are made of the molybdenum alloy TZM, 150 mm high and 32 mm in diameter, are fixed to the actuator piston and load cell respectively through internally water cooled stainless steel extension rods. The specimen is placed coaxially on the lower anvil.

3.2.2.2 Centorr Control Consoles

The Centorr control console contains controls and instrumentation for monitoring and operation. Silicon controlled rectifiers (SRC) provide accurate variation of the power into the hot zone. System and operating protection are provided by failsafe component operations, proper sequencing, interlock of controls, and water flow interlocks.

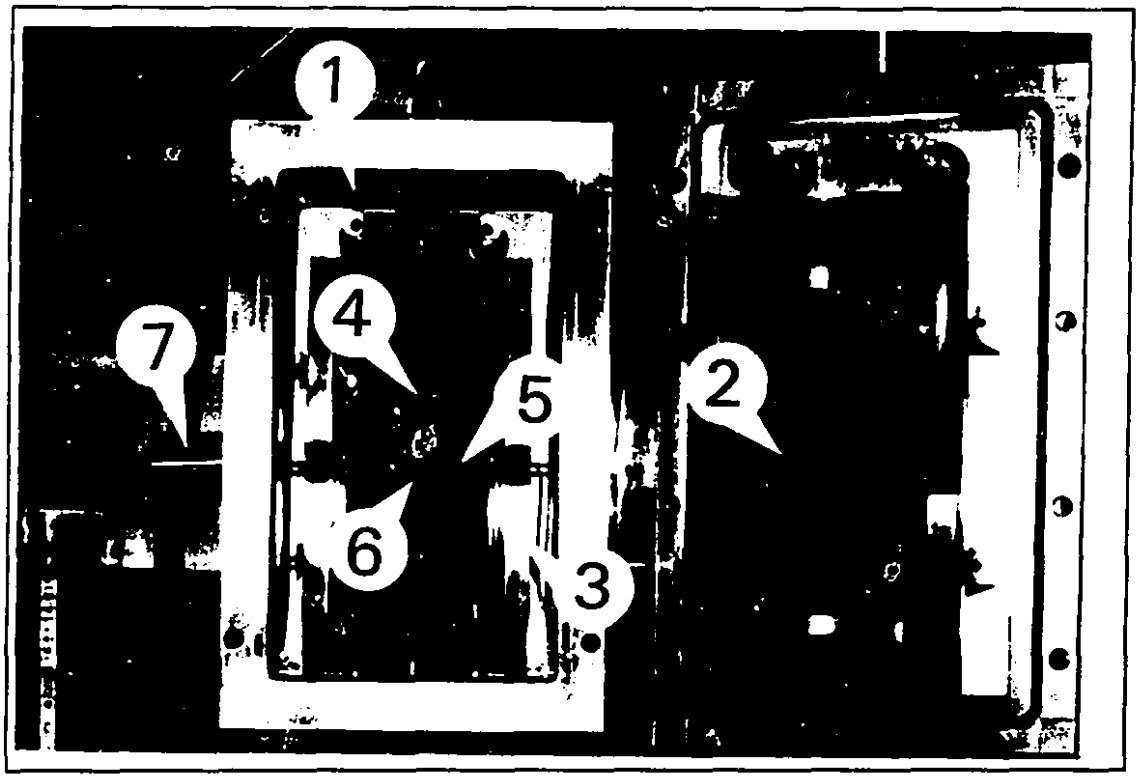

Fig. 3.4 An interior view of the Centorr high temperature, high vacuum furnace: (1) vacuum chamber; (2) tungsten mesh heating elements; (3) shields; (4) TZM anvils; (5) thermocouples; (6) specimen; and (7) specimen pusher.

3.2.2.3 Semi-automatic Vacuum Pumping System

The semi-automatic vacuum pumping system, mainly a 0.1 m high speed diffusion pump backed by an 8.6×10^{-3} m^3/s mechanical pump, enables a relatively high vacuum of 10^{-6} to 10^{-5} torr to be attained in the testing chamber. The pumping system is controlled by a function switch which is interlocked to assure the proper sequential operation of the valves. All the present experiments were carried out in a vacuum better than 10^{-5} torr.

3.2.2.4 Temperature Instrumentation

A J-type plat/plat-10% rhod thermocouple was placed close to the center of the furnace chamber and linked to a Leeds and Northrup (L&N) current adjusting type (CAT) temperature recorder and controller. The CAT controller supplied an output current proportional to the temperature deviation from the set point. To control the temperature in the furnace chamber, the current output of the controller was translated into a power input appropriate to the furnace by means of an SRC (silicon controlled rectifier) power package.

In order to measure the specimen temperature in the present investigation, two K-type Chromel-Alumel thermocouples were used. One of these was employed as the operating thermocouple and placed in contact with the specimen. The other was used for reference and verification, and was not in contact with the sample. The purpose of using a reference thermocouple was to test for failure of the operating thermocouple or for the lack of contact with the specimen and, therefore, to check whether the indicated temperature is correct.

3.2.2.5 Helium Quenching Device

To quench samples for examination of their structures by microscopy, a helium quenching device was designed and installed for the present investigation. The quenching device consists of a sample pusher and a gas

quenching cup. The pusher was mounted on the wall of the furnace chamber, and designed to push the sample down into the quenching cup. The quenching cup was fixed onto the internally water cooled flange outside the hot zone of the chamber. One of the shields on the bottom of the furnace was replaced with a new one which has a hole to allow the sample to pass through.

The quenching procedure used in the present experiments can be described as follows:

(1) shut off the furnace power on completion of the test;

(2) close the valve between the chamber and the diffusion pump immediately after the above procedure;

(3) push the sample down by turning the pusher while opening the electrically operated valve to introduce high purity helium into the quenching cup.

A cooling rate greater than 60 °C/s was achieved in the present samples by using the quenching device in this way.

CHAPTER 4

DEVELOPMENT OF THE CREEP METHOD

4.1 SOLUTION TREATMENT

As reviewed at the end of Chapter 2, it has frequently been reported that precipitation takes place during deformation when creep tests are carried out on solution treated materials. Such strain-induced precipitation has a great influence on the shape of creep curves. In view of these experimental observations, a solution treatment was performed immediately prior to the testing of each specimen. This treatment led to:

1) the complete dissolution of the sulfides in the electrical steels and of the C-rich carbonitride in the Ti steel;

2) about the same initial grain size in all the S-bearing electrical steels tested; and

3) stable microstructures in the tested steels before the application of the load.

4.1.1 THE DETERMINATION OF SOLUTION TEMPERATURES

4.1.1.1 Evaluation of the Equilibrium Dissolution Temperatures

In order to select the experimental conditions for solution treatment, it is essential to have information about the equilibrium dissolution temperature of each steel. Referring back to the previous results described in §2.2.2 regarding the MnS solubility product in electrical steels, the expression

$$log\ (L_{MnS}) = -\frac{9{,}800}{T} + 3.74 \qquad (2.8)$$

was selected for this purpose because its predictions, as demonstrated by Petrova et al.,[70] coincide satisfactorily with the experimental observations for a wide range of manganese and sulfur concentrations. The equilibrium dissolution temperatures evaluated by using this equation for MnS in the electrical steels tested in this study were 1031 °C for electrical steel D, 1218 °C for electrical steel A, 1242 °C for electrical steel C and 1249 °C for electrical steel B. For the 0.25% Ti steel, the equilibrium dissolution temperature of TiC was already calculated by Liu[77] to be 1208 °C.

To ensure the first objective of the solution treatment, the complete dissolution of the particles present in the as-received plates, the actual solution temperature should be raised approximately 50 °C above the estimated equilibrium dissolution temperature.[77, 148] This is why the following solution temperatures were at first selected in the present work: 1300 °C for electrical steels B and C, 1270 °C for electrical steel A, 1260 °C for the Ti steel, and 1080 °C for electrical steel D.

4.1.1.2 Temperature-Grain Size Relationship

For the second and third purposes of the solution treatment, i.e. to produce the same initial grain size and stable microstructures prior to loading in the four electrical steels, the reheating temperature versus mean grain size relationship was determined for these materials. Individual samples were reheated to different temperatures, held at temperature for half an hour and then water quenched. The information concerning the grain growth rates and equilibrium microstructures was acquired by means of optical microscopy.

Two sets of typical micrographs showing the same areas in two specimens are presented in Figures 4.1 and 4.2. The first specimen was taken from the 0.085% Mn-0.028% S steel and the second from the 0.070% Mn-0.021% S grade. Both specimens were first photographed before starting the heat treatment (see Figures 4.1a and 4.2a) and then inspected again after reheating at 1200 °C for half an hour (see Figures 4.1b and 4.2b). By comparing the two micrographs, it is apparent that grain boundary migration and grain growth took place during the heat treatment. As a means of measuring the grain size and grain growth rate in these microstructures, the linear intercept method was applied to twenty micrographs of each specimen. The dependence of mean grain size on reheating temperature for the four steels obtained in this way is presented in Table 4.1 and Figure 4.3. It is clear that the mean grain size increases as the reheating temperature is increased. In general, this situation arises because the grain boundary mobility increases as the temperature is increased. In the present case, the increase in the mean grain size is also associated with the temperature dependence of two of the inhibiting features:

1) the dissolution and coalescence of the dispersed MnS particles at elevated temperatures;

2) the decrease in the equilibrium amount of sulfur segregated at the grain boundaries as the temperature is increased.

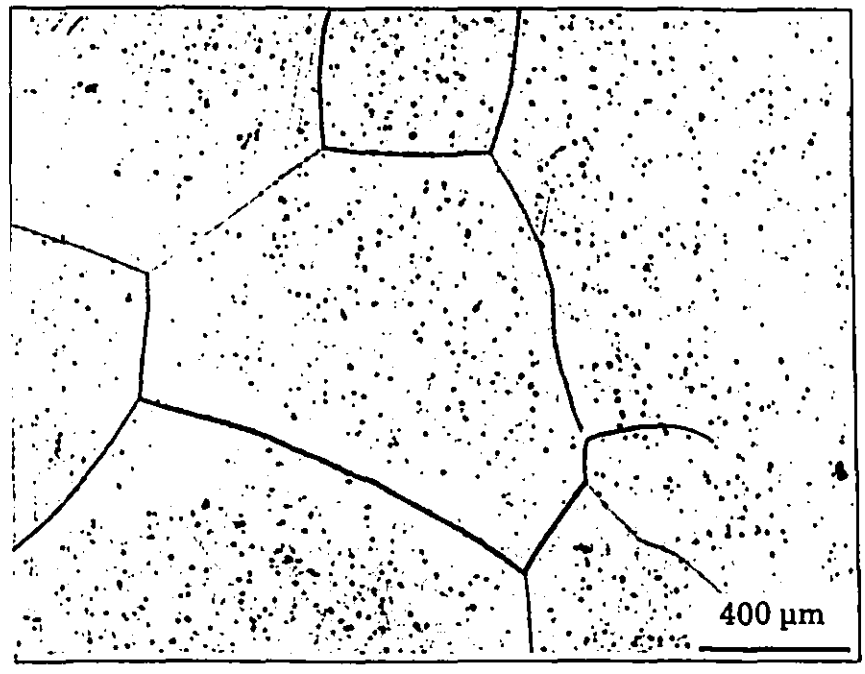

(a)

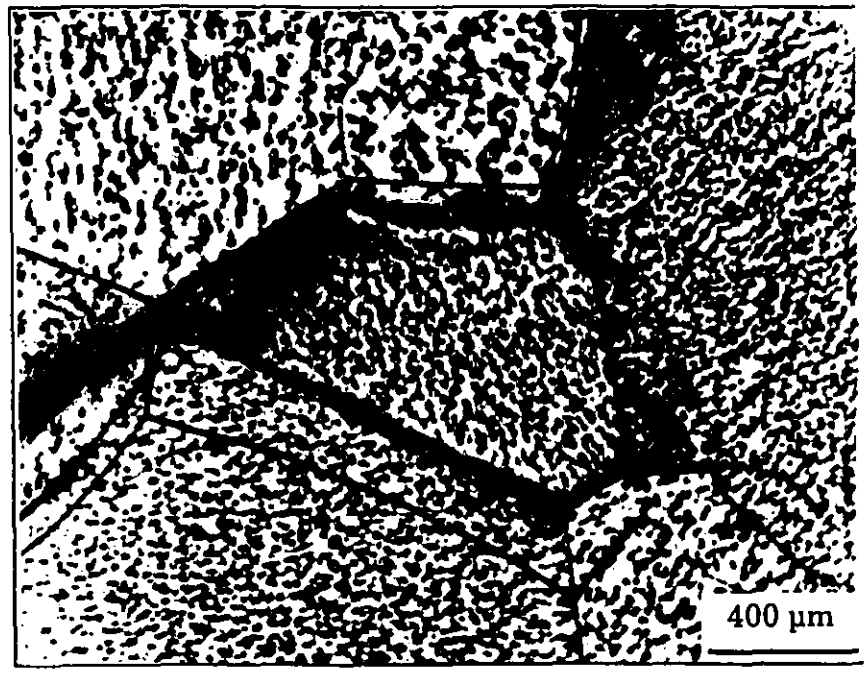

(b)

Fig. 4.1 Grain boundary migration during reheating in the case of the 0.085% Mn-0.028% S steel: (a) at room temperature, and (b) after reheating at 1200 °C for 30 minutes.

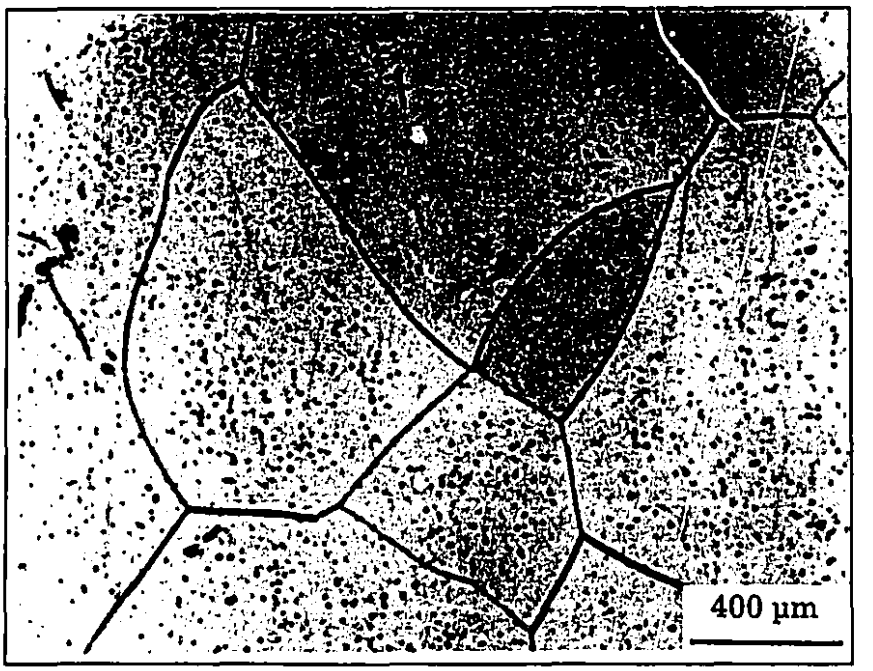

(a)

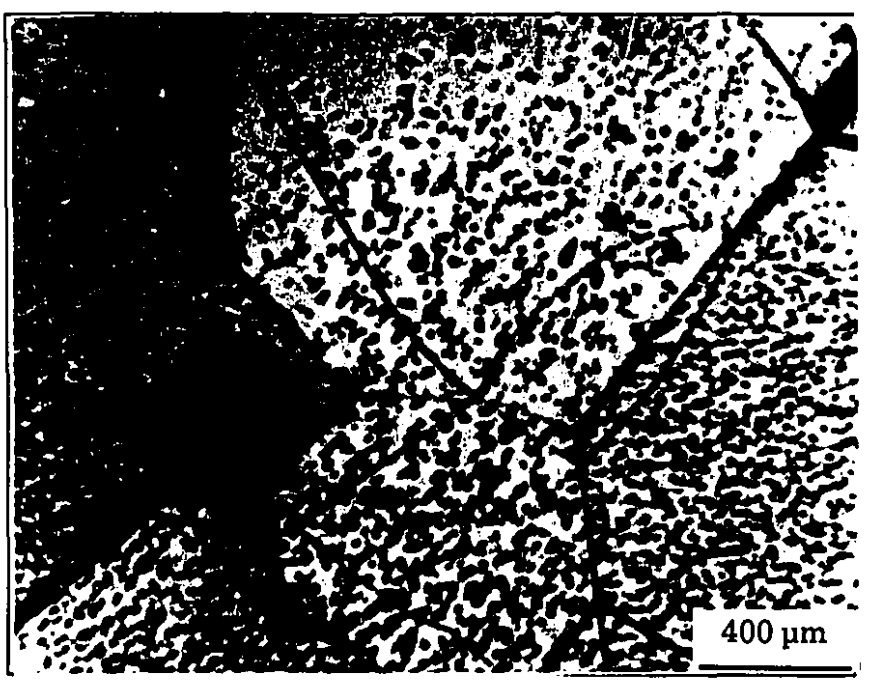

(b)

Fig. 4.2 Grain boundary migration during reheating in the case of the 0.070% Mn-0.021% S steel: (a) at room temperature, and (b) after reheating at 1200 °C for 30 minutes.

Table 4.1
The Dependence of Grain Size in the Electrical Steels on the Reheating Temperature

Temperature (°C)	Grain Size (mm)			
	0.004% S	0.015% S	0.021% S	0.028% S
1100	1.7±0.19	1.3±0.16	1.0±0.12	0.7±0.11
1200	1.9±0.21	1.5±0.18	1.4±0.18	1.1±0.15
1300	2.4±0.28	2.1±0.25	2.0±0.23	1.9±0.21
1350	3.2±0.38	3.0±0.32	3.0±0.31	2.9±0.29

These findings are illustrated in Figure 4.3, which shows that, at a given temperature, the mean grain size decreases as the sulfur concentration is increased. However, when the temperature reaches 1300 °C and above, the difference in mean grain size in the three steels containing 0.015, 0.021 and 0.028% S is not large and falls into the error interval. This can be clearly seen from the data listed in Table 4.1. Since increasing the grain size means decreasing the grain-boundary area and hence decreasing the total grain boundary interfacial energy per unit volume of the specimen, the residual driving force for further growth will automatically decrease with grain growth. Thus, the above observations indicate that the driving force for grain growth in each of these steels is no longer sufficient to sustain further growth when the microstructure attains a certain size. In other words, the thermodynamic stability associated with the largest possible practical grain size in these steels can be obtained after half an hour of reheating at this temperature. The mean grain size of the 0.004% S steel at 1200 °C is comparable to those of the three other electrical steels at 1300 °C.

Taking the above experimental results into account, only three different solution temperatures were finally chosen in the present work: 1200 °C for electrical steel D (0.042% Mn-0.004 %S), 1260 °C for the 0.25% Ti steel, and

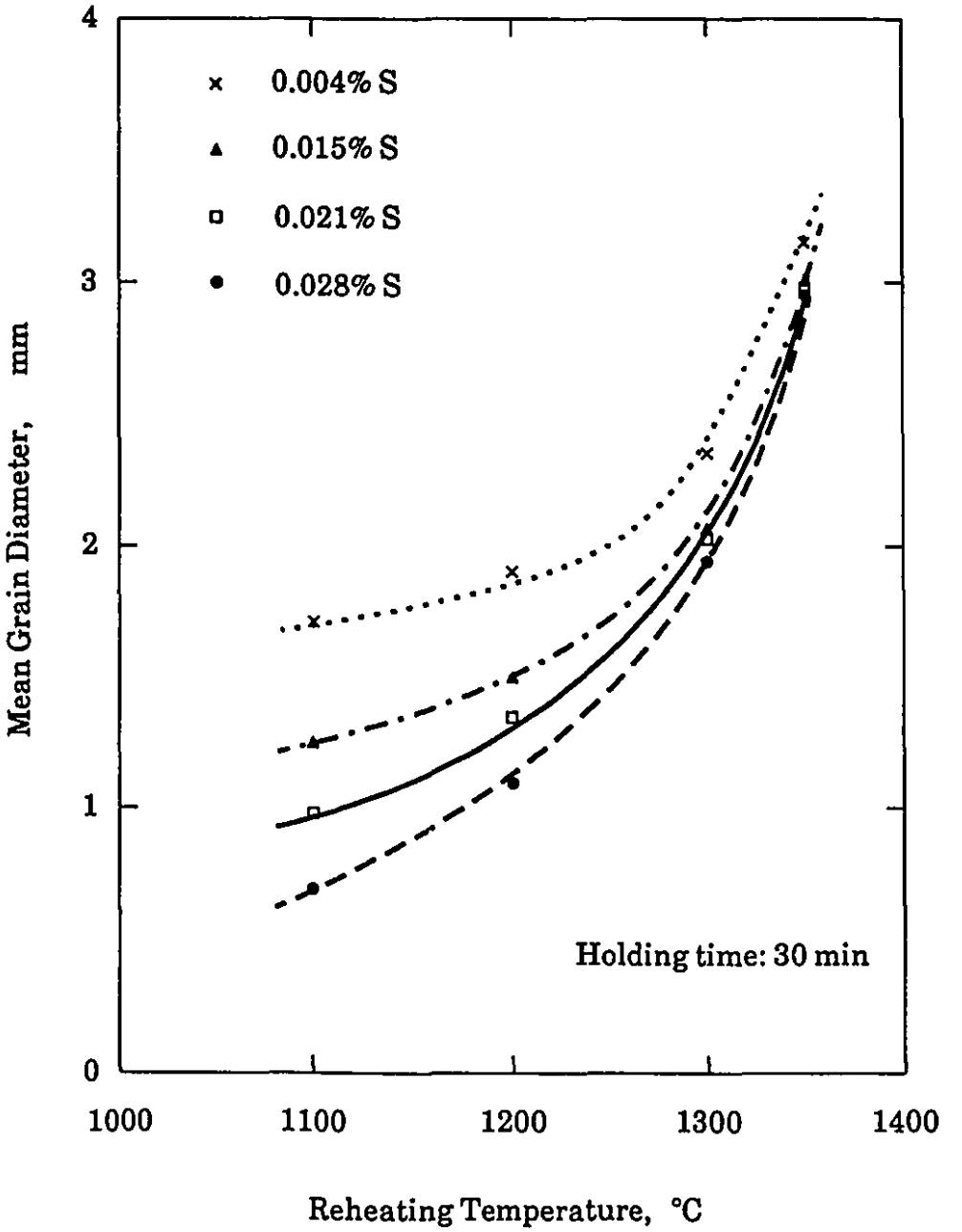

Fig. 4.3 Dependence of the mean grain size on reheating temperature in the four electrical steels.

1300 °C for the other three steels. The solution time employed in the actual tests was also half an hour, since it was considered to be long enough to dissolve the small particles[77] and to stabilize the microstructure.[148]

4.1.2 MEASUREMENT OF THE COOLING RATE AFTER SOLUTION TREATMENT

After solution treatment, each specimen was immediately cooled to the test temperature by switching off the furnace power supply. The time required for the specimen to cool from its solution temperature to different test temperatures was repeatedly measured by means of the operating thermocouple. The results revealed that the temperature can be expressed as an exponential function of time in the range from 1300 °C to 800 °C:

$$T = A\,exp(-\alpha t) \quad (°C) \tag{4.1}$$

where T is the temperature, t is the cooling time, and A and α are constants which depend on the initial temperature, or the solution temperature. The repeatability of this function was excellent as long as the thermocouple was in good contact with the specimen. As an example, some typical results showing the temperature-time relationship for a specimen cooled from 1300 °C to the test temperatures are presented in Figure 4.4. The nonlinear regression fitting of these results led to the following equation:

$$T = 1300\,exp(-0.002t) \quad (°C) \tag{4.2}$$

For simplicity, the mean cooling rate of each specimen can be taken as approximately 2 °C/s in the present experimental range.

4.2 STRESS RELAXATION TESTING

As previously mentioned, the stress relaxation method is particularly well suited for following precipitation in austenite because it is relatively

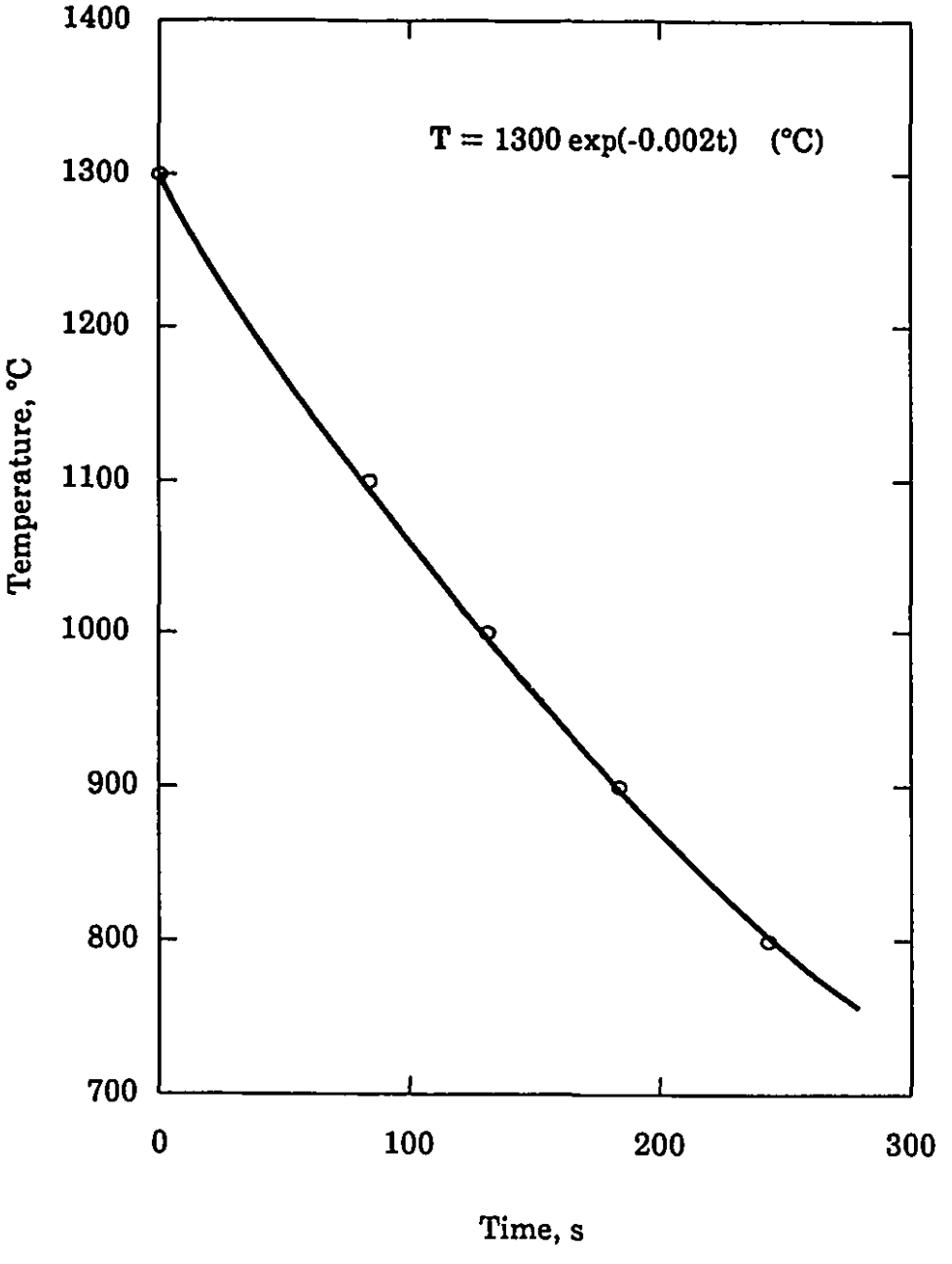

Fig. 4.4 Decrease in furnace temperature after switching off the power supply.

accurate, not very time consuming, and does not involve large sampling errors. Indeed, in the early stages of the present investigation, an initial attempt was made to employ this method to determine the kinetics of MnS precipitation in electrical steels A, B and C. The thermomechanical treatment schedule for this purpose is shown in Figure 4.5. Before prestraining, solution treatment was carried out on each specimen at 1300 °C. After such treatment, the specimen was immediately cooled to the test temperature along the exponential of Eq. (4.1). The test temperatures employed in these experiments were 800 °C, 900 °C and 1000 °C. As soon as the test temperature was reached, a prestrain of 5 percent was applied at a true strain rate of 0.1 s^{-1}. Following such a prestrain, stress relaxation was begun and monitored by the program previously developed by Liu and Jonas for the case of precipitation in austenite.[147]

The stress relaxation data obtained in this way should result in a combination of the basic logarithmic curve and a stress increment caused by precipitation, $\Delta\sigma$; i.e. in[77]

$$\sigma = \sigma_o - \alpha \ln(1 + \beta t) + \Delta\sigma \qquad (4.3)$$

According to Liu[77] and Djahazi,[78] the first point at which $\Delta\sigma$ starts to differ from zero, and the point where $\Delta\sigma$ has its maximum value can be taken to represent the precipitation start and finish times, respectively.

However, the stress relaxation results obtained on the present electrical steels showed that the stress decreased sharply to near zero about one second after prestraining, as illustrated in Figure 4.6. This indicates that the internal stress in the specimens was almost entirely relaxed well before the start of MnS precipitation and thus the stress increment $\Delta\sigma$ could not be detected in the later stages of the relaxation. As a result, neither the initiation nor the completion of MnS precipitation could be detected by the stress relaxation method in the electrical steels . A detailed explanation of why this method is not effective for investigating the precipitation events occurring in the ferrite phase is given in Chapter 8.

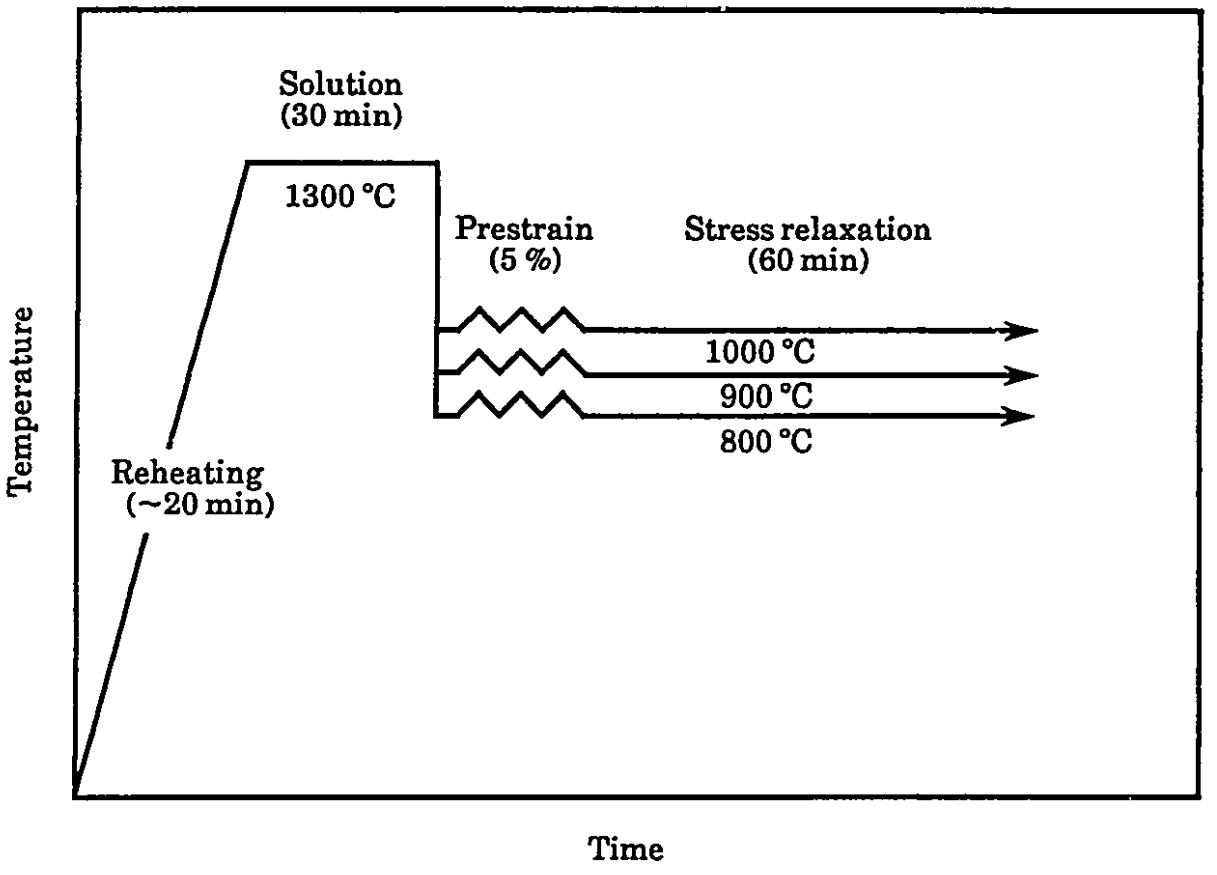

Fig. 4.5 Thermomechanical treatment schedule for stress relaxation testing.

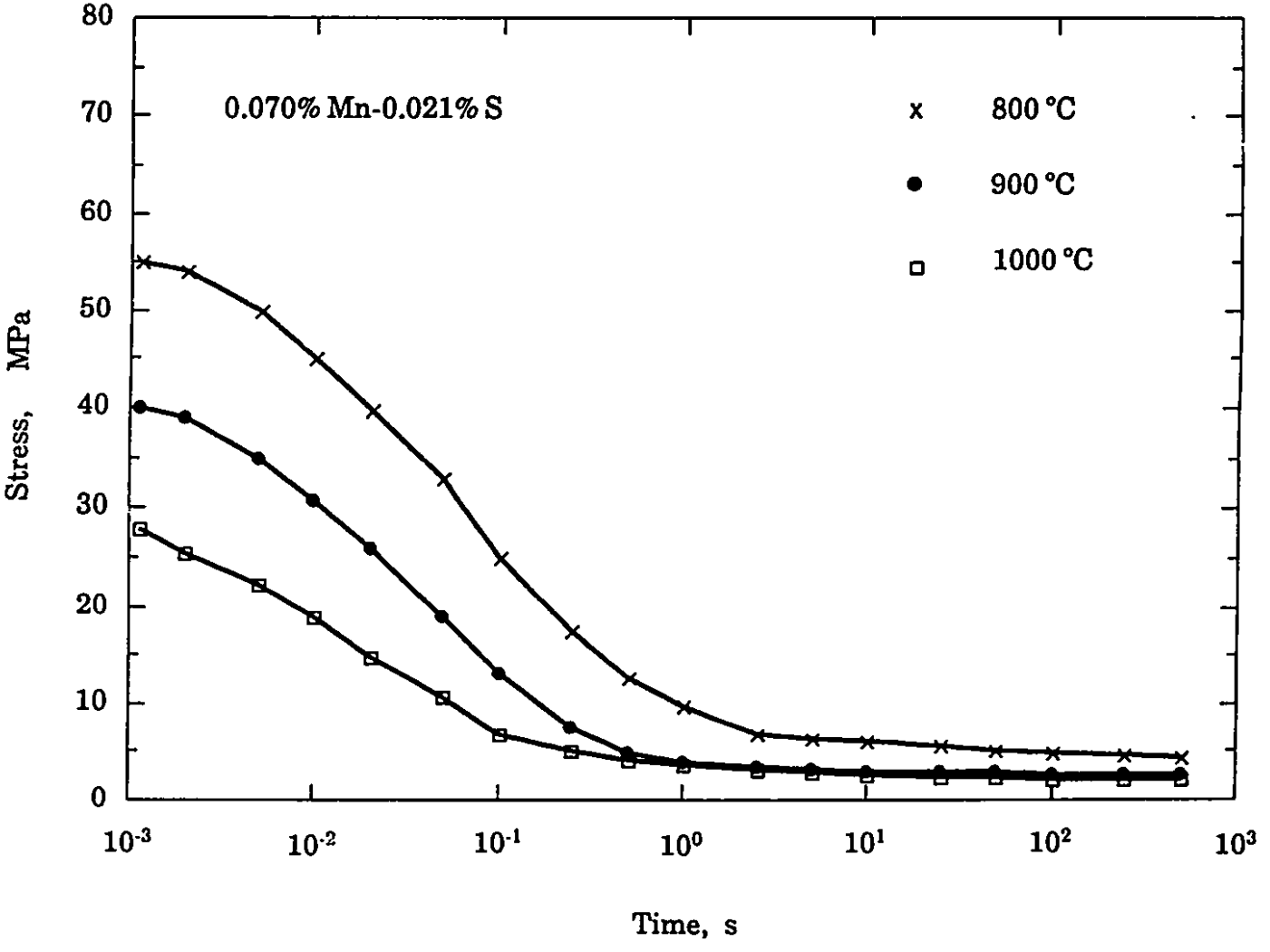

Fig. 4.6 Typical data obtained during the stress relaxation of the 0.070% Mn-0.021% S steel after a 5 percent prestrain at 800 °C, 900 °C and 1000 °C.

4.3 A NEW CREEP TECHNIQUE FOR INVESTIGATING PRECIPITATION DURING HOT DEFORMATION

After the failure of the stress relaxation method to detect MnS precipitation in the electrical steels, an effort was made to find an alternative mechanical technique suitable for investigating the progress of precipitation in these ferritic steels, as well as in other austenitic steels. The method of creep testing described below was developed in response to this objective.

4.3.1 THERMOMECHANICAL TREATMENT SCHEDULE

The thermomechanical treatment schedule used for the present creep tests is presented in Figure 4.7. As in the schedule outlined above for the stress relaxation tests, each specimen was solution treated prior to the application of the load for half an hour at the solution temperature selected for each steel and described in §4.1.1. As soon as the solution treatment was completed, the specimen was cooled to the test temperature by shutting off the furnace. The test temperatures ranged from 800 °C to 1100 °C for the electrical steels and from 900 °C to 1100 °C for the Ti steel. On attaining the test temperature, a holding interval of 1 minute was employed to permit the specimen temperature to become uniform. A constant stress was then applied to the specimen for up to 1 hour and the strain was recorded continuously. A detailed description is given in §4.3.3. During each creep test, the temperature was held constant to within ± 1 °C.

4.3.2 CALIBRATION OF THE TOOLING CONTRACTION

Since cooling from the solution to the test temperature is involved in the current experiments, the machine tooling unavoidably contracts as the temperature is decreased. Hence, the creep data from unmodified tests would contain a contribution from the temperature-induced contraction, which would obviously interfere with the determination of the precipitation kinetics during the first few hundred seconds of deformation. To correct for the length change

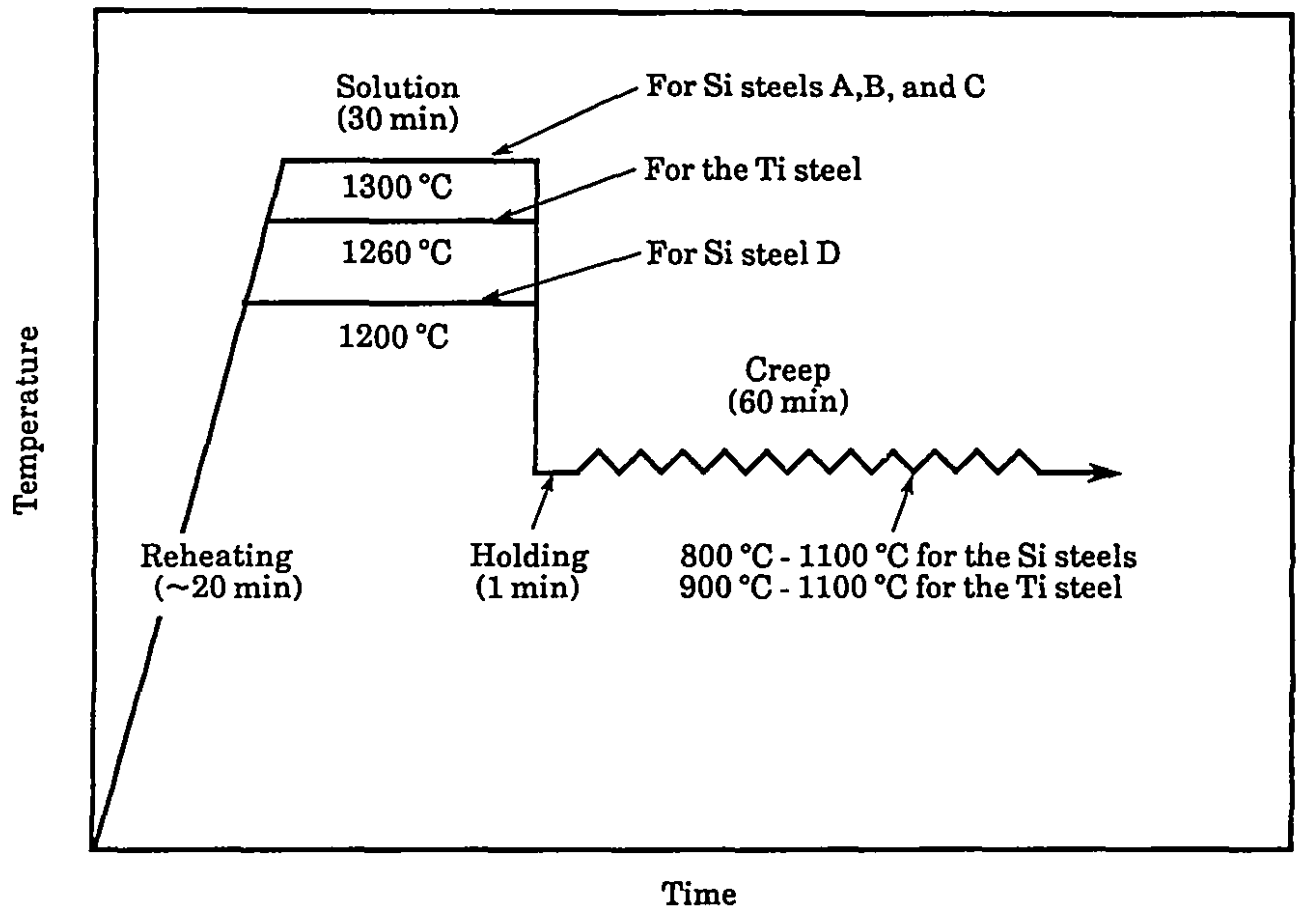

Fig. 4.7 Thermomechanical treatment schedules for the creep tests.

contribution from the cooling, the ram displacement due to the temperature decrease must first be acquired as a function of time. This problem was solved by using the so-called "dummy test piece method", which was first devised by Liu and Jonas for stress relaxation testing.[147] However, it was modified in the present work. The most important features of the method include:

1) A ceramic (Al_2O_3) dummy specimen with the same dimensions as the steel samples was used so that the contraction of the specimen due to cooling could be ignored.

2) The tools passed through the same temperature cycle during "dummy testing" as during an actual creep test.

3) A constant load of only 1 kg was applied to the dummy specimen.

4) For each test temperature, the measured ram displacements were stored as axial contractions of the tooling. These data were employed for correction of the raw creep data by subtracting the tool length decrease from the apparent creep strain.

The software used for the above operations during stress relaxation testing was separate from the master program, thus unnecessarily complicating the procedure. The improvement introduced by the present researcher consists of simplifying this software so that the correction routine can be incorporated directly into the master monitoring program. This modification is described in more detail in the next subsection. For simplicity , only the corrected creep data are reported below.

4.3.3 COMPUTER MONITORING AND DATA ACQUISITION

The computer monitoring of and data acquisition for the present creep tests were programmed in MTS BASIC/RT 11 (see §3.2.1.3); this program is listed in Appendix I. A number of real-time routines, such as mode switching (MSW1), dump circuit (EDMP and SDMP), analog command output (FG1), data acquisition (DACQ), data saving (AOUT), data recalling (AINP) and

certain graphics functions (PHYL, SCAL, AXES, LABL, CPOS, CNTR and COMM), were written in assembly language and also used in this program.

The flow chart of the creep test monitoring program is illustrated in Figure 4.8. As soon as solution treatment of the specimen was completed, the test was automatically carried out by inputting "yes" on the keyboard of the Tektronix terminal. As shown in this figure, the MSW1 routine was switched to the stroke control mode in the present program. Before cooling, an automatic dump check was carried out to prepare for the application of the load. When the cooling operation began, "yes" was input simultaneously with the shutting off of the furnace power. The cooling time was recorded from this point on. This elapsed time was compared with that required for the specimen to cool from its solution temperature to the test temperature plus 1 minute for temperature stabilization (see §4.3.1). During this period, the positioning loop was continuously in operation so as to keep the surface of the upper anvil in contact with the specimen.

As soon as temperature stabilization was achieved, the program exited from the positioning loop and a constant preset stress σ_s was applied to the specimen. It is important to note that the preset stress must be carefully selected if precipitation is to be detected by the present creep technique. A more extensive account of the determination of the stress will be made in the next subsection. During straining, both the current stress and the true strain were continuously measured and read into the computer by calling the DACQ routine. According to the value of the measured stress, i.e. whether it was smaller or 1 percent greater than the preset stress σ_s, or was within 1 to 1.01 σ_s, argument I of FG1 was replaced by a new value, i.e. I=I-1, I=I+1, or I=I, respectively. Consequently, the piston was made to move down 1 machine unit (1/204.7 mm), or up the same distance, or was maintained at its original position. As a result, the applied stress increased, decreased or maintained its previous value. The same procedure was repeated continuously so that the applied stress did not differ by more than 1 percent from the preset value during the whole period of the test. In this way, a total of 125 pairs of stress and true strain data points were sampled and recorded during each test. To save memory space in the computer and distribute the mean values of these experimental data points smoothly along the log(time) scale, the length of the

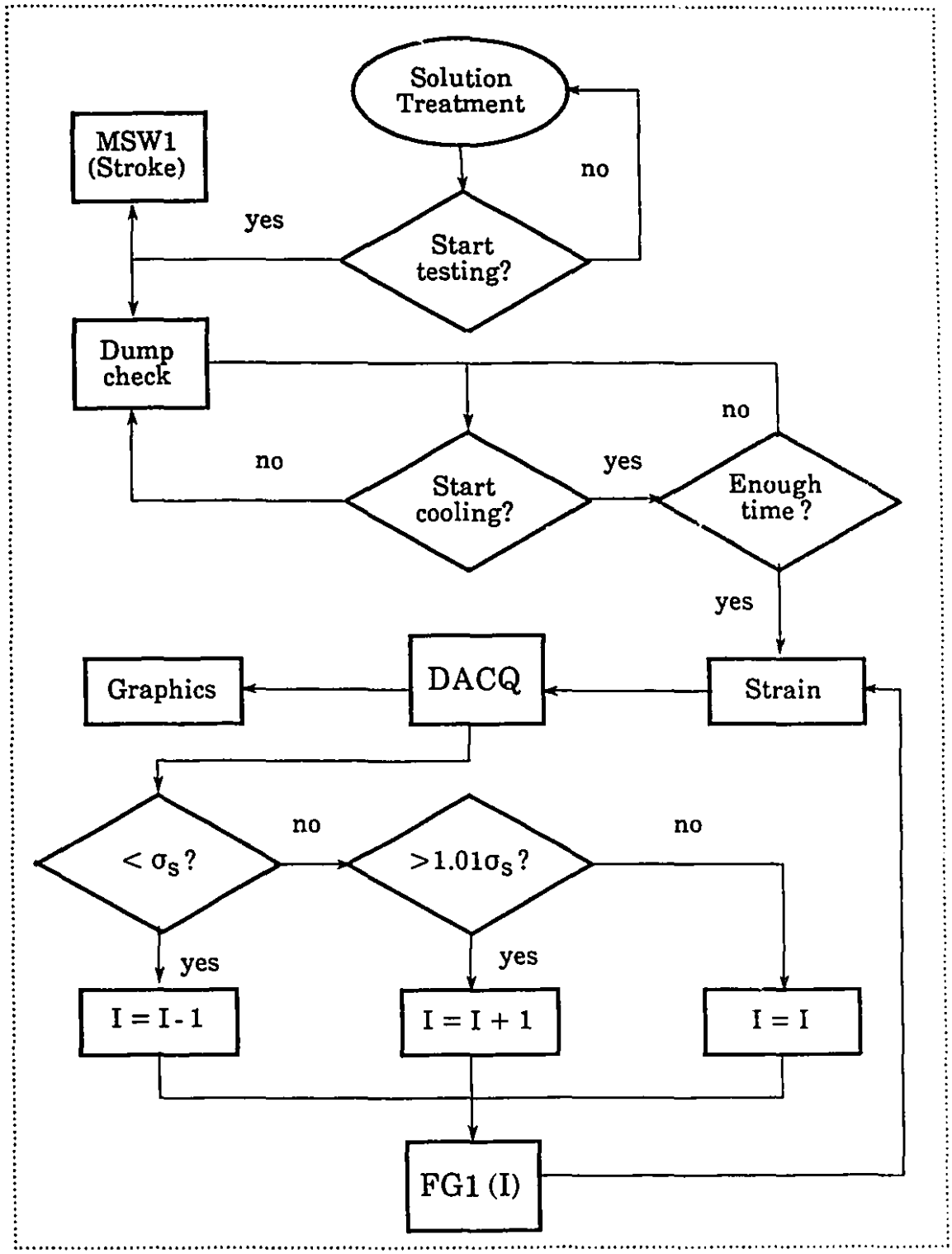

Fig. 4.8 Flow chart of the creep test monitoring program.

datum interval was designed so that it increased with elapsed time. When these experimental results were printed, several graphics routines interfaced the program with the Tektronix 4010 graphics terminal and the Tektronix 4631 hardcopy device for scaling the X, Y ranges, labeling the X, Y axes and plotting the X,Y coordinate related data.

4.3.4 DETERMINATION OF THE PRESET STRESS FOR EACH EXPERIMENT

As mentioned in the preceding subsection, the level of the preset stress must be carefully selected if precipitation events are to be investigated by means of the present creep method. On a trial basis, it was found that the creep rate is sensitive to the occurrence of precipitation when the applied stress corresponds to the steady state stress of the steel hot compressed at a strain rate of about 10^{-4} s^{-1}. Thus, preliminary tests were first carried out to determine the flow curves of the steels at a strain rate of 10^{-4} s^{-1} directly at each temperature of interest without employing any prior solution heat treatment. The computer monitoring program for these tests is listed in Appendix II. As an example, one of the true stress-true strain curves established in this way at 900 °C is shown in Figure 4.9 for electrical steel A. Here, the steady state stress in the region in which the net rate of work hardening is approximately zero is readily seen. The values defined in this way were employed as applied stresses for each test temperature of interest.

4.3.5 CONVENTIONAL CREEP TESTING

In order to define the basic shapes of the creep curves for the electrical steels, conventional creep testing was carried out. Some results for electrical steel A are illustrated in Figure 4.10a. In this case, the thermomechanical treatment shown in the inset was carried out. The test was performed at 900°C after half an hour of aging at the same temperature so that no precipitation took place during deformation. During such tests, the steel was stressed at 900°C for as long as one hour. Figure 4.10a shows that, after a primary stage of creep lasting for a few hundred seconds, the creep rate remains

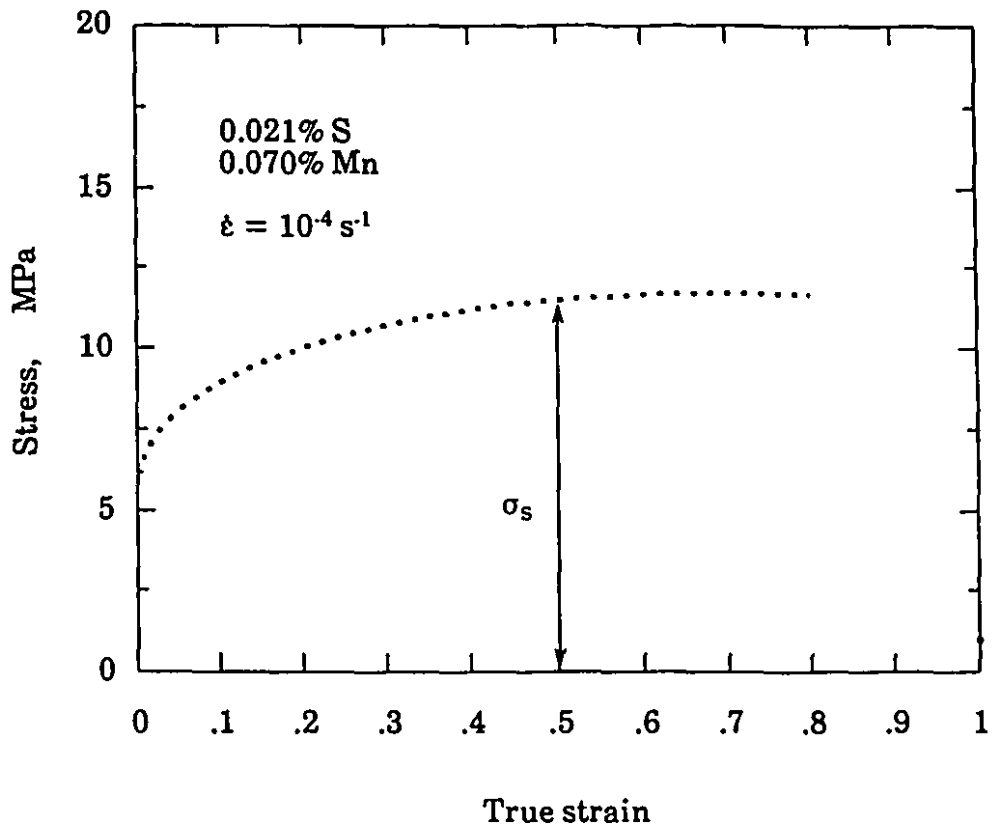

Fig. 4.9 Typical flow curve obtained at a strain rate of 10^{-4} s^{-1} in electrical steel A at 900 °C.

approximately constant during the secondary stage of creep until the end of the test. When the data are plotted in terms of strain *vs* log(time), as in Figure 4.10b, it is evident that the true strain increases smoothly as log(time) increases, and no plateau is present on this curve.

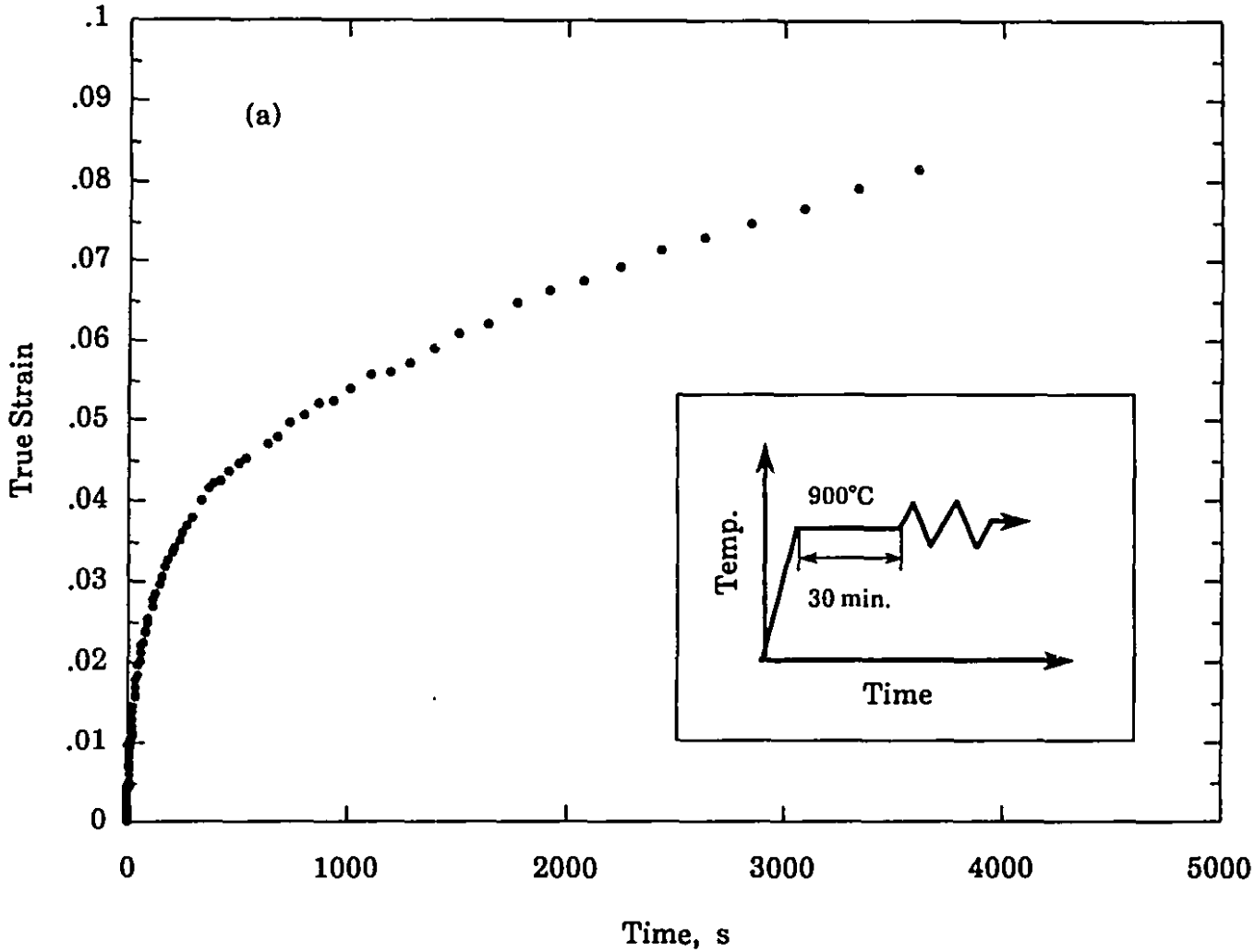

Fig. 4.10 Typical true strain curve obtained during the conventional creep testing of electrical steel A at 900 °C. The data are plotted against (a) time and (b) log(time).

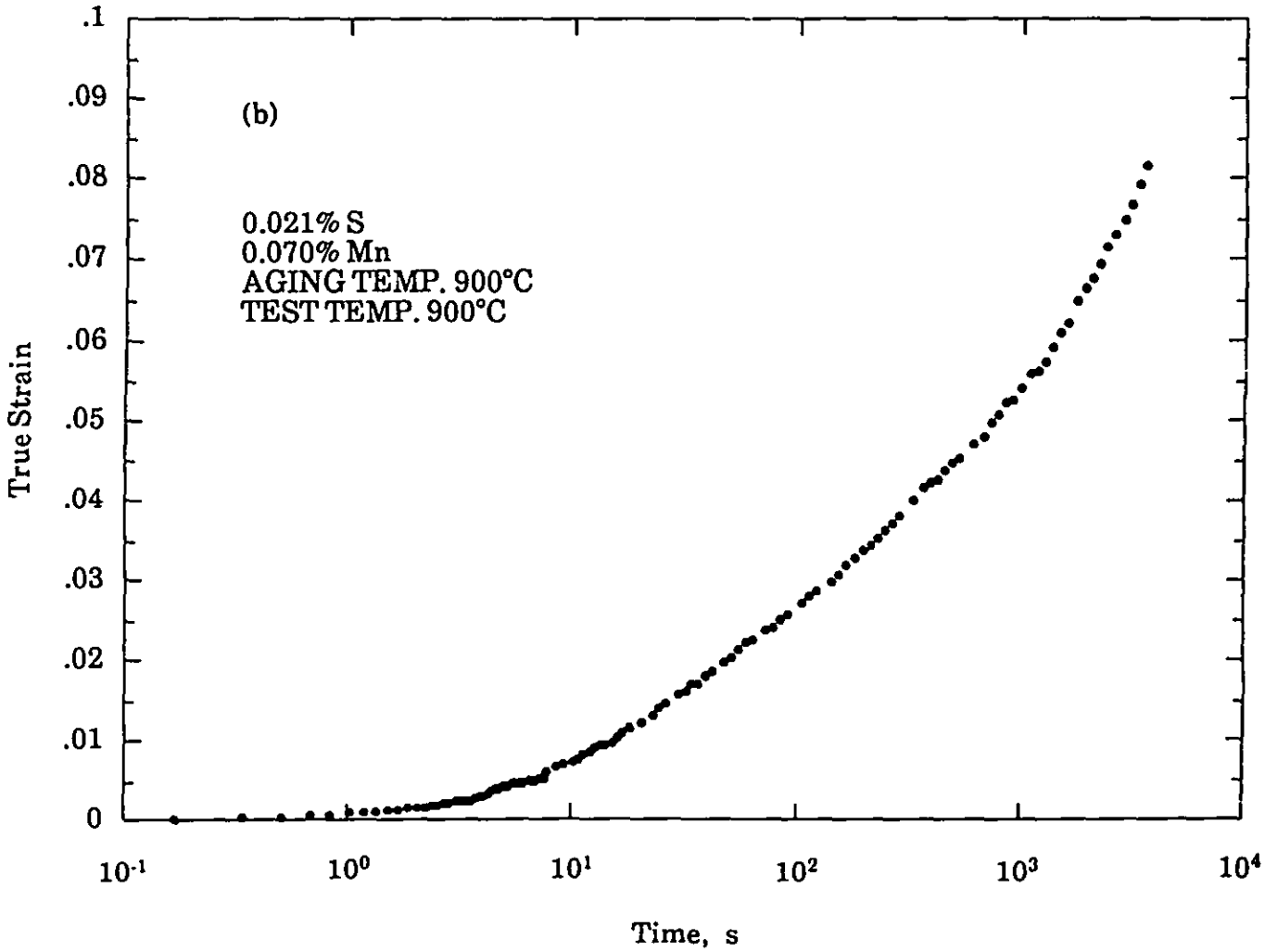

Fig. 4.10 Typical true strain curve obtained during the conventional creep testing of electrical steel A at 900 °C. The data are plotted against (a) time and (b) log(time).

4.3.6 A TYPICAL EXPERIMENTAL CURVE

Figure 4.11 illustrates some typical creep data acquired by the present technique on electrical steel A at 900°C when precipitation is taking place. From this figure, it can be seen that the creep curve recorded under these conditions departs from the generally observed, i.e. conventional behavior. The slope of the creep strain vs. log(time) curve first increases during loading and then decreases after about 15 s of creep. The slope begins to increase again at about 420 s. The points on the curve at which the plateau begins and ends, as will be demonstrated in more detail in the next chapter, can be attributed to the occurrence of precipitation during creep. By identifying these two points as P_s (precipitation start time) and P_f (precipitation finish time), the precipitation-time-temperature relationships for MnS in the four electrical steels and Ti(CN) in the 0.25% Ti steel were established in the present investigation. The mechanical test results are presented in the next chapter, together with some illustrative photographs obtained by means of optical and electron microscopy.

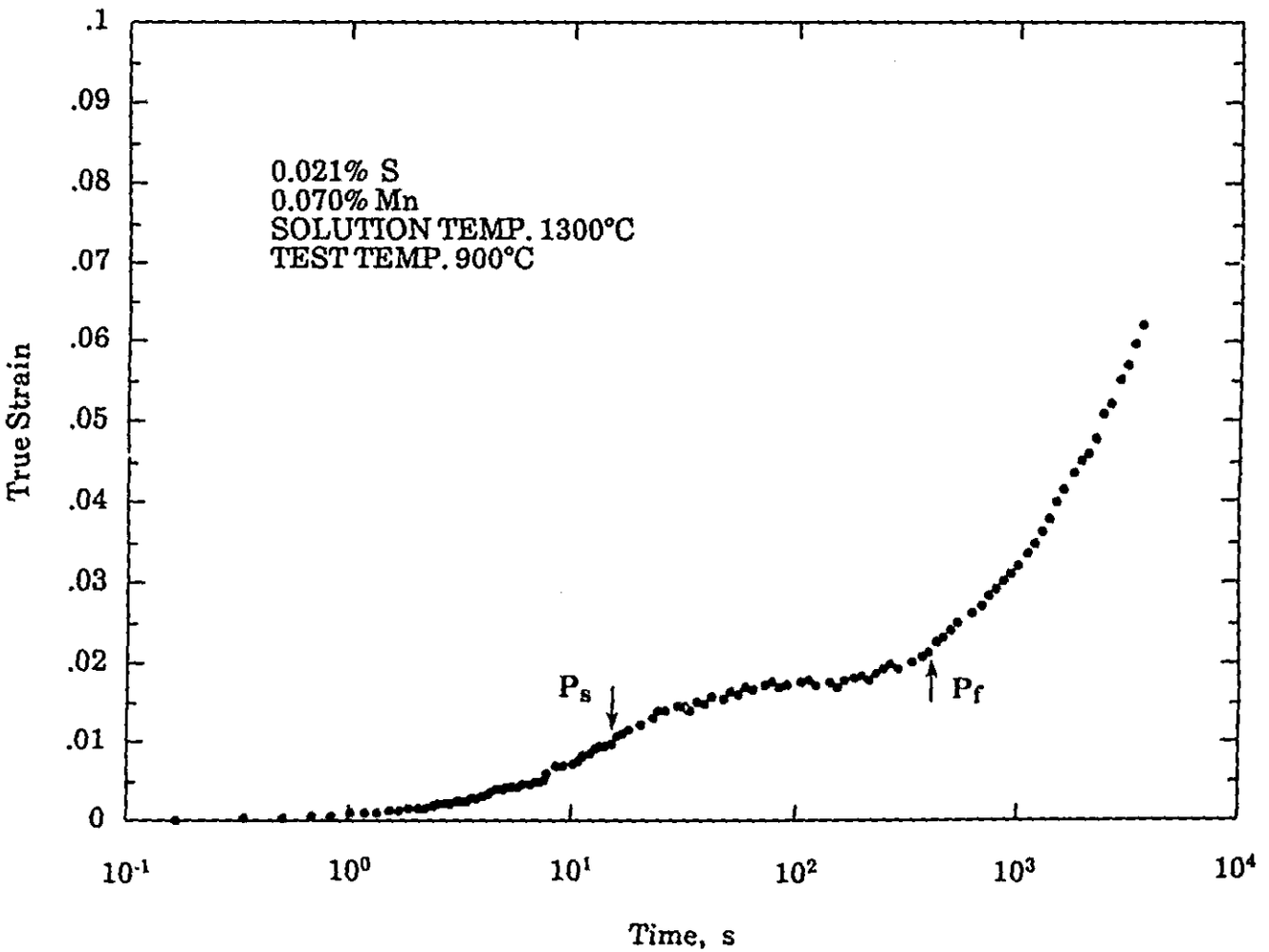

Fig. 4.11 Typical true strain-log(time) curve determined by the present creep technique on electrical steel A at 900 °C.

CHAPTER 5

EXPERIMENTAL RESULTS

5.1 MECHANICAL TEST RESULTS

5.1.1 FLOW BEHAVIOR DURING PRELIMINARY TESTING

5.1.1.1 Case of the Electrical Steels

The four sets of true stress-true strain curves that resulted from the preliminary tests (see §4.3.4) on the electrical steels are presented in Figures 5.1 - 5.4. These curves were determined at a constant strain rate of about 10^{-4} s^{-1} over the temperature range from 800 °C to 1100 °C. The curves can be divided into three regimes of behavior: a pre-yield region, a work hardening region and a steady state region. The first region is that of the microstrain deformation which takes place during the interval when the plastic strain rate in the specimen increases from zero to the approximate strain rate of the test, i.e. 10^{-4} s^{-1}. The second region begins when macroscopic yielding takes place after the microstrain interval. This region is characterized by a rate of work

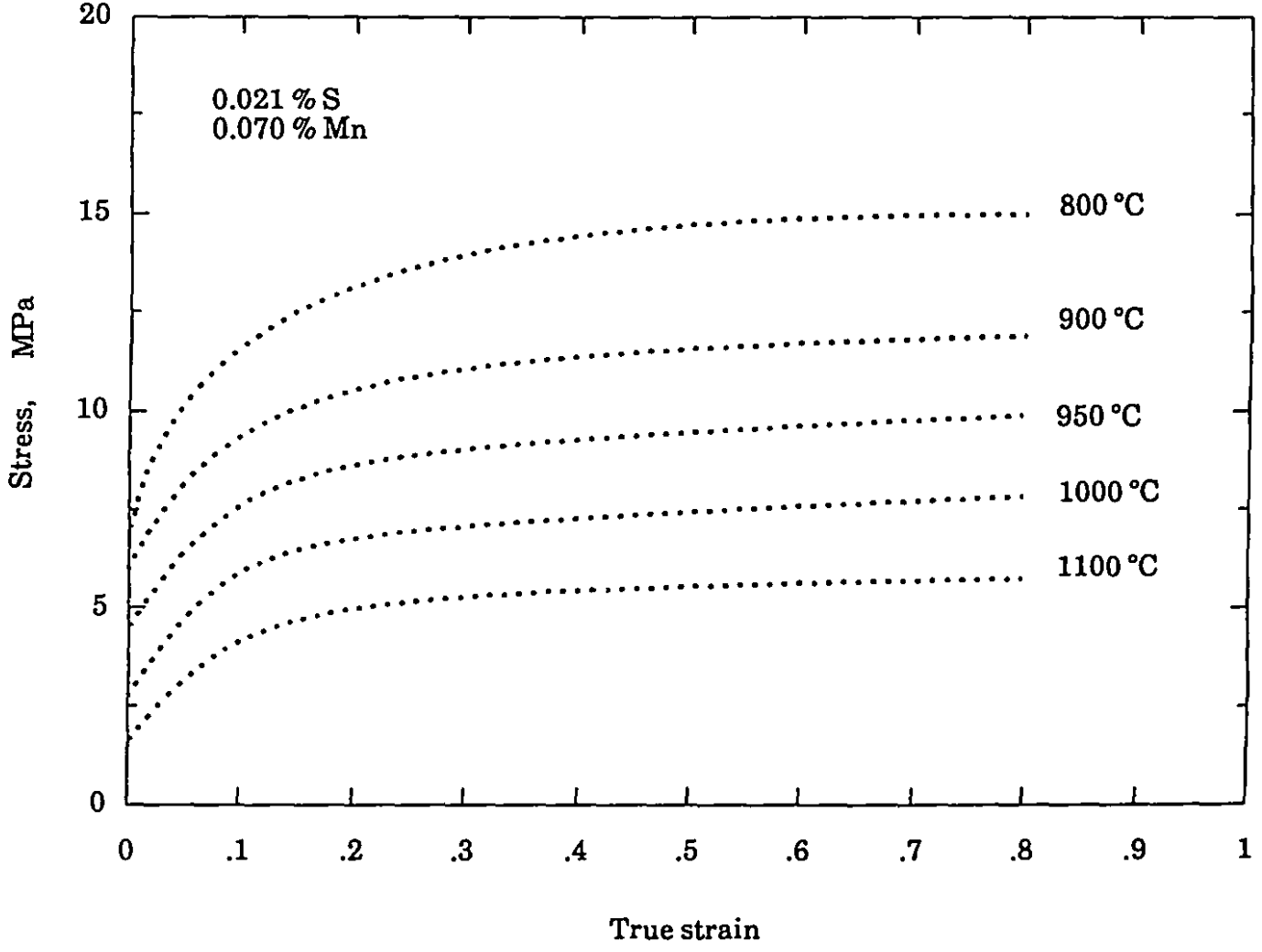

Fig. 5.1 Flow curves obtained at a strain rate of 10^{-4} s^{-1} for electrical steel A.

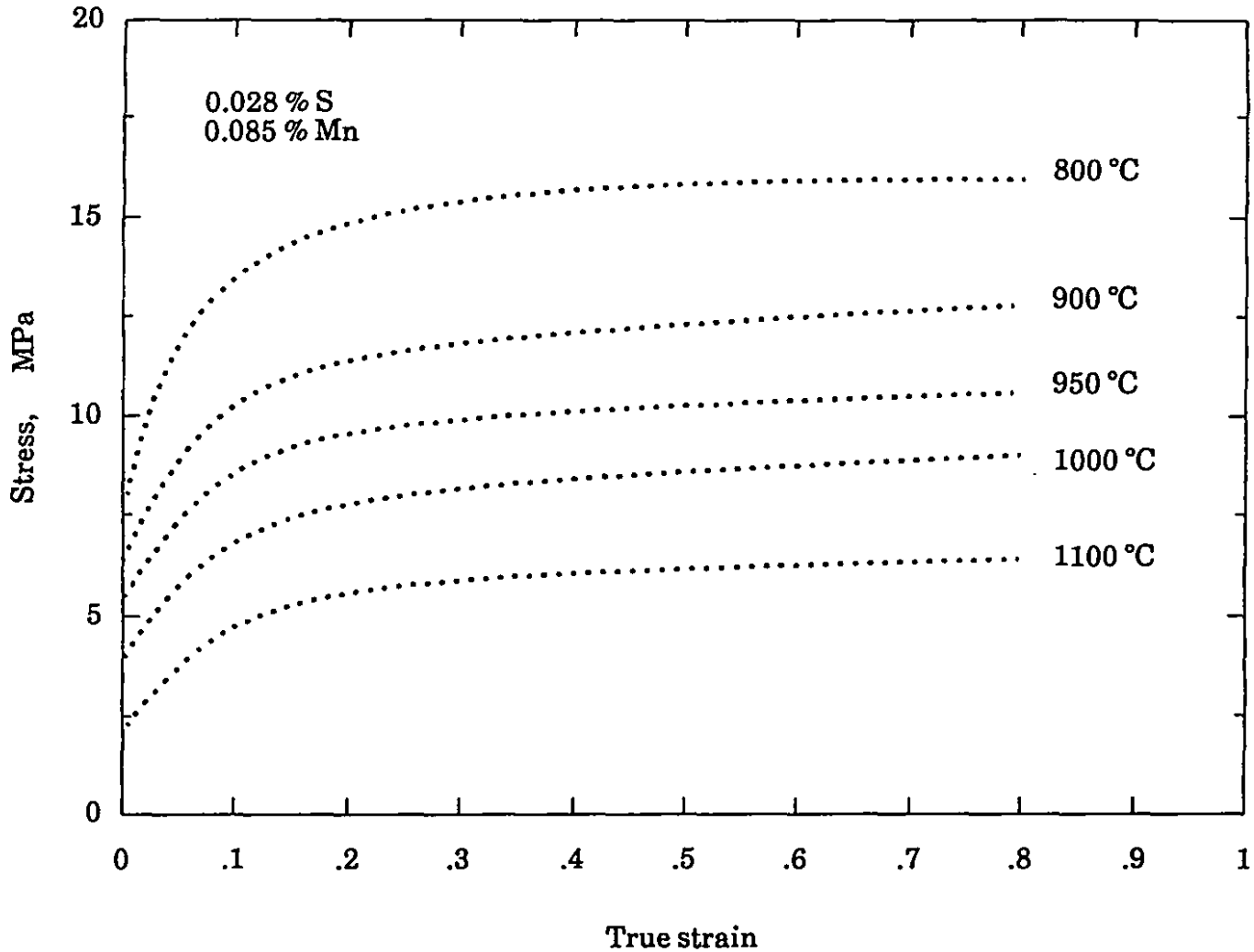

Fig. 5.2 Flow curves obtained at a strain rate of 10^{-4} s^{-1} for electrical steel B.

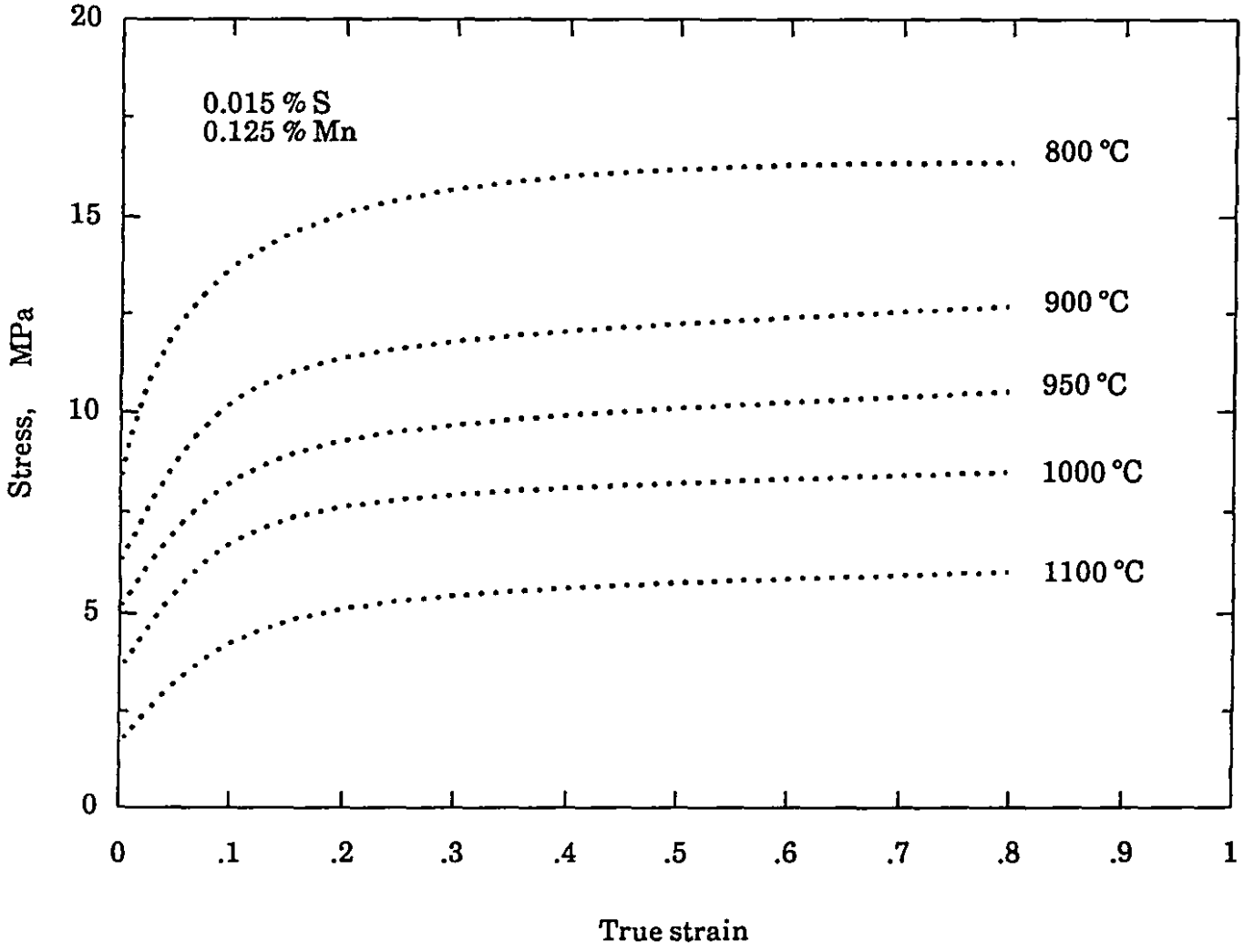

Fig. 5.3 Flow curves obtained at a strain rate of 10^{-4} s^{-1} for electrical steel C.

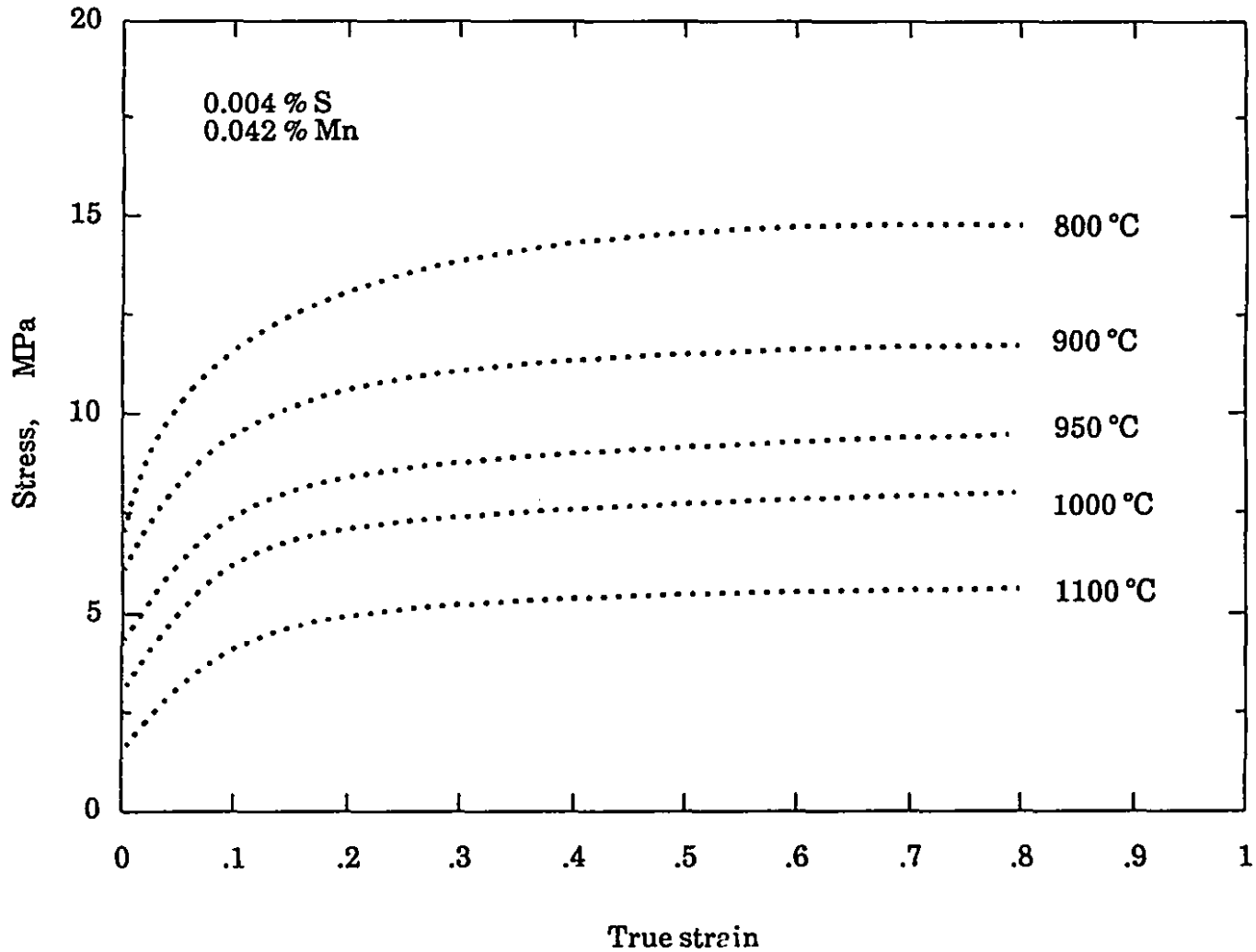

Fig. 5.4 Flow curves obtained at a strain rate of 10^{-4} s^{-1} for electrical steel D.

hardening which decreases with increasing strain. In the third region, steady state flow is observed where the net rate of work hardening is nearly zero, a condition which is similar to secondary creep. The steady state stresses in this region were used as the applied stresses for each electrical steel in the present creep tests, the exact values of which are listed in Table 5.1.

Table 5.1
Applied Stresses (MPa) Employed in the Creep Experiments

Temperature (°C)	Steel				
	0.028% S	0.021% S	0.015% S	0.004% S	0.25% Ti
800	15.8	15.0	16.0	14.8	-
900	12.9	11.8	12.5	11.6	7[illegible]
950	10.6	9.2	10.1	9.0	68
1000	8.9	7.6	8.3	7.8	56
1050	-	-	-	-	42
1100	7.6	5.6	6.0	5.6	27

5.1.1.2 Case of the Ti Steel

The flow curves determined at 10^{-4} s^{-1} in the temperature range from 900 °C to 1100 °C in the Ti steel are presented in Figure 5.5. It is clear from this figure that the occurrence of dynamic recrystallization modifies the appearance of the flow curves. A region of work hardening is displayed immediately after the yield is exceeded. The flow stress rises to a maximum at the peak strain ε_p, where the rate of work hardening is equal to zero. Then, as

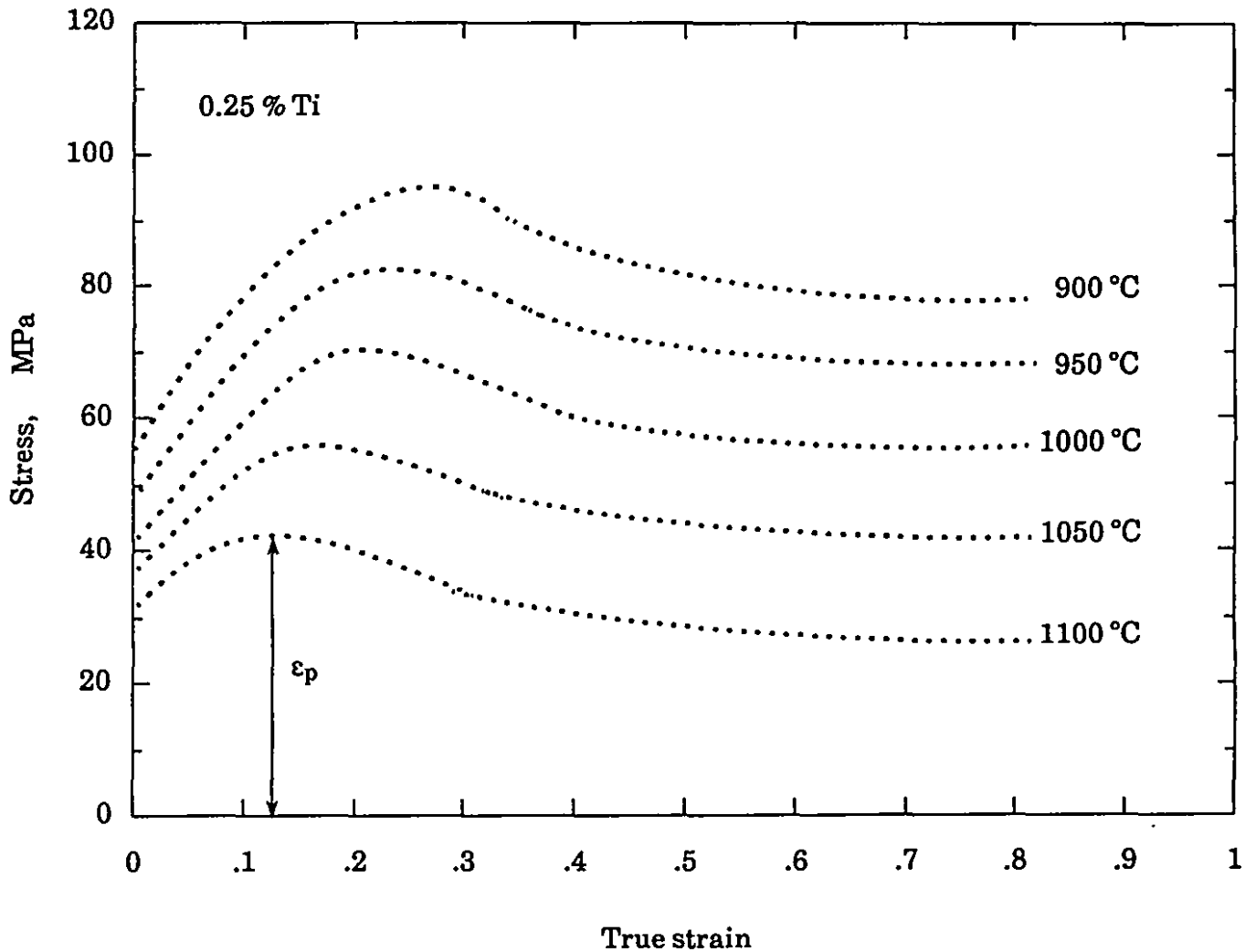

Fig. 5.5 Flow curves obtained at a strain rate of 10^{-4} s^{-1} for the Ti steel.

a result of dynamic recrystallization, the net rate of work hardening becomes negative and the flow stress diminishes to a value between the yield and peak stresses. Experimentally, this value was taken as the preset stress applied in the creep tests carried out on the Ti steel, as shown in Table 5.1. It should be mentioned here that the initiation of recrystallization, which can influence the kinetics of precipitation, was avoided during the present creep tests because the total applied strain was well below ε_p.

5.1.2 QUASI-EMPIRICISM IN CONVENTIONAL CREEP

The essential features of conventional creep curves exhibited by electrical steels were already described in §4.3.5. As revealed in Figure 4.9b, a logarithmic function cannot represent the relationship between the strain and the creep time. Logarithmic creep is not therefore taking place. Neither is anelastic creep, as the strain is not recoverable in the present case. Similar conditions apply to the Nabarro-Herring-Coble types of creep. This is because, as stated in Chapter 2, this type of creep only becomes dominant at very high temperatures, under very low stresses, and when the grain size of the specimen is very fine. Since a mid level of stress was employed on the specimens during testing, and the grain dimensions of electrical steels are quite large (about 2 mm at 1300 °C, as can be seen from Figure 4.2 and Table 4.1), only Andrade creep is considered in the analysis below.

Fitting the creep data obtained on the electrical steels into the Andrade formula:

$$\varepsilon = \beta t^n + Kt \qquad (5.1)$$

the empirical parameters β, K and n were determined by means of a least squares method. The values established in this way for electrical steel A are given in Table 5.2. We are thus led by the experimental data to the following two conclusions:

Table 5.2
Values of the Parameters in the Andrade Equation Determined for Electrical Steel A

Temperature (°C)	Andrade Parameter		
	n	β ($\times 10^3$, s^{1-n})	K ($\times 10^5$)
800	0.34	1.26	1.88
900	0.36	1.44	2.20
950	0.37	1.56	2.33
1000	0.38	1.68	2.47
1100	0.41	1.89	2.78

(1) The transient period of creep in electrical steels is quite short because the exponent n is much less than 1 (refer back to §2.3.2.3).

(2) Both β and K increase with an increase in temperature, which indicates that the strain is an increasing function of temperature during such tests.

The strain rate-time relations are computable if the experimental parameters β, K and n are inserted into the rate equation of Andrade creep:

$$\dot{\varepsilon} = n\beta t^{n-1} + K \tag{2.26}$$

As a result, the time dependence of the strain rate for electrical steel A tested

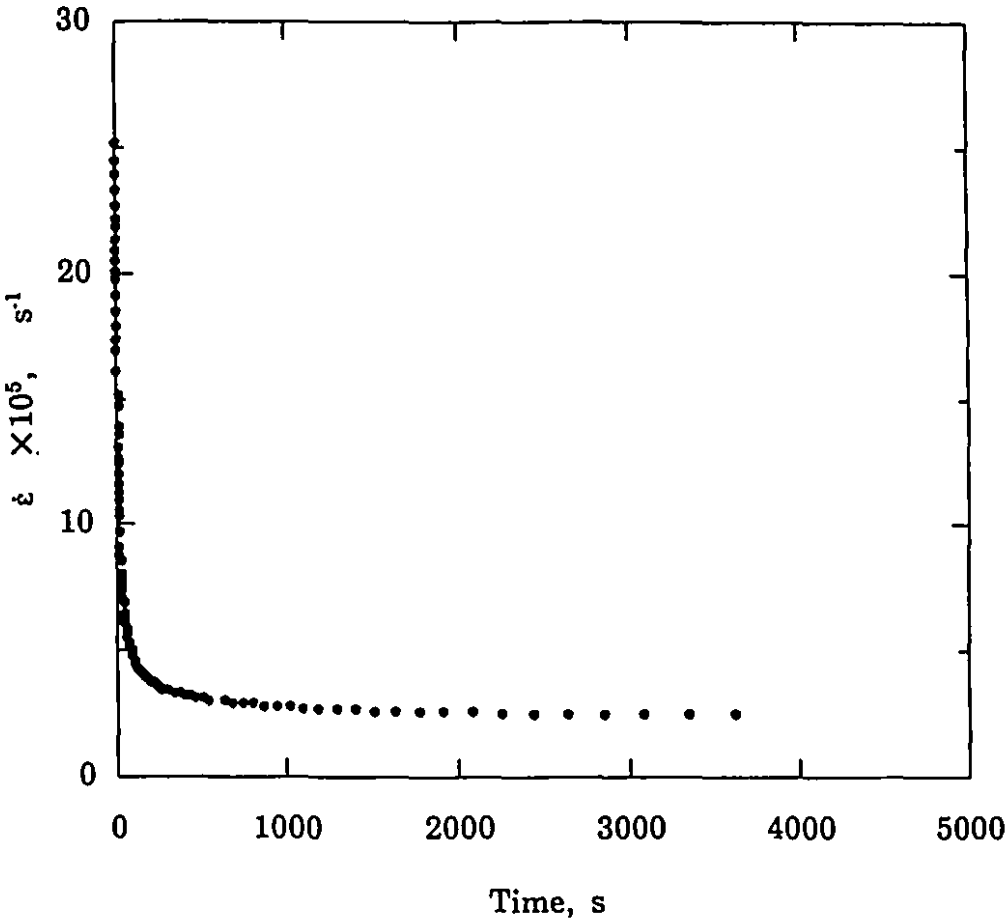

Fig. 5.6 Strain rate estimated from the experimental Andrade parameters for the conventional creep of electrical steel A at 900 °C.

conventionally at 900 °C takes the form illustrated in Figure 5.6. It is evident from this figure that the strain rate first decreases and then gradually approaches a constant value. In consideration of the semi-log plot of strain versus creep time shown in Figure 4.9b, the slope of this curve was also estimated, the results of which are sketched in Figure 5.7. This diagram shows that such a semi-log slope increases with increasing log(time).

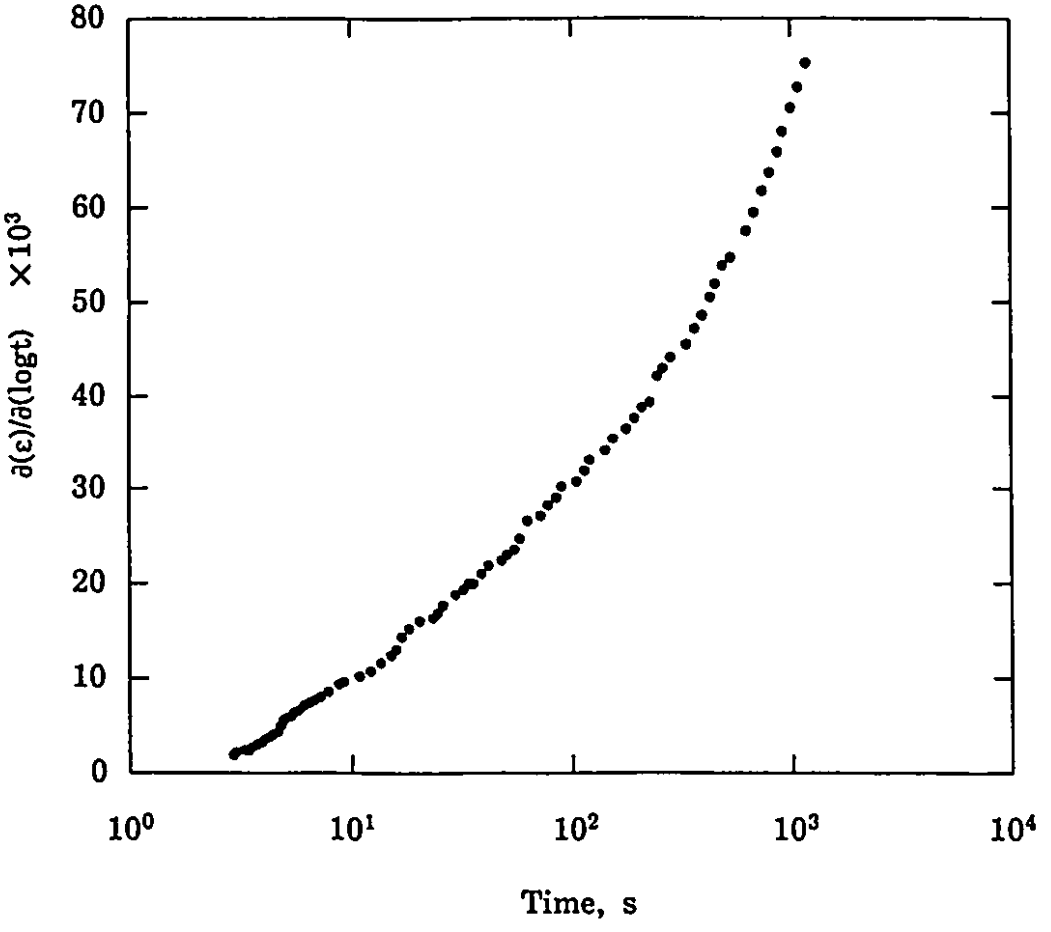

Fig. 5.7 Change in the slope of the strain - log(time) curve estimated from the conventional creep data for electrical steel A at 900 °C.

5.1.3 PRESENT EXPERIMENTAL CURVES

In sets of five, the true strain-log(time) curves acquired by the present creep technique on the five experimental steels are presented in Figures 5.8 - 5.12. Clearly, the higher the testing temperature, the larger the creep strain observed on these curves. By direct comparison with the conventional creep data given in Figure 4.9b, it can also be seen that the resultant strain-

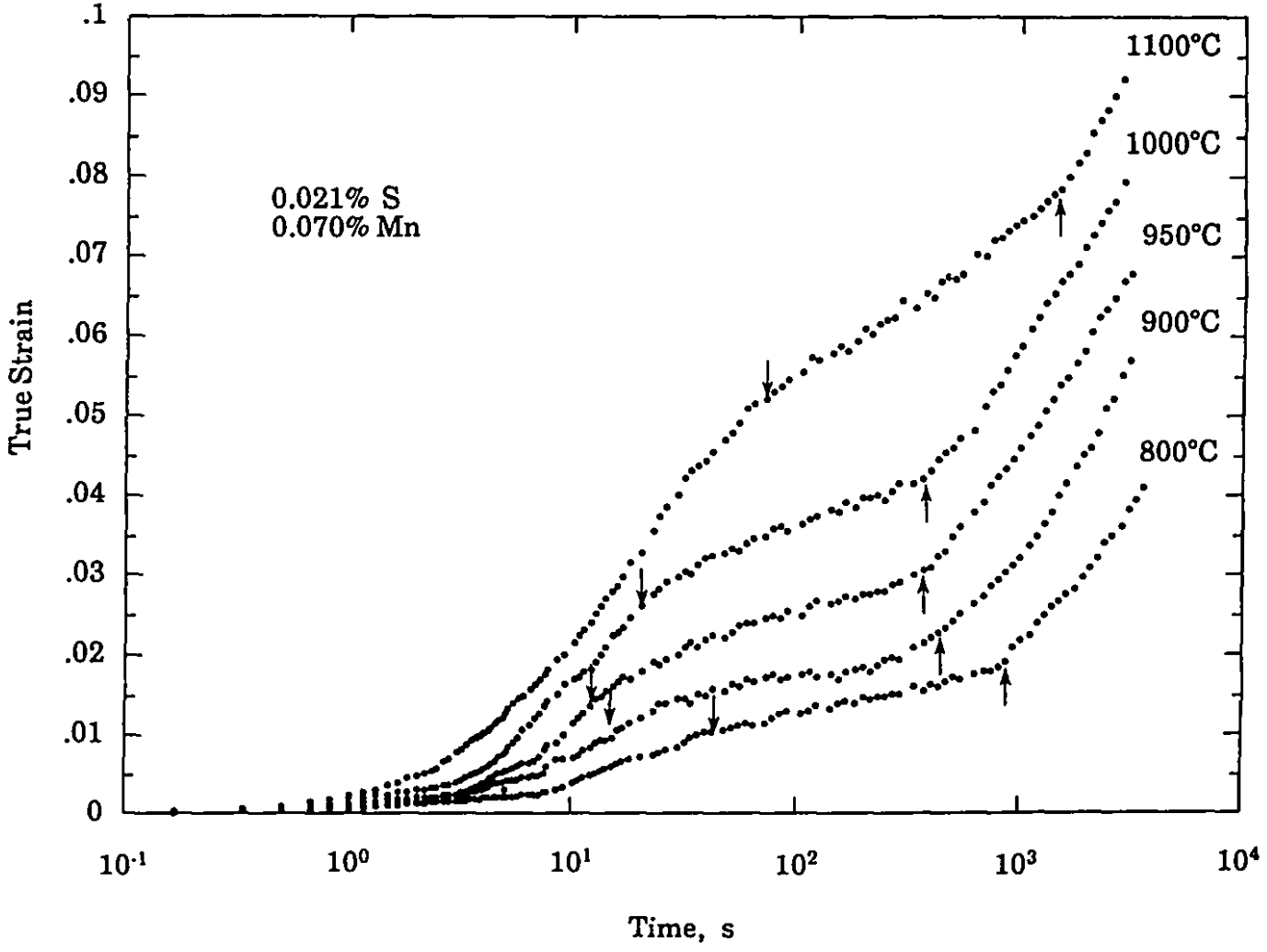

Fig. 5.8 Creep strain vs log(time) curves obtained by the present technique for electrical steel A.

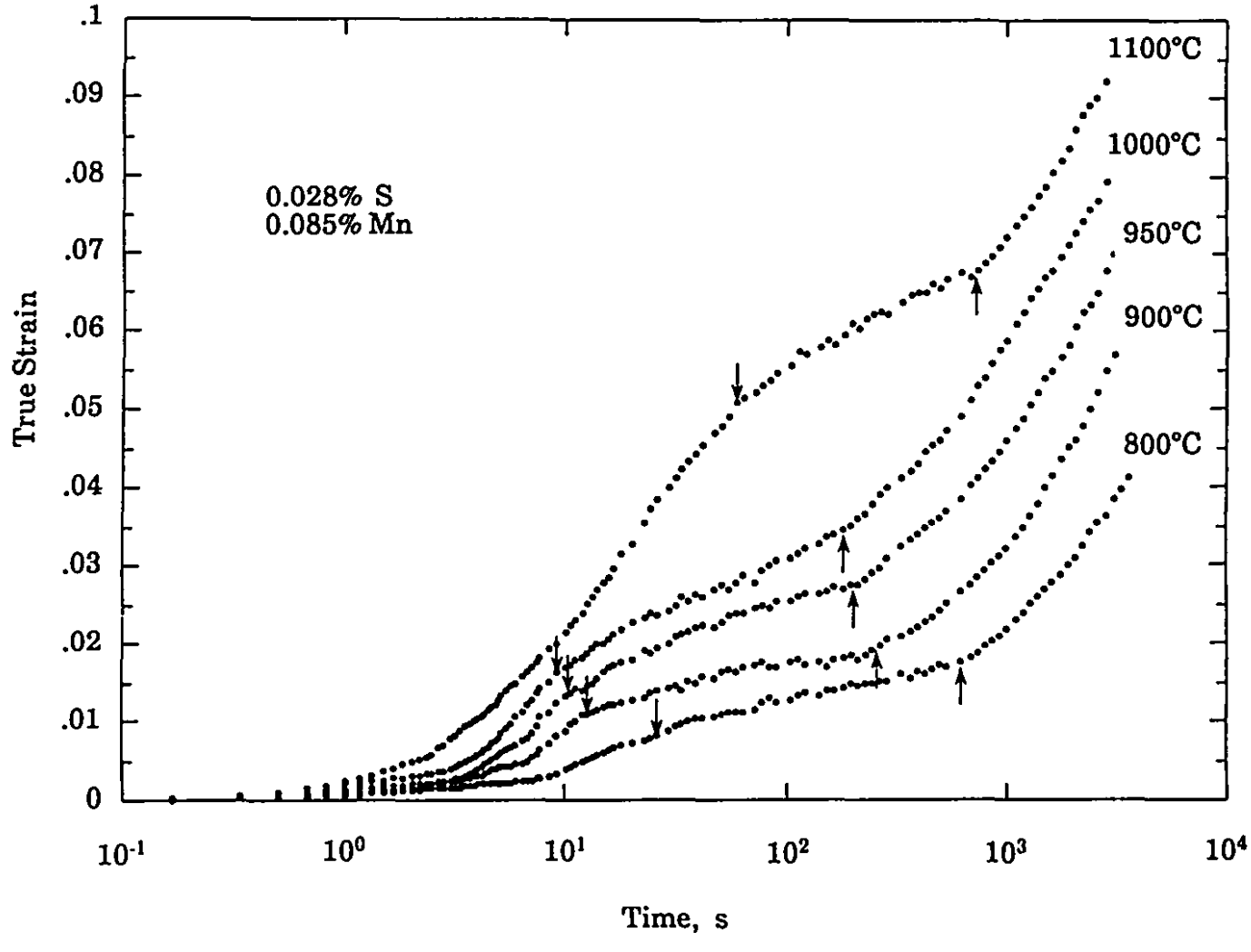

Fig. 5.9 Creep strain vs log(time) curves obtained by the present technique for electrical steel B.

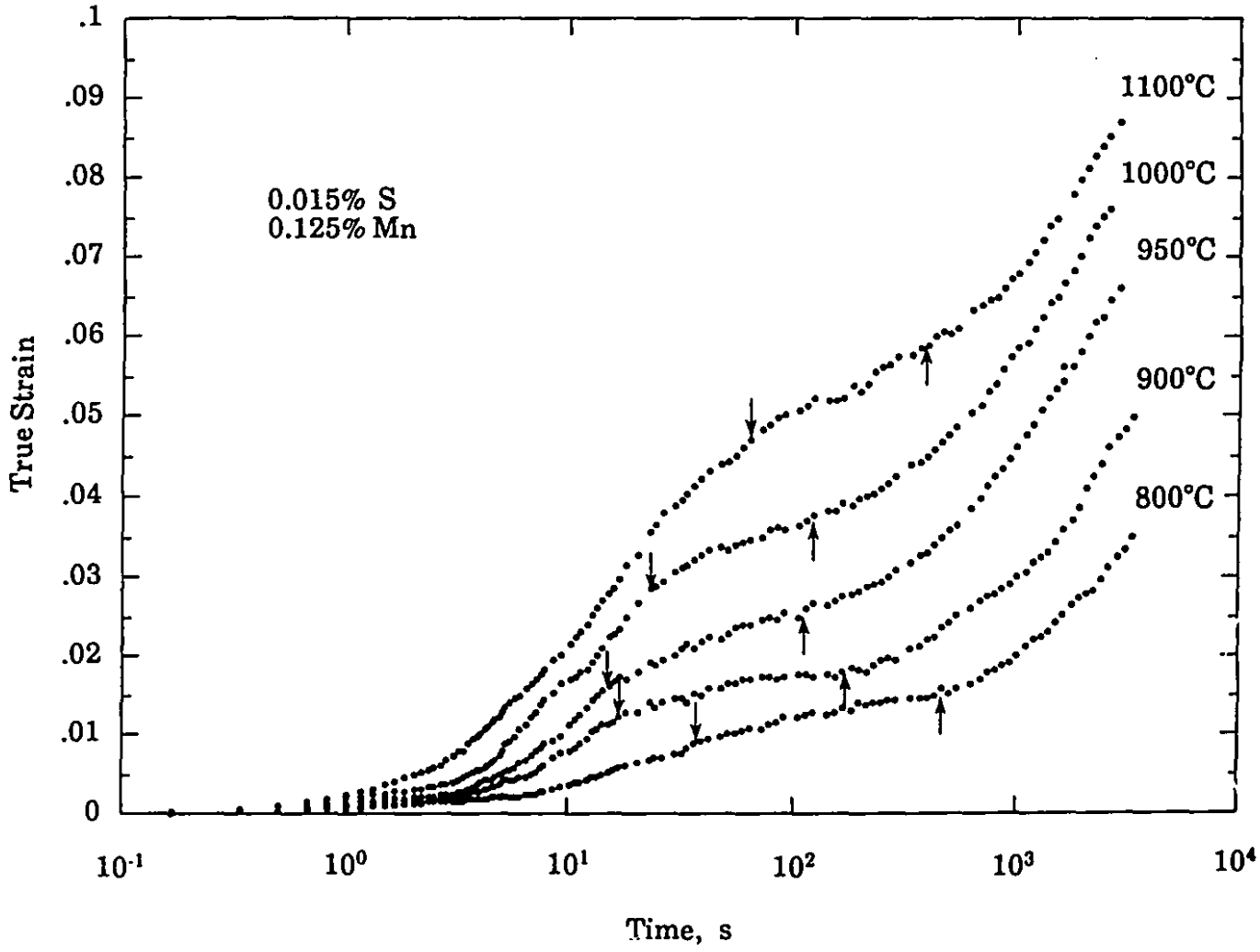

Fig. 5.10 Creep strain vs log(time) curves obtained by the present technique for electrical steel C.

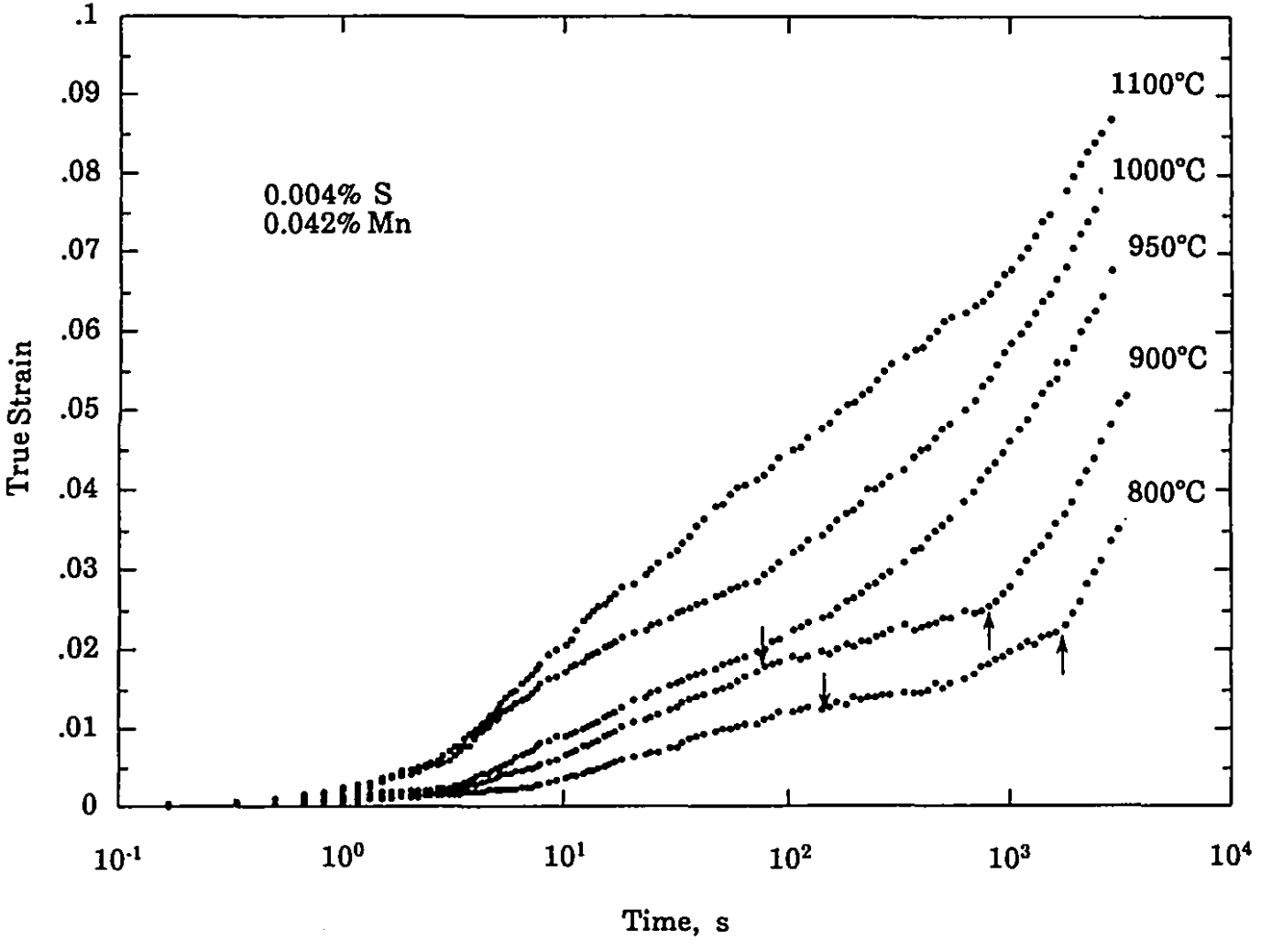

Fig. 5.11 Creep strain vs log(time) curves obtained by the present technique for electrical steel D.

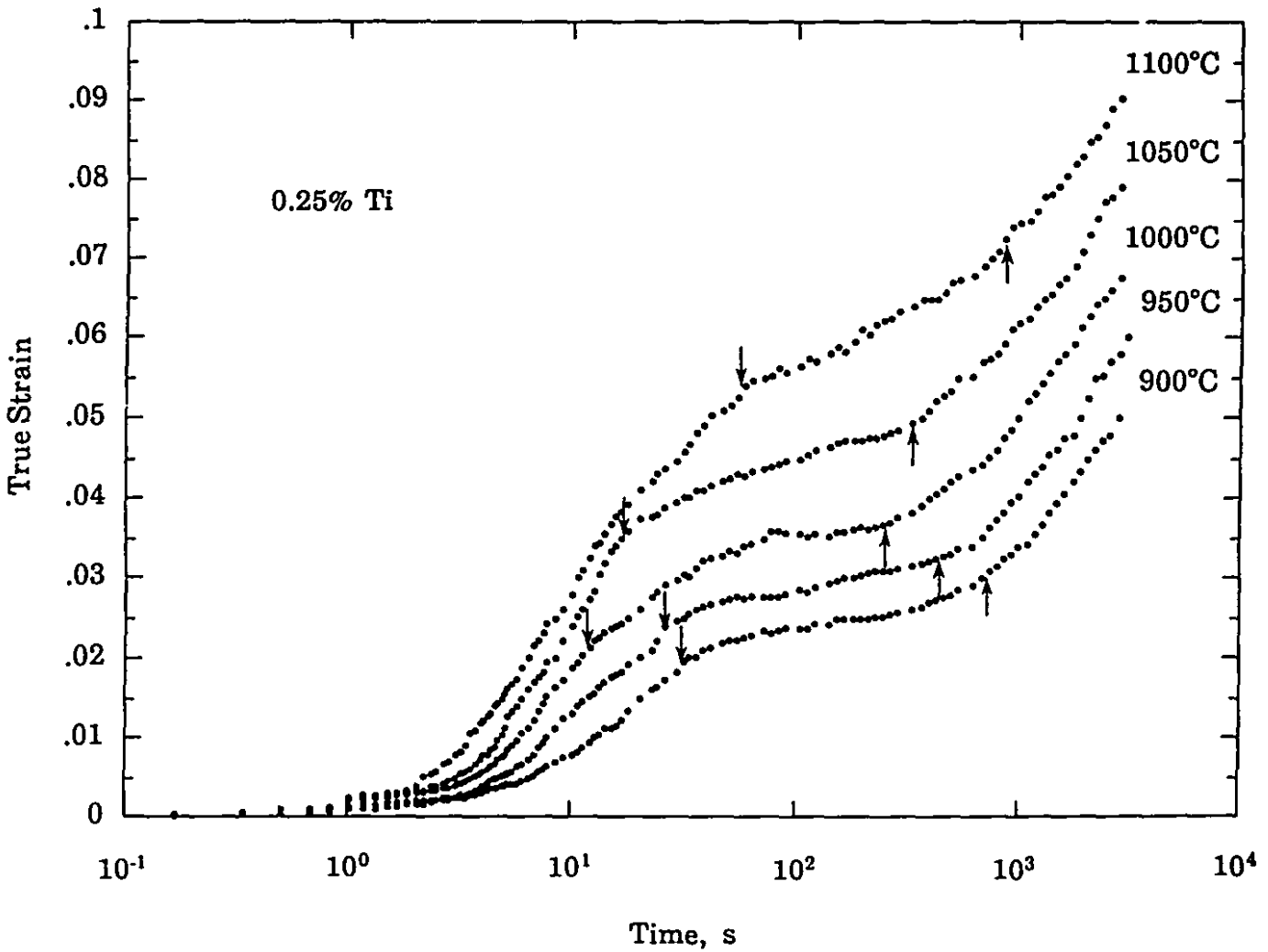

Fig. 5.12 Creep strain vs log(time) curves obtained by the present technique for the Ti steel.

log(time) curves display departures from their conventional creep behaviors when these steels are stressed after solution treatment. Such departures indicate the occurrence of precipitation during testing. On further examination of these experimental diagrams, it can be observed that the strain decrement or strain plateau becomes more marked as the testing temperature is decreased. Clearly, such a temperature effect is associated with the variation in the volume fraction of the precipitates formed during creep, since the latter is a decreasing function of temperature. As a matter worthy of note, the plateaus disappear entirely at 950 °C and above on the curves for the 0.042% Mn-0.004% S steel, as shown in Figure 5.11. This indicates that no significant precipitation takes place in this steel when the testing temperature is above 950 °C.

The plateau on the strain-log(time) curve, or the change in creep rate, is evaluated further in Figure 5.13, where the slope of the present experimental curve for electrical steel A at 900 °C is plotted against log(time). In contrast to the curve presented in Figure 5.7, this plot shows that the slope first increases, then, as will be demonstrated in much more detail later when electron microscopy results are introduced, decreases immediately after the initiation of precipitation and increases again when the latter is complete. Consequently, the two points on the present experimental curves at which the plateau begins and ends can be identified as P_s (precipitation start time) and P_f (precipitation finish time), respectively. These two points can also be evaluated more precisely in terms of the second derivatives of the strain with respect to log(time). The latter, according to Figure 5.13, change from positive to negative at P_s and become positive again at P_f. Thus, P_s and P_f can be defined by the following equations:

$$\left.\frac{\partial^2(\varepsilon)}{\partial(\ln t)^2}\right|_{t=p_s} = 0, \quad and \quad \left.\frac{\partial^3(\varepsilon)}{\partial(\ln t)^3}\right|_{t=p_s} < 0 \qquad (5.2a)$$

$$\left.\frac{\partial^2(\varepsilon)}{\partial(\ln t)^2}\right|_{t=p_f} = 0, \text{ and } \left.\frac{\partial^3(\varepsilon)}{\partial(\ln t)^3}\right|_{t=p_f} > 0 \qquad (5.2b)$$

where ε is the creep strain and t is the creep time. The precipitation start P_s and finish P_f times determined in this way are indicated by arrows in the above experimental diagrams. We will return to the analysis of these two

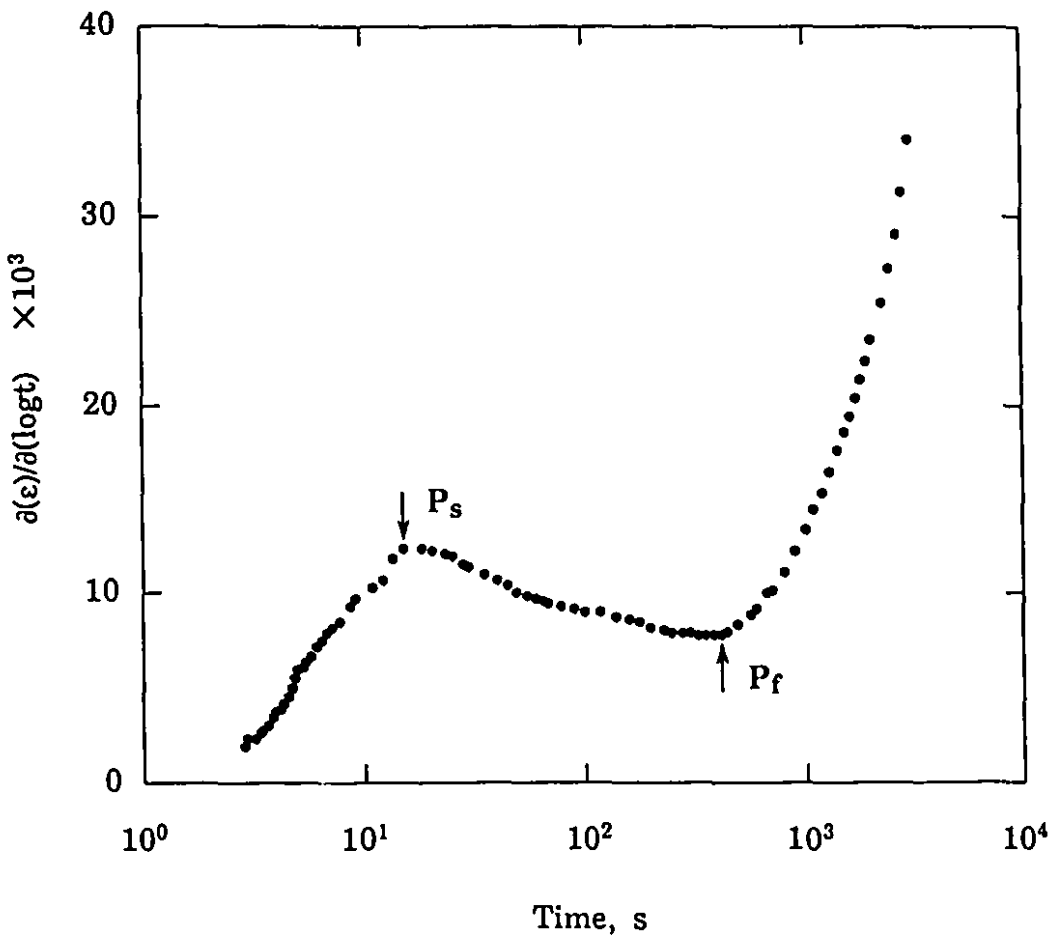

Fig. 5.13 Change in the slope of the strain - log(time) curve estimated from the creep data obtained by the present technique for electrical steel A at 900 °C.

points in the second part of this chapter where the experimental results obtained by means of electron microscopy are presented.

5.1.4 PRECIPITATION-TIME-TEMPERATURE DIAGRAMS

In order to collect the experimental results in a single location, the P_s and P_f times determined on all the tested steels are listed in Table 5.3. The results for the four electrical steels are also presented in Figure 5.14 in the form of precipitation-time-temperature (PTT) diagrams. It is apparent from this figure that the curves for MnS precipitation in these ferritic steels are of the classical C-shape, with the nose at a minimum time of about 9 seconds at 1000 °C for the 0.085% Mn-0.028% S steel, at 12 seconds and 950 °C for the 0.070% Mn-0.021% S steel and at 14 seconds and 950 °C for the 0.125% Mn-0.015% S steel. Since both the P_s and P_f times for the 0.042% Mn-0.004% S steel are detectable solely at and below 900 °C, the PTT curve for this steel is based on only two experimental points and is thus represented by a dotted line in Figure 5.14.

As mentioned in §2.2.6.4, such C-curve kinetics indicate that this kind of precipitation is controlled by the supersaturation and diffusion of the precipitate-forming elements Mn and S. Above the nose, with increasing temperature, the supersaturation continuously decreases until it reaches zero at the equilibrium dissolution temperature. Accordingly, the nucleation rate for precipitation becomes increasingly slower as the temperature is increased. On the other hand, longer times are also required below the nose to start precipitation when the temperature is decreased. This is due to the slower diffusivities at the lower temperatures.

Detailed examination of these PTT curves makes it evid[illegible] that the P_s curve for the 0.085% Mn-0.028% S steel is located at the highest temperatures and shortest times, even though it approaches the P_s curves for the 0.070% Mn-0.021% S and 0.125% Mn-0.015% S steels at very high temperatures, e.g. at about 1100 °C. This indicates that the driving force for MnS nucleation in this steel is the highest among the four steels. Comparison between the latter two P_s curves reveals that there is little difference in the precipitation start times

Table 5.3
P_s and P_f Times Determined by the Creep Technique

Steel	Temperature (°C)	Time (s)	
		P_s	P_f
0.070% Mn-0.021% S	800	42	920
	900	15	420
	950	12	350
	1000	20	380
	1100	76	1410
0.085% Mn-0.028% S	800	26	600
	900	12	240
	950	10	180
	1000	9	170
	1100	58	800
0.125% Mn-0.015% S	800	40	440
	900	16	150
	950	14	110
	1000	21	120
	1100	68	430
0.042% Mn-0.004% S	800	150	1900
	900	80	960
0.25% Ti	900	32	760
	950	25	410
	1000	12	250
	1050	17	340
	1100	55	950

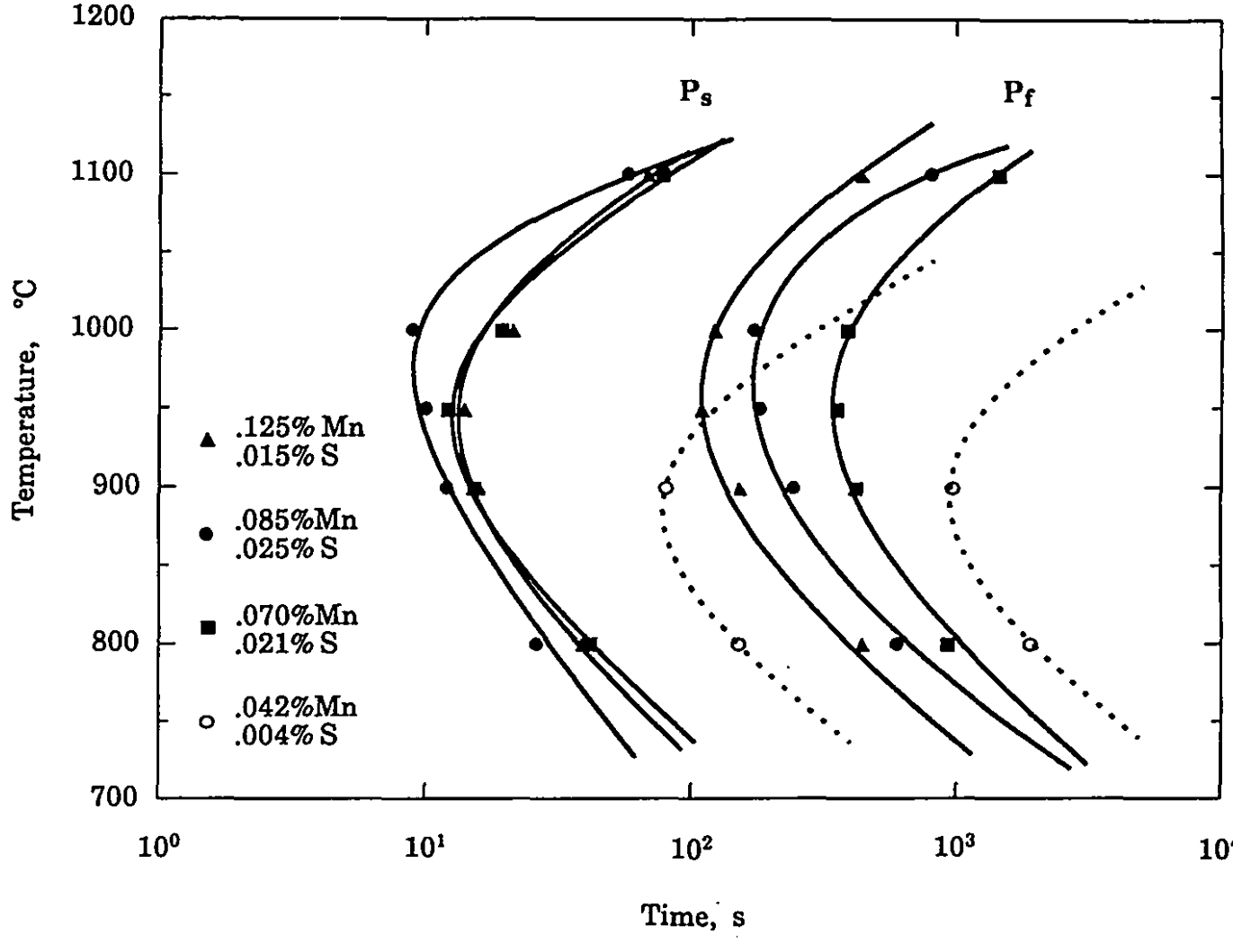

Fig. 5.14 PTT curves for the four electrical steels acquired by the present technique.

between the 0.070% Mn-0.021% S and 0.125% Mn-0.015% S steels. The similarity of the P_s times suggests that the driving forces in the two materials are nearly identical. In addition, a general trend can also be found on all the P_f curves. That is, the P_f times are shifted to shorter times as the Mn concentration is increased.

The PTT curves for the Ti bearing steel, together with the results obtained from the earlier stress relaxation technique[147] (represented by dashed lines), are shown in Figure 5.15. It is important to note that experimental points were readily obtained by the creep method at 1100 °C, conditions under which the stress relaxation test is too insensitive to detect changes in the state of precipitation. The reasons for the higher sensitivity of the creep technique are of considerable practical interest and will be discussed in more detail in Chapter 8.

5.2 MICROSTRUCTURAL RESULTS

5.2.1 EVOLUTION OF PRECIPITATION DURING CREEP

5.2.1.1 Preparation of the Carbon Replicas

As shown above, an alloy in which a second phase is precipitated displays departures from conventional creep behavior. Direct structural evidence for this phenomenon was obtained on electrical steels A, B, and C with the aid of extraction replicas. The samples used for this purpose were tested under the experimental conditions described previously and were helium quenched after increasing creep times. One of the quenching schedules employed is shown in the first diagram of Figure 5.16. Samples *b* and *e* were helium quenched close to the P_s and P_f times defined above, while samples *c* and *d* were quenched between P_s and P_f. Sample *a* was quenched prior to P_s, sample *f* after P_f, and sample *g* at the end of the test. Complete information regarding the quench times selected at different temperatures for each steel is provided in Table 5.4.

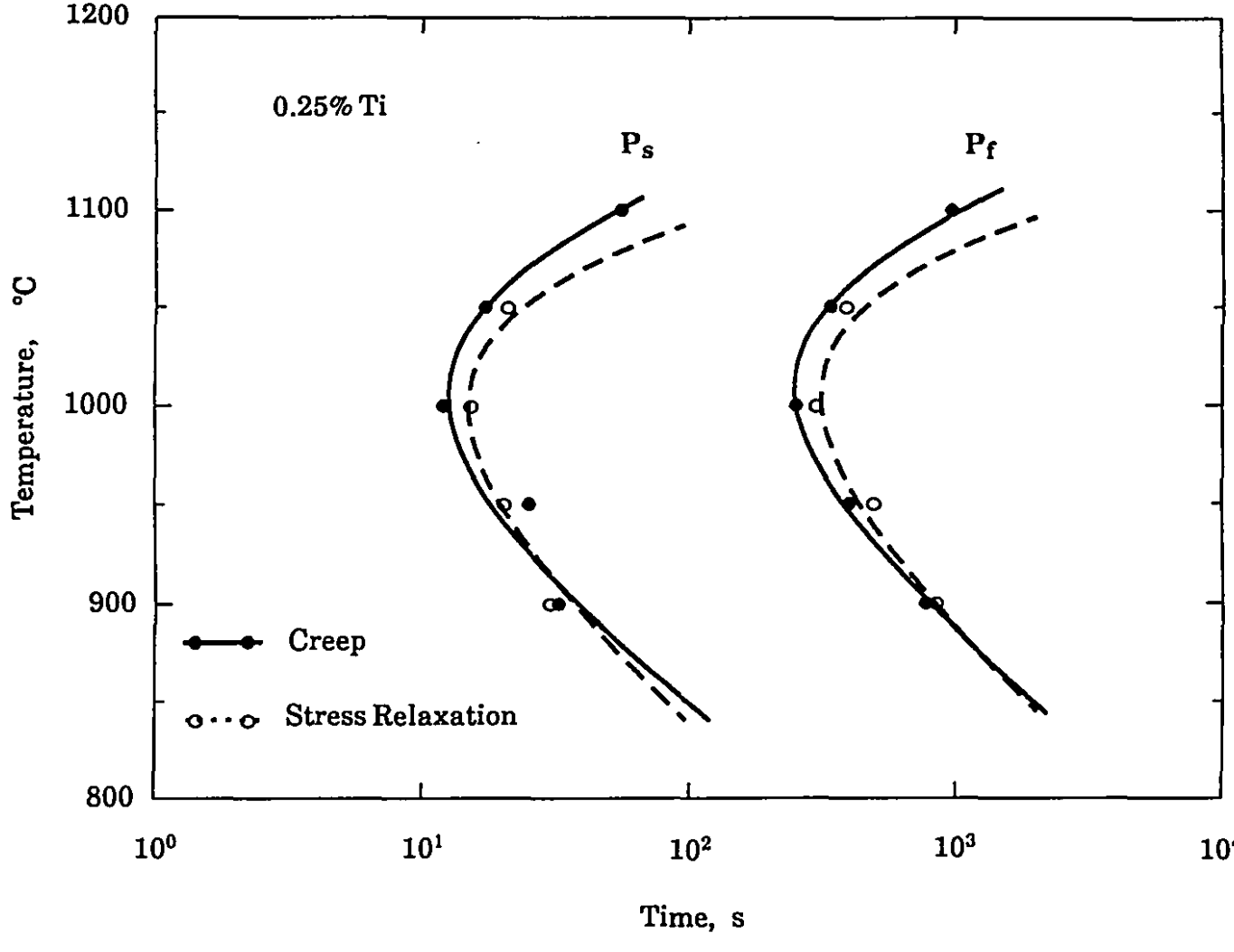

Fig. 5.15 Comparison of the PTT curves obtained for the 0.25 pct Ti steel by the present technique with those determined by the stress relaxation method.

Table 5.4
Identification of the Samples Used for the Microstructural Examinations

Steel	Temperature (°C)	Creep Time Before Quenching (s)
0.085% Mn-0.028% S	800	26, 60, 240, 600, 1200
	900	12, 60, 240, 1200
	1000	9, 60, 170, 1200, 3600
0.070% Mn-0.021% S	800	42, 420, 920, 3600
	900	5, 15, 60, 200, 420, 1200, 3600
	1000	42, 200, 380, 1200
0.125% Mn-0.015% S	800	40, 120, 440, 1200, 3600
	900	16, 150, 1200
	1000	21, 120, 1200

The helium quenched samples were first cut parallel to the compression direction with a low speed diamond saw operated with a coolant. The resulting pieces were then mounted in bakelite and the sectioned surfaces were ground using silicon carbide papers. They were prepared by mechanical polishing with 6 μm diamond paste and 0.3 μm alumina, and by electrolytic polishing in a 50-50 solution by volume of 30 pct H_2O_2-85 pct H_3PO_4. The polished samples were lightly etched in 1 pct HNO_3-99 pct C_2H_5OH. Subsequently, the polished-and-etched surfaces were coated with a carbon layer about 30 nm thick in a vacuum evaporator. The carbon layer was then cut into 3 mm x 3 mm squares with a scalpel blade, released by an electrolyte containing 10% perchloric acid, 70% ethanol, 10% butanol and 10% distilled water, and finally placed on TEM copper grids.

5.2.1.2 Progress of MnS Precipitation

In order to establish the state of the microstructure, particularly the evolution of MnS precipitation during creep, the freshly precipitated particles in the carbon replicas were examined in a JEOL-100 CX scanning transmission electron microscope fitted with a PGT system IV energy dispersive X-ray spectrometer (EDS) for the chemical analysis of individual particles. For the sake of brevity, only the results obtained on electrical steel A at 900 °C will be reported here in detail.

In Figure 5.16, electron micrographs are presented for electrical steel A undergoing creep at 900 °C. The size distribution of the particles in each sample is also shown in this figure. The detailed description of the procedure used for determining these size distributions will be given in the next subsection. No sign of fresh precipitates was found in the sample which was quenched prior to P_s (Figure 5.16a), while very small precipitates ranging from about 2 to 25nm were occasionally observed after 15 seconds of creep (Figure 5.16b). Noting that this is the P_s time identified by the present technique at this temperature, the above observations thus support the interpretation that it is the formation of these precipitates that arrests the creep rate.

As the creep time was increased to 60 and further to 200 seconds, the density of precipitates increased significantly and the particle size distribution broadened to cover the range from 2 to 80nm, as illustrated in Figures 5.16c and 5.16d, respectively. When the creep time was prolonged to P_f, the mean size of the precipitates increased continuously, but the density of the particles decreased, as shown for 420 seconds in Figure 5.16e. This indicates that P_f is associated with the start of the dissolution of small particles and the coarsening of the large precipitates, as in the case of stress relaxation[77,78]. The significant particle coarsening taking place after P_f is illustrated in Figures 5.16f and 5.16g.

It should be added here that similar observations with respect to the progress of precipitation were made at the other testing temperatures and/or for the other steels.

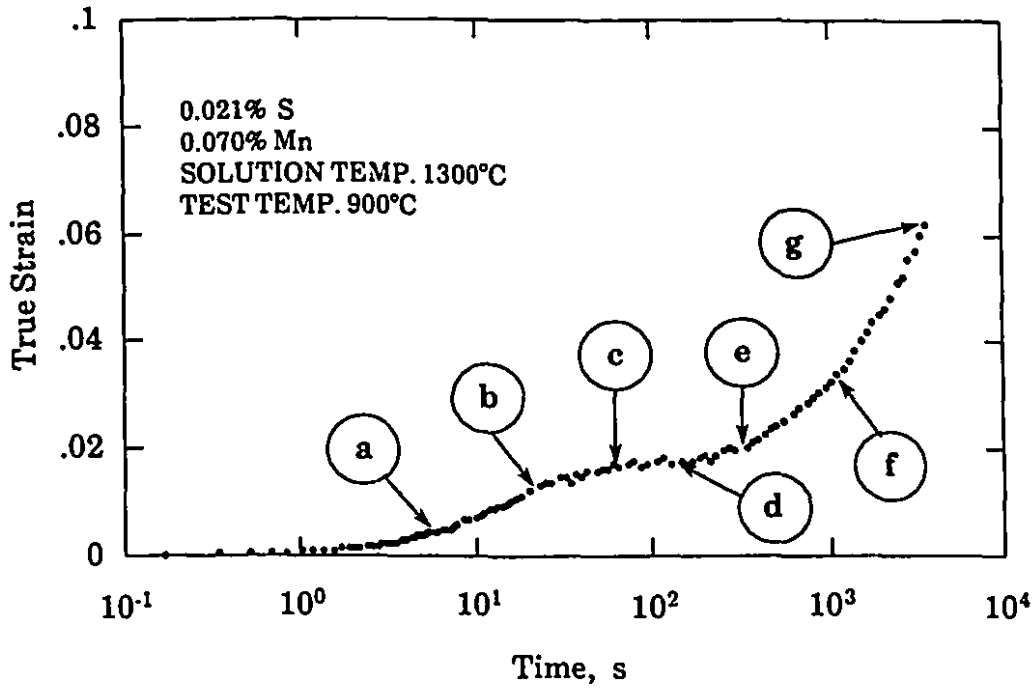

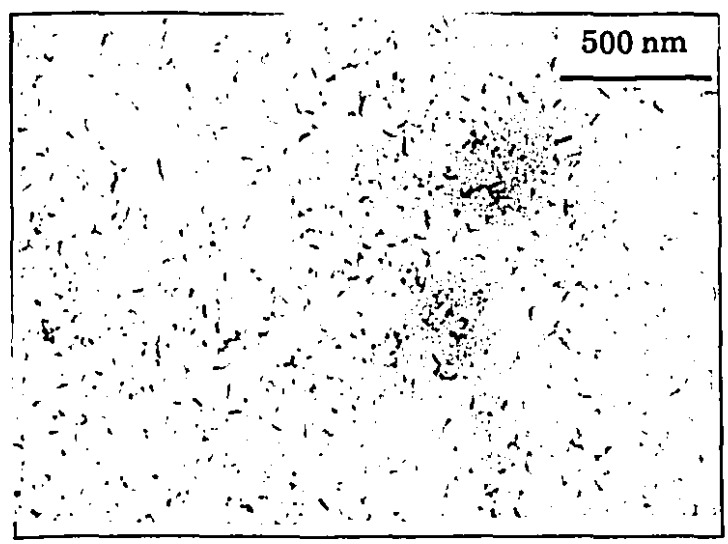

(a)

Fig. 5.16 Carbon extraction replicas showing the progress of MnS precipitation in samples of electrical steel A undergoing creep at 900 °C: (a) 5 s, (b) 15 s, (c) 60 s, (d) 200 s, (e) 420 s, (f) 1200 s, and (g) 3600 s.

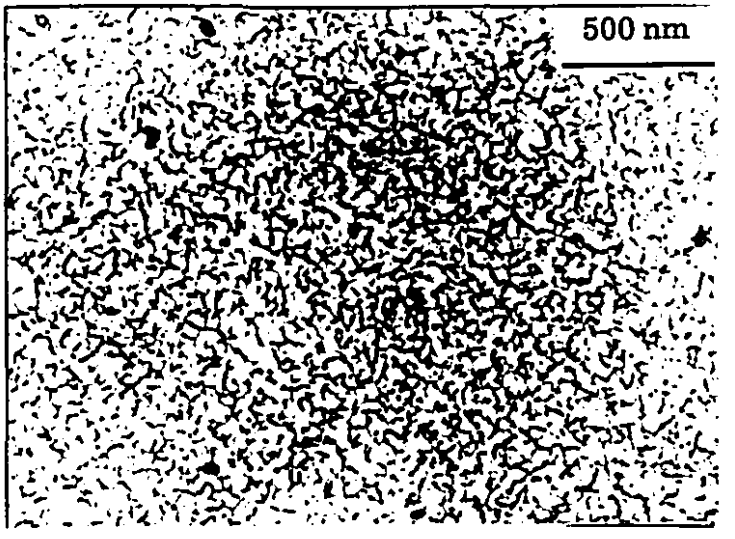

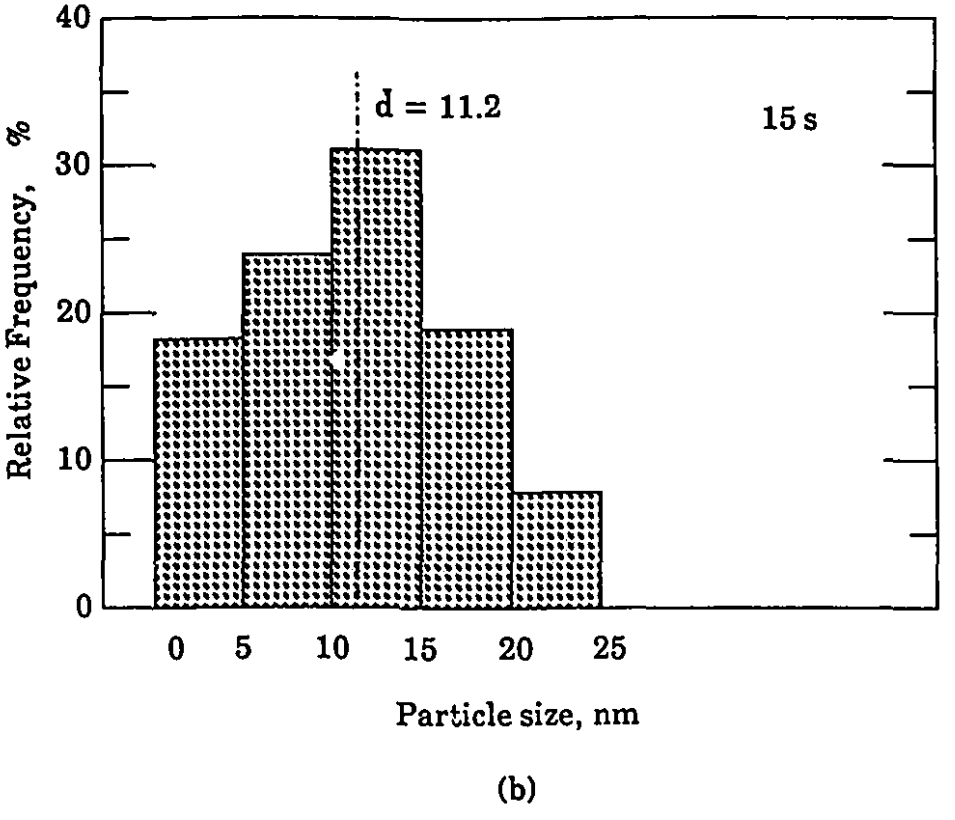

(b)

Fig. 5.16 Carbon extraction replicas showing the progress of MnS precipitation in samples of electrical steel A undergoing creep at 900 °C: (a) 5 s, (b) 15 s, (c) 60 s, (d) 200 s, (e) 420 s, (f) 1200 s, and (g) 3600 s.

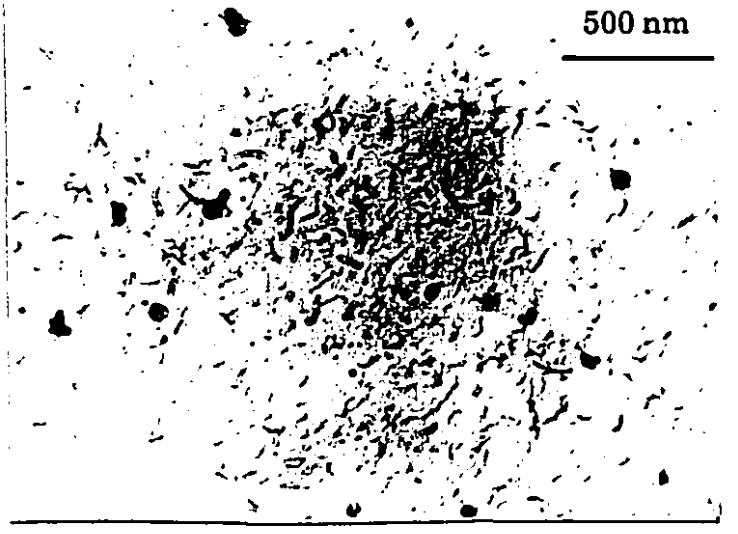

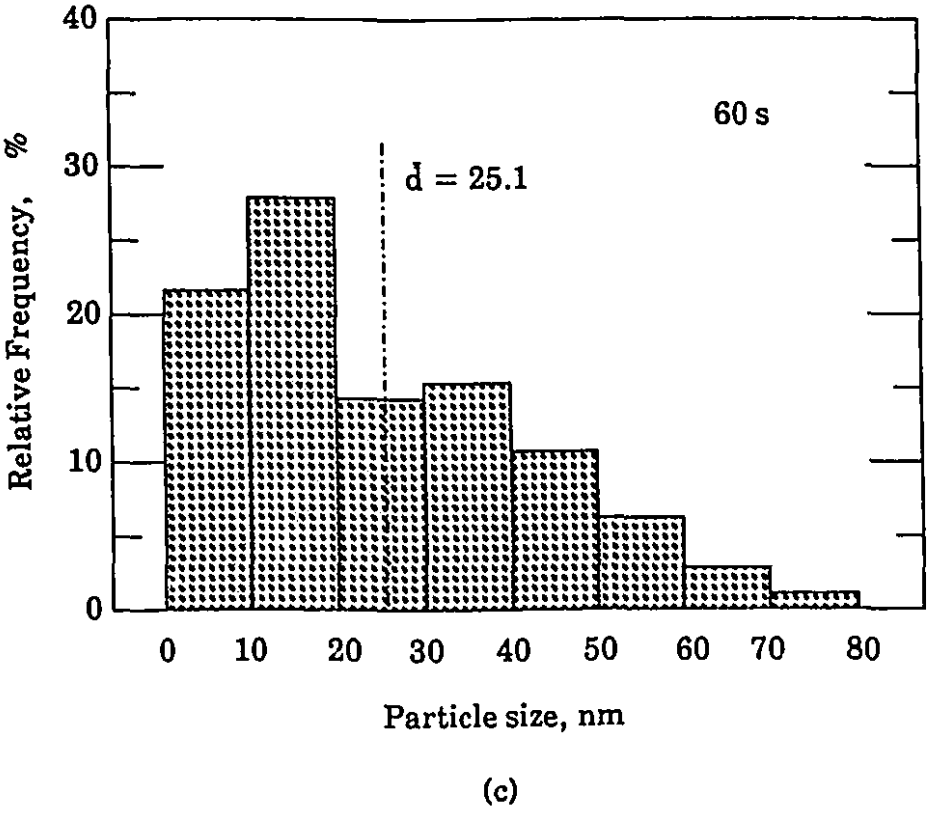

(c)

Fig. 5.16 Carbon extraction replicas showing the progress of MnS precipitation in samples of electrical steel A undergoing creep at 900 °C: (a) 5 s, (b) 15 s, (c) 60 s, (d) 200 s, (e) 420 s, (f) 1200 s, and (g) 3600 s.

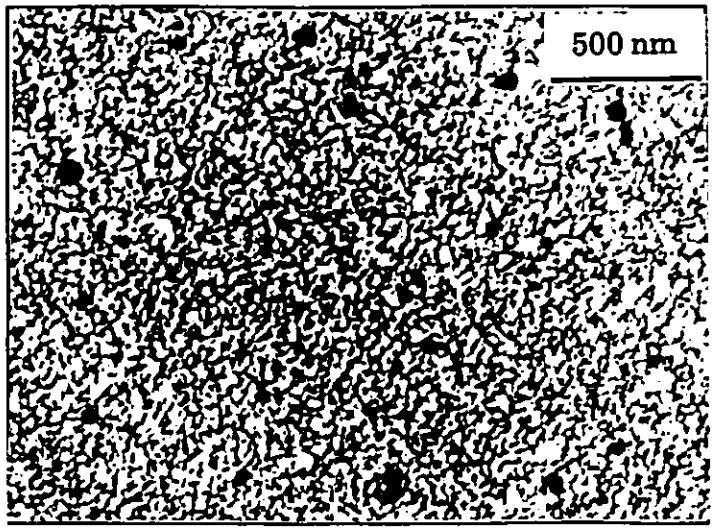

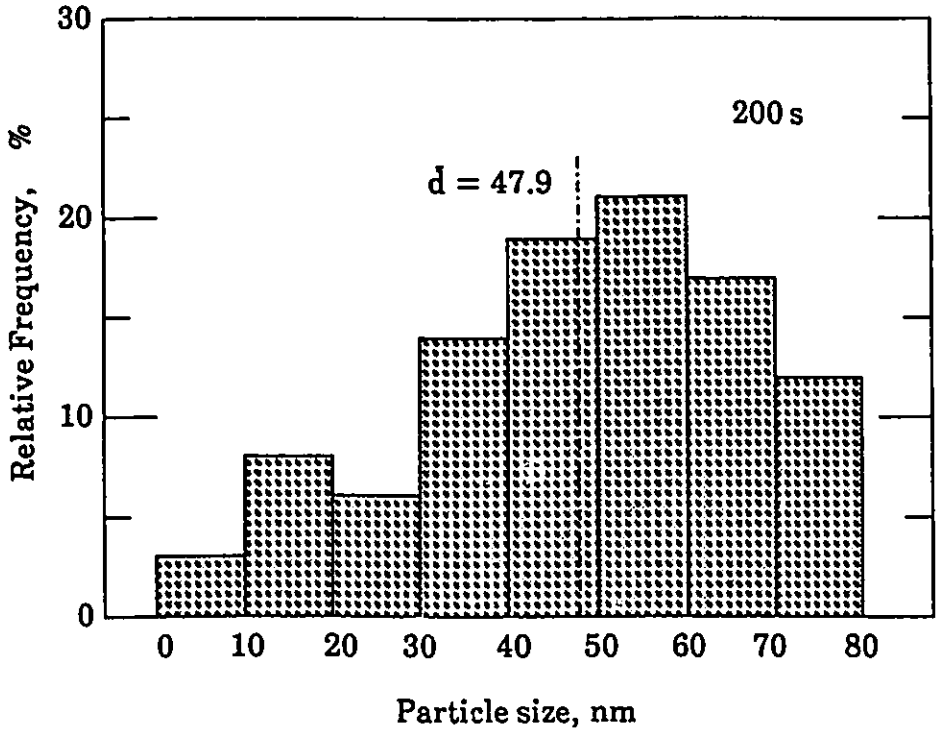

(d)

Fig. 5.16 Carbon extraction replicas showing the progress of MnS precipitation in samples of electrical steel A undergoing creep at 900 °C: (a) 5 s, (b) 15 s, (c) 60 s, (d) 200 s, (e) 420 s, (f) 1200 s, and (g) 3600 s.

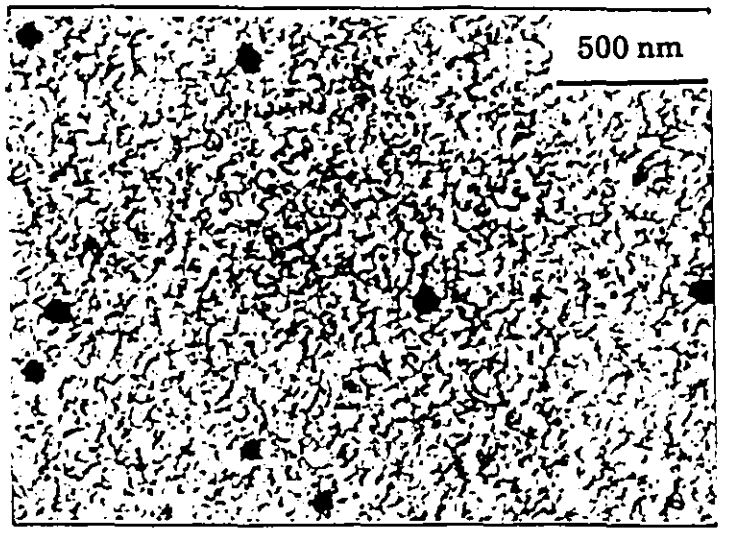

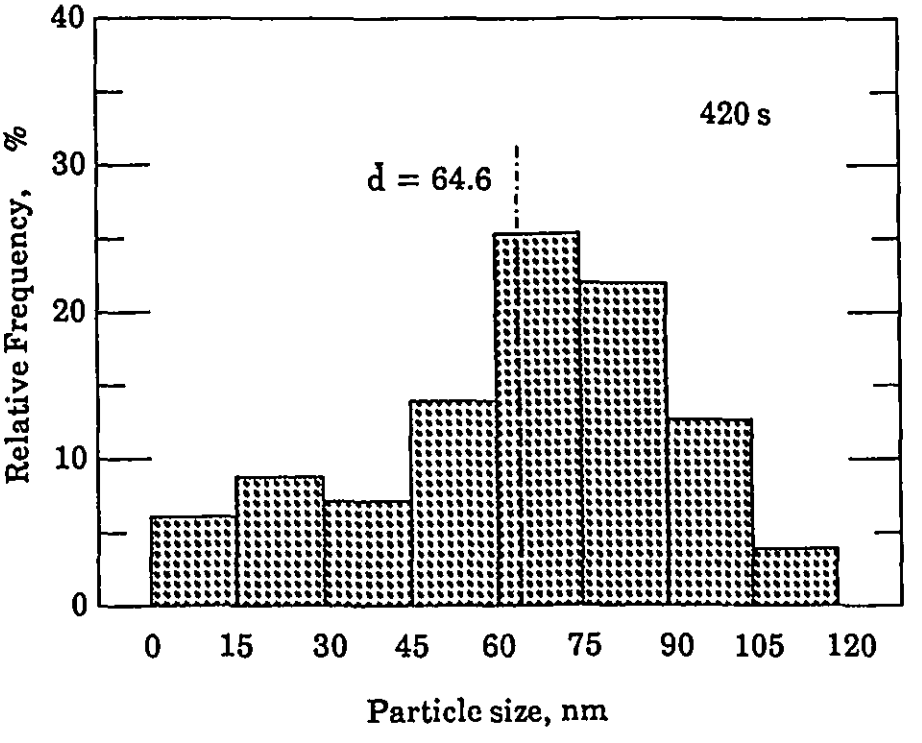

(e)

Fig. 5.16 Carbon extraction replicas showing the progress of MnS precipitation in samples of electrical steel A undergoing creep at 900 °C: (a) 5 s, (b) 15 s, (c) 60 s, (d) 200 s, (e) 420 s, (f) 1200 s, and (g) 3600 s.

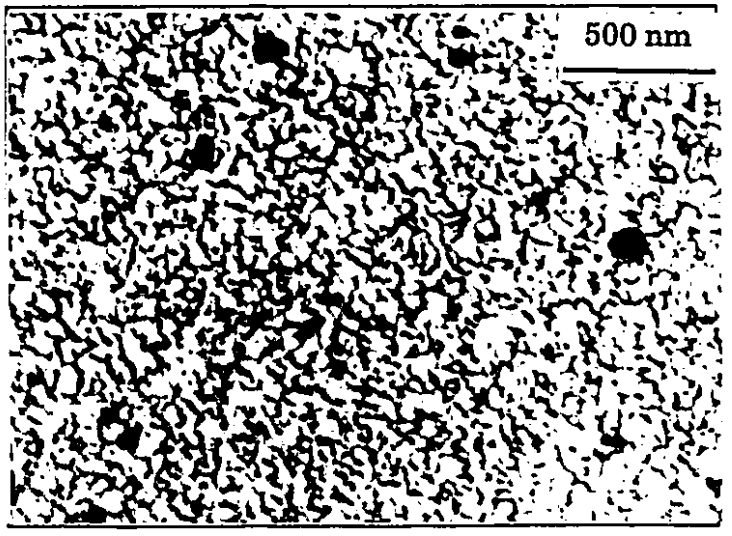

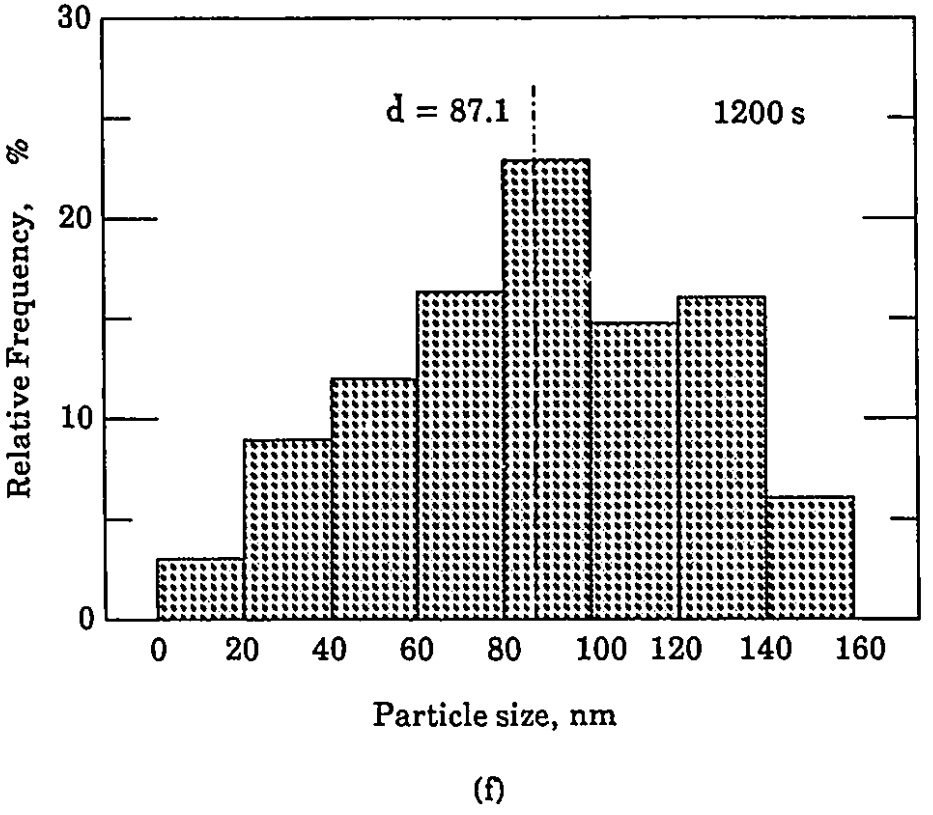

(f)

Fig. 5.16 Carbon extraction replicas showing the progress of MnS precipitation in samples of electrical steel A undergoing creep at 900 °C: (a) 5 s, (b) 15 s, (c) 60 s, (d) 200 s, (e) 420 s, (f) 1200 s, and (g) 3600 s.

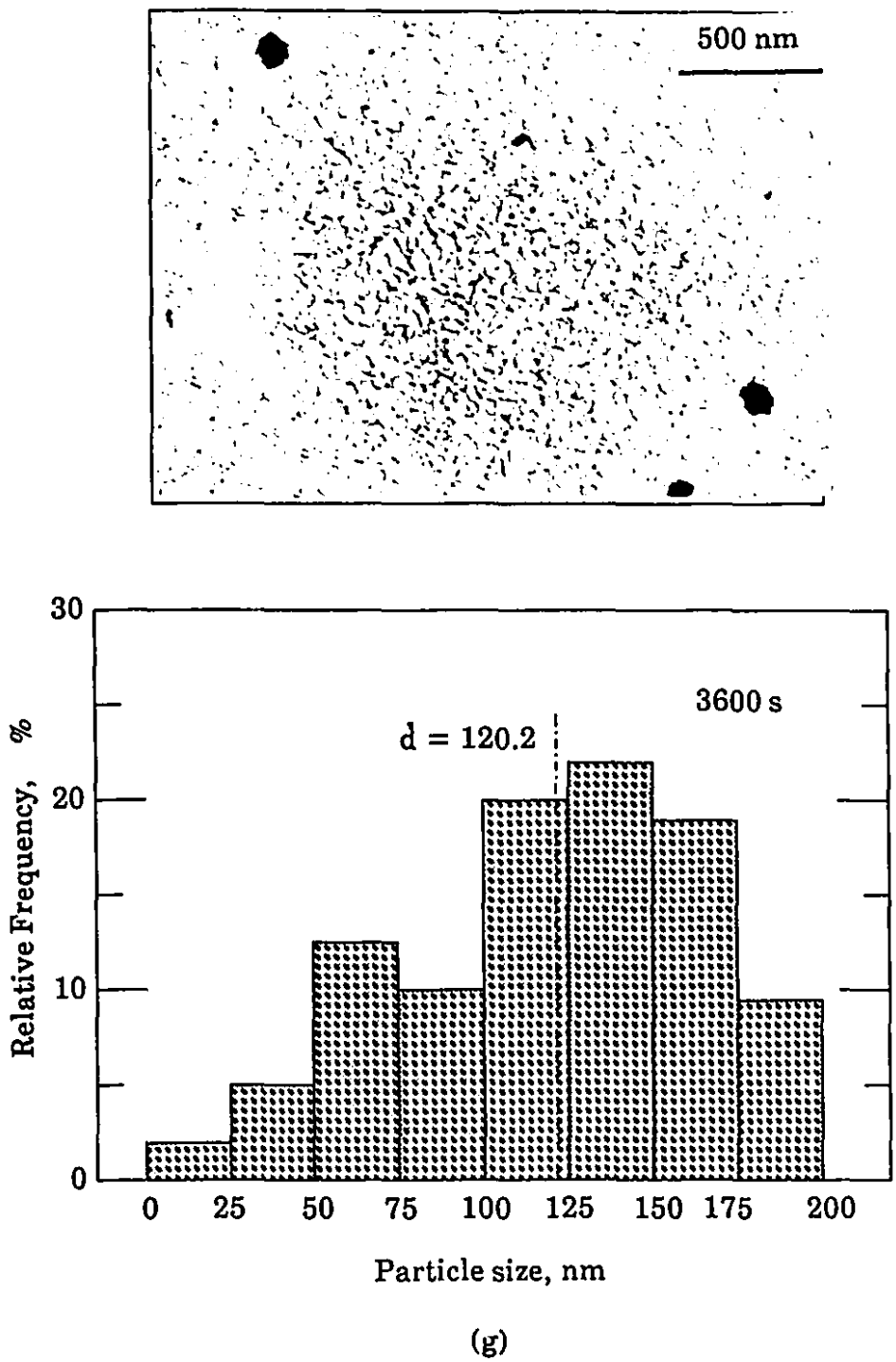

Fig. 5.16 Carbon extraction replicas showing the progress of MnS precipitation in samples of electrical steel A undergoing creep at 900 °C: (a) 5 s, (b) 15 s, (c) 60 s, (d) 200 s, (e) 420 s, (f) 1200 s, and (g) 3600 s.

5.2.1.3 Particle Size Distributions

In an effort to understand the influence of testing temperature and steel composition on the progress of MnS precipitation, the particle size distribution was determined for each specimen. For this purpose, the resulting micrographs were enlarged to a magnification of at least 100,000 and the diameters of the particles were measured with the help of a 7 power monocular capable of giving a precision of ± 0.1 mm. It is worth noting here that the relatively large particles, especially those precipitated at the later stages of precipitation, are not easily extracted by the carbon replicas. In order to avoid missing these large particles, scanning electron microscopy was also employed in the present investigation. Some examples of these micrographs will be presented in §5.2.3 below.

The size distributions determined on electrical steels A, B and C at 800 °C, 900 °C and 1000 °C are summarized in Figures 5.17 to 5.19, respectively. Also displayed in these graphs are the mean particle diameters computed from each distribution. It can be seen from these figures that all the distributions are in the form of normal probabilities. They tend to shift to the right and become wider with increasing test time. On closer examination, it is found that both the mean and the variance of the distribution increase as the test temperature is increased. For instance, the mean diameter of the particles in electrical steel A at 800 °C is about 66 nm at the end of the test, while this value at 1000 °C is as large as 140 nm after only 1200 seconds of creep. This indicates that the growth and coarsening rates of the precipitates are greater at higher temperatures.

An important point which should be mentioned here is that the size distribution and the related mean values reported in Figures 5.17 - 5.19 are surface quantities. Using the equations given by Ashby and Ebeling[186]:

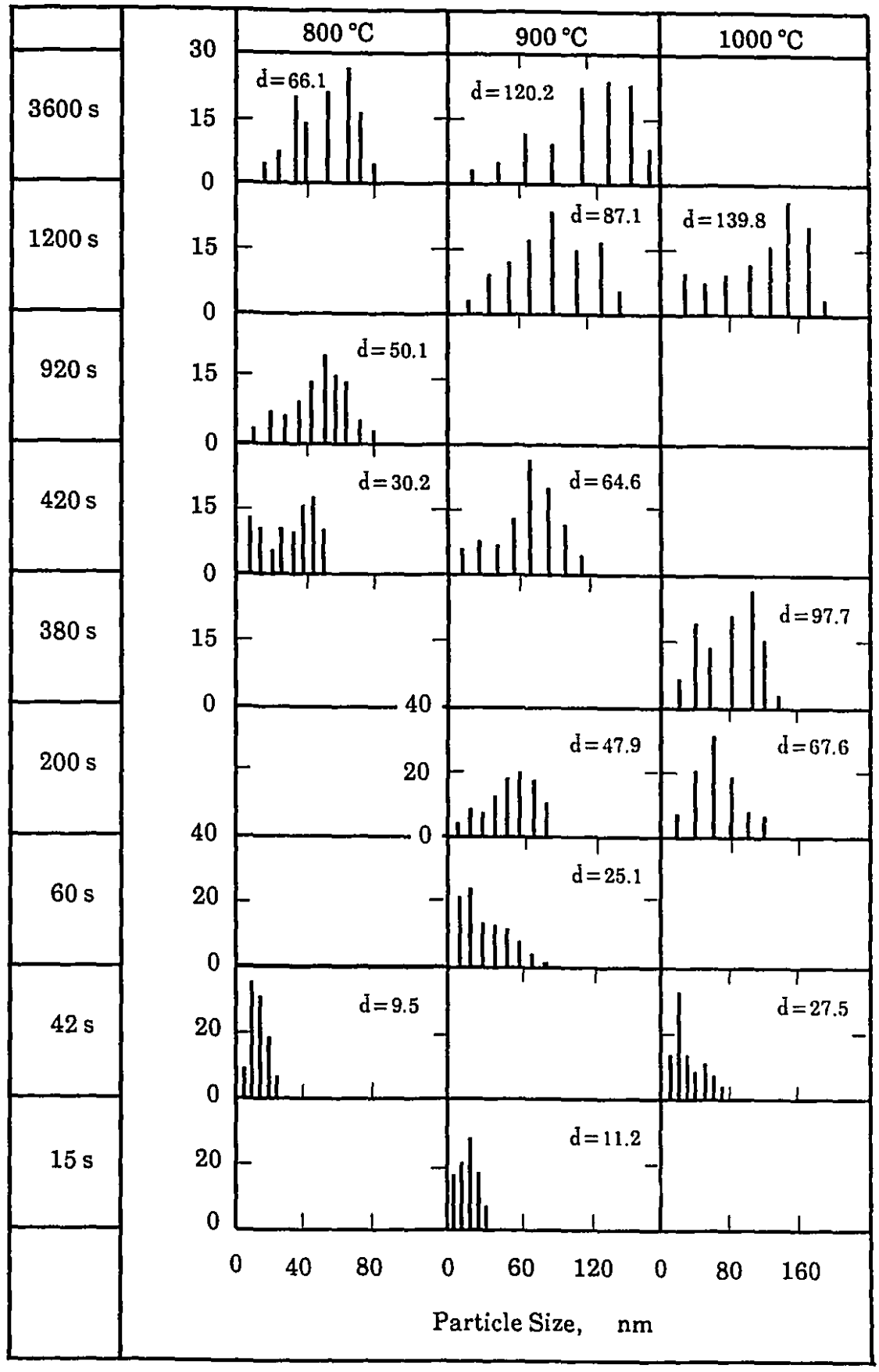

Fig. 5.17 Evolution of the size distribution of the MnS particles during the creep of electrical steel A at the three test temperatures.

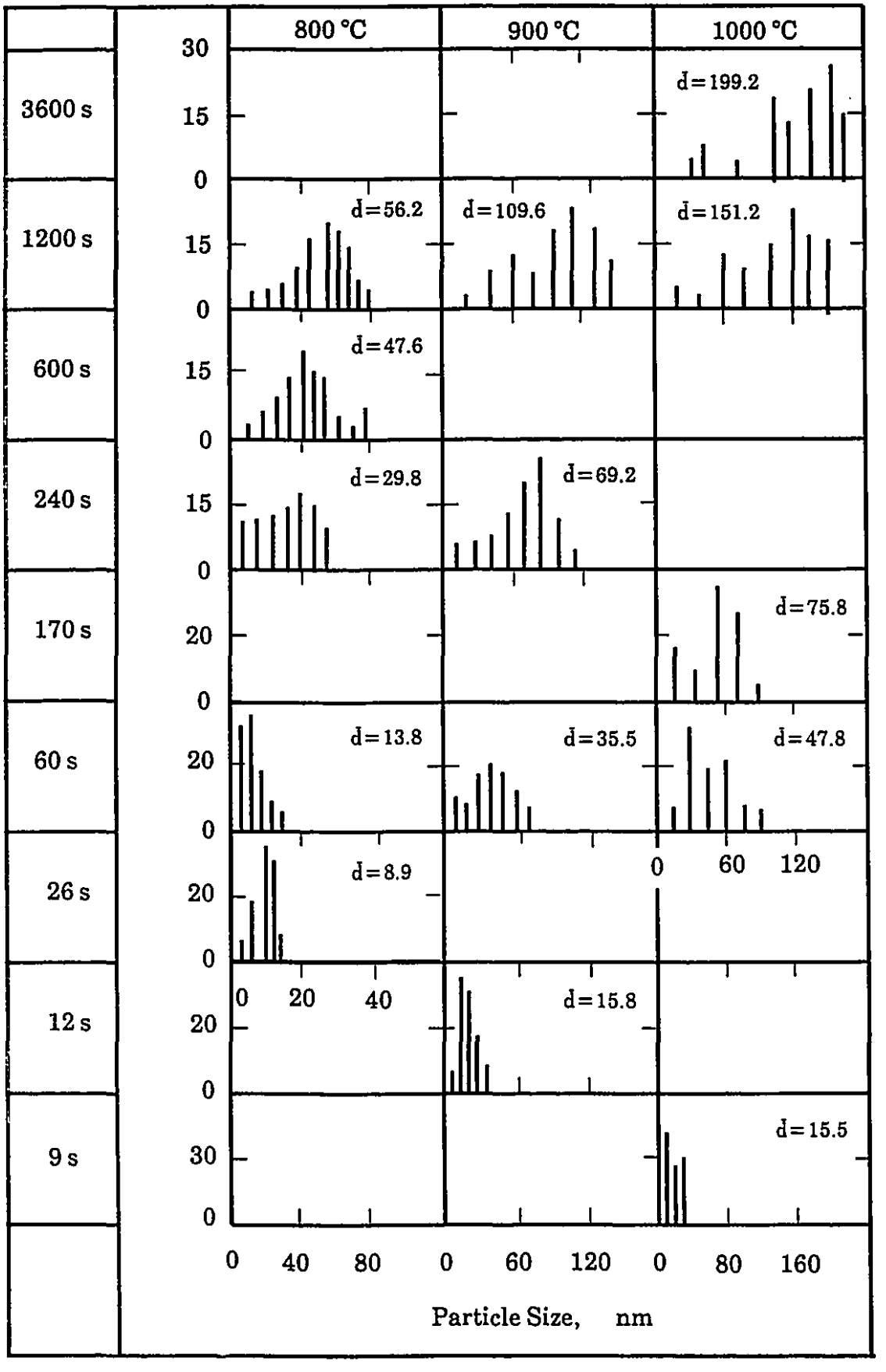

Fig. 5.18 Evolution of the size distribution of the MnS particles during the creep of electrical steel B at the three test temperatures.

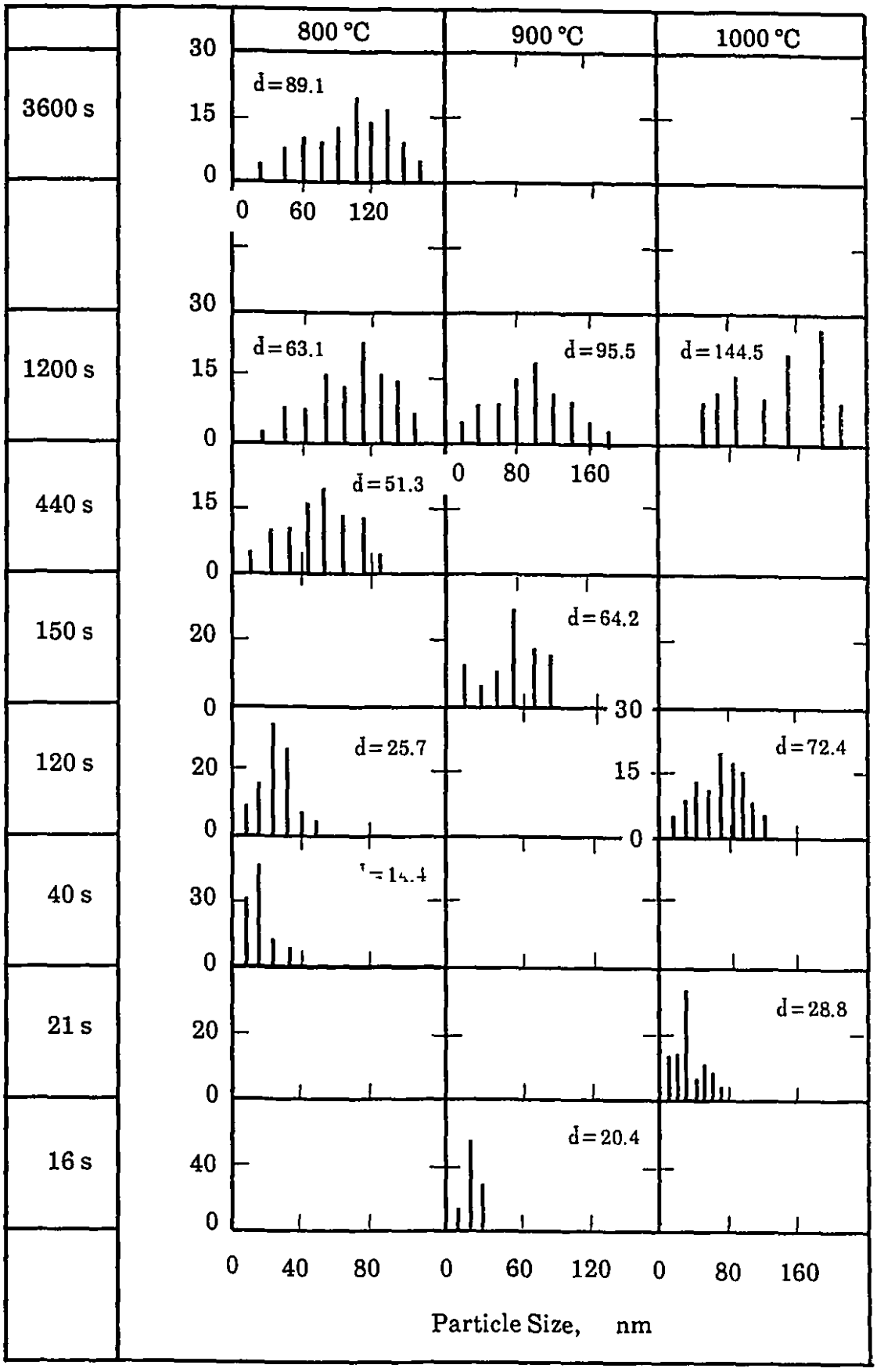

Fig. 5.19 Evolution of the size distribution of the MnS particles during the creep of electrical steel C at the three test temperatures.

$$\bar{d}_v = \frac{\bar{d}_s}{1+(\frac{S.D._{(s)}}{\bar{d}_s})^2} \qquad (5.3)$$

$$S.D._{(v)} = \frac{S.D._{(s)}}{1+(\frac{S.D._{(s)}}{\bar{d}_s})^2} \qquad (5.4)$$

the surface mean diameters $\bar{d}_s$ and standard deviations $S.D._{(s)}$ were converted into the corresponding volume quantities $\bar{d}_v$ and $S.D._{(v)}$. The values of the measured $\bar{d}_s$'s and $S.D._{(s)}$'s as well as the calculated $\bar{d}_v$'s and $S.D._{(v)}$'s are listed in Tables 5.5 - 5.7 for the above three steels, respectively. These tables make it clear that the mean particle sizes and standard deviations of the distributions are functions of time and temperature. They increase with an increase in either the testing temperature or the time.

To determine the influence of steel composition on the progress of MnS precipitation, the mean diameters pertaining to the three steels are plotted versus creep time in Figures 5.20 - 5.22 for 800 °C, 900 °C and 1000 °C, respectively. Examination of these figures leads to the following conclusions:

1) Each log($\bar{d}_v$)-log(time) curve consists of two parts, both of which are approximately linear.

2) The transition times observed on these curves are close to the precipitation finish times measured in the creep tests (noted by the arrows in these figures). This observation again demonstrates the validity of the new technique for monitoring the progress of precipitation at high temperatures.

Table 5.5

Surface and Volume Mean Particle Sizes and Standard Deviations Pertaining to Electrical Steel A

Temperature (°C)	Time (s)	Surface quantities		Volume quantities	
		$\bar{d}_s$ (nm)	S.D.$_{(s)}$	$\bar{d}_v$ (nm)	S.D.$_{(v)}$
800	42	9.5	3.2	8.5	2.9
	420	30.2	7.4	28.5	7.0
	920	50.1	9.2	48.5	8.9
	3600	66.1	11.8	64.1	11.4
900	15	11.2	3.8	10.0	3.4
	60	25.1	6.5	23.5	6.1
	200	47.9	8.9	46.3	8.6
	420	64.6	11.5	62.6	11.1
	1200	87.1	15.2	84.5	14.8
	3600	120.2	24	115.6	23.1
1000	42	27.5	6.8	25.9	6.4
	200	67.6	12.4	65.4	12.0
	380	97.7	18.3	94.4	17.7
	1200	139.8	27.5	134.6	26.5

Table 5.6

Surface and Volume Mean Particle Sizes and Standard Deviations Pertaining to Electrical Steel B

Temperature (°C)	Time (s)	Surface quantities		Volume quantities	
		$\bar{d}_s$ (nm)	S.D.$_{(s)}$	$\bar{d}_v$ (nm)	S.D.$_{(v)}$
800	26	8.9	2.8	8.1	2.5
	60	13.8	4.3	12.6	3.9
	240	29.8	7.3	28.1	6.9
	600	47.6	8.8	46.0	8.5
	1200	56.2	9.8	54.5	9.5
900	12	15.8	5.1	14.3	4.6
	60	35.5	7.9	33.8	7.5
	240	69.2	12.9	66.9	12.5
	1200	109.6	19.8	106.1	19.2
1000	9	15.5	4.9	14.1	4.5
	60	47.8	8.9	46.2	8.6
	170	75.8	14.4	73.2	13.9
	1200	151.2	38.6	141.9	36.2
	3600	199.2	44.8	189.6	42.6

Table 5.7

Surface and Volume Mean Particle Sizes and Standard Deviations Pertaining to Electrical Steel C

Temperature (°C)	Time (s)	Surface quantities		Volume quantities	
		d_s (nm)	S.D.$_{(s)}$	d_v (nm)	S.D.$_{(v)}$
800	40	14.4	4.6	13.1	4.2
	120	25.7	6.6	24.1	6.2
	440	51.3	9.4	49.6	9.1
	1200	63.1	10.8	61.3	10.4
	3600	89.1	15.7	86.4	15.2
900	16	20.4	6.1	18.7	5.6
	150	64.2	11.3	62.3	11.0
	1200	95.5	17.8	92.3	17.2
1000	21	28.8	7.1	27.1	6.7
	120	72.4	13.6	70.0	13.1
	1200	144.5	31	138.1	29.6

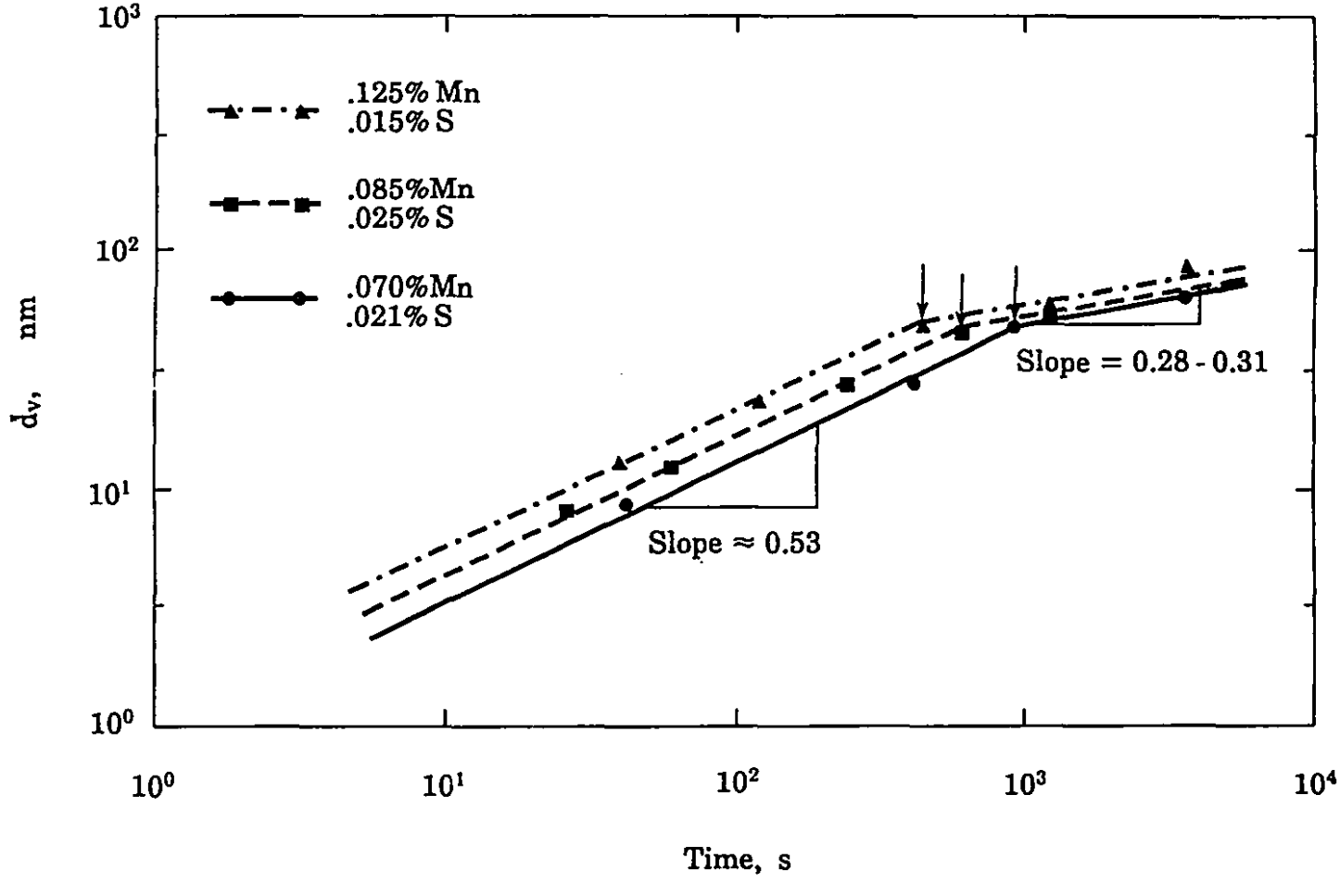

Fig. 5.20 Dependence of mean particle size ($\bar{d}_v$) on creep time at 800 °C.

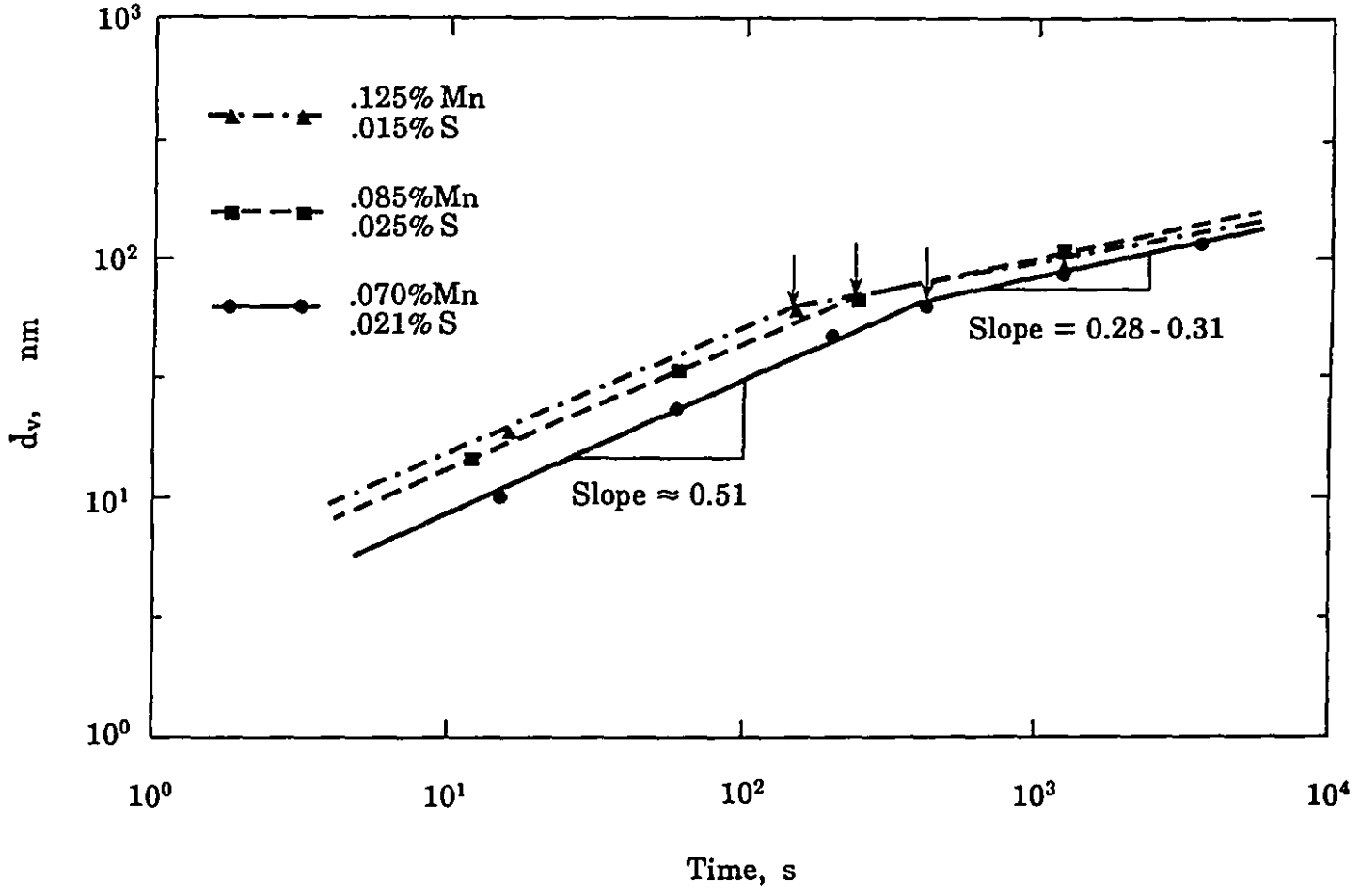

Fig. 5.21 Dependence of mean particle size ($\bar{d}_v$) on creep time at 900 °C.

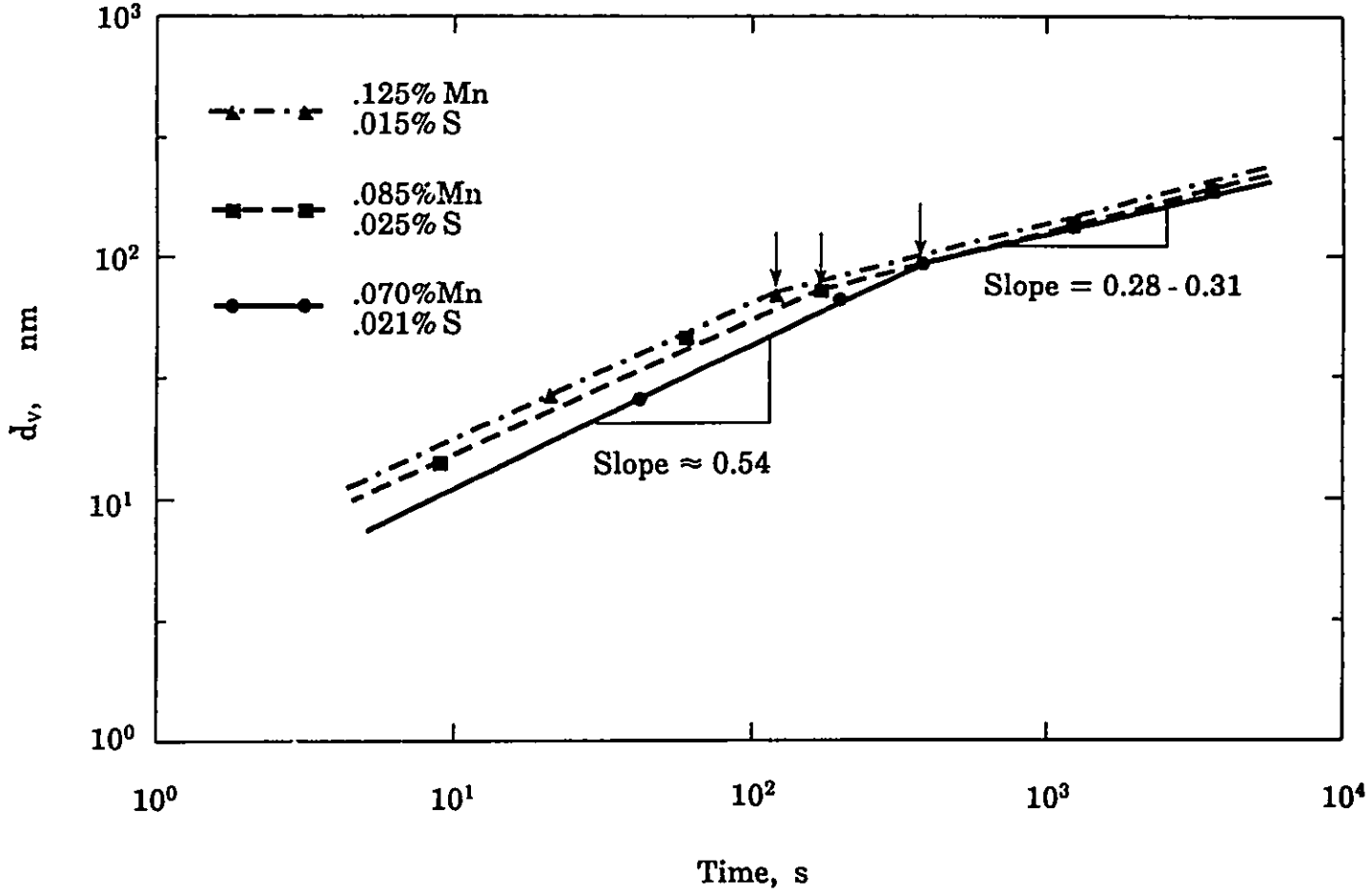

Fig. 5.22 Dependence of mean particle size (d_v) on creep time at 1000 °C.

3) The mean particle sizes corresponding to the transition (or P_f) times at a given temperature increase with increasing Mn concentration.

4) Although the different curves go through their transitions at different times, the first and second portions are approximately parallel to each other. This indicates that the growth and coarsening mechanisms of MnS precipitation are much the same in the different steels.

5) The first parts of the curves have higher slopes (from 0.51 to 0.54) than the second ones (from 0.28 to 0.31), indicating that the growth rate is greater than the coarsening rate for such precipitation.

6) Finally and perhaps more interestingly, the first slope of about 0.5 indicates that a diffusion process rather than an interface reaction is controlling the growth of the particles (see §2.2.6.3). The second slope of about 0.3 , on the other hand, reveals that coarsening of the precipitates may be controlled by both bulk diffusion and grain boundary diffusion.

The above features of the curves will be discussed in more detail in Chapter 7.

5.2.2 IDENTIFICATION OF THE PARTICLES

The freshly precipitated particles in the electrical steels were identified by examining their X-ray spectra. Two typical results are presented in Figures 5.23 and 5.24: the first was acquired on a carbon extraction replica and the second directly on a quenched specimen. Both reveal the strong Mn and S peaks associated with most of the particles formed in these steels. It should be pointed out that the Si peaks visible in the second EDX spectrum are due to this element's presence in the matrix and the Fe peaks are from the matrix itself. Thus, it can be concluded that the manganese sulfide precipitates are responsible for the hardening effect observed during the creep of the four electrical steels tested. As for the Ti steel, some previous research[77,120,147] has already confirmed that TiC plays the key role in strengthening the steel

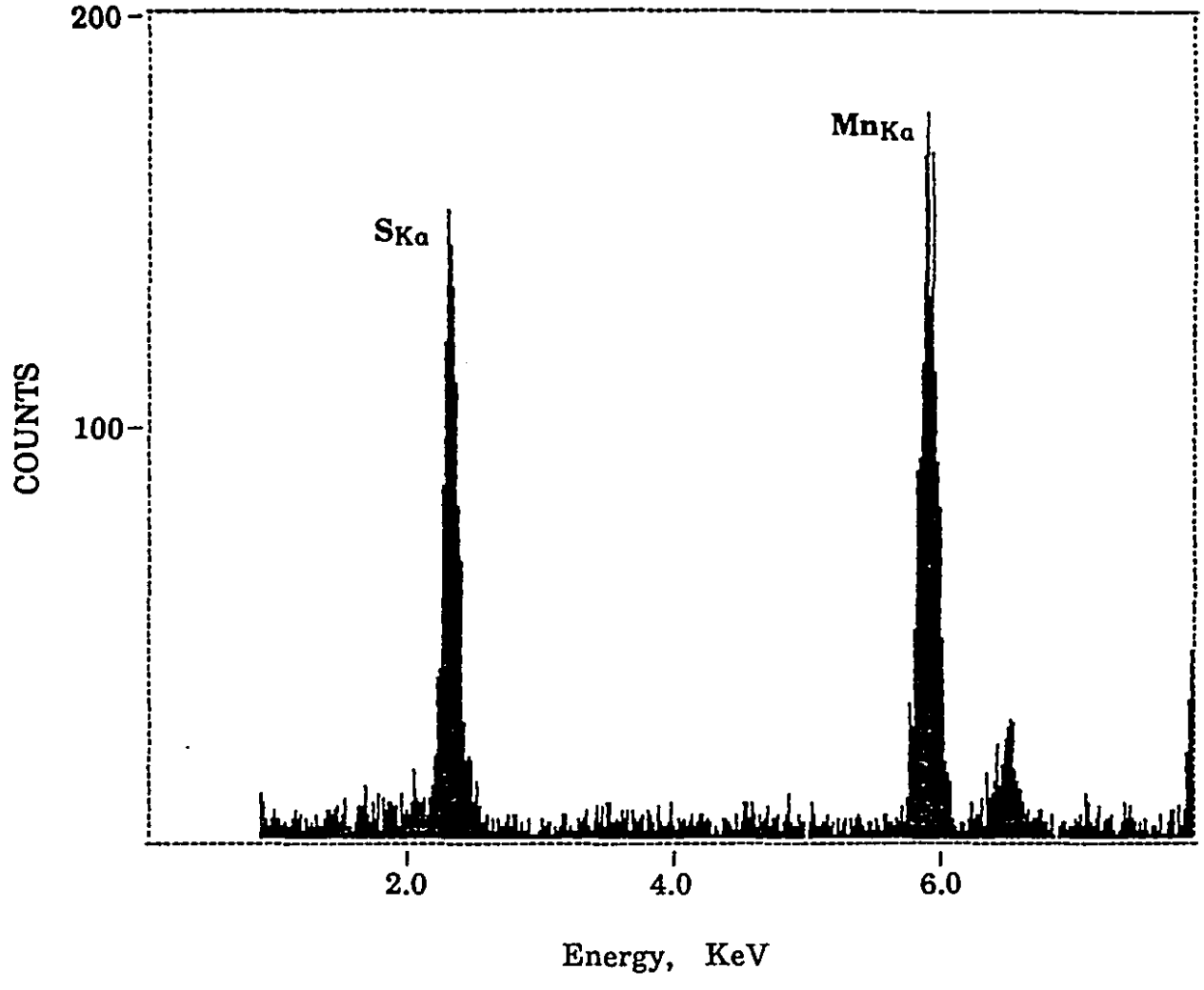

Fig. 5.23 Typical X-ray spectrum of MnS particles displaying strong Mn and S peaks obtained on a carbon extraction replica.

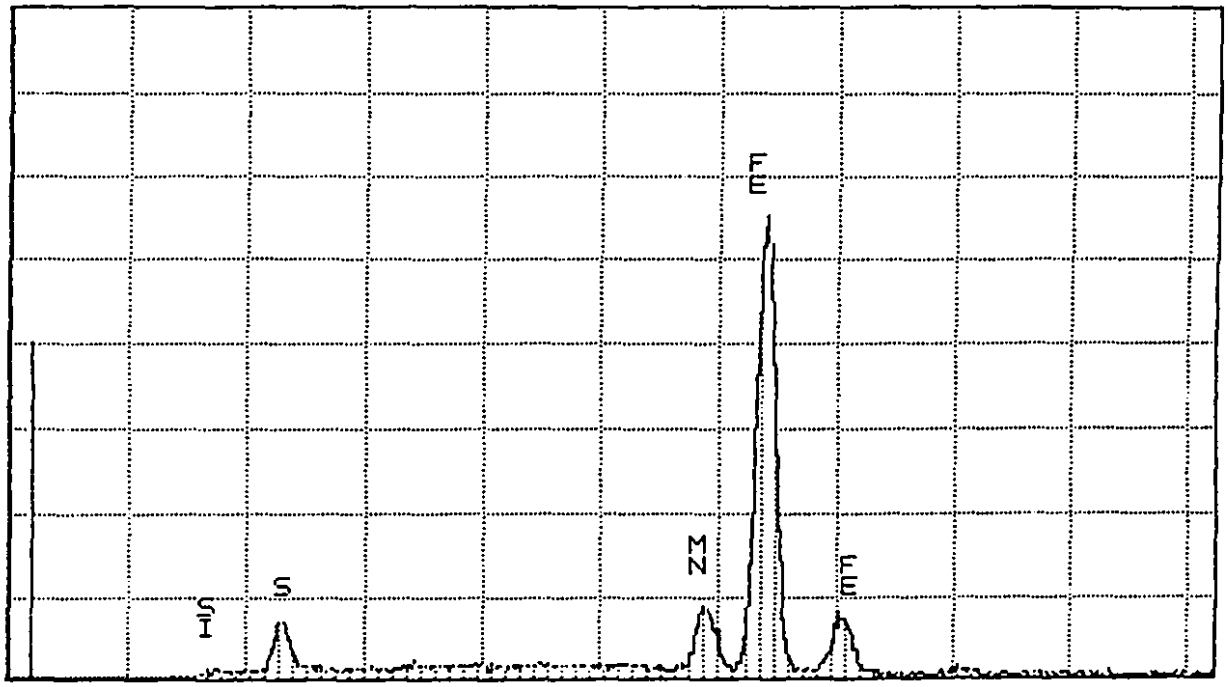

Energy, KeV

Fig. 5.24 Typical X-ray spectrum of MnS particles displaying strong Mn and S peaks obtained on a quenched specimen.

during deformation. In order to save time, the EDX technique was not applied to this steel.

5.2.3 NUCLEATION SITES FOR MnS PRECIPITATION

As mentioned above, in addition to the carbon extraction replicas, direct observations were also made of the quenched specimens by means of scanning electron microscopy (SEM) for measurement of the particle size distribution. Two micrographs acquired for this purpose are shown in Figure 5.25. These photographs were obtained at the end of creep testing, one of electrical steel C (0.125% Mn-0.015% S) at 800 °C and the other of electrical steel B (0.085% Mn-0.028% S) at 1000 °C. These pictures not only provide information regarding the particle size distribution, but also about the nucleation sites. The micrograph at the top of Figure 5.25 demonstrates that some precipitates are nucleated within grains. From this picture, as well as those presented in Figure 5.16, it can be seen that the particles are not randomly located within the grains but are, instead, heterogeneously distributed in a cell-like manner. As reviewed in §2.2.4, this type of distribution suggests that the MnS precipitates are nucleated on dislocations or on the sub-boundaries formed during deformation. In addition, the photograph at the bottom of Figure 5.25 clearly shows that grain boundaries are also nucleation sites for this type of strain-induced precipitation in electrical steels.

In order to investigate further these two types of nucleation sites, two kinds of special observations were made on each steel. The first was performed on some heavily etched specimens that can reveal subgrain structures. A good example is shown in Figure 5.26, which illustrates the dislocation substructure present in electrical steel B after 1200 seconds at 800 °C. Although some particles may have been removed by the heavy etch, it is also explicit in this micrograph that the sub-boundaries act as nucleation sites for precipitation. The second kind of observation was focused on the precipitates nucleated at grain boundaries. Typical morphologies of such precipitates in electrical steel B after 1200 seconds of creep at four different temperatures are presented in Figure 5.27. By comparing these photographs, it appears that

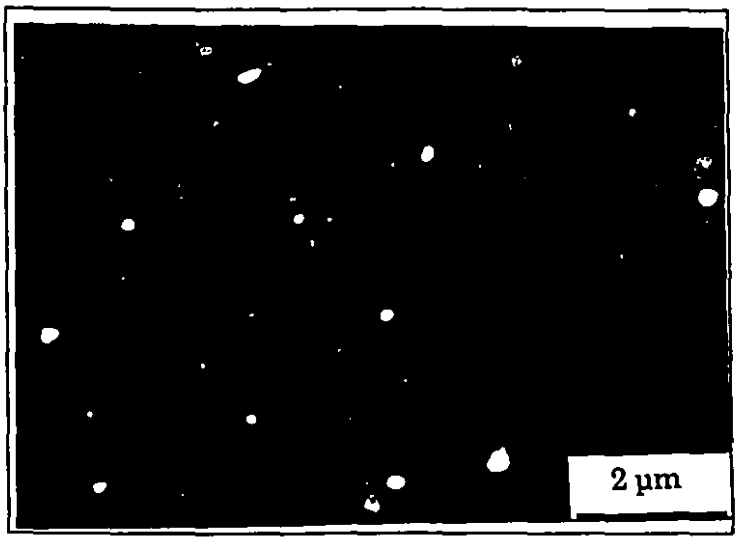

(a)

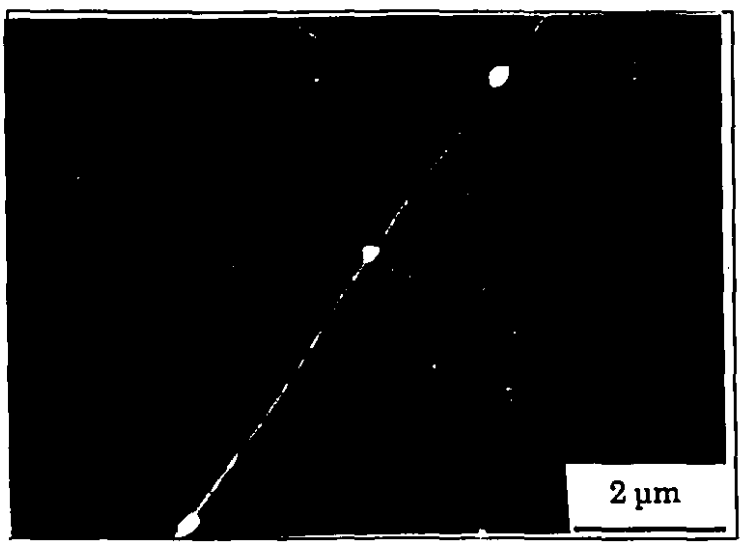

(b)

Fig. 5.25 Distribution of MnS particles revealed by SEM after testing (a) electrical steel C at 800 °C, and (b) electrical steel B at 1000 °C.

Fig. 5.26 Micrograph showing the MnS particles nucleated on the substructure of electrical steel B after 1200 seconds of creep at 800 °C.

more and more precipitates nucleate on grain boundaries as the testing temperature is raised.

Finally, it is worth mentioning that phenomena similar to those shown in the above micrographs were also observed in the other electrical steels and thus they will be given further consideration in the chapters that follow.

5.2.4 GRAIN DEFORMATION AND GRAIN BOUNDARY SLIDING

As demonstrated above, both grain boundaries and dislocation substructures are favorable sites for the nucleation of MnS precipitates. To investigate the influence of each nucleation mode on the creep behavior, and to understand the mechanisms that influence the present precipitation-

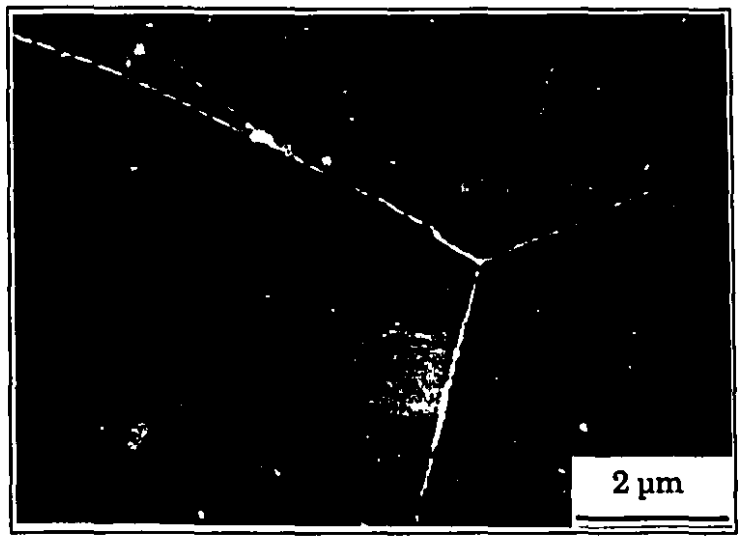

(a)

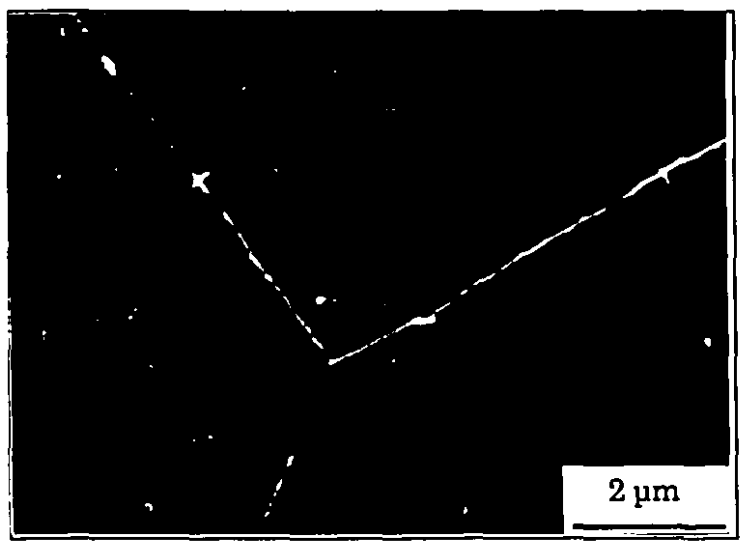

(b)

Fig. 5.27 MnS particles nucleated at grain boundaries in electrical steel B after 1200 seconds of creep at (a) 800 °C, (b) 900 °C, (c) 1000 °C, and (d) 1100 °C.

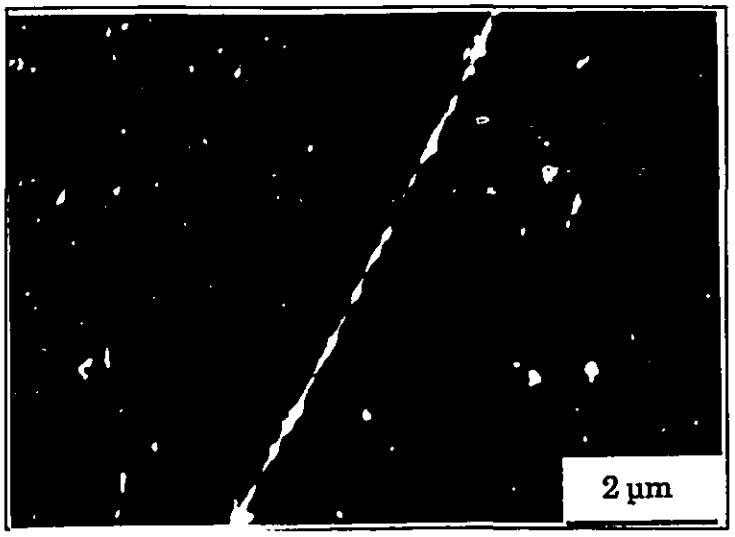

(c)

(d)

Fig. 5.27 MnS particles nucleated at grain boundaries in electrical steel B after 1200 seconds of creep at (a) 800 °C, (b) 900 °C, (c) 1000 °C, and (d) 1100 °C.

monitoring technique, it is necessary to have some knowledge of the microstructural changes taking place during testing. In this context, some experimental evidence will now be provided regarding grain deformation as well as grain boundary sliding.

5.2.4.1 Grain Deformation

During creep, the deformation occurring within grains is so obvious that the deformed grains can be readily observed on any specimen by optical microscopy. An example of these observations is given in Figure 5.28, where a grain in a sample of 0.070% Mn-0.021% S steel is presented twice. In this figure, the upper picture shows the state of this grain immediately after solution treatment, but before deformation, while the lower one illustrates the condition of the grain after testing at 950 °C. It should be pointed out that, to preserve the original boundaries of the grain, the specimen was not repolished before taking the second photograph. This is why this picture is less clear than the first. However, comparison of the two micrographs demonstrates that considerable deformation takes place within the grains during testing. Thus, we come to the conclusion that deformation of the grains makes a great contribution towards the overall creep strain in the electrical steels.

5.2.4.2 Observations of Grain Boundary Sliding

In a manner similar to the one used for the examination of grain deformation, the grain boundary sliding occurring during creep was studied in rather more detail. The sampling schedule employed in this investigation for electrical steel A undergoing creep at 1000 °C is shown in Figure 5.29. In these tests, all samples were helium quenched and observed after solutionizing but before loading. In order to reveal whether or not grain boundary sliding takes place during creep, and, if it does, to estimate quantitatively the amount of grain boundary sliding occurring during each stage of testing, the positions of some grain boundaries were marked by lines. Subsequently, each specimen was again reheated to the solution temperature and tested under the

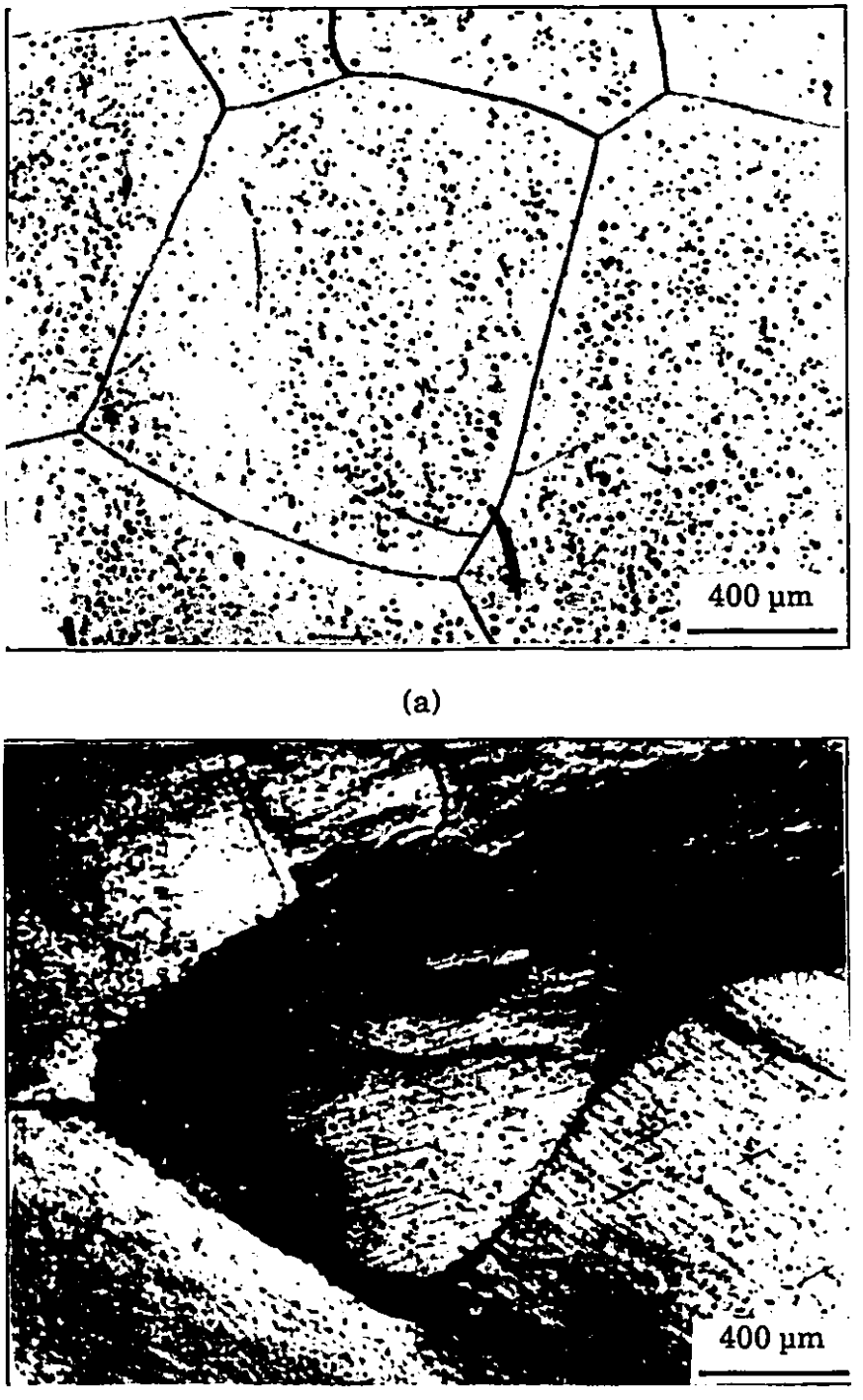

Fig. 5.28 Grain deformation occurring in a sample of electrical steel A tested at 950 °C: (a) before straining, and (b) after testing.

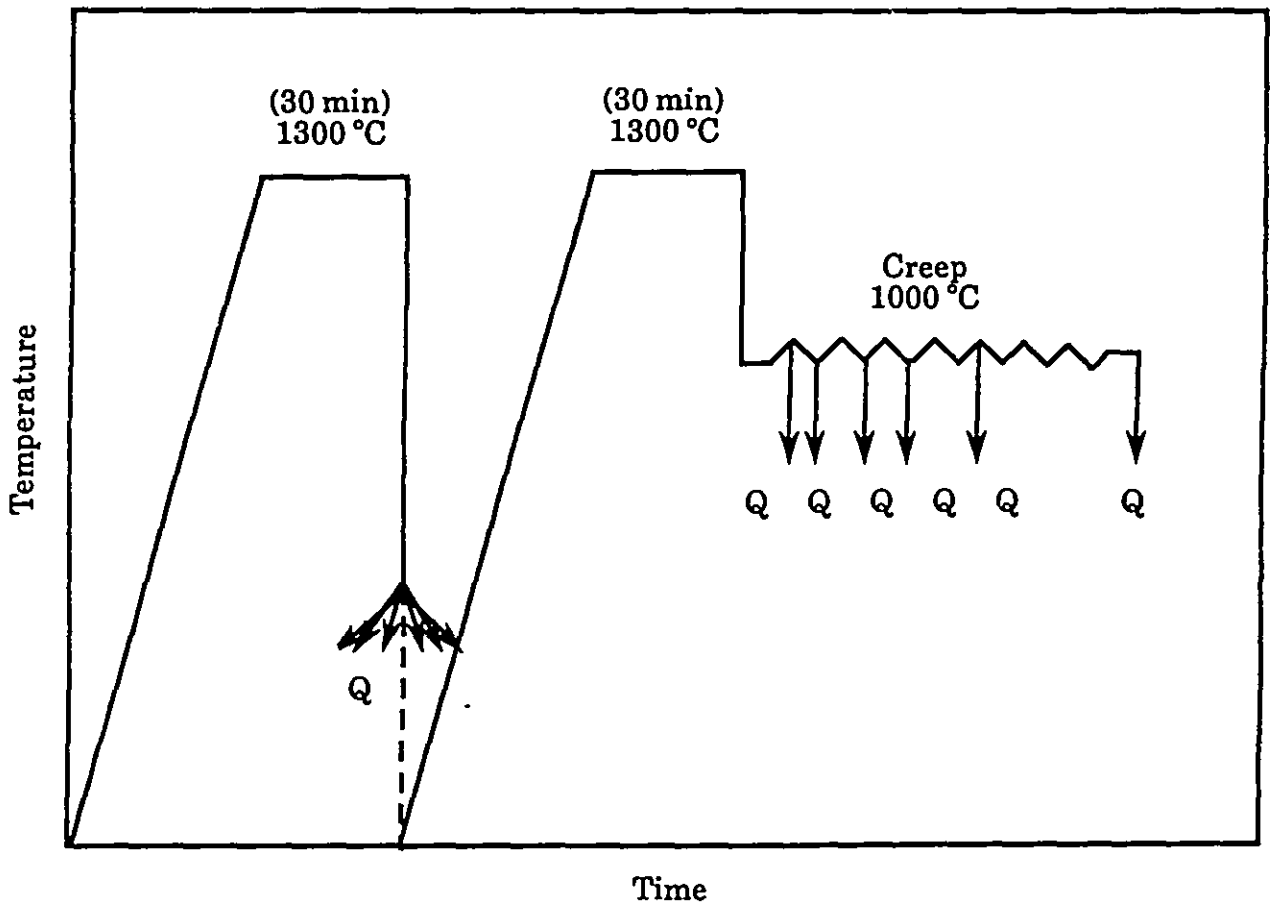

Fig. 5.29 Sampling schedule employed for the investigation of grain boundary sliding during the creep of electrical steel A at 1000 °C.

experimental conditions of the previous tests. After increasing creep times, the specimens were requenched and rechecked by optical microscopy.

Some results typical of this group of experiments are presented in Figures 5.30 to 5.35. The upper micrograph in each figure reveals the original state of each specimen prior to the application of the load. To mark the position of the specific grain boundary, a line perpendicular to the boundary was carved on the surface of the sample. In sharp contrast to the top pictures, the lower photographs demonstrate the occurrence of grain boundary sliding during deformation. As can be seen, the amount of grain boundary sliding is a function of the creep time. If creep has occurred for only a few seconds, grain boundary sliding has not yet begun (see Figure 5.30). Since grain boundary sliding, as described by LeMay[150] and Ashby et al.[172], can be regarded as Newtonian viscous in nature, such a process necessarily requires time before it can be observed. Once it starts, however, its extent increases with increasing creep time, as illustrated by the lower photographs of Figures 5.31 - 5.35, where specific grain boundaries are presented after increasing creep times. A detailed evaluation of the relationship between the amount of grain boundary sliding and the creep time is given next.

5.2.4.3 Evaluation of Grain Boundary Sliding

Since it is very time consuming to measure the amount of grain boundary sliding that occurs during each stage of creep, the present work was restricted to electrical steel A deformed at 1000 °C. In this investigation, the grain boundary contributions were evaluated quantitatively, and more than 20 boundaries on each specimen were analyzed in this way. The displacement of each boundary after a specified creep time was carefully measured on the resulting micrographs.

McLean[187] once carried out an extensive investigation of grain boundary sliding in pure aluminum during creep. Based on the assumption that the grain boundaries were planes inclined at 45° to the compression (or tension) axis, he proposed the following equation to relate the measured displacements of individual boundaries to the creep strain:

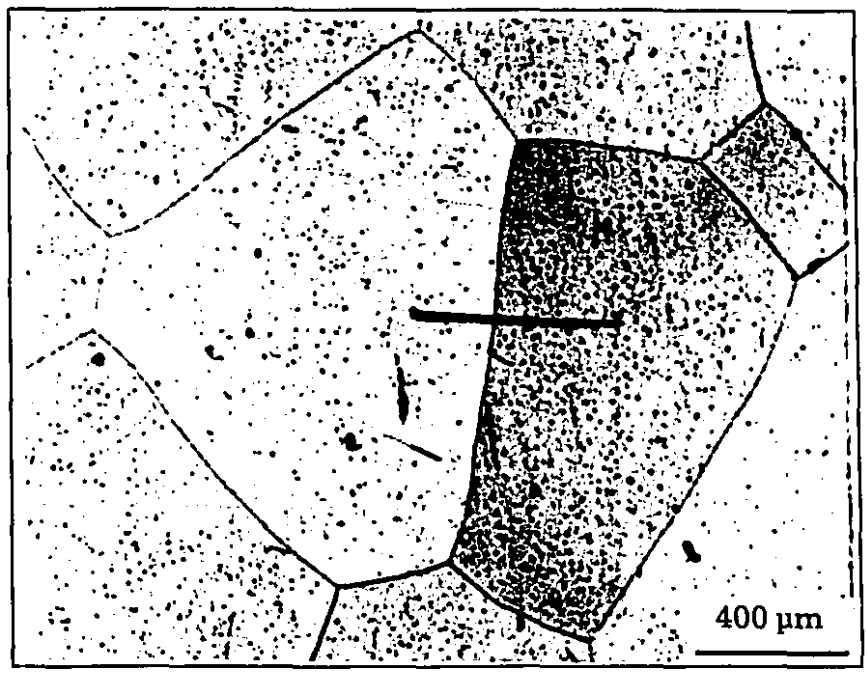

(a)

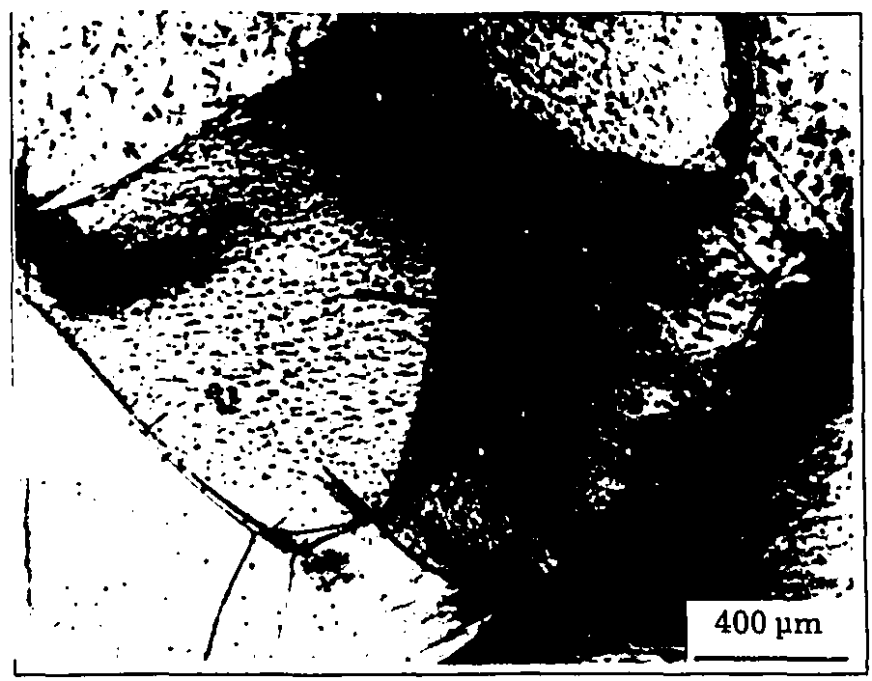

(b)

Fig. 5.30 Grain boundary sliding in electrical steel A tested at 1000 °C: (a) before deformation, and (b) after 5 seconds of creep.

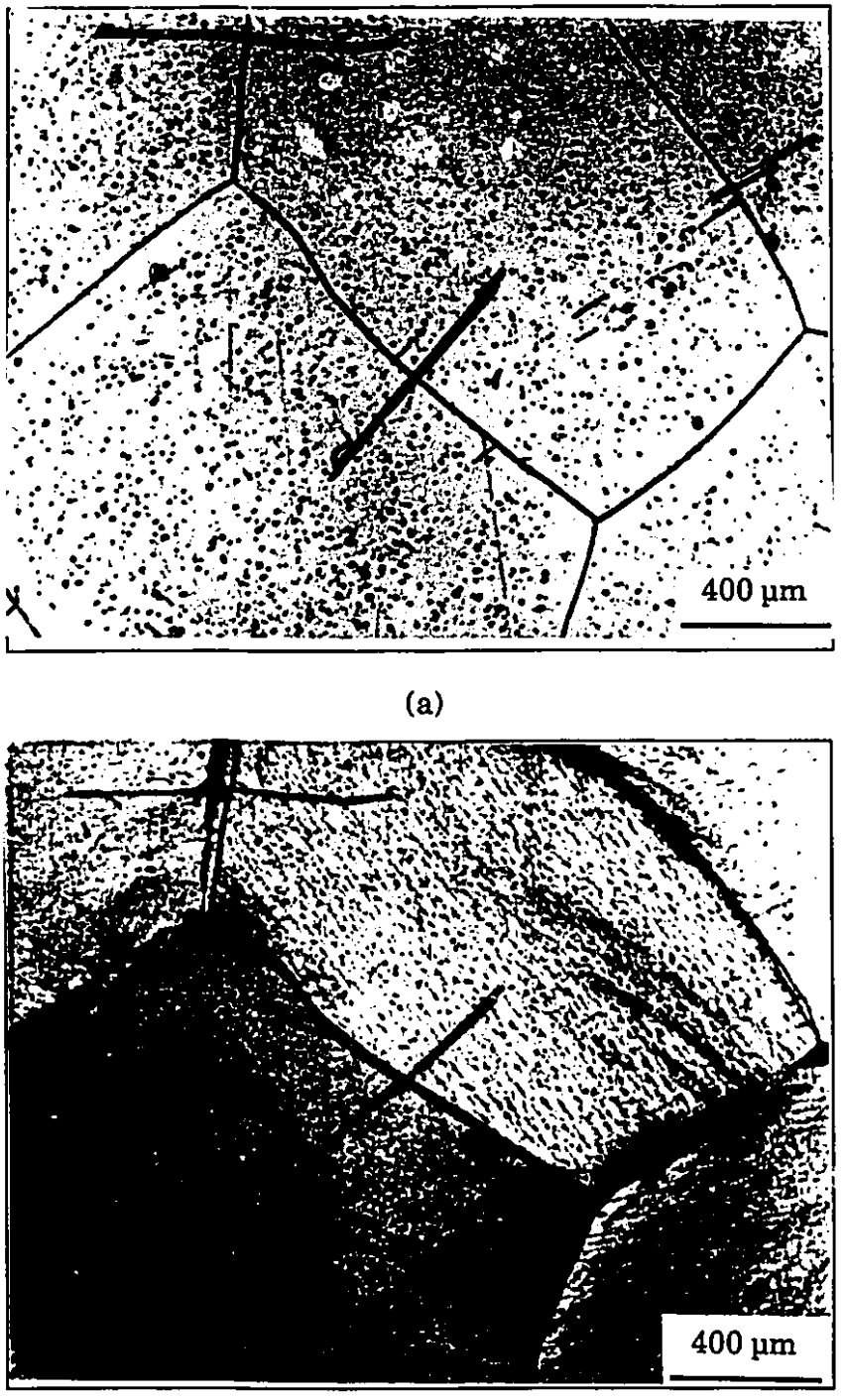

Fig. 5.31 Grain boundary sliding in electrical steel A tested at 1000 °C: (a) before deformation, and (b) after 20 seconds of creep.

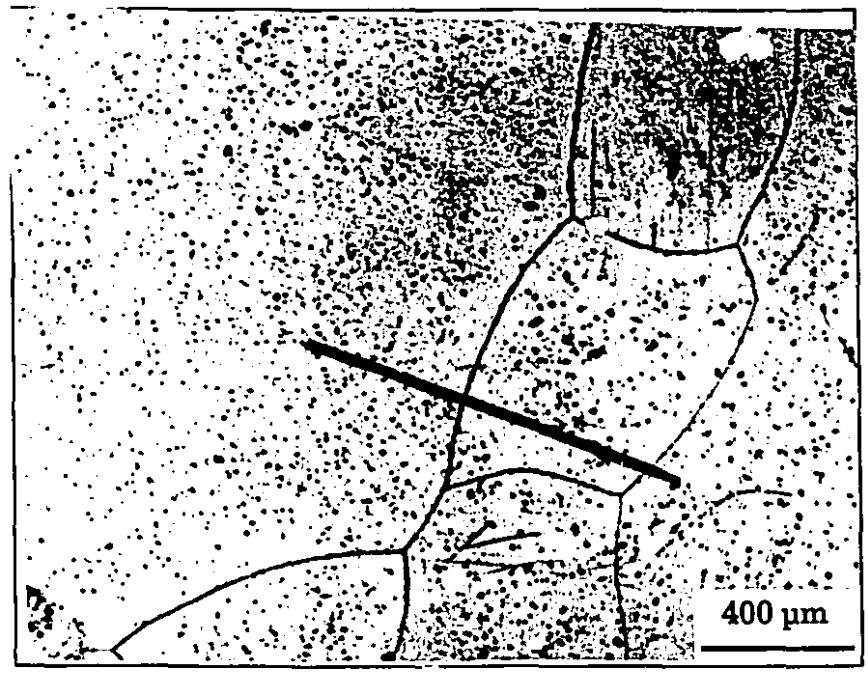

(a)

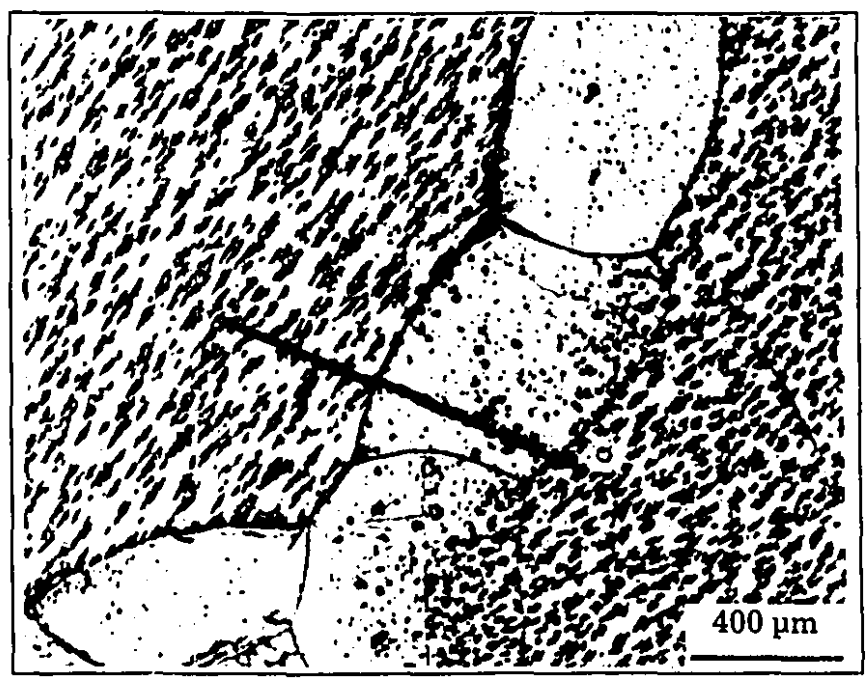

(b)

Fig. 5.32 Grain boundary sliding in electrical steel A tested at 1000 °C: (a) before deformation, and (b) after 200 seconds of creep.

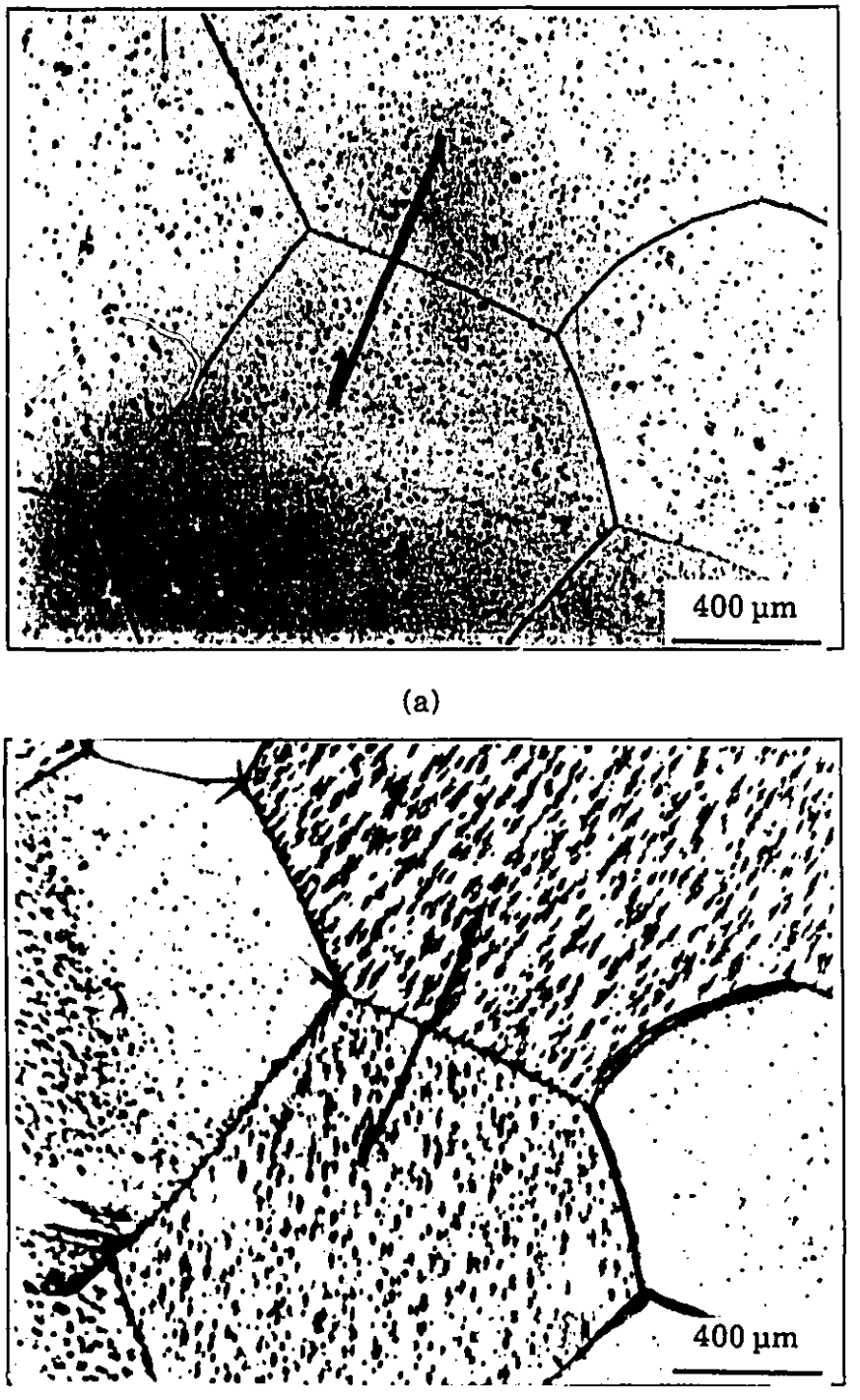

Fig. .33 Grain boundary sliding in electrical steel A tested at 1000 °C: (a) before deformation, and (b) after 380 seconds of creep.

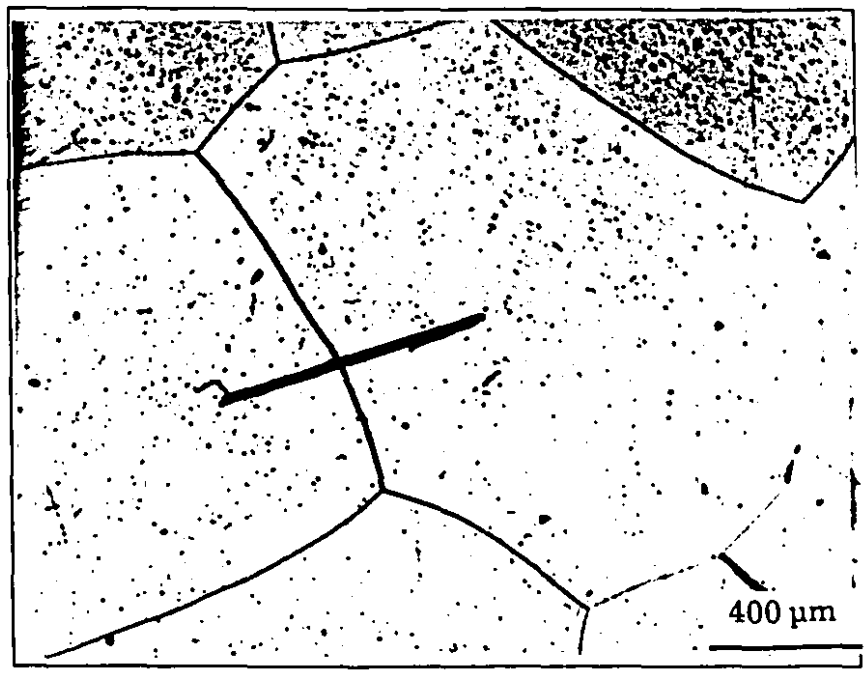

(a)

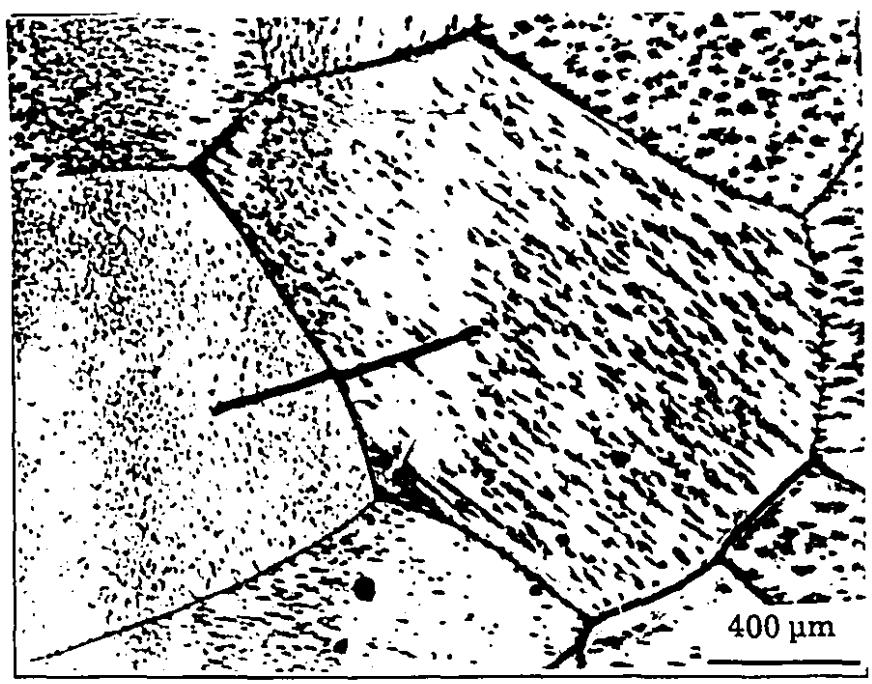

(b)

Fig. 5.34 Grain boundary sliding in electrical steel A tested at 1000 °C: (a) before deformation, and (b) after 1200 seconds of creep.

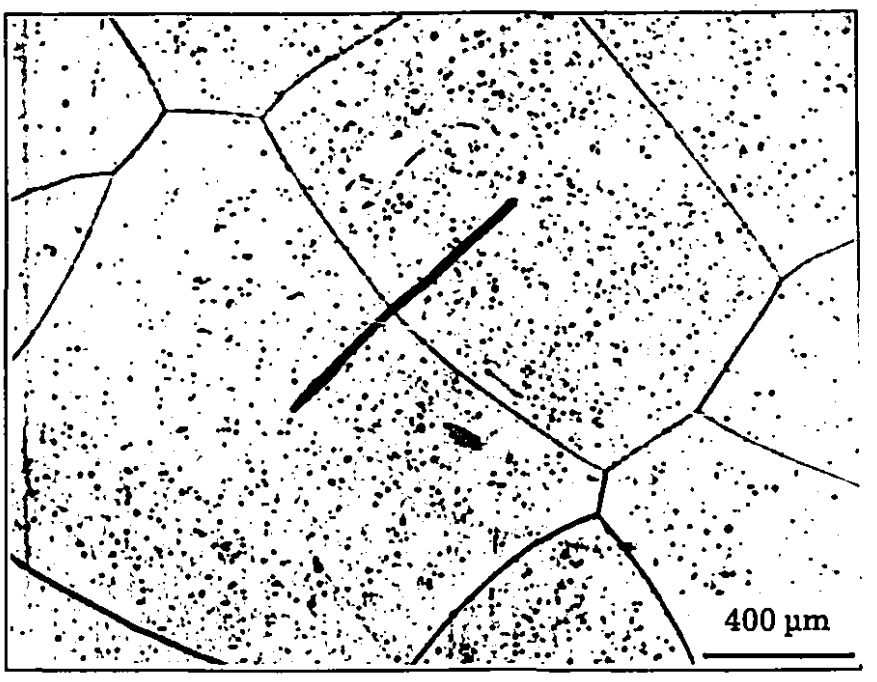

(a)

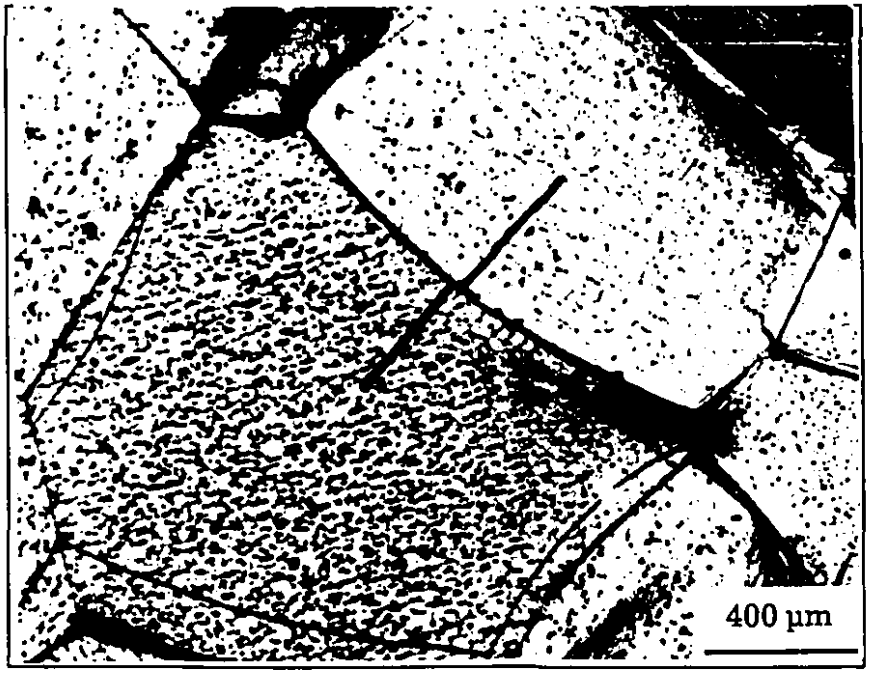

(b)

Fig. 5.35 Grain boundary sliding in electrical steel A tested at 1000 °C: (a) before deformation, and (b) after 3600 seconds of creep.

$$\varepsilon_{gb} = \frac{1}{\sqrt{2}} n_g \bar{p} \tag{5.5}$$

where ε_{gb} is the overall strain due to grain boundary sliding, n_g the number of grains per unit of axial length, and $\bar{p}$ the mean displacement of the boundaries. Eq. (5.5) is somewhat of an oversimplification, involving as it does the assumption that all the grain boundaries are at 45° to the compression axis. Geometrically, some grain boundary displacements can occur without contributing at all to the overall strain, so that the mean boundary displacement is not exactly indicative of the strain contribution made by the boundaries. By considering the contribution made by each boundary, McLean's model was taken a little further in this investigation. For this purpose, we have taken

$$\varepsilon_{gb} = \frac{n_g}{n_{gb}} \Sigma p_i \cos(\Theta_i) \tag{5.6}$$

where n_{gb} is the number of grain boundaries measurements made on the specimen, and p_i and θ_i are the displacement and angle to the compression axis of individual boundaries, respectively.

With the help of the above equation, the values of ε_{gb} at different creep times were estimated for electrical steel A stressed at 1000 °C. The results of this analysis are presented in Figure 5.36, together with the total strain recorded during the creep test. From this figure it appears that, under this experimental condition, grain boundary sliding contributes about one-sixth to one-tenth the total strain. This is probably true, but some uncertainty still arises from the fact that the orientations of individual boundaries relative to the compression axis are not fixed during testing. Fortunately, the present study was only aimed at investigating the influence of precipitation on grain boundary sliding, rather than on the process of sliding itself. Thus, our attention was drawn to the difference between the sliding rates of particle-free and of precipitate-containing boundaries. The results of some experiments which were specifically directed towards this objective are now presented.

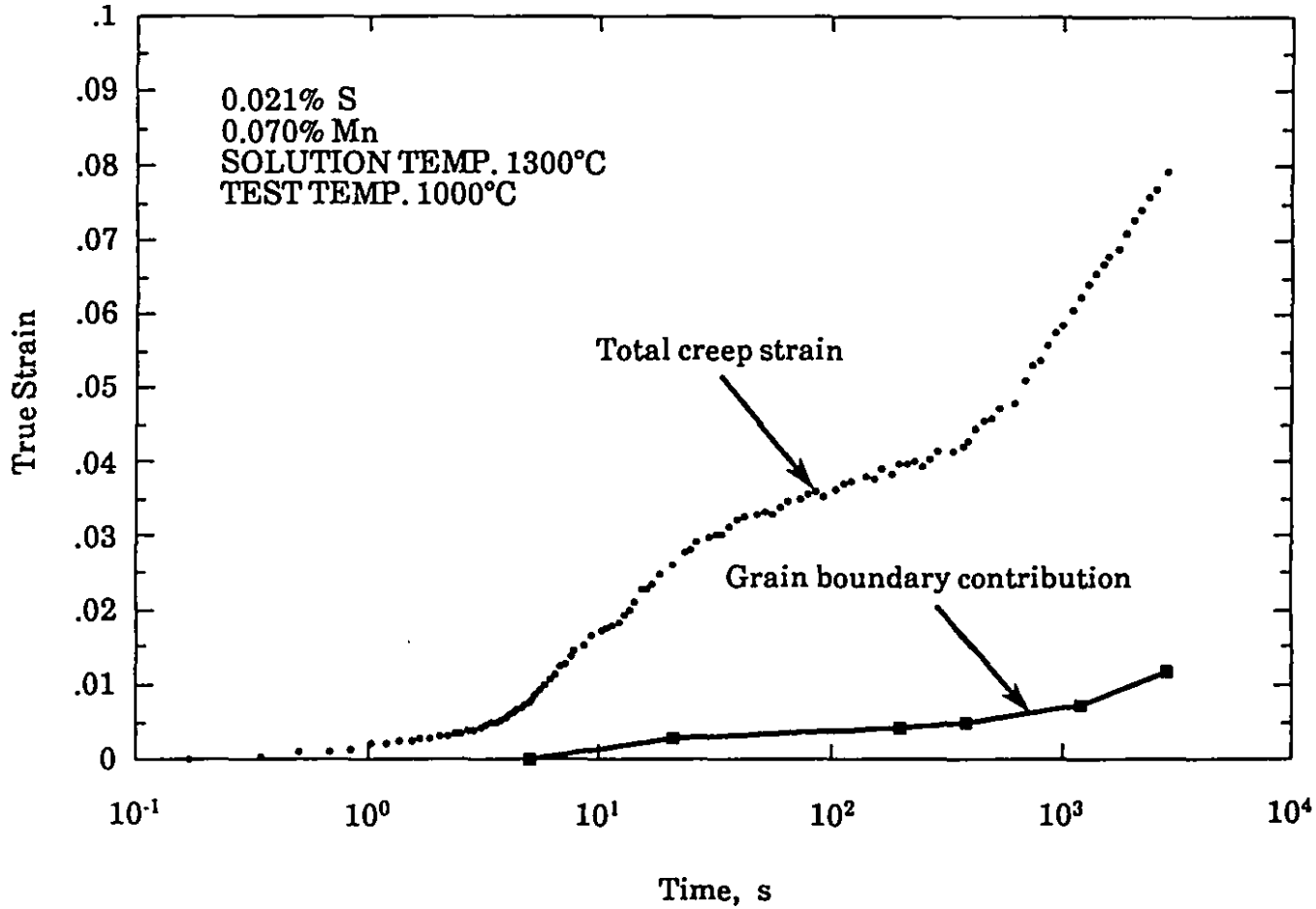

Fig. 5.36 Total creep strain and the contribution due to grain boundary sliding in samples of electrical steel A tested at 1000 °C.

Using the procedure described above, the strain contributed by grain boundary sliding during conventional creep (see §4.3.5) was also evaluated. This group of experimental results is given in Figure 5.37. For purposes of comparison, the ε_{gb} data of Figure 5.36 for the solution-treated tests are reproduced here, but, are presented on a linear instead of a semilog scale. Although the absolute values of ε_{gb} are, as discussed above, somewhat uncertain, the differences in sliding behavior revealed in this way are believable. As is readily evident from the figure, the ε_{gb} - time curve obtained in the absence of precipitation, the case of conventional creep testing, is linear after a brief transient. According to the experimental results, the values of the sliding-induced strain, ε_{gb}, in the two cases, are almost identical for the first 20 seconds, as shown in the inset. After this time, the ε_{gb} - time curve determined in the presence of precipitation deviates from the conventional curve, and the slope of this curve decreases, even though the value of ε_{gb} continuously increases. Since 20 seconds is the precipitation start time previously detected by the present technique for this experimental condition (see Table 5.3), it can be concluded from the above observation that precipitation (perhaps, grain boundary precipitation in particular) can arrest grain boundary sliding.

To reveal more clearly the influence of precipitation on the process of grain boundary sliding, the sliding rate was calculated from the current measurements. These results are plotted against *log(time)* in Figure 5.38. It can be seen from the lower curve in this figure that the sliding rate decreases after the P_s time. But, it tends to recover its value slightly when the creep time is further increased to 380 seconds, the precipitation finish time in this case. Another important point involves the results acquired beyond the P_f time. That is, although the sliding rate increases after this time, it is still lower than the one evaluated in the absence of precipitation (upper curve). This suggests that the coarsened particles also have a blocking effect on grain boundary sliding, even though their influence is weaker than that of the finely-dispersed precipitates.

All the experimental evidence presented so far confirms the view that the creep of electrical steels is not a simple process. In practice, grain boundary sliding is accompanied by deformation within the grains.

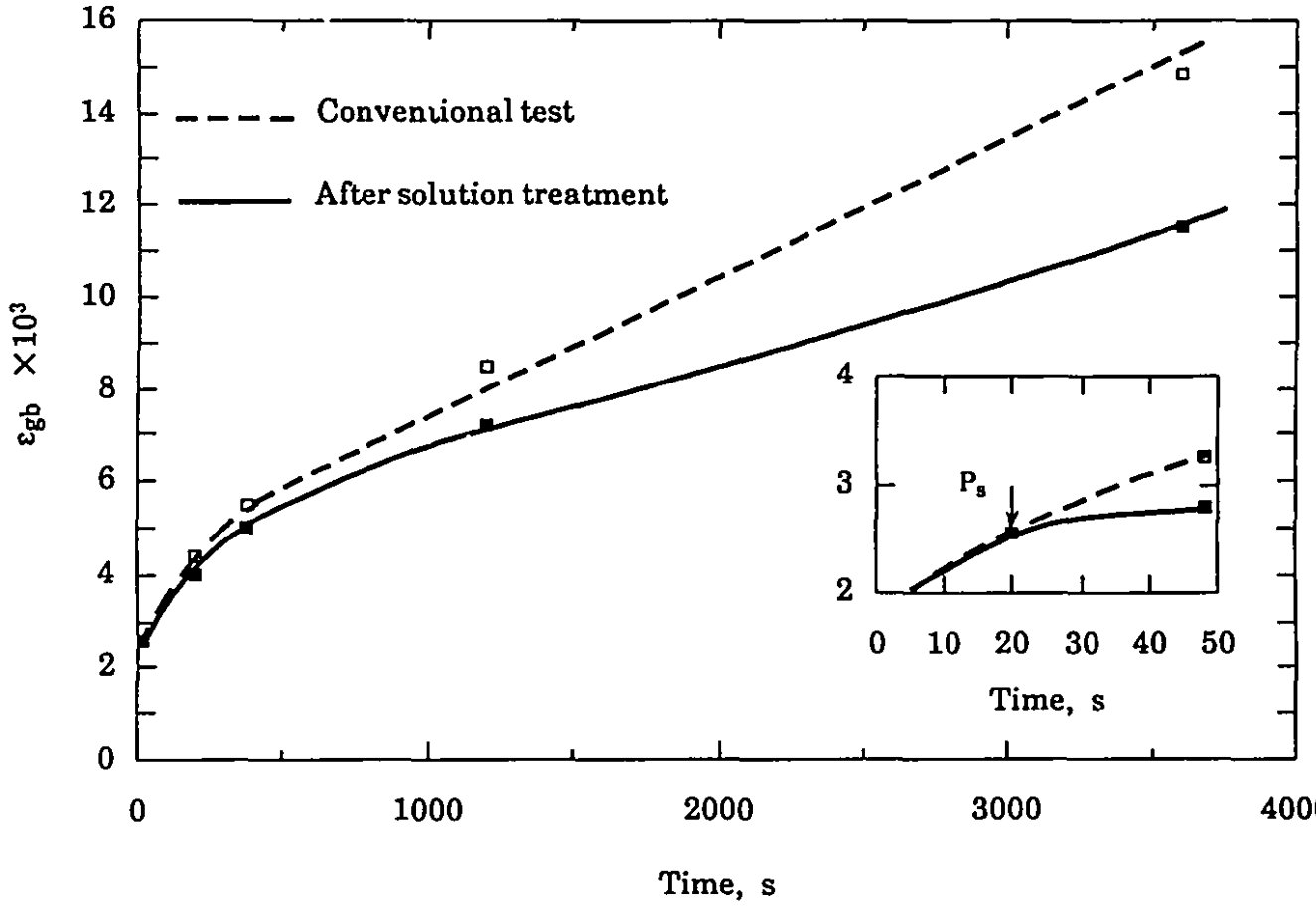

Fig. 5.37 Creep strain contributed by grain boundary sliding in samples of electrical steel A stressed at 1000 °C.

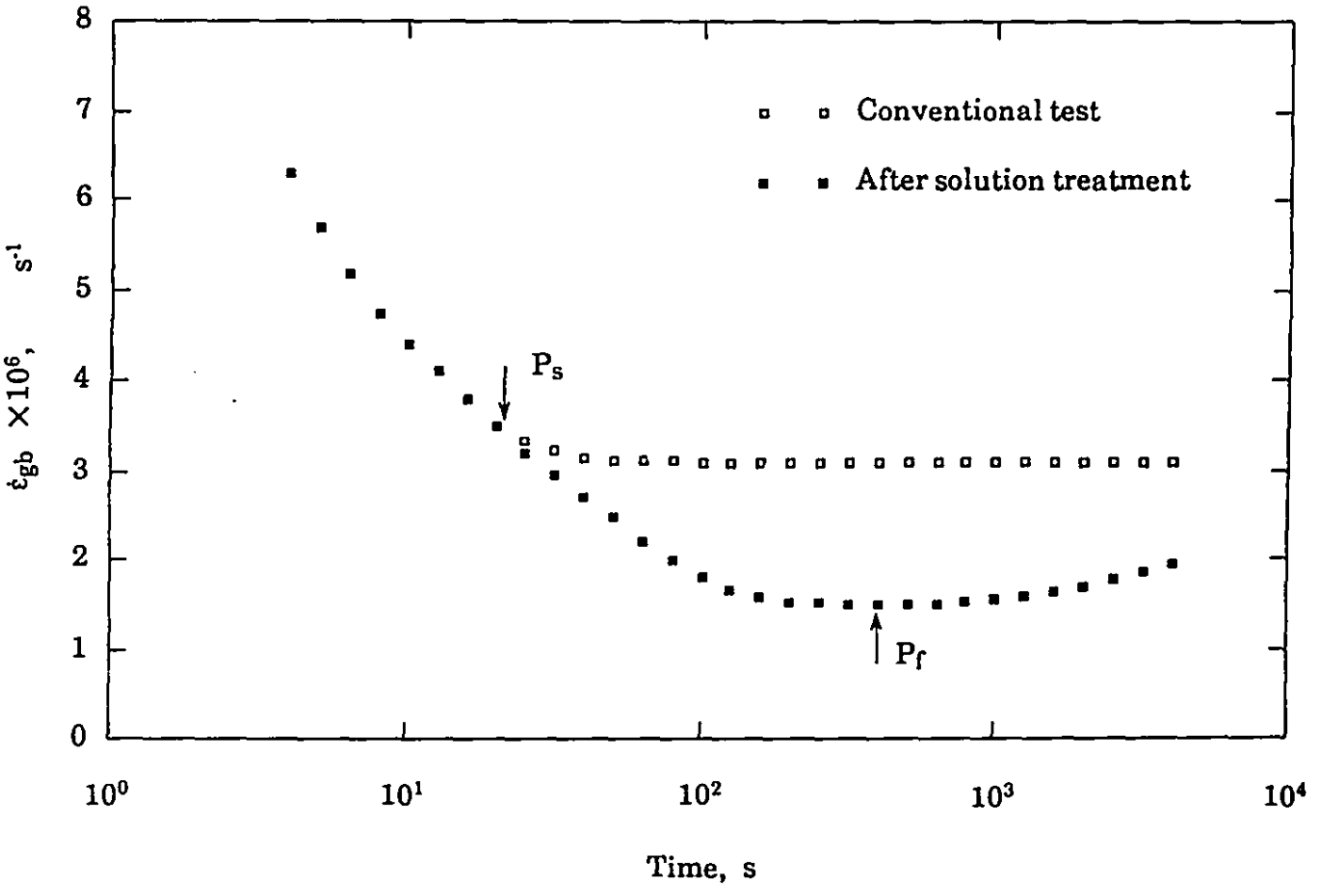

Fig. 5.38 Grain boundary sliding rate estimated for the samples of electrical steel A stressed at 1000 °C.

Considering the findings regarding the nucleation and evolution of precipitation, it becomes apparent that the two deformation processes are both affected by MnS precipitation. In the chapters that follow, the nucleation, growth and coarsening of MnS precipitation will be discussed, followed by an analysis of how MnS precipitation influences the creep behavior of electrical steels.

CHAPTER 6

NUCLEATION OF MnS PRECIPITATION

In the present study, the precipitation of MnS in electrical steels during hot deformation was investigated by means of both a new creep technique and electron microscopy. As described in the preceding chapter, it was found that the precipitation-time-temperature curves are C-shaped in all of the tested steels. The nose of the PTT curves shifts to higher temperatures and shorter times as the S and Mn concentrations are increased. Further observations indicated that the precipitates nucleate on both dislocations and grain boundaries. These results raise two interesting questions:

1) where does the nucleation of MnS precipitation first begin, on dislocations or at grain boundaries? and

2) which nucleation mode is responsible for the precipitation start times determined by the present technique?

These questions will be discussed in this chapter in terms of nucleation thermodynamics and nucleation kinetics. The experimental results will be compared with the predictions of these theories, and the differences between nucleation on dislocations and at grain boundaries will be analyzed. An attempt will also be made to explain qualitatively how the positions of P_s curves are influenced by the chemical compositions of the steels.

6.1 THERMODYNAMICS OF MnS NUCLEATION

6.1.1 GENERAL

The nucleation of a second phase in solids has been extensively analyzed by many metallurgists, physicists and physical chemists.[120, 188-191] Regardless of some detailed differences between these models, the thermodynamics of this process can always be understood in terms of the free energy change associated with the formation of a nucleus:

$$\Delta G_{tot} = V(\Delta G_{chem} + \Delta G_{\varepsilon} + \Delta G_{vac}) + S\gamma + W \qquad (6.1)$$

where

ΔG_{chem} = the chemical free energy change (often termed chemical driving force) associated with a unit volume of precipitates,

ΔG_{ε} = the elastic strain energy per unit volume of precipitate when nucleation occurs in the absence of a dislocation or a vacancy,

ΔG_{vac} = the volume free energy change due to the presence of non-equilibrium vacancies

γ = unit interfacial free energy of the nucleus-matrix interface,

W = the interaction energy (i.e., the additional energy change produced when precipitates form in a high energy area such as a grain boundary, dislocation or dislocation substructure), and

V, S = volume and surface area of the nucleus, respectively.

Nucleation can proceed at a perceptible rate only if the total free energy change $\Delta G_{tot} < 0$. The chemical driving force ΔG_{chem} is the difference in chemical free energy between the product and parent phases,[77] which always

benefits nucleation. The strain energy ΔG_ε, arising from the size misfit between the nucleus and the matrix, always diminishes the net driving force and hence the rate of nucleation. As indicated by Russell,[116] the strain energy associated with a solid state phase transformation is essentially irrelevant to incoherent nucleation. In this case, the effective driving force is obtained by summing the chemical and vacancy terms with the surface and interaction terms. On the other hand, excess vacancies do not contribute directly to the driving force for coherent nucleation because the coherent interphase boundary is neither a source nor a sink for vacancies. However, vacancies may markedly accelerate the mass transport involved in coherent nucleation and, thus, increase the nucleation rate through the quicker transfer of atoms to the critical nucleus. As it lies between the coherent and incoherent cases, semi-coherent nucleation is by far the most difficult to analyze. Both strain energy and excess vacancies play parts in the total free energy change in this case. Vacancies may annihilate at the disordered parts of the interface and relieve a part of the strain energy. The thermodynamic driving forces, if there is supersaturation, may then be altered in this way.

In Eq. (6.1), the interfacial energy γ always has a positive value and, like the strain energy, is a barrier to nucleation. The interaction energy W behaves as a driving force for nucleation. As the interactions between a nucleus and a dislocation or grain boundary are rather complicated, the interaction energy is often assumed to reduce the interfacial energy as a result of the presence of a dislocation or grain boundary.[118] On the basis of the above assumption, Eq. (6.1) can be rewritten in the following simplified form:

$$\Delta G_{tot} = V(\Delta G_{chem} + \Delta G_\varepsilon + \Delta G_{vac}) + S\xi\gamma \qquad (6.2)$$

where ξ is a factor, the value of which is always less than or equal to 1. The change in interfacial energy due to the incorporation of the interaction energy may be quite significant in some instances. These matters will be considered in more detail later when the nucleation kinetics are discussed. All of the other factors in Eq. (6.2) will be evaluated individually in the subsections that follow.

6.1.2 CHEMICAL DRIVING FORCE FOR MnS NUCLEATION

The chemical driving force enters into Eqs. (6.1) and (6.2) in a central way and must be known with some accuracy if the thermodynamics and kinetics of nucleation are to be calculated or even estimated. As just defined, the chemical driving force is the chemical free energy change when unit volume of a precipitate is formed in the parent phase. For the formation of MnS nuclei in one mole of a ferrite matrix, the decrease in the Gibbs free energy can be evaluated from the criterion proposed by Aaronson and Kinsman:[190]

$$\Delta G_{MnS} = f_m G_{MnS} + (1 - f_m) G_\alpha - G_{\alpha o} \tag{6.3}$$

where f_m is the mole fraction of MnS nuclei, and G_{MnS}, G_α and $G_{\alpha o}$ represent the molar free energies of MnS precipitates, the remaining ferrite, and the original matrix, respectively.

On the assumption that the MnS nuclei are in equilibrium with the matrix, the following formula was derived from Eq. (6.3) for evaluating the chemical driving force for MnS precipitation in ferrite:

$$\Delta G_{chem} = \frac{RT}{2V_m^{MnS}} \left[ln\left(\frac{a_{Mn}^{\alpha e}}{a_{Mn}^{\alpha o}}\right) + ln\left(\frac{a_S^{\alpha e}}{a_S^{\alpha o}}\right) \right] \tag{6.4}$$

Here, V_m^{MnS} indicates the molar volume of MnS, $a_i^{\alpha o}$ and $a_i^{\alpha e}$ are the activities (or the thermodynamic concentrations) of i in the original matrix and in ferrite at equilibrium with MnS, respectively, and R and T have their usual meanings. The details of this derivation are presented in Appendix III and the application of the above equation to the present steels is described below.

6.1.2.1 Activities of Mn and S in the Original Matrix

According to Eq. (6.4), the chemical driving force for the nucleation of MnS precipitates in electrical steels can be calculated if the activities of Mn and S in both the equilibrium ferrite and original matrix are close at hand. A

number of investigators[192-197] have shown that alloying elements influence the thermodynamic activities of Mn and S in iron. Usually, the activity is proportional to the respective concentration:[198]

$$a_i = \gamma_i X_i \tag{6.5}$$

where γ_i is the activity coefficient of component i (i=Mn and S) and X_i is the mole fraction of i in iron. In many instances, it is convenient to use weight percent as the composition coordinate. In this case,

$$a_i = f_i [i] \tag{6.6}$$

Here f_i is the activity coefficient of i based on the weight percent coordinate, and [i] is the weight percent of i in iron.

Both γ_i and f_i are frequently obtained from the formulations first proposed by Wagner,[199] and extended subsequently by Lupis and Elliott,[200] Sigworth and Elliott,[201] and Pelton and Bale:[202]

$$ln(\gamma_i) = ln(\gamma_i^o) + \Sigma\{\varepsilon_i^j X_j\} + higher\ order\ terms \tag{6.7a}$$

$$ln(f_i) = \Sigma\{e_i^j [j]\} + higher\ order\ terms \tag{6.7b}$$

Here γ_i^o is the value of γ_i at infinite dilution, and ε_i^j and e_i^j are first order interaction parameters based on the mole fraction and weight percent composition coordinates, respectively. The transformation of the interaction parameters from one composition coordinate to the other can be accomplished by the equations developed by Lupis and Elliott:[200]

$$\varepsilon_i^j = 230 \frac{M_j}{M_{Fe}} e_i^j + \frac{M_{Fe} - M_j}{M_{Fe}} \tag{6.8}$$

where M_j and M_{Fe} are the atomic weights of element j and iron, respectively.

Ideally, all the alloying elements dissolved in the matrix should be involved when the above equations are employed. For simplicity, however,

and because of the lack of interaction parameters in the literature, only the elements C, Mn, S and Si present in the electrical steels were taken into account in this investigation. Neglecting the higher order terms in Eqs. (6.7a) and (6.7b), the interaction parameters f_{Mn} and f_S, and subsequently the activities in the original matrices a_{Mn}^{o} and a_S^{o} were calculated for the four electrical steels of interest. The thermodynamic data utilized in the calculation, including the ε_i^j and e_i^j found in the literature, are summarized in Table 6.1. Figures 6.1a and 6.1b show the calculated relations between temperature and activity over the range from 700 °C to 1200 °C for Mn and S, respectively. As indicated in these figures, the two activities are expected to depend directly on their respective overall concentrations in the steels and only slightly on the temperature. It appears, however, that the activity of S is more sensitive to temperature than that of Mn.

Table 6.1

Interaction Parameters Employed in the Thermodynamic Analysis

Published in Terms of the Weight Percent Coordinate	Ref.
$\varepsilon_S^S = 233/T - 0.153$	[201]
$\varepsilon_S^C = 0.11$	[201]
$\varepsilon_{Mn}^C = -0.07$	[201]
$\varepsilon_{Mn}^S = -0.0039$	[201]*
Published in Terms of the Mole Fraction Coordinate	
$\varepsilon_S^S = 7.76$	[202]
$\varepsilon_S^{Mn} - \varepsilon_{Mn}^S = -28418/T + 12.8$	[203]
$\varepsilon_{Mn}^{Mn} = -175.6/T + 2.406$	[77]

* Evaluated from the relationship:

$$\varepsilon_{Mn}^S = \varepsilon_S^{Mn}(M_{Mn}/M_S)$$

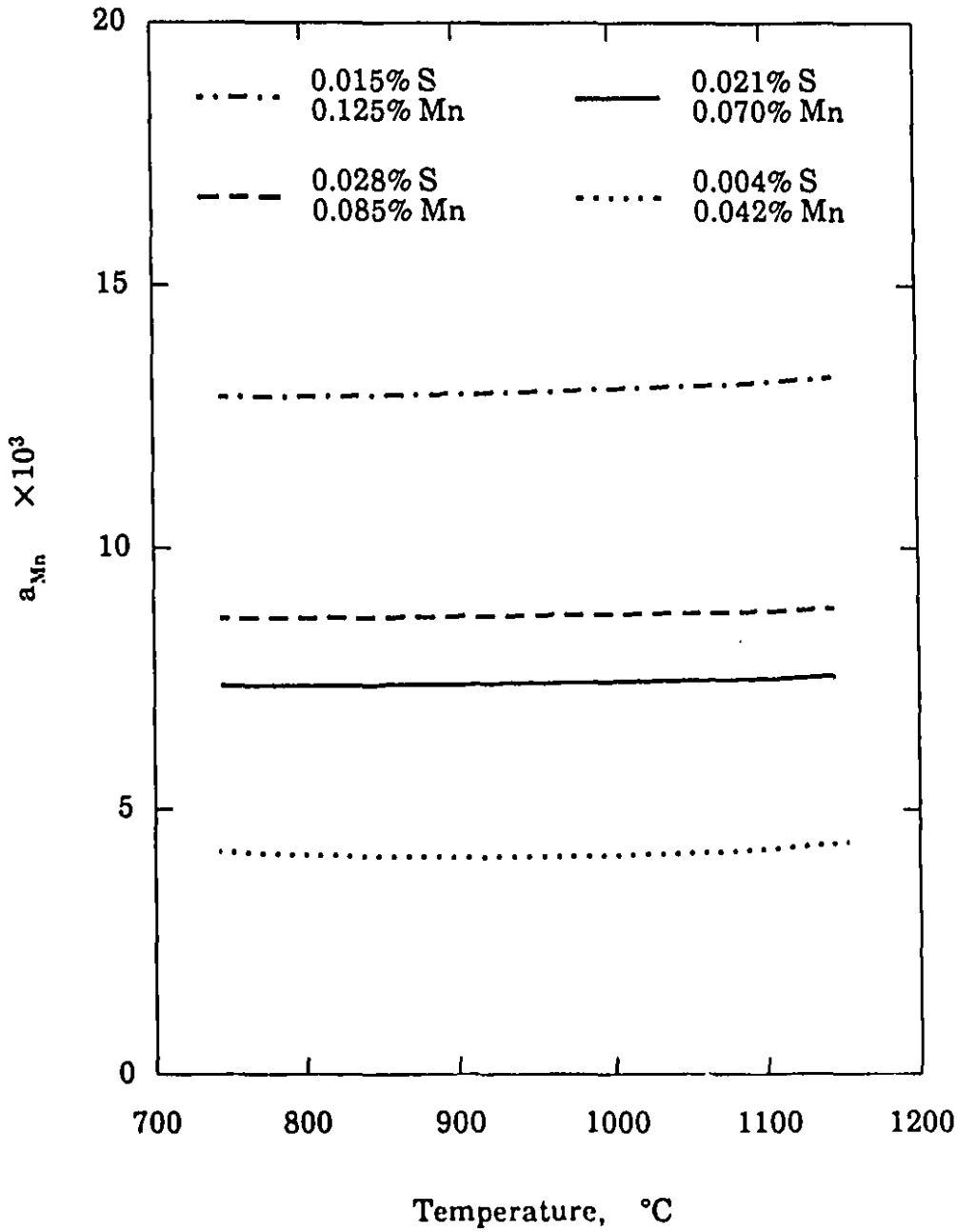

Fig. 6.1a Mn activities in the original matrices of the four electrical steels.

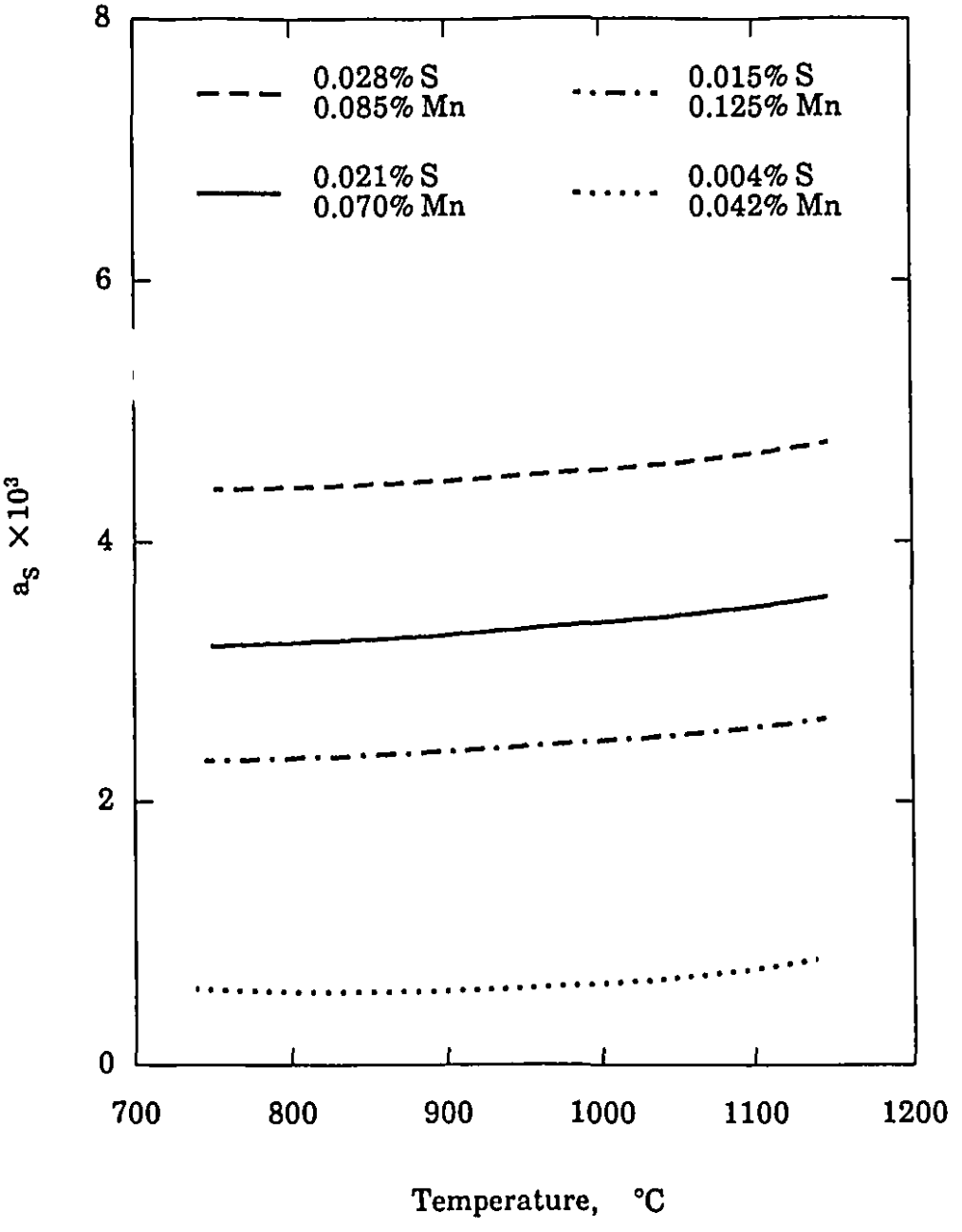

Fig. 6.1b S activities in the original matrices of the four electrical steels.

6.1.2.2 Activities of Mn and S in Equilibrium

By assuming that the nucleus/ferrite equilibrium is closely approached during the nucleation of MnS precipitates, the concentrations of Mn and S in equilibrium can be estimated from their solubility product:

$$log\ [Mn]^{\alpha e}[S]^{\alpha e} = -\frac{9{,}800}{T} + 3.74 \qquad (2.8)$$

where the parameters in parentheses are the concentrations of Mn and S in equilibrium.

The mass conservation of Mn and S during nucleation entails the following equalities:

$$X_{Mn}^{\alpha o} = f_m X_{Mn}^{MnS} + (1 - f_m) X_{Mn}^{\alpha e} \qquad (6.9)$$

$$X_{S}^{\alpha o} = f_m X_{S}^{MnS} + (1 - f_m) X_{S}^{\alpha e} \qquad (6.10)$$

By simultaneously solving Eqs. (2.8), (6.9) and (6.10), together with the following relationship

$$X_i = [\%i]\frac{M_{Fe}}{100M_i} \qquad (i = Mn, S) \qquad (6.11)$$

the concentrations of Mn and S in equilibrium were first estimated in the temperature range between 700 °C and 1200 °C for the four electrical steels. On multiplying by their respective activity coefficients, the activities were subsequently calculated; the outcomes are summarized in Figures 6.2a and 6.2b. It is evident from these calculations that the equilibrium activities are strong functions of temperature. As the temperature is reduced, less and less Mn and S are contained in the parent matrix; thus the values of $a_{Mn}^{\alpha e}$ and a_S^{α} decrease. This result indicates that the supersaturation and, therefore, the chemical driving force increase with temperature decrease in this way.

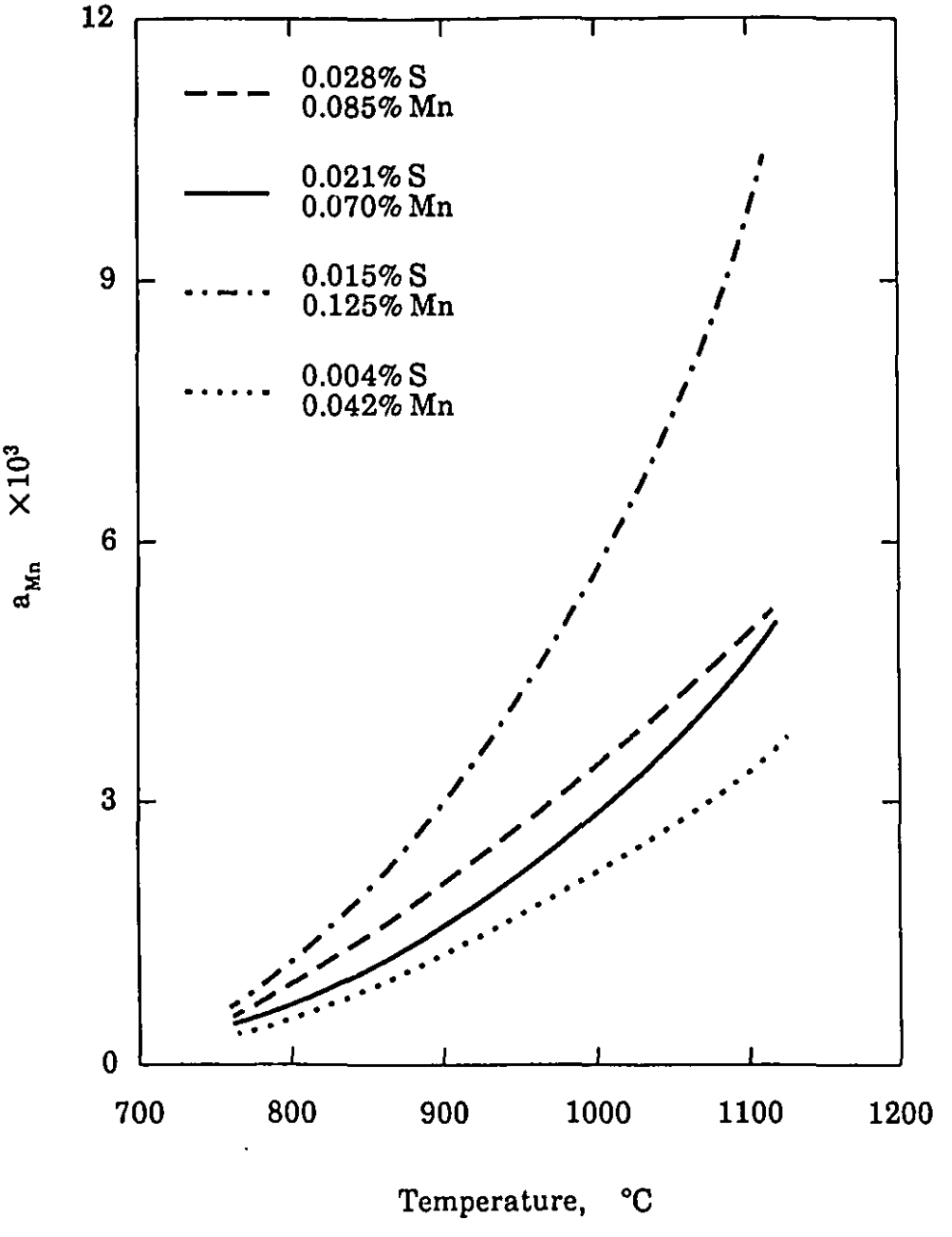

Fig. 6.2a Equilibrium Mn activities in the four electrical steels.

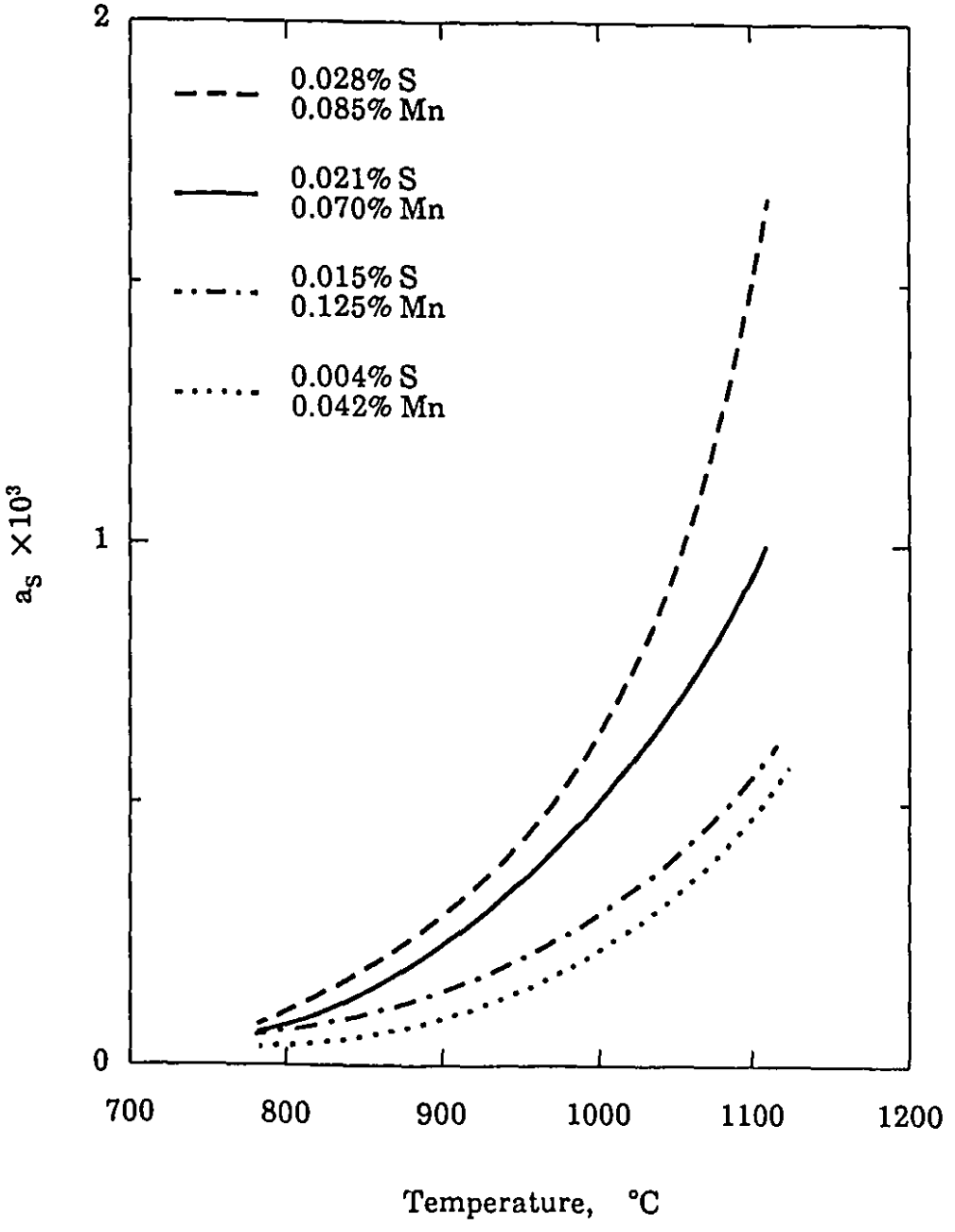

Fig. 6.2b Equilibrium S activities in the four electrical steels.

The chemical driving force for the nucleation of MnS precipitates can be evaluated from Eq. (6.4) if the molar volume V_m^{MnS} is available. Indeed, this factor can be calculated from[120]

$$V_m^{MnS} = N_o \frac{a_{MnS}^3}{8} \tag{6.12}$$

where N_0 is Avogadro's number and a_{MnS} is the lattice parameter of MnS. Using the value a_{MnS} = 5.226 Å given by Kiessling and Lange,[61] ΔG_{chem} was estimated for the four electrical steels and the results are presented in Figure 6.3. It is evident from this figure that, as expected, the calculated driving forces for the four electrical steels decrease monotonically as the temperature is increased. Except for the 0.042% Mn - 0.004% S steel, the driving forces for the other three steels approach each other in the temperature range above about 1080 °C. This feature corresponds to the almost equivalent precipitation start times at 1100 °C determined by the present technique for the three steels. The three curves divide into two branches below 1080 °C: the 0.085% Mn - 0.028% S steel goes to the highest level, but the other two curves still bunch together. This observation agrees very well with the experimental results presented in the previous chapter, where the P_s times of the 0.080% Mn - 0.025% S steel are the shortest and those of the other two steels are nearly identical over the whole testing temperature range. As for the 0.042% Mn - 0.004% S steel, the driving force, as expected, remains at the lowest level.

6.1.3 STRAIN ENERGY ASSOCIATED WITH MnS NUCLEATION

Another factor in Eq. (6.2), the volume elastic strain energy ΔG_ε, will be evaluated in the present subsection. As is known, the formation of a microcluster, which is fully or partly coherent with the matrix, requires the straining of both lattices,[204, 205] except in the unusual case when both phases have the same crystal structure and lattice spacing. Generally, a precipitate first evolves from an initially coherent embryo. Whether the coherency is maintained or lost during nucleation depends on the lattice misfit between the two phases; in other words, on the strain energy created by the nucleus.

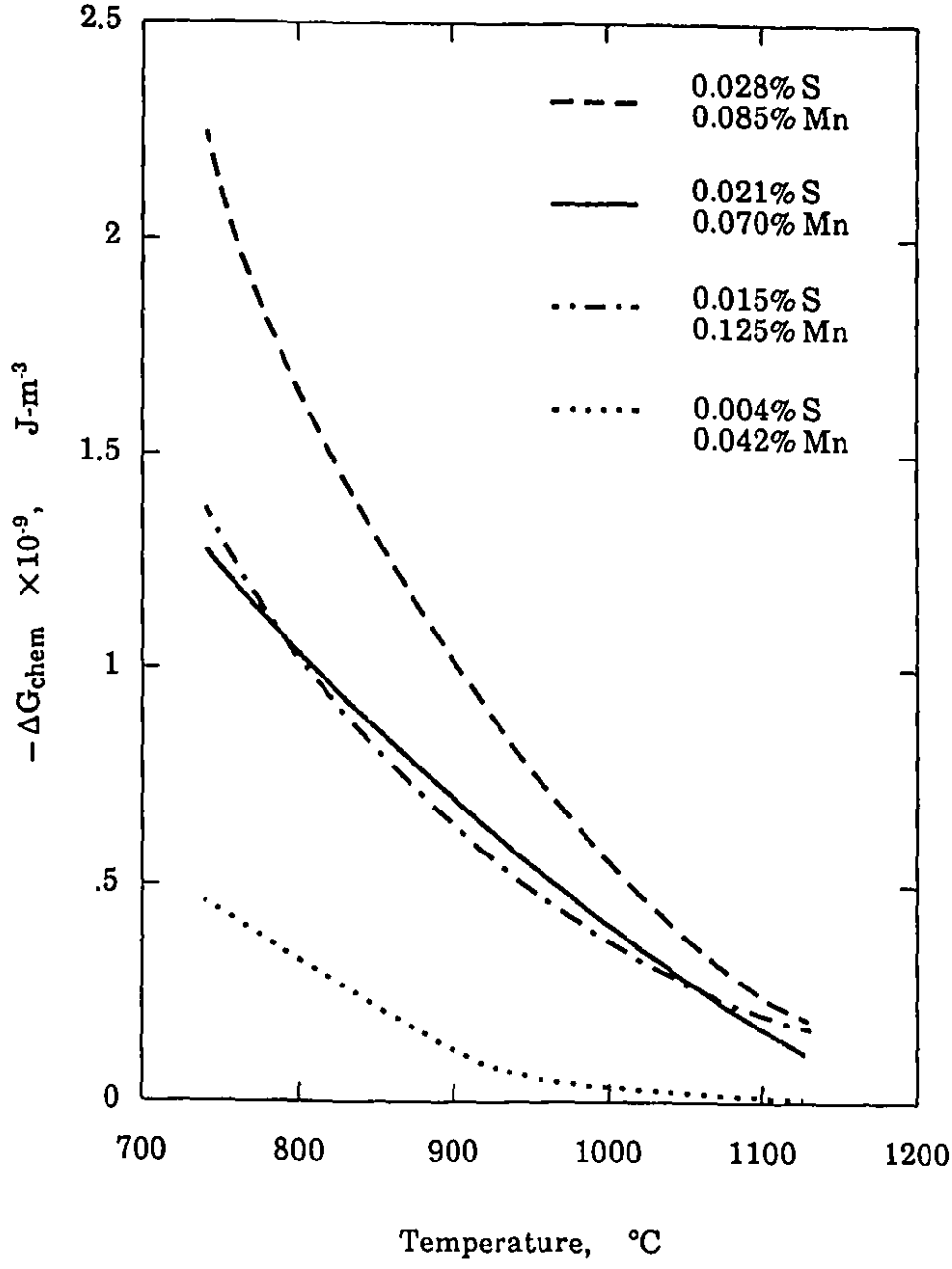

Fig. 6.3 Calculated chemical driving forces for MnS nucleation in the four electrical steels.

As a basic case, the elastic strain energy associated with a coherent particle, which means a one-to-one matching of atoms everywhere along the precipitate/matrix interface, has been investigated by Aaronson and Lee,[117] Mott and Nabarro,[206] Laszlo,[207] Eshelby,[208] Christian,[209] and Barnett et al.[210, 211] Among these treatments, the model most commonly used was proposed by Eshelby. This model deals with the dilation that accompanies precipitation and gives the elastic strain energy per unit volume of precipitated particle:

$$\Delta G_{\varepsilon} = 2\mu_{\alpha\text{-}Fe} \frac{(1 + \nu_{\alpha\text{-}Fe})(\varepsilon^T)^2}{(1 - \nu_{\alpha\text{-}Fe})} \tag{6.13}$$

where

$\mu_{\alpha\text{-}Fe}$ = shear modulus of the matrix,
$\nu_{\alpha\text{-}Fe}$ = Poisson's ratio, and
ε^T = the stress-free transformation strain, equal to 1/3 the transformation volume change. In the present case, ε^T has the following value:

$$\varepsilon^T = \frac{1}{3}\left(\frac{a^3_{MnS} - a^3_{\alpha\text{-}Fe}}{a^3_{MnS}}\right) \tag{6.14}$$

Here, a_{MnS} and $a_{\alpha\text{-}Fe}$ are the lattice constants of the MnS precipitates and the ferrite, respectively.

Applying the related physical data listed in Table 6.2 to the above equations, the elastic strain energies accompanying the formation of coherent MnS nuclei in ferrite were estimated over the testing temperature range of 800-1100 °C. The results of the computation are shown in Figure 6.4. In comparison with Figure 6.3, it can be seen that the elastic strain energy ΔG_{ε} is one order of magnitude greater than the absolute value of the chemical driving force, ΔG_{chem}. This comparison shows why the nucleation of MnS in ferrite cannot take place in coherent form: that is, the coherent nature of the embryos cannot be retained in the later stages of nucleation. The possible structures

Table 6.2

Values of the Parameters Used in the Analysis of the Volume Strain Energy Associated with MnS Nucleation in Ferrite

Parameter or Variable	Ref.
a_{MnS} = 5.226 Å	[61]
$a_{\alpha\text{-}Fe}$ = 2.86 Å	[212]
$\nu_{\alpha\text{-}Fe}$ = 0.3	[213]
$\mu_{\alpha\text{-}Fe} = 6.4\times10^{10}\times[1 - 0.81(T - 300)/T_M]$ J-m^{-3}	[214]
T_M = 1810 °K	[214]

must therefore be incoherent or, at the very least, semi-coherent. Only in this way, through the introduction of vacancies and/or dislocations into the precipitate/matrix interface, can the strain energy of MnS precipitates be relaxed simultaneously with nucleation.

The question may be raised at this point as to how much of the strain energy is relieved during the loss of coherency. It is difficult to propose a precise answer because the entire process is too complicated for analysis here. In order to simplify the problem, the present study was restricted to just the critical situation instead of the whole process. In this context, the term "critical" refers to the turning point where the unstable microcluster becomes a stable nucleus in the thermodynamic sense. By noting that the free energy barrier goes through a maximum when the nucleus attains its critical size, a successful nucleus will be created if the barrier can be overcome at this moment. Thus, an appropriate alternative approach to the question of strain energy loss is to evaluate its association with a critical nucleus/matrix interface. A detailed treatment of this topic will be presented later in the next section and in Appendix IV.

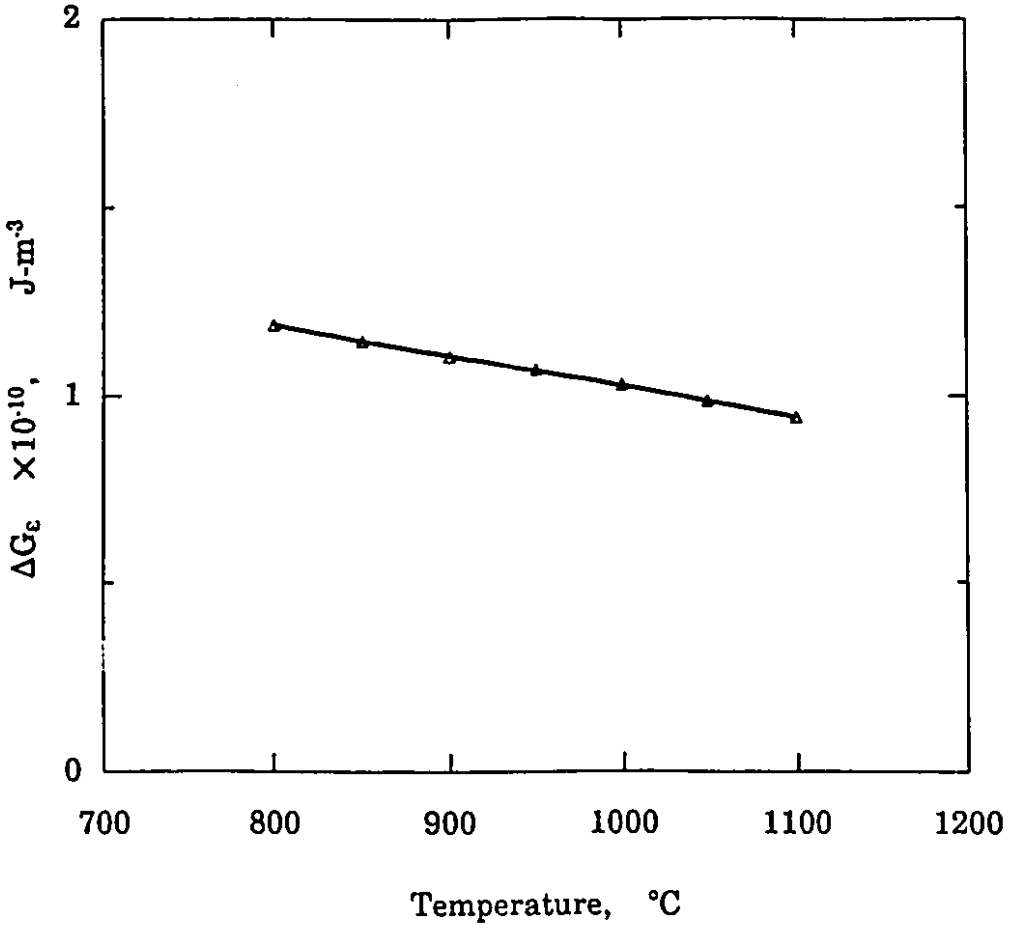

Fig. 6.4 Volume strain energy calculated by Eshelby's model for MnS nucleation in ferrite.

6.1.4 VACANCY EFFECTS

As described in the previous subsection, the vacancies in thermal equilibrium exert an influence on the relaxation of the elastic strain energy associated with nucleation. Indeed, excess vacancies, which are continuously

produced during creep testing, further enhance the driving force for MnS nucleation in ferrite. This subsection describes the detailed investigation of such effects.

6.1.4.1 Equilibrium Vacancy Concentration

The equilibrium concentration of thermal vacancies can be determined from:[215]

$$X_v^0 = exp(\frac{\Delta S_v^f}{k}) exp(\frac{-\Delta H_v^f}{kT}) \qquad (6.15)$$

where X_v^0 is the equilibrium vacancy concentration, k is the Boltzmann constant, ΔS_v^f is the entropy change, and ΔH_v^f is the activation enthalpy of vacancy formation when one atom is taken from its lattice site and placed on the crystal surface. The values of ΔS_v^f and ΔH_v^f in α-iron, measured and reported by Schaefer and Matter et al.,[216,217] are $\Delta S_v^f = (1.0 \pm 0.5)k$ and $\Delta H_v^f = (1.60 \pm 0.15)eV$.

It should be noted here that the vacancies in thermal equilibrium can relieve the strain energy on the nucleus/matrix interface.[116] Hart[218] and Holl,[219] however, have pointed out that the *non-equilibrium* vacancy concentration can further introduce a driving force into the nucleation reaction as well as a chemical component. This concept was later put on a quantitative basis for the case of incoherent/semi-coherent nucleation by Russell.[220] This will now be discussed in relation to the present experiments.

6.1.4.2 Excess Vacancies Generated during Deformation

Considerable experimental evidence indicates that plastic deformation, like quenching, significantly increases the vacancy concentration.[215,221] The vacancies in excess beyond those in thermal equilibrium depend on the amount of strain according to the following relation:[221-223]

$$\Delta X_v \simeq 10^{-4}\varepsilon \tag{6.16}$$

Excess vacancy concentrations are known to have a profound effect on the nucleation rate, especially when the microcluster/matrix interface is partially or wholly disordered.[218-220] In the present tests, non-equilibrium vacancies are continuously generated during deformation. This behavior is quite unlike quenching, in which the excess vacancies are produced almost instantaneously and then gradually disappear. In the present case, the vacancy supersaturation is continuously being set up and is thus able to enhance the thermodynamic driving force for the nucleation of MnS precipitates in a continuous fashion. In addition, the non-equilibrium vacancies can migrate to and incorporate themselves into the nucleus/matrix interface, thereby relieving the transformation strains.

The increase in vacancy concentration due to deformation before the completion of nucleation can be estimated by integrating Eq. (6.16) from t =0 to t = P_S. However, it is important to note that some of the non-equilibrium vacancies can diffuse to the grain boundaries and be annihilated there before precipitation occurs. Only those left within the grains contribute to the vacancy supersaturation and thus to the driving force for MnS nucleation. In order to establish the effective excess vacancy concentration, the diffusion distance of a vacancy in ferrite was first evaluated from:[224]

$$y = \sqrt{(2D_v t)} \tag{6.17}$$

where t is the time, and D_v the vacancy diffusion coefficient in ferrite, whose value was given by Schaefer et al.[216] as

$$D_v = 0.5\, exp\left(\frac{-1.28\, eV}{kT}\right) \quad cm^2 s^{-1} \tag{6.18}$$

Applying the above two equations to the present test conditions, the diffusion distance, y, during the time interval [0, Ps] in electrical steel A was evaluated to be about 0.05 mm at 900 °C. This is the maximum possible diffusion distance for any non-equilibrium vacancy before MnS nucleation occurs at this temperature. Bearing in mind that the average grain diameter

$$\Delta G_{vac} = -\frac{3\varepsilon^T}{\omega} kT \ln\left(\frac{X_v^{eff}}{X_v^{\theta}}\right) - 9\left|kT \ln\left(\frac{X_v^{eff}}{X_v^{\theta}}\right)\right|^2 \left|\frac{(1-\nu_{\alpha\text{-}Fe})}{4E\omega^2}\right| \qquad (6.20)$$

Here E indicates Young's modulus, ω represents the atomic volume of the precipitates, and $\nu_{\alpha\text{-}Fe}$ and ε^T have the same meanings as in Eq. (6.13). The first term in the above equation corresponds to the annihilation of vacancies to relieve the volumetric mismatch.[116] It can be seen from this term that the supersaturation of vacancies intensifies the thermodynamic driving force if the nuclei have a larger atomic volume than the matrix ($\varepsilon^T > 0$), as in the present case for MnS precipitation. The second term in Eq. (6.20) corresponds to the annihilation of the non-equilibrium vacancies not needed to relieve the misfit.[116]

Using the equation given above, the driving forces due to the excess vacancies generated during the deformation of the four electrical steels were estimated over the temperature range from 800 °C to 1100 °C; the calculated results are shown graphically in Figure 6.5. It is evident from the figure that the vacancy supersaturation in the present tests is so large that ΔG_{vac} has the same magnitude in the electrical steels as the chemical driving force ΔG_{chem}. The dependence on temperature of ΔG_{vac} is different from that of ΔG_{chem}. As the temperature is increased, the absolute values of ΔG_{vac} increase until near the nose temperatures. Above these temperatures, however, they decrease with increasing temperature.

6.1.5 INTERFACIAL ENERGY BETWEEN THE MnS NUCLEI AND THE FERRITE

The last factor in Eq. (6.2), the interfacial energy γ, will be evaluated in this subsection.

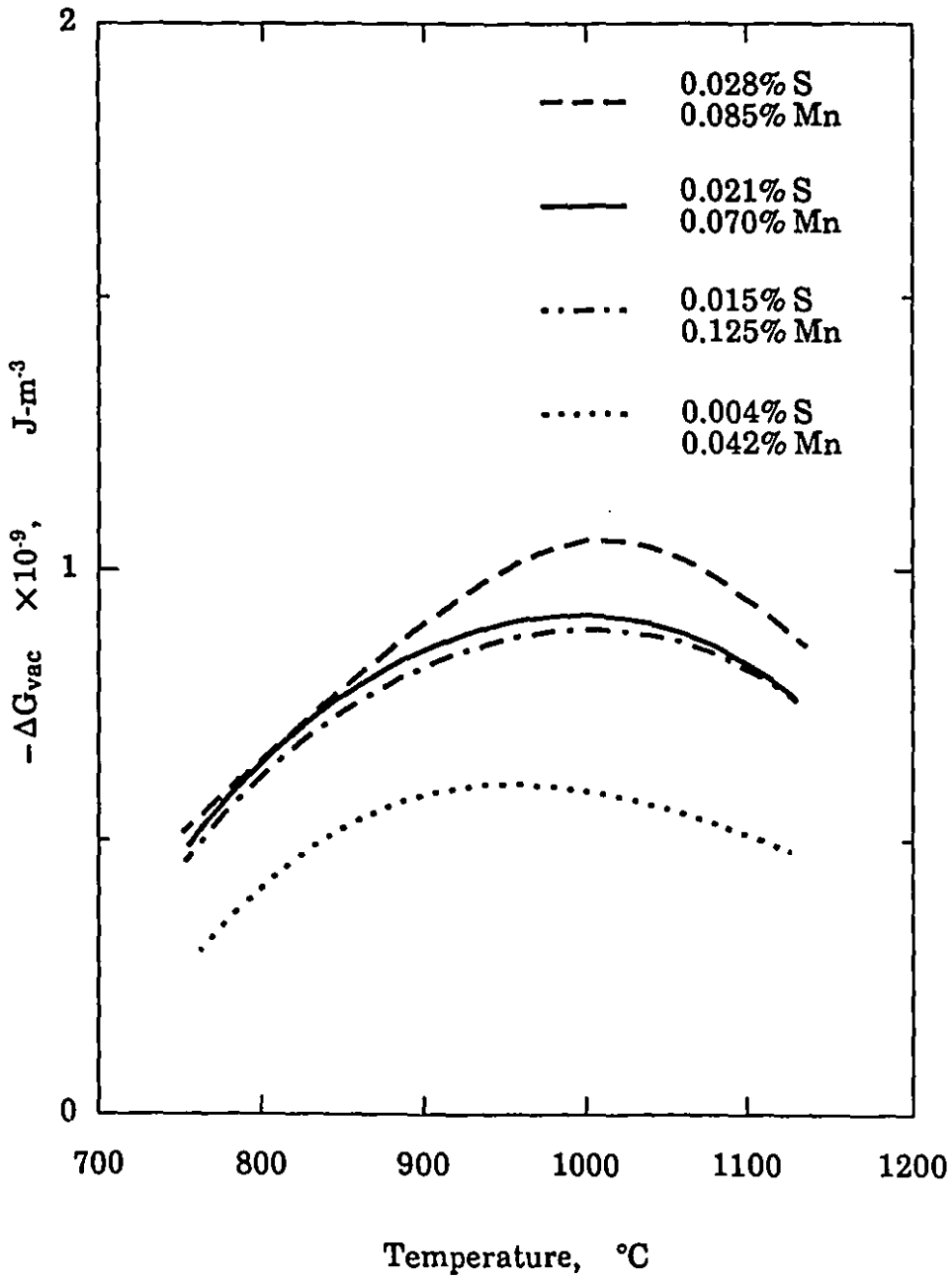

Fig. 6.5 Driving forces for MnS nucleation due to the presence of deformation vacancies in the four electrical steels calculated by Russell's model.

6.1.5.1 Chemical Component of the Interfacial Energy

Imagining that the two phases, say the particle and the matrix, are first separated and then rejoined to form the interphase boundary, Turnbull[225] presented a calculation for the energy increment required to form the boundary:

$$\gamma_c = \frac{\Delta H\, N_s\, Z_s\, (X^M - X^P)^2}{N_o\, Z_l} \tag{6.21}$$

where

N_S = atoms per unit area of the interface,
N_0 = Avogadro's number,
Z_S = number of the bonds per atom across the interface,
Z_l = lattice coordination number,
ΔH = heat of formation of the precipitates in a dilute solution (the matrix), and
X^M, X^P = concentrations of precipitate forming elements in the matrix and nucleus, respectively.

As γ_c is determined primarily by the enthalpy of mixing and the composition difference between the two phases, it is often referred to as the chemical component of the interfacial energy. It corresponds to the difference between the energies of the bonds broken in the separation process and of the bonds made in forming the interphase boundary.

6.1.5.2 Structural Component of the Interfacial Energy

For interphase boundaries accommodating the mismatch between the two crystal structures, Turnbull[225] considered the interfacial energy to be made up of two components, one being chemical (γ_c given by Eq. (6.21)) and the other structural (γ_{st}), so that:

$$\gamma = \gamma_c + \gamma_{st} \tag{6.22}$$

Unlike γ_c, the structural part, γ_{st}, is related to the self-energy of the interface dislocations. As the MnS nucleus has the same structure as the ferrite, but a different lattice spacing,[61] the structural component of the interfacial energy at the nucleus/matrix interface can be obtained from:[226]

$$\gamma_{st} = \frac{\mu_{\alpha\text{-}Fe}\, a_{\alpha\text{-}Fe}}{4\pi^2}\left[1 + \Psi - (1 + \Psi^2)^{1/2}\right] \tag{6.23}$$

where $\Psi = 2\pi|\varepsilon^T|/(1 - \nu_{\alpha\text{-}Fe})$, and $\mu_{\alpha\text{-}Fe}$, $a_{\alpha\text{-}Fe}$, ε^T and $\nu_{\alpha\text{-}Fe}$ have the same meanings as before.

Using the above equations and the numerical values given in Tables 6.2 and 6.4, the unknowns γ_c and γ_{st} were first calculated. The total interfacial energy γ was then computed and is presented in Figure 6.6. As can be seen, it

Table 6.4
Parameters Used in the Analysis of the Interfacial Energy between MnS Nuclei and Ferrite

Parameter or Variable		Ref.
ΔH	$= 205.2$ kJ-mol^{-1}	[212]
N_S	$= \sqrt{2}/a_{\alpha\text{-}Fe}^2$	‡
Z_S	$= 2$	‡
Z_l	$= 8$	‡

‡ Assuming that the interface is (110).

is a weak function of temperature, varying only through the shear modulus of the matrix $\mu_{\alpha\text{-}Fe}$. The total interfacial energy ranges from 0.563 to 0.614 J-m^{-2} at the current temperatures, which agrees with the typical interfacial energy of 0.595 J-m^{-2} between the sulfide and α-iron measured by Van Vlack.[227]

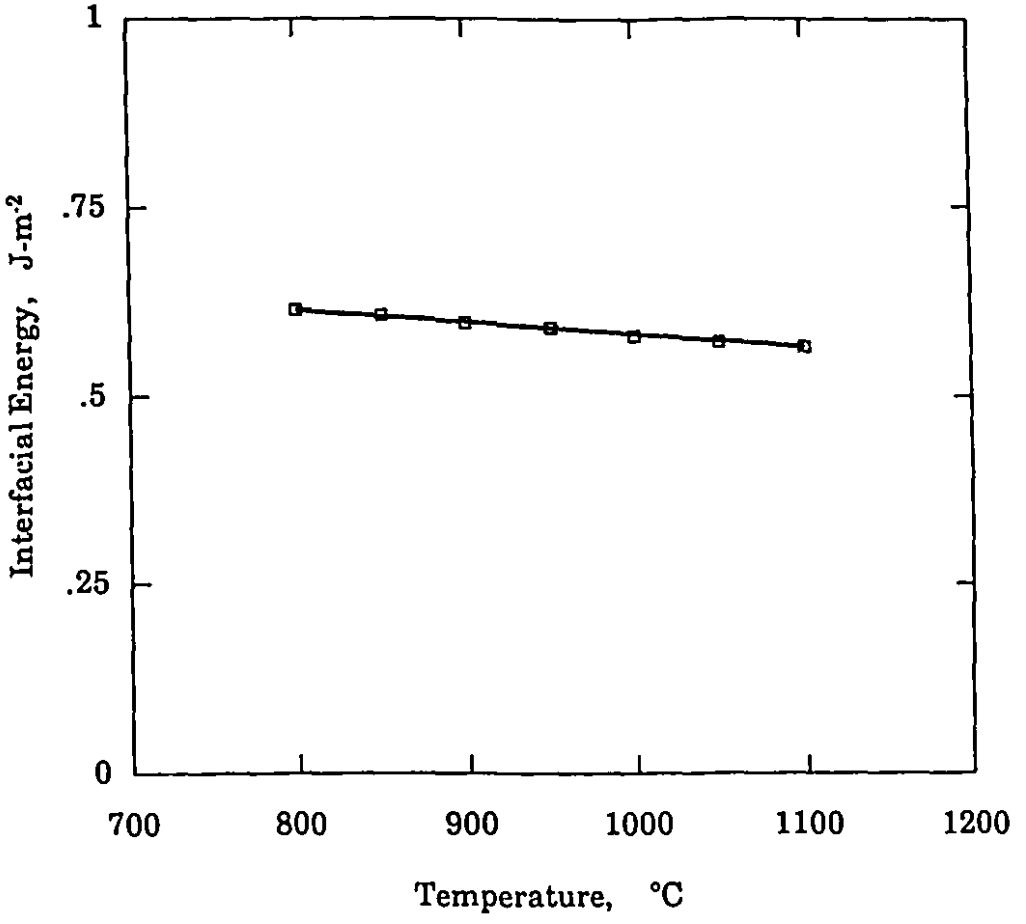

Fig. 6.6 Interfacial energy between MnS nuclei and ferrite calculated using Turnbull's model.

6.2 KINETICS OF MnS NUCLEATION

The various theories of nucleation kinetics appear at first to differ widely. With few exceptions, however, all can be developed from the following principles:

1) The probability of nucleation is proportional to exp(–W*/kT), where W* is the minimum work required to make the system unstable with respect to transformation. Gibbs[228] described the significance of W* in phase stability and expressed it as the free energy of forming a critical nucleus.

2) The decay of microscopic fluctuations can be described by the macroscopic decay laws due to Onsager.[229]

3) The number of nucleation sites is specific to the system and to the type of nucleation process being considered.[116]

Two kinds of kinetic models will be proposed in this section. Since the MnS precipitates in electrical steels, as shown in the previous chapter, nucleate either on dislocations or at grain boundaries, one of the models was developed for the former process and the other for the latter.

6.2.1 REDUCTION OF INTERFACIAL ENERGY

As mentioned earlier in this chapter, additional energy is produced when nucleation occurs in a high energy area, contributing to the reduction in the interfacial energy. Two reduction factors will be evaluated in this subsection, one for nucleation on dislocations and the other for nucleation on grain boundaries.

6.2.1.1 Reduction Factor for Nucleation on Dislocations

It was concluded by Dollins,[189] Barnett,[210] Cahn,[230] Gomez-Ramirez and Pound,[231] and Larché,[232] that the nuclei in solid transformations are formed preferentially on dislocations due to the release of the strain energy and the reduction of the interfacial energy. Larché[232] used the formalism of Eshelby[8] to show that the catalytic effect of the dislocation (for a spherical microcluster) was to reduce the interfacial energy to the value

$$\gamma - \frac{\mu_{\alpha-Fe}\, b\,(1+\nu_{\alpha-Fe})|\varepsilon^T|}{9\pi(1-\nu_{\alpha-Fe})} \tag{6.24}$$

In other words, the interfacial energy is reduced in this case by the following factor:

$$\xi^{dis} = 1 - \left[\frac{\mu_{\alpha-Fe}\, b\,(1+\nu_{\alpha-Fe})|\varepsilon^T|}{9\pi(1-\nu_{\alpha-Fe})}\right]/\gamma \tag{6.25}$$

In the above two equations, b is the Burgers vector and γ the interfacial energy estimated using Eq. (6.22); the other parameters have the same meanings as before.

6.2.1.2 Reduction Factor for Nucleation on Grain Boundaries

Studies of solid-solid nucleation have shown that, in a number of alloy systems, the boundaries between grains are good nucleation sites.[88-91,233] The most common situation is one in which two grains form an interface for the nucleation of second phase particles. The grains on either side of such an interface are generally assumed to be essentially oriented at random. Three grains meet along a line, and four grains meet at a point. Since such locations are particularly choice nucleation sites,[116] here we only consider the case of nucleation at the planar interface between grains (instead of at three-grain or four-grain junctions). Accordingly, the equilibrium angle between two grains, ϕ, can be obtained via the modified Gibbs-Wulff construction,[234,235] as shown in Figure 6.7. The result is the same as that obtained by the usual force

balance argument:

$$\cos(\phi) = \frac{\gamma_{gb}}{2\gamma} \tag{6.26}$$

where γ_{gb} and γ are the average values of grain boundary energy in α-iron and of the nucleus/matrix interfacial energy. If we follow Johnson et al,[236] then the reduction of interfacial energy is related to the angle ϕ, so that

$$\xi^{gb} = \left| 2 f(\phi) \right|^{\frac{1}{3}} \tag{6.27}$$

where ξ^{gb} is the reduction factor due to the contribution of the grain boundary energy, and the function $f(\phi)$ takes the form

$$f(\phi) = \frac{2 - 3\cos(\phi) + \cos(\phi)^3}{4} \tag{6.28}$$

Making use of the values of b = 2.48 Å,[214] γ_{gb} = 0.76 J-m^{-2},[227] and the other physical parameters presented in Table 2 and Figure 6.6, the reduction factors applicable to the present testing temperature range were calculated. The results are shown in Figure 6.8, the mean value of which is about 0.57 for nucleation on dislocations and 0.55 for nucleation on grain boundaries. It can therefore be concluded that the reduction in interfacial energy is quite significant in both cases. As described earlier, the reduction factor ξ is a measure of the interaction energy between a nucleus and a dislocation or a grain boundary, depending on the nucleation site. It should almost be independent of steel composition or of the amount of deformation. It is also worth noting that the reduction factor increases slightly with temperature when nucleation takes place on dislocations, while it remains constant for nucleation at grain boundaries. The change in the former is due to the decrease in the shear modulus $\mu_{\alpha\text{-}Fe}$, and the constancy of the latter is due to the equilibrium angle ϕ, which remains almost constant with temperature.

Recently, some researchers analyzed the nucleation kinetics of carbide precipitation on dislocations[78, 118, 120] in terms of classical nucleation theory.

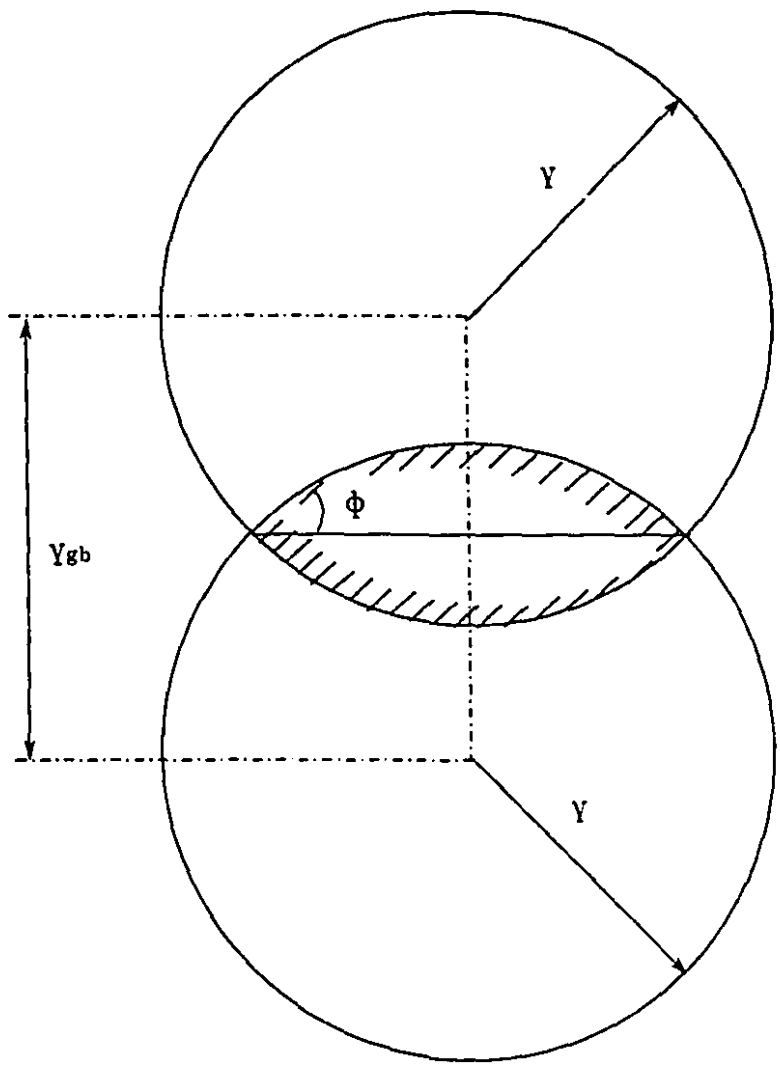

Fig. 6.7 Gibbs-Wulff construction for a nucleus at a grain boundary.[234,235]

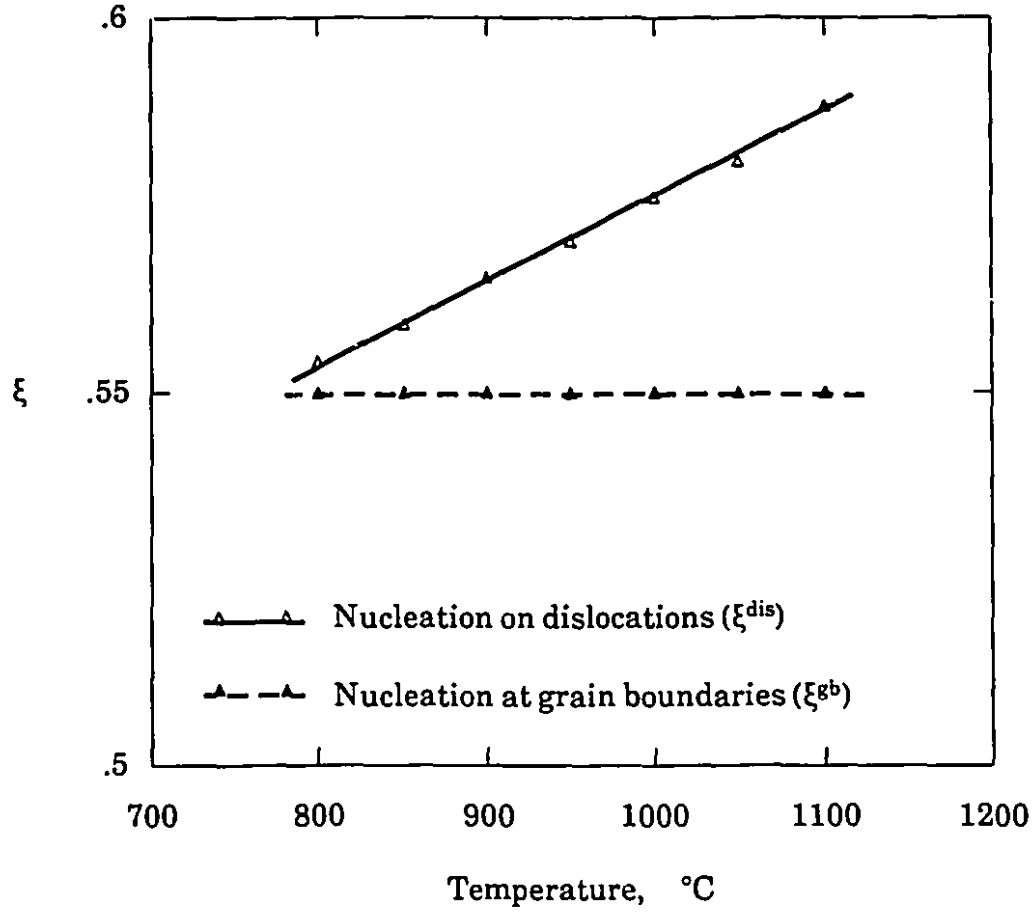

Fig. 6.8 Reduction factors of interfacial energy between MnS nuclei and ferrite.

The reduction factors reported in their investigations ranged from 0.35 to 0.55. The difference between the present work and their findings suggests that the interaction energies associated with sulfide nucleation are smaller than those associated with the nucleation of carbides.

6.2.2 DENSITY OF NUCLEATION SITES

In the case of nucleation on dislocations, the volumetric nucleation site density, N^{dis}, is proportional to the dislocation density ρ:[116]

$$N^{dis} = \frac{\rho}{a_{\alpha\text{-}Fe}} \tag{6.29}$$

In a stressed metal, ρ can be evaluated approximately from the relationship:[151,237]

$$\rho = \left[\frac{2\pi\sigma_a}{M b \mu_{\alpha\text{-}Fe}} \right]^2 \tag{6.30}$$

where σ_a is the applied stress and M is the mean Taylor factor. If this value of dislocation density is substituted into Eq. (6.30), the following equation is obtained for evaluating the number of potential nucleation sites generated by the dislocations:

$$N^{dis} = \frac{(2\pi\sigma_a / M b \mu_{\alpha\text{-}Fe})^2}{a_{\alpha\text{-}Fe}} \tag{6.31a}$$

For grain boundary nucleation, the number of nucleation sites is approximately:[116]

$$N^{gb} = \frac{!}{a^2_{\alpha\text{-}Fe} d_g} \tag{6.31b}$$

where d_g is the average grain diameter.

With the aid of the current experimental data (see Tables 4.1, 5.1 and 6.2) and the values b = 2.48 Å,[214] and M = 2.74,[238] the number of potential nucleation sites was calculated for the two cases: the outcomes are presented in Figure 6.9. It is clear that dislocations can provide many more sites for nucleation than grain boundaries. From the figure, it can also be seen that the density of dislocation sites decreases rapidly as the temperature is increased, which is due to the fact that the applied stress σ_a in Eq. (6.31a) continuously

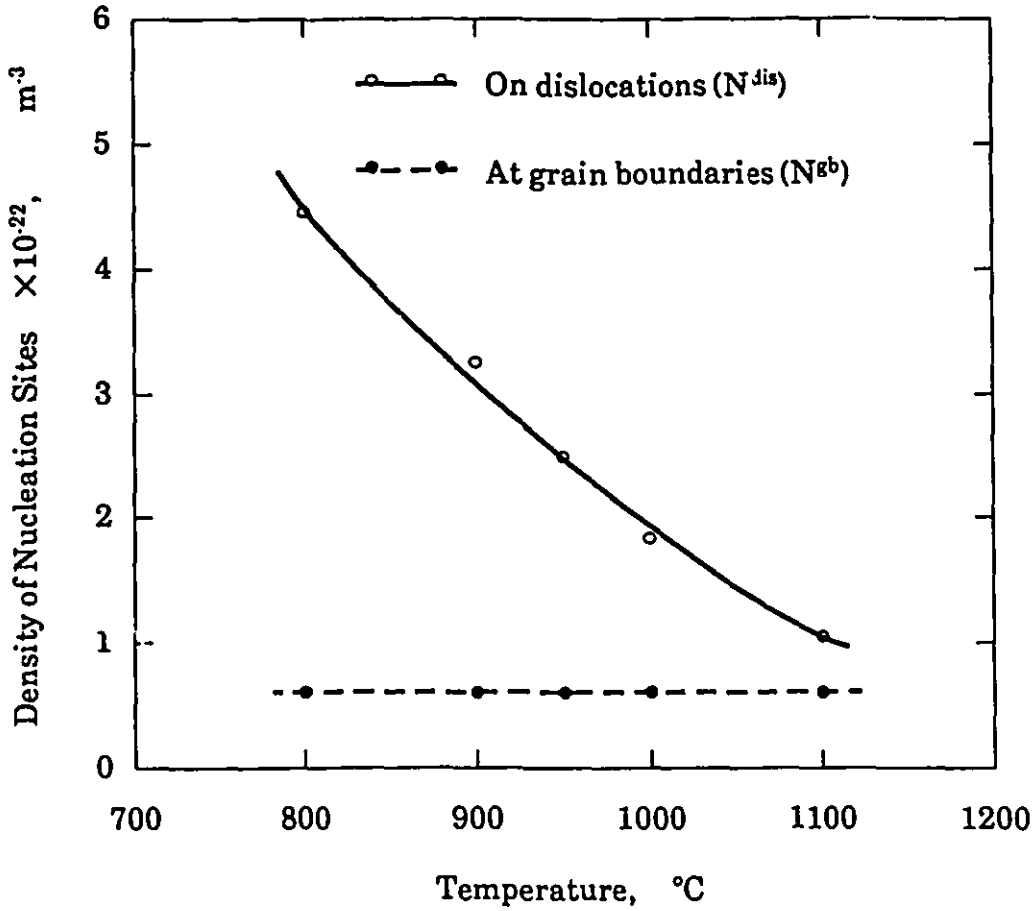

Fig. 6.9 Densities of potential nucleation sites for MnS precipitation predicted for nucleation on dislocations and for nucleation on grain boundaries.

decreases and the dislocation density quickly diminishes with increasing temperature. On the other hand, since grains reach equilibrium with each other, as previously described, after the solution treatment, their average diameter is constant at different test temperatures. Thus, the density of the grain boundary nucleation sites estimated using Eq. (6.31b) remains essentially unchanged as the temperature is varied.

6.2.3 CRITICAL VALUES

Referring back to Eq. (6.2), it is clear that the effective driving force for nucleation is the volume free energy change during transformation, which is equal to the sum of the chemical driving force ΔG_{chem} and the vacancy term ΔG_{vac}, minus the volume strain energy ΔG_{ε}. The barrier to nucleation is the effective interfacial energy $\xi\gamma$. Thus the total free energy change for the formation of a spherical embryo can be divided into two parts; a volume component which is negative, and a surface component which is positive. The diameter at which the contribution of the former is first able to prevent the latter from further increasing the total free energy change, is termed d*, the critical diameter; and the corresponding values are termed critical values. In what follows, two important critical values, the critical interfacial energy and critical free energy, will be evaluated for the formation of a MnS nucleus.

6.2.3.1 Coherency of Critical Nucleus/Matrix Interface

As previously mentioned, predicting the strain energy associated with the critical nucleus is valuable for investigations of nucleation thermodynamics and kinetics. Since the experimental determination of this value is extremely difficult, if not impossible, some theoretical treatments have been proposed for this purpose.[239-241] Of these approaches, the model developed by Liu and Jonas[241] is preferable because it is not only physically realistic, but is also in qualitative agreement with the experimental results.

By employing the parameters required by this model, the critical value, ΔG_{ε}^*, pertaining to the MnS nucleus/matrix interface was calculated. The details of the calculation are presented in Appendix IV. As shown there, the results predicted by the model reveal that the critical interface has very low coherency, so that the strain energy, compared to the corresponding coherent state, drops down to 1-3%. This indicates that the strain energy is significantly smaller than the chemical driving force at this critical condition. Such a critical strain energy is used for the analysis of MnS nucleation that follows.

6.2.3.2 Critical Free Energy

According to principle 1 stated at the beginning of this section, the critical free energy is one of the most important quantities influencing the nucleation rate. This parameter can be found by differentiating the ΔG_{tot} of Eq. (6.2) with respect to d, setting the resulting expression equal to zero, solving for the critical diameter and substituting it back into Eq. (6.2):[117]

$$\Delta G^* = \frac{16\,\pi\,\xi^3\,\gamma^3}{3\,(\Delta G_{chem} + \Delta G_c^* + \Delta G_{vac})^2} \qquad (6.32)$$

For nucleation on dislocations, pipe diffusion is likely to play a role in the very early stages of nucleation, but not after solute atoms are depleted on the dislocations. The diffusion of atoms from the matrix to the dislocations, i.e. bulk diffusion, can be assumed to be dominant under these conditions. Thus, the critical free energy for nucleation on dislocations can be written as

$$\Delta G^*_{dis} = \frac{16\,\pi\,(\xi^{dis}\,\gamma)^3}{3\,(\Delta G_{chem} + \Delta G_c^* + \Delta G_{vac})^2} \qquad (6.33a)$$

In the case of nucleation at grain boundaries, on the other hand, there should be enough solute atoms for the formation of nuclei on the grain interfaces. As a result, the transportation of atoms along grain boundaries greatly aids the nucleation process. According to Russell,[116] $\Delta G_{vac} = 0$ in this case. The equation for evaluating the critical free energy for nucleation at grain boundaries therefore becomes

$$\Delta G^*_{gb} = \frac{16\,\pi\,(\xi^{gb}\,\gamma)^3}{3\,(\Delta G_{chem} + \Delta G_c^*)^2} \qquad (6.33b)$$

The critical free energies within the present test temperature range, 800 °C to 1100 °C, were predicted using the above two equations. As an example, the results obtained for electrical steel B are shown in Figure 6.10. It

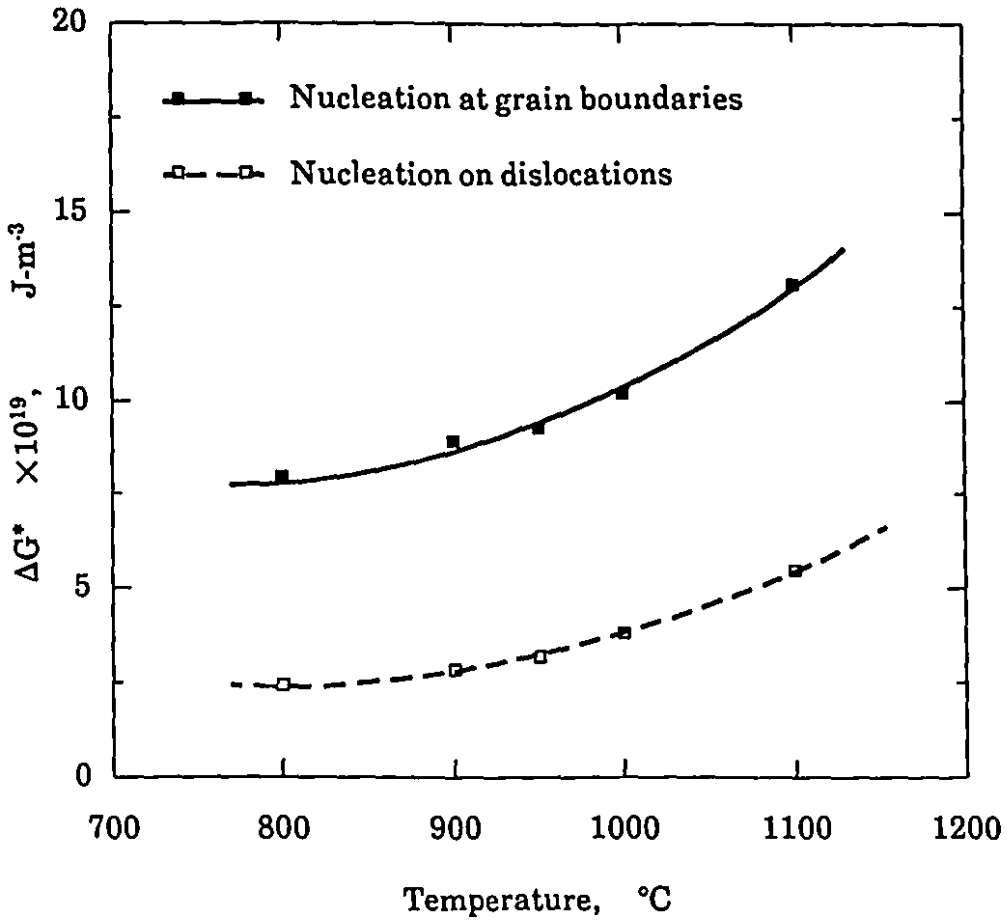

Fig. 6.10 Critical free energies predicted for MnS nucleation in electrical steel B.

is of interest that the values are higher for nucleation at grain boundaries than for nucleation on dislocations. The difference between the two quantities is mainly caused by the presence and absence of ΔG_{vac} in Eqs. (6.33a) and (6.33b) and indicates that the energy barrier (or the minimum work required) is larger for nucleation at grain boundaries than on dislocations.

6.2.4 MODELS FOR PREDICTING Ps TIMES

In terms of classical nucleation theory (see §2.2.6.2), the C-shaped PTT curves obtained in the present investigation indicate that the following equation can be used for describing the nucleation rate J of MnS per unit volume:[112,115-117]

$$J = Z\beta^* N \exp(-\Delta G^*/kT) \tag{2.11}$$

where Z is the Zeldovich non-equilibrium factor and β* the rate at which atoms are added to the critical nucleus, the product of which was written by Russell[116] as:

$$Z\beta^* = \frac{D\dot{X}}{a^2_{\alpha\text{-}Fe}} \tag{6.34}$$

Here D and X are the effective diffusivity and concentration of the element which is rate controlling the nucleation process. Since the diffusivity of S is much faster than that of Mn in α-iron,[242] the latter has been assumed to be the rate controlling element for MnS nucleation in the present study. The nucleation rate can thus be expressed as follows:

$$J = \frac{D^{eff}_{Mn} X^{\alpha o}_{Mn}}{a^2_{\alpha\text{-}Fe}} N \exp(-\Delta G^*/kT) \tag{6.35}$$

As precipitation proceeds, the untransformed portion in a unit volume of ferrite, η_u, is continuously reduced from 1 to 0. As a result, the number of nuclei formed during a time t can be represented by

$$\Theta = J\int_0^t \eta_u \, dt \tag{6.36}$$

In the general case, the transformed portion is considered to be so small at the early stages of precipitation that $\eta_u = 1$. In this way, the critical number of

nuclei which must be formed for precipitation to be detected at P_s can be written as

$$\Theta^* = J P_s \tag{6.37}$$

The combination of Eqs. (6.35) and (6.37) leads to

$$P_s = \frac{\Gamma}{N D^{eff}_{Mn} X^{\alpha o}_{Mn}} \exp(\Delta G^*/kT) \tag{6.38}$$

where

$$\Gamma = \Theta^* a^2_{\alpha\text{-}Fe} \tag{6.39}$$

Two different models were developed from the above expression for the precipitation start time in order to take into account the two different nucleation modes. The first describes nucleation on dislocations and is given by

$$P^{dis}_s = \frac{\Gamma}{N^{dis} D^m_{Mn} X^{\alpha o}_{Mn}} \exp(\Delta G^*_{dis}/kT) \tag{6.40}$$

where $D_{Mn}{}^m$ is the effective diffusivity of Mn atoms in the deformed matrix. It is worth noting that non-equilibrium vacancies markedly accelerate the diffusion process. $D_{Mn}{}^m$ in the present case is, therefore, much higher than its equilibrium value D_{Mn}, and was estimated from the following relation:

$$D^m_{Mn} = \frac{X^{eff}_v}{X^{\theta}_v} D_{Mn} = \frac{X^{eff}_v}{X^{\theta}_v} D_o \exp\left(-\frac{Q_{Mn}}{RT}\right) \quad cm^2 s^{-1} \tag{6.41}$$

Here, $X_v{}^{eff}$ and $X_v{}^{\theta}$ are the effective and equilibrium vacancy concentrations, respectively, D_0 is the frequency factor, and Q_{Mn} is the activation energy for the diffusion of Mn in ferrite in the absence of excess vacancies. A detailed explanation of the reason why the above relation was adopted will be given in the next chapter.

The second model is for nucleation at grain boundaries and has the form

$$P_s^{gb} = \frac{\Gamma}{N^{gb} D_{Mn}^{gb} X_{Mn}^{ao}} exp(\Delta G_{gb}^{*}/kT) \qquad (6.42)$$

where D_{Mn}^{gb} is the effective diffusivity of Mn atoms along grain boundaries. Because of the absence of data regrading D_{Mn}^{gb}, the following treatment was adopted, which recognizes that the total diffusion barrier Q_{Mn} includes two components, the activation enthalpy of vacancy formation and that associated with the translation of the atom:

$$D_{Mn}^{gb} = D_o exp(-\frac{Q_{Mn} - \Delta H_v^f}{RT}) \quad cm^2 s^{-1} \qquad (6.43)$$

The above treatment is based on the assumption that the total barrier Q_{Mn} can be reduced to (Q_{Mn} - ΔH_v^f) because a grain boundary is an excellent vacancy sink.[116]

The coefficient Γ in Eqs. (6.40) and (6.42) can be determined by employing the experimental results measured at P_S for Θ^*. The other parameters, i.e. N^{dis}, N^{gb}, ΔG^*_{dis} and ΔG^*_{gb}, were evaluated above using Eqs. (6.31a), (6.31b), (6.33a) and (6.33b) and were presented in Figures 6.9 and 6.10. As regards the unknown quantities, D_0, Q_{Mn} and ΔH_v^f, their values have been reported by previous investigators[216, 217, 242] as $D_0 = 0.35\ cm^2 s^{-1}$, $Q_{Mn} = 52.5$ kcal-mole^{-1} and $\Delta H_v^f = 1.60$ eV.

Both of these models can be employed for predicting the start of MnS nucleation in ferrite. By this means, the P_S times in electrical steel B were estimated in the present work. The results obtained are compared with the experimental data in Figure 6.11. As can be seen from this figure, at higher temperatures, the nucleation-at-grain-boundaries model is in good agreement with the experimental points. But, at lower temperatures, the nucleation-on-dislocations model is closer to the measured values. Similar conclusions can be drawn from Figure 6.12, where the P_S-temperature curves calculated by the two models are compared with the respective experimental points for the other

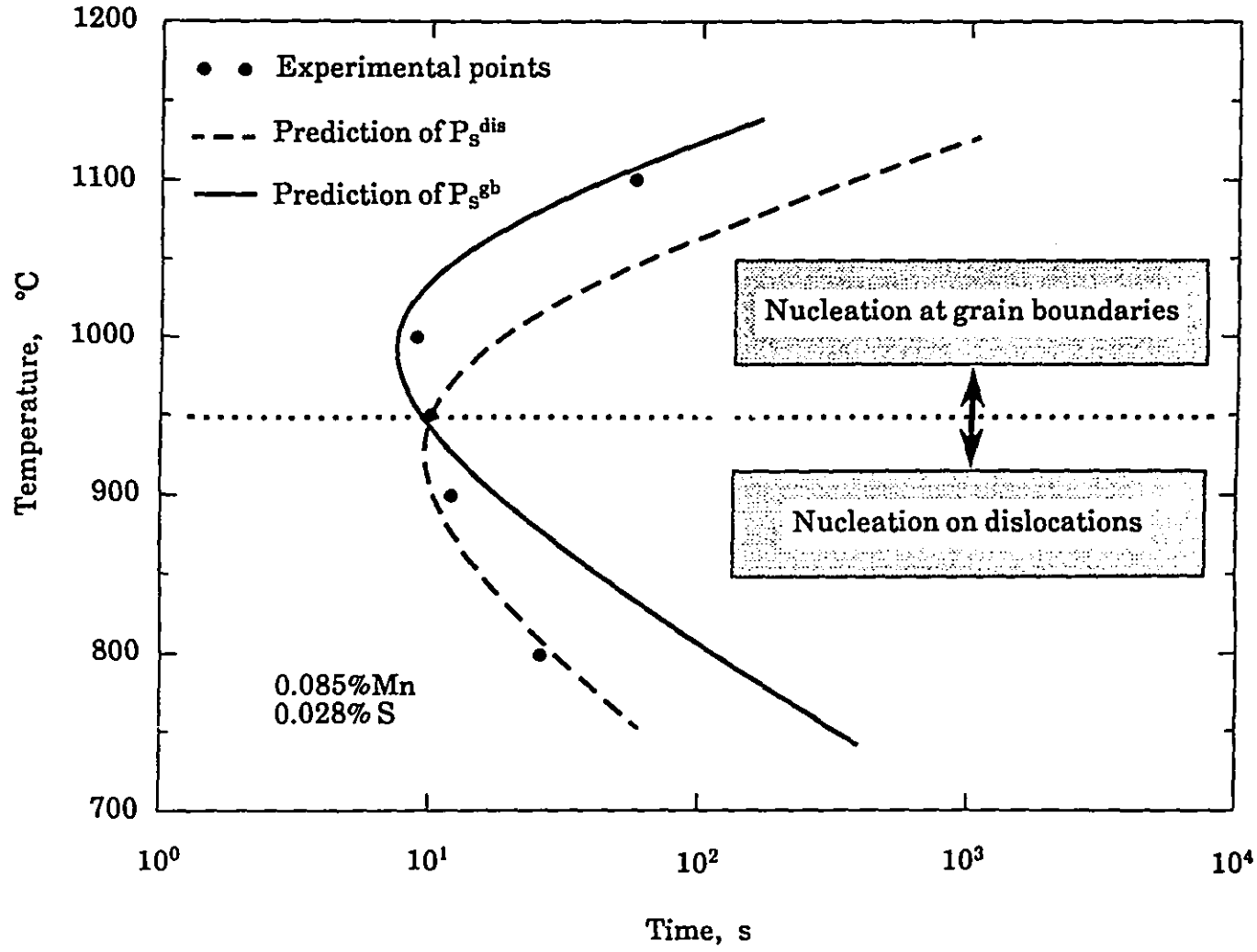

Fig. 6.11 Comparison between measured and predicted P_s values for electrical steel B.

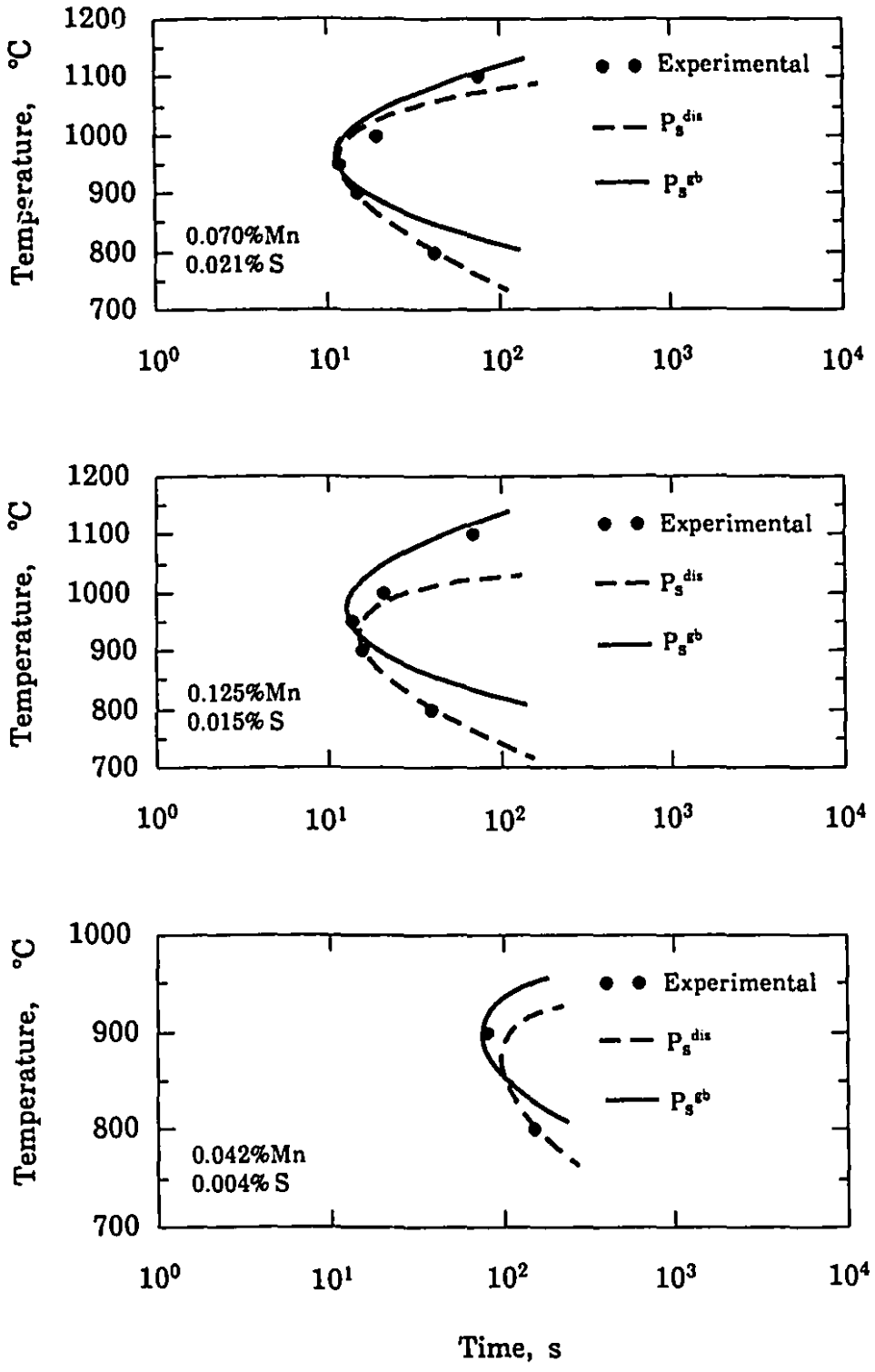

Fig. 6.12 Comparison between the measured and predicted P_S values for electrical steels A, C and D.

three electrical steels. The general conclusion can therefore be drawn that the nucleation of strain-induced MnS precipitates on dislocations is more important at lower temperatures, while nucleation at grain boundaries becomes more dominant as the temperature is increased.

The strong tendency for nuclei to be formed on dislocations at lower temperatures is clearly because the dislocation density is higher at lower testing temperatures, and thus the nucleation site density is higher. On the other hand, the observation that nucleation at grain boundaries is preferred at higher temperatures is probably due to the difference in the diffusivities for the two processes. Diffusion along grain boundaries is faster in this range than matrix diffusion. Thus, when the testing temperature is so high that dislocations can only provide slightly more nucleation sites than grain boundaries, nucleation at grain boundaries is more rapid. This is supported by literature evidence that MnS precipitation takes place preferentially at grain boundaries in the absence of deformation.[61] The micrographs shown in Figure 5.27 of the present study also support this interpretation.

Figures 6.11 and 6.12 also indicate that the present technique is suitable for the detection of both nucleation modes: precipitation on dislocations is detected first at lower temperatures and, as the temperature is increased, nucleation at grain boundaries becomes measurable at an early stage of the creep test.

CHAPTER 7

GROWTH AND COARSENING OF MnS PARTICLES

After nucleation, the new MnS particles grow into their surroundings by draining manganese and sulfur from the iron matrix. In Chapter 5, it was pointed out that the dimensions of MnS precipitates increase as the square root of the growth time between P_s and P_f. After P_f, however, the growth rate decreases so that the slopes of log($\bar{d}_v$) - log(time) curves decrease to about 0.3. This observation indicates that the evolution of growing MnS particles during hot deformation can be divided into two stages: growth and coarsening. In this chapter, the general nature of each stage is discussed. Accordingly, much of this chapter is devoted to a comparison between the theoretical predictions and the experimental results obtained in the present investigation. It will become apparent that the basic ideas of the existing theories are valid, but some modifications are also required, principally because of the complexities associated with the dynamic case.

7.1 GROWTH OF MnS PARTICLES

The parabolic relationship between MnS particle size and time in the growth stage indicates that the growth kinetics of MnS precipitates are diffusion controlled. This is related to the parabolic increase in the diameter of the diffusion field around the particles during the growth period. As a precipitate grows, the area around the particle is gradually solute-depleted, i.e., the concentrations of manganese and sulfur approach the local equilibrium in this region. Any increase in the mobility of the interphase boundary at such low supersaturation cannot accelerate the growth. The rate of growth is thus controlled by the diffusion of either Mn or S atoms from the matrix to the growing precipitates. The kinetics of such diffusion-controlled growth are discussed below.

7.1.1 GROWTH RATE EQUATION FOR MnS PRECIPITATION

7.1.1.1 Theoretical Rate Equation

Referring back to §2.2.6.3, it will be recalled that the following rate equation can be employed to describe diffusion-controlled growth:

$$\bar{r}^2 - \bar{r}_0^2 = K_2 t \tag{7.1}$$

where

$$K_2 = \alpha_2 D_m \Omega \tag{7.2}$$

All the parameters in Eqs. (7.1) and (7.2) were already defined in §2.2.6.3. It is worth noting that the growth of a stable particle can only occur after its nucleation. Based on the assumption that each MnS particle has the critical diameter at the precipitation start time P_S detected in the present study, Eq. (7.1) can be modified to read:

$$\bar{r}^2 - (r^*)^2 = K_2(t - P_s) \tag{7.3}$$

where r* is the critical radius of a MnS nucleus.

Since the experimental results illustrated in Figure 5.14 indicate that the P_f curve is shifted to shorter times as the Mn concentration is increased, it is reasonable to assume that the diffusion of Mn controls the growth of MnS particles. Thus, D_m of Eq.(7.2) can be replaced by the diffusion coefficient of Mn in α-iron, D_{Mn}. Furthermore, according to Doherty,[123] α_2 and Ω in this equation can be taken as:

$$\alpha_2 = 2 \tag{7.4}$$

and

$$\Omega = \frac{X_{Mn}^{\alpha o} - X_{Mn}^{\alpha e}}{X_{Mn}^{MnS} - X_{Mn}^{\alpha e}} \tag{7.5}$$

where each X_i^j has the meaning described in the last chapter. Hence, the average radius of the growing MnS particles at time t can be written as

$$\bar{r} = \left[(r^*)^2 + 2 D_{Mn} \frac{X_{Mn}^{\alpha o} - X_{Mn}^{\alpha e}}{X_{Mn}^{MnS} - X_{Mn}^{\alpha e}} (t - P_s)\right]^{\frac{1}{2}} \tag{7.6}$$

Using the approach employed previously in §6.2.3.2 for deriving the critical free energy ΔG*, the value of r* of Eq. (7.6) can be obtained from the following formula:

$$r^* = - \frac{2 \xi \gamma}{\Delta G_{chem} + \Delta G_c^* + \Delta G_{vac}} \tag{7.7}$$

The Mn diffusivity in α-iron takes the form:

$$D_{Mn} = D_o \exp(-Q_{Mn}/RT) \qquad cm\,s^{-1} \qquad (7.8)$$

where D_0 is the frequency factor and Q_{Mn} the activation energy for the diffusion of Mn in ferrite, the values of which have been reported by Askill[242] as $D_0 = 0.35\ cm^2 s^{-1}$ and $Q_{Mn} = 52.5$ kcal-mole^{-1}.

This model was used to predict the mean radius of MnS precipitates during diffusion-controlled growth. Unfortunately, the calculated results were not in acceptable agreement with the experimental ones. A typical example is shown in Figure 7.1 for electrical steel A tested at 900 °C. It can be seen from this figure that the predictions are much lower than the experimental values. In comparison with the measured data, the predicted mean particle sizes are too small by factors of 2 to 5 in almost all cases.

7.1.1.2 Modifications Required for the Dynamic Case

It is not surprising that the growth rate predicted by the model is much lower than that actually observed in the experiments. A reasonable explanation for this may be that the model described above does not give consideration to the effects of deformation; that is, it is a *static* and not a *dynamic* model. As it has been generally recognized that plastic deformation can greatly accelerate precipitation,[84, 88, 133] a modification of this model is required under the present experimental conditions.

The nucleation kinetics discussed in the above chapter demonstrated that the influence of deformation on MnS nucleation can be interpreted in terms of the additional driving force associated with the excess vacancies and the greater nucleation site density provided by the higher density of dislocations. The question arises at this point as to how diffusion controlled *growth* is stimulated by plastic deformation. The same question can be asked regarding the diffusion of the precipitate-forming elements under dynamic conditions.

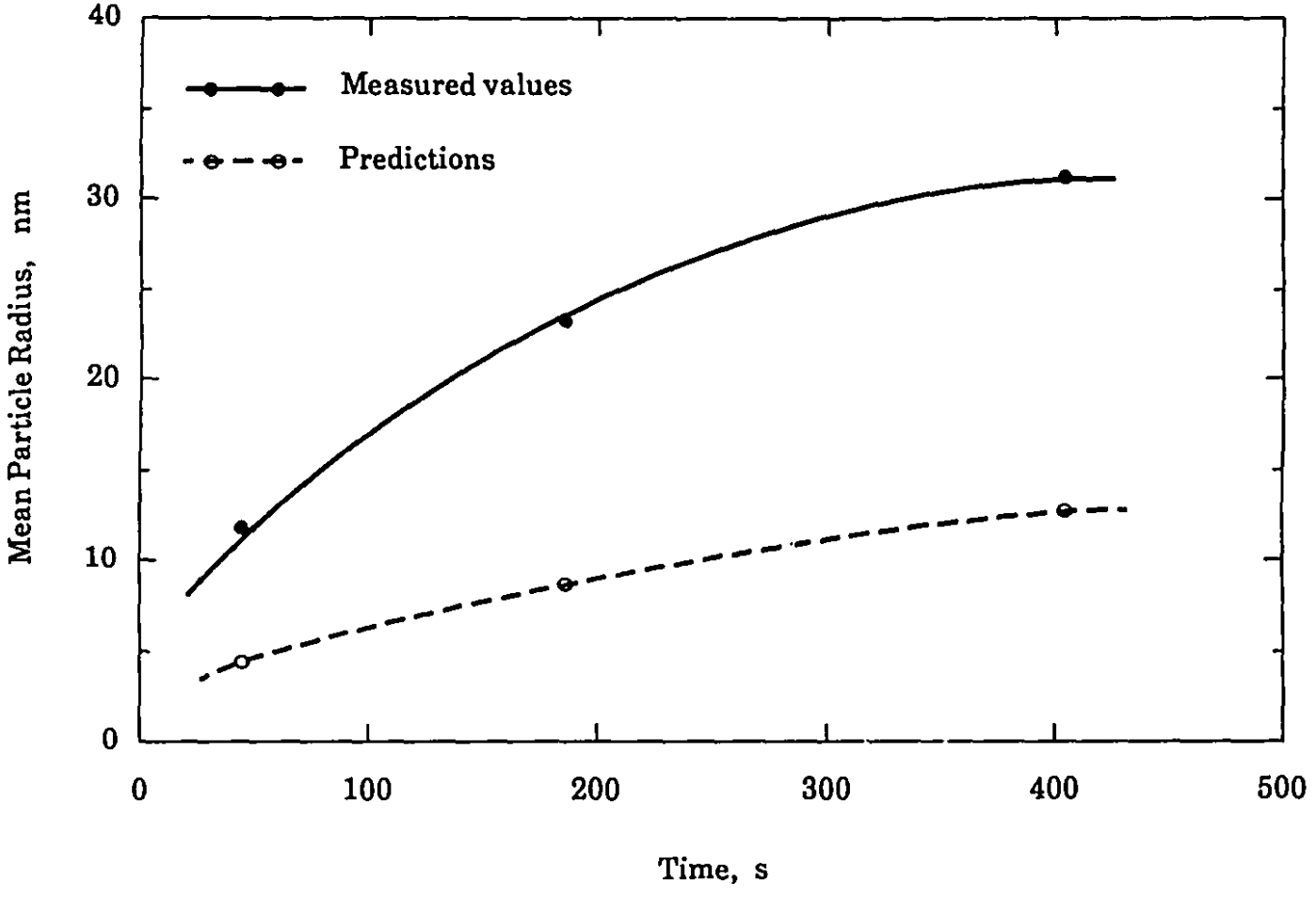

Fig. 7.1 Comparison of the growing particle size measured in electrical steel A at 900 °C as a function of time after P_s with predictions by the classical diffusion-controlled growth model.

Since the value of D_{Mn} in Eq. (7.8) is generally measured under thermal equilibrium conditions, the effects of equilibrium vacancies are taken into account when this value is employed. Under the present creep testing conditions, however, excess vacancies are produced by the deformation, as discussed in §6.1.4.2. These vacancies make an additional contribution to the diffusion process and their presence allows the Mn atoms to move more easily. A quantitative estimate of the increase in the diffusivity is possible and is given below.

With respect to self diffusion in metals and alloys, the diffusion of an atom in the matrix is considered to involve the following two operations:[243]

(1) creation of a vacancy next to the atom in the matrix, and
(2) atom migration into the vacancy.

As the diffusion behavior of Mn atoms is similar to that of iron atoms, a reasonable inference can be drawn : D_{Mn} includes two components, the concentration of vacancies, X_v^θ, and the mobility of atoms, M. That is,

$$D_{Mn} = X_v^\theta M \tag{7.9}$$

If the interaction energy between vacancies and Mn atoms is neglected, a similar expression can be given when deformation vacancies are present in the matrix:

$$D_{Mn}^m = X_v^{eff} M \tag{7.10}$$

where $D_{Mn}{}^m$ was already introduced in the previous chapter; it is the effective diffusivity of Mn atoms in the deformed matrix.

From Eqs. (7.9) and (7.10), we have

$$D^m_{Mn} = \frac{X^{eff}_v}{X^{\theta}_v} D_{Mn} \tag{7.11}$$

In this way, the effective diffusivity can be estimated from the ratio (X_v^{eff}/X_v^{θ}). Accordingly, the rate equation for the diffusion controlled growth of MnS precipitates can be specified as

$$\bar{r} = \left[(r^*)^2 + K^m_2 (t - P_s)\right]^{\frac{1}{2}} \tag{7.12}$$

where

$$K^m_2 = 2 D_o \frac{(X^{\alpha o}_{Mn} - X^{\alpha e}_{Mn}) X^{eff}_v}{(X^{MnS}_{Mn} - X^{\alpha e}_{Mn}) X^{\theta}_v} exp(- \frac{Q_{Mn}}{RT}) \tag{7.13}$$

Employing the values of X_v^{eff} and X_v^{θ} obtained from Eqs. (6.15) and (6.19) in the above two equations, the growth rate of MnS particles was recalculated in this modified manner. The results obtained for electrical steels A, B and C at different temperatures are presented in Figures 7.2 to 7.4, together with the corresponding experimental values. As indicated in these figures, there is good agreement between the predictions and the experimental data in every case. Thus Eq. (7.12) can be used to represent the growth kinetics of strain-induced MnS precipitation. It also suggests that the assumption regarding Mn diffusivity is a physically reasonable one. Consequently, it can be expected that the above type of treatment could be extended to other kinds of precipitation under dynamic conditions.

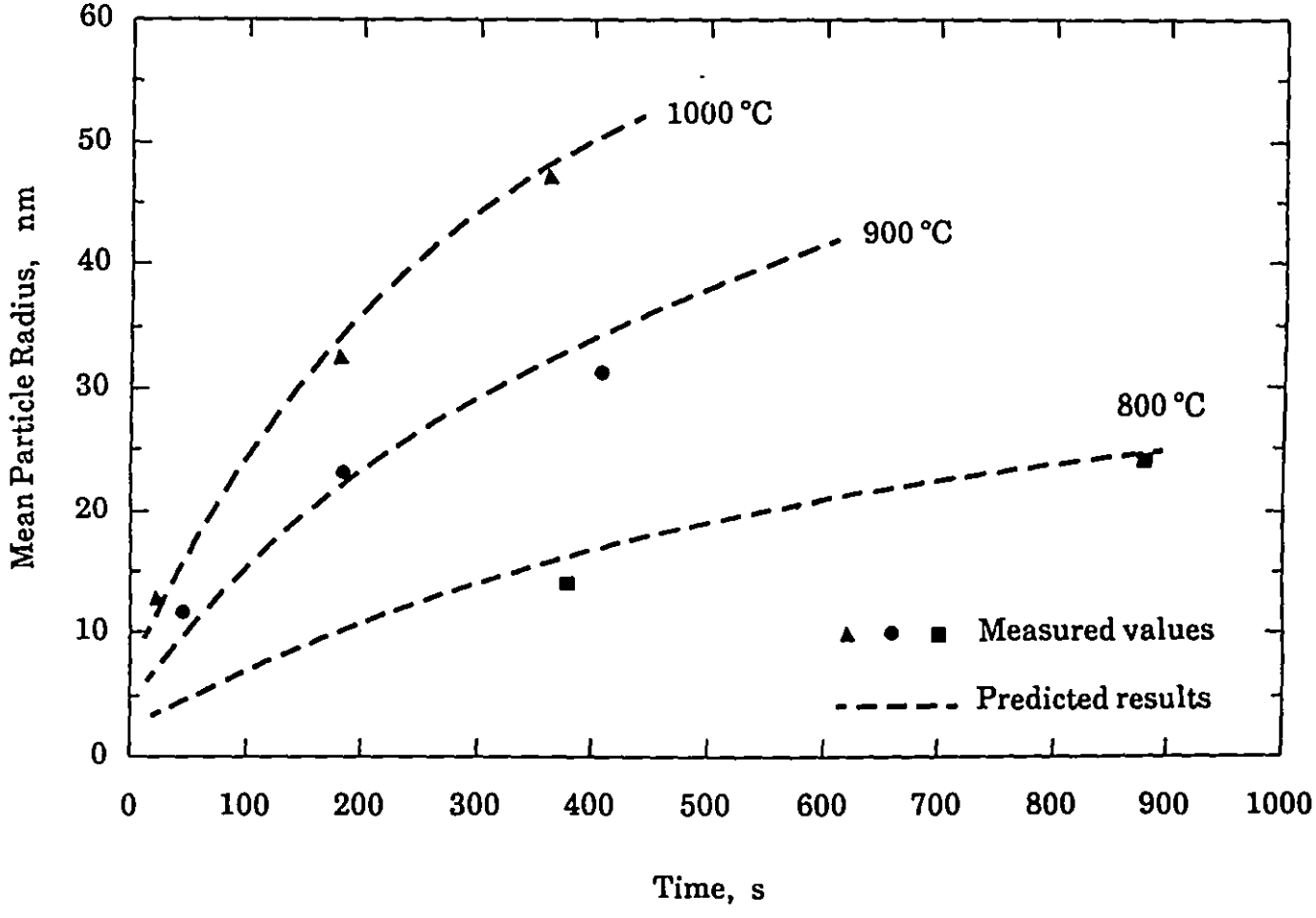

Fig. 7.2 Comparison of the time dependence of the particle size measured in electrical steel A (after P_s) with the predictions obtained from the modified growth model.

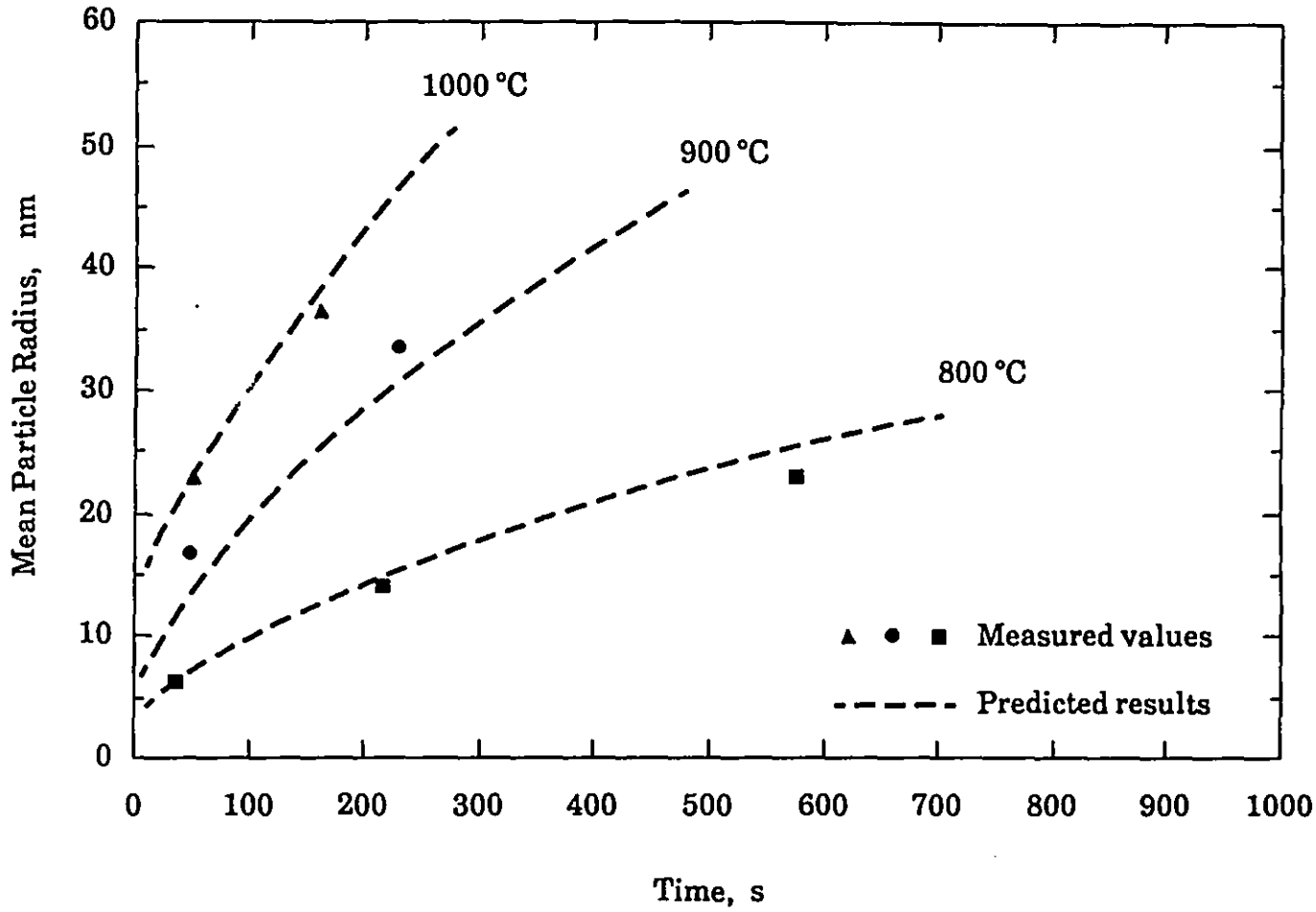

Fig. 7.3 Comparison of the time dependence of the particle size measured in electrical steel B (after P_S) with the predictions obtained from the modified growth model.

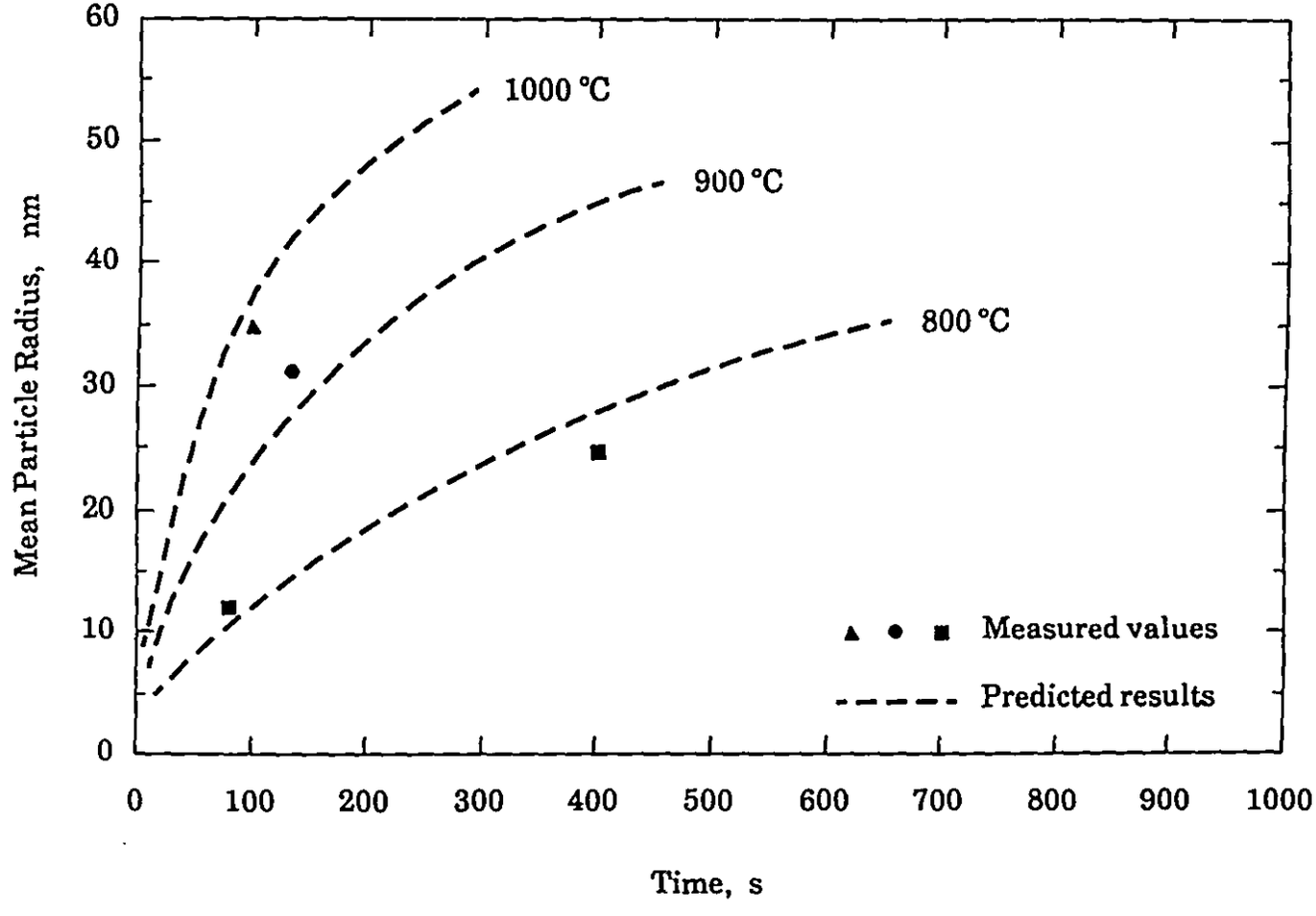

Fig. 7.4 Comparison of the time dependence of the particle size measured in electrical steel C (after P_s) with the predictions obtained from the modified growth model.

7.1.2 MODEL FOR PREDICTING THE P_f TIMES

7.1.2.1 Assumptions Made for the P_f Model

Let r_f represent the average radius of the growing MnS particles at the precipitation finish time P_f. The value of r_f can then be calculated using Eq. (7.12) because

$$r_f = \left[(r^*)^2 + K_2^m (P_f - P_s)\right]^{\frac{1}{2}} \tag{7.14}$$

Alternatively, P_f can be estimated from

$$P_f = P_s + \frac{1}{K_2^m}\left[r_f^2 - (r^*)^2\right] \tag{7.15}$$

if r_f is known.

In order to apply this model to the prediction of P_f times for MnS precipitation, the following assumptions were made in the present study:

(1) That the volume fraction of precipitate attains its maximum possible value at the P_f time, i.e., 100 % of the available MnS is precipitated out by the time the precipitation finish time is reached.

(2) That all the particles are nucleated at the P_s time, so that the number of particles can be considered to remain constant during the interval $[P_s, P_f]$.

Since P_s, r^* and K_2^m of Eq. (7.15) can be computed from first principles, P_f times can be predicted by this equation if r_f values can be obtained independently. For the purpose of calculating r_f, it is necessary to know the equilibrium volume fraction of MnS particles. In the subsection that follows, the equilibrium volume fractions of MnS particles are evaluated at the various test temperatures used.

7.1.2.2 Equilibrium Volume Fractions of MnS Precipitates

According to the analysis presented in §6.1.2.2, the equilibrium mole fraction of MnS particles, f_m, can be calculated using either Eq. (6.9) or Eq. (6.10). Once f_m is known, the equilibrium volume fraction f_v can be derived from

$$f_v = f_m \frac{V_m^{MnS}}{V_m^{\alpha-Fe}} = f_m \frac{a_{MnS}^3}{a_{\alpha-Fe}^3} \tag{7.16}$$

where V_m^{MnS} and $V_m^{\alpha\text{-}Fe}$ are the molar volumes of the MnS particles and of α-iron, respectively, and a_{MnS} and $a_{\alpha\text{-}Fe}$ are their lattice constants.

Using the above equation, the dependence on temperature of the equilibrium volume fractions of MnS in electrical steels A, B and C were determined. The results pertaining to the temperature range from 700 °C to 1300 °C are displayed in Figure 7.5. A solution temperature can be observed for all three steels (see §4.1.1.1). Below this temperature, the volume fraction of equilibrium MnS particles increases with decreasing temperature. Above this temperature, the volume fraction is zero.

7.1.2.3 Calculation of the Average Particle Size at P_f

Based on the first assumption made in §7.1.2.1 and considering a unit volume of matrix, the average particle radius r_f can be related to f_v in the following way:

$$f_v = \Theta \frac{4}{3} \pi r_f^3 \tag{7.17}$$

where Θ is the number of MnS nuclei formed in unit volume of the matrix. Furthermore, the second assumption made in §7.1.2.1 enables us to substitute for Θ:

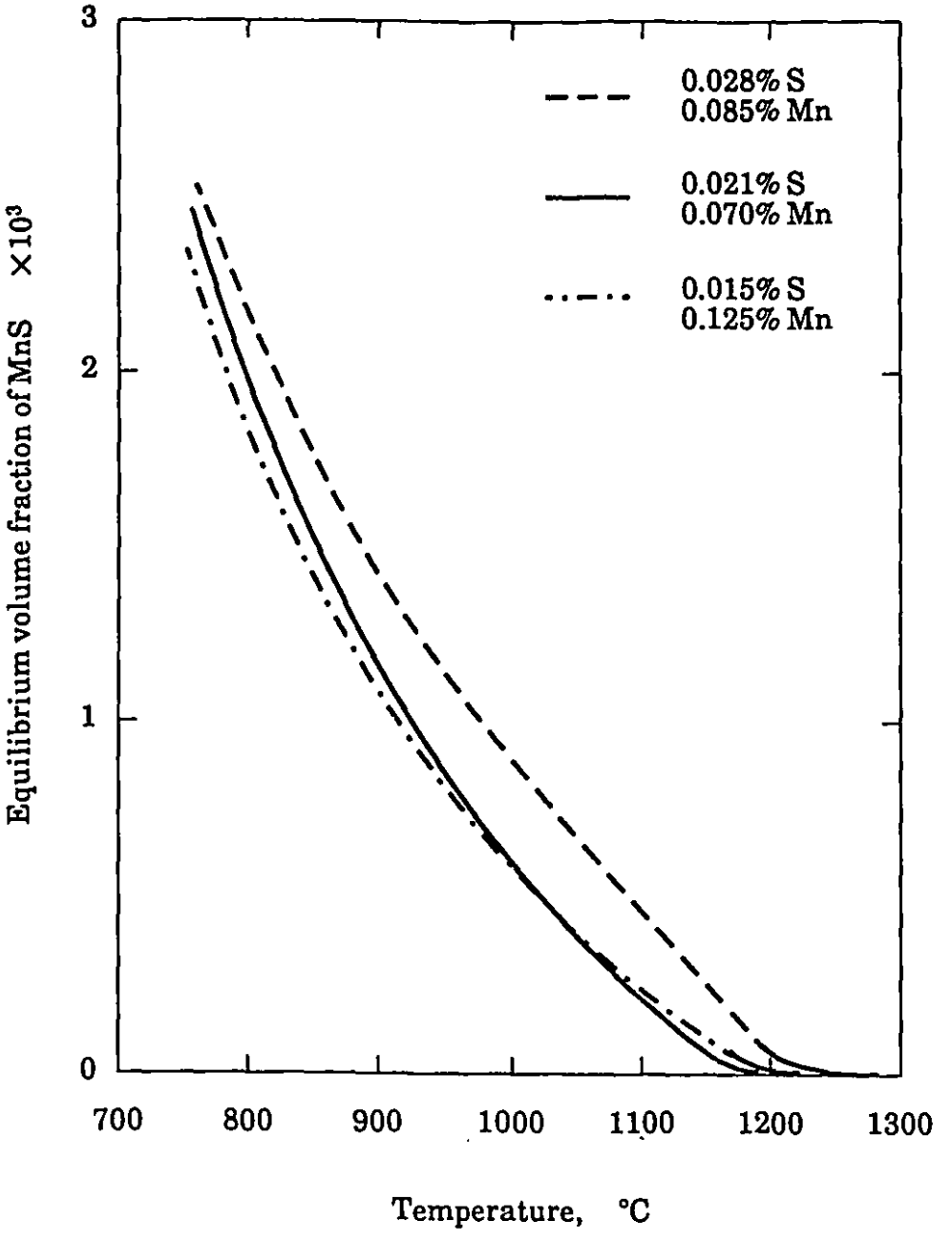

Fig. 7.5 Equilibrium volume fraction of MnS precipitates calculated over the test temperature range in the three electrical steels.

$$\Theta = \Theta^* \tag{7.18}$$

Θ^* in the above equation was defined in §6.2.4. Combining Eqs. (7.17) and (7.18), we have

$$r_f = \left[\frac{3}{4\pi} \frac{f_v}{\Theta^*} \right]^{\frac{1}{3}} \tag{7.19}$$

It should be pointed out that the values of r_f calculated in this way are greater than those actually measured at the precipitation finish time P_f. For instance, the calculated results are 39.3, 42.4 and 38.4 nm for electrical steels A, B and C at 900 °C, while the corresponding experimental data are 31.3, 33.5 and 31.2 nm (see Tables 5.5 - 5.7). This is partly due to the second assumption, which supposes that all the MnS nuclei are fully formed at P_s and that their number remains unchanged between P_s and P_f. Instead, it can be concluded from the nucleation theories discussed in the preceding chapter that the nucleation of MnS precipitation occurs gradually over a brief time period, rather than suddenly and completely at $t = P_s$. This suggests in turn that some of the nuclei were created *after* P_s. As a result, the average radius of the particles at P_f should be smaller than that estimated from Eq. (7.19). In addition, the first assumption, i.e. that precipitation is 100 % complete at P_f, is also an oversimplification. This is perhaps another reason for the larger values of r_f predicted by Eq. (7.19). A modifying factor, η_m, is therefore proposed in the present investigation for calculating r_f, as given by

$$r_f = \eta_m \left[\frac{3}{4\pi} \frac{f_v}{\Theta^*} \right]^{\frac{1}{3}} \tag{7.20}$$

Comparison with the experimental results indicates that η_m in the above equation is about 0.8 for MnS precipitation. As a result, Eq. (7.20) can be further simplified to

$$r_f = \frac{1}{2} \left[\frac{f_v}{\Theta^*} \right]^{\frac{1}{3}} \tag{7.21}$$

7.1.2.4 Application of the P_f Model

By substituting Eq. (7.21) into Eq. (7.15), we have

$$P_f = P_s + \frac{1}{K_2^m}\left[\frac{1}{4}\left(\frac{f_v}{\Theta^*}\right)^{\frac{2}{3}} - (r^*)^2\right] \tag{7.22}$$

which can be employed directly for predicting P_f times. It is important to note that the parameters on the right hand side of the above equation (P_s, r^*, K_2^m and f_v) can be evaluated theoretically from Eqs. (6.40), (6.42), (7.7), (7.13) and (7.16). This means that the model of Eq. (7.22) can be used without fitting the experimental P_f data. With the help of the model, P_f times were estimated for electrical steels A, B and C at the different test temperatures. The calculated and observed values are compared in Figure 7.6. It can be seen from this figure that the P_f times determined in the above way are somewhat greater than the experimental ones. As discussed above, these differences can be linked to the assumptions made at the beginning of this section. However, the predictions do not seem to deviate too far from physically acceptable values. Thus, the model developed here is valuable as a theoretical means of estimating precipitation finish times.

7.2 COARSENING OF MnS PARTICLES

Following the end of growth by solid solution depletion, the MnS particles attain their equilibrium volume fraction. However, this does not mark the end of particle growth because the size distribution of the precipitates is associated with a high interface area, which raises the free energy of the system. To reduce this energy, the larger particles grow continuously by consuming the smaller ones while maintaining a constant volume fraction of precipitate. That is, the coarsening process results in the redissolution of the smaller particles with higher free energies to the benefit of

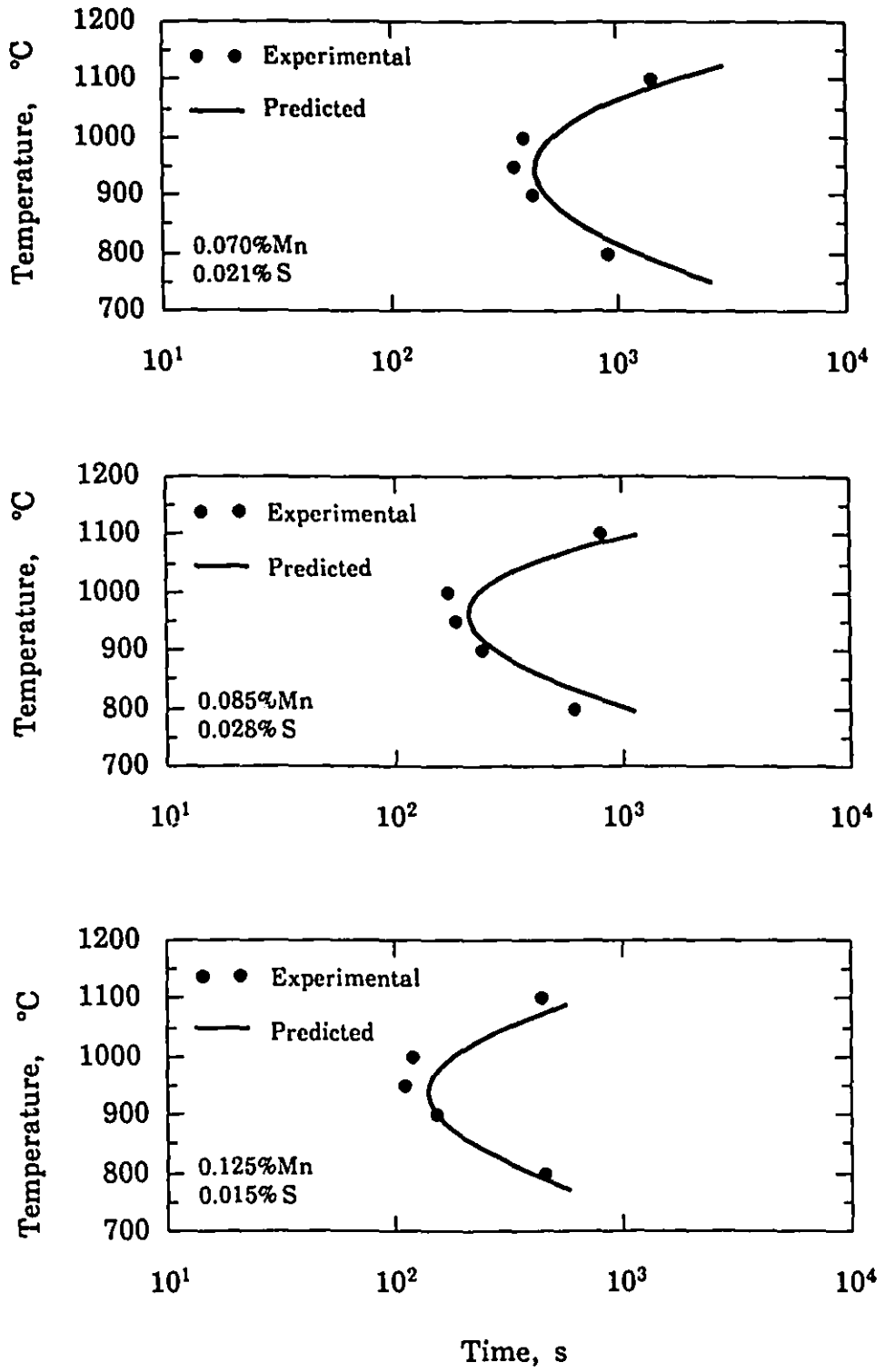

Fig. 7.6 Comparison between measured and predicted P_f values for electrical steels A, B and C.

the larger ones. This process is commonly called "Ostwald ripening". In the sections that follow, the characteristics of MnS ripening will be investigated.

7.2.1 APPARENT ACTIVATION ENERGY FOR COARSENING

As reviewed in Chapter 2, the kinetics of precipitation during the coarsening stage are well described by

$$\bar{r}^n - \bar{r}_0^n = a \frac{D}{T} t \tag{7.23}$$

Here a is a temperature independent factor and D is the diffusion coefficient of the rate controlling element, the values of which depend on the specific mechanism that controls the coarsening process (see §2.2.6.3). For the coarsening of MnS precipitates under the conditions of the present experiments, Eq. (7.23) can take a form similar to Eq. (7.3)

$$\bar{r}^n - r_f^n = \frac{K_c}{T} (t - P_f) \tag{7.24}$$

where r_f is the average radius of the particles at P_f and K_c is given by

$$K_c = a D = a D_0 exp(-Q/RT) \tag{7.25}$$

A nonlinear regression analysis was applied to Eq. (7.24) and the exponent n was found to be about 3.4 (as demonstrated by Figures 5.20 - 5.22). This is between the value of 3 associated with the bulk diffusion mechanism and that of 4 attributable to grain boundary diffusion (see §2.2.6.3). This indicates that coarsening of the MnS particles is probably controlled by a mixture of these two processes.

From Eq. (7.24), we also have

$$K_c = \frac{\bar{r}^n - r_f^n}{t - P_f} T \qquad (7.26)$$

Fitting the current experimental data for $\bar{r}$, r_f and P_f into this equation yielded values of K_c at different temperatures. The results are plotted in Figure 7.7 in the form of *log(K_c) vs 1/T*. From this plot and Eq. (7.25), the apparent activation energy for the coarsening of MnS was found to be 36.5 kcal-mole^{-1}. This is significantly lower than the value of Q_{Mn} associated with the equilibrium bulk diffusivity D_{Mn}, 52.5 kcal-mole^{-1}, and even less than those associated with the effective bulk diffusivity D_{Mn}^{m}, values of which fall between 45.0 and 50.0 kcal-mole^{-1}. This again indicates that the coarsening of MnS particles is not solely controlled by bulk diffusion. A possible diffusion mechanism for the coarsening of MnS particles will now be proposed below.

7.2.2 POSSIBLE DIFFUSION MECHANISMS FOR PARTICLE GROWTH AND PARTICLE COARSENING

In order to clarify the difference between the diffusion processes operating during growth and during coarsening, two two-dimensional representations of a particle distribution geometry are given in Figure 7.8. The one displayed in the upper diagram represents a group of precipitates undergoing growth by solute depletion. As can be seen from the diagram, some of the particles (particles 1, 4 and 7) are located at a grain boundary and the others (particles 2, 3, 5, and 6) are distributed within the matrix. The heavy arrows indicate the motion of solute atoms (Mn and S atoms) to the growing particles. Clearly, the growth of the particles in the matrix is controlled by bulk diffusion. For the growth of the particles located at the grain boundary, the solute atoms diffuse directly to the particles along the boundary in the very early stages of growth. When the boundary becomes solute depleted, the atoms will first be transported from the iron matrix to the boundaries by matrix diffusion and then move to the particles along the boundary. Since diffusion in the matrix is much slower than along a grain boundary, the key step in this transport process is probably bulk diffusion.

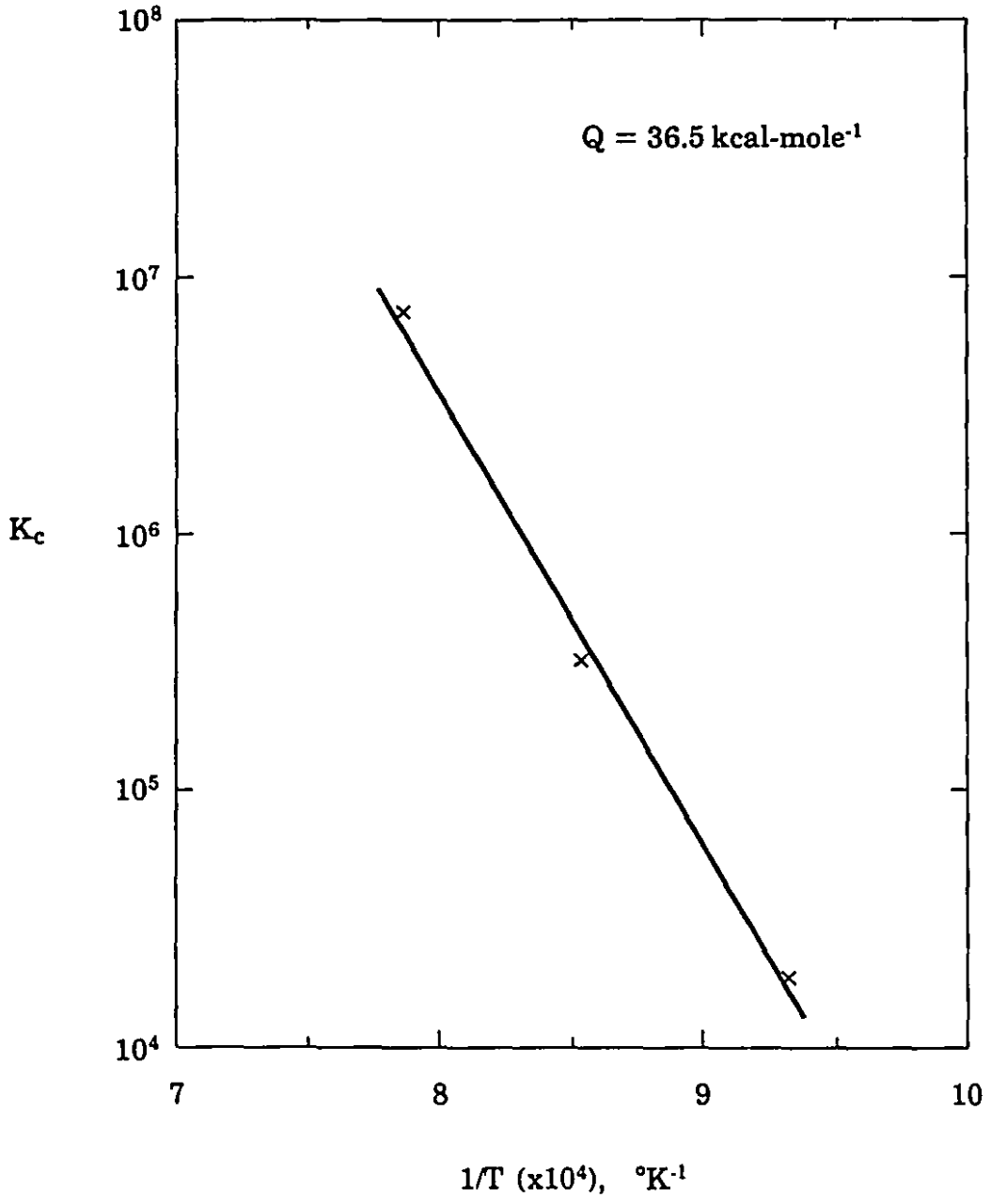

Fig. 7.7 Dependence of the MnS particle coarsening parameter K_c on temperature.

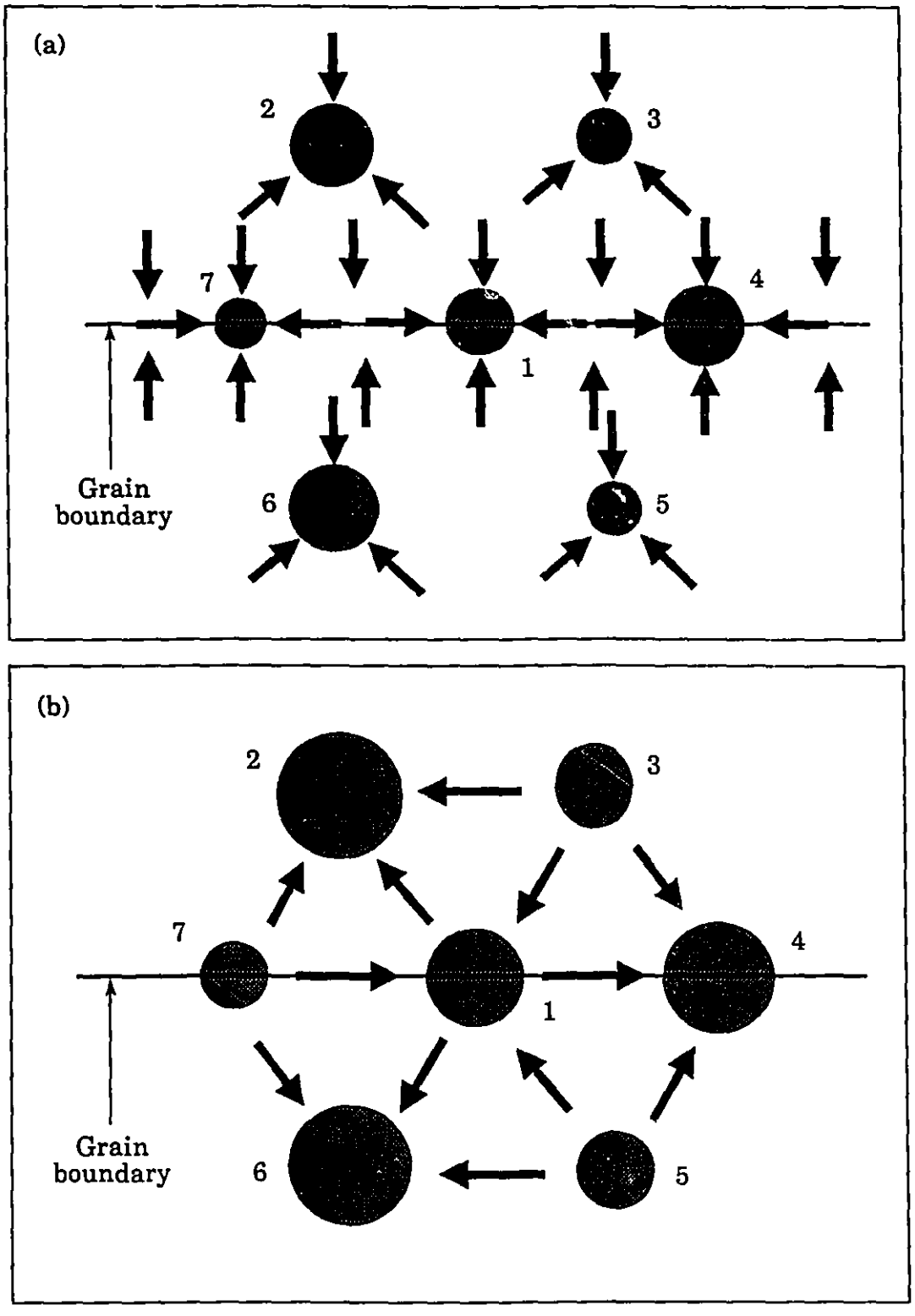

Fig. 7.8 Two-dimensional representations of the diffusion process occurring during (a) growth and (b) coarsening of the MnS particles.

The lower diagram in Figure 7.8 shows the same group of particles during the coarsening stage. In this case, precipitation has attained its maximum volume fraction so that the solute atoms travel directly from the smaller to the larger ones, also indicated by the heavy arrows in this diagram. In this case, the diffusion mode depends on the exact path between adjacent particles. For example, the movement of atoms from particle 3 to particle 2 (or from particle 5 to particle 6) is accomplished by matrix diffusion while the movement from particle 1 to particle 4 (or from particle 7 to particle 1) takes place by diffusion along the grain boundary. It therefore seems reasonable to conclude that the overall coarsening of these particles is controlled by both bulk and grain boundary diffusion.

To further clarify the diffusion mechanisms described above, the following additional comments will be made:

(1) The excess vacancies generated by deformation are likely to enhance matrix diffusion, both in the growth and coarsening stages, as demonstrated above.

(2) During the period of increasing volume fraction, the particles on dislocations can be treated in the following way: the diffusion process can be considered to involve two steps: i) from the matrix to dislocations, and ii) along the dislocations to particles. The first step is expected to be dominant in this case.

(3) As will be analyzed in the next chapter, the dislocations become unpinned from the precipitates in the ripening stage. Under these conditions, the particles which were nucleated on dislocations lose their effectiveness in pinning them. Thus, they can be treated in the same manner as those in the matrix, and diffusion along dislocations can be neglected. As a result, only matrix and grain boundary diffusion play roles in the coarsening of MnS particles.

CHAPTER 8

CREEP MECHANISMS ASSOCIATED WITH THE INFLUENCE OF MnS PRECIPITATION

At this point in the discussion, the influence of MnS precipitation on the creep behavior of electrical steels will be analyzed. Only after completing this, will it be possible to understand why the new technique is successful in detecting the occurrence of precipitation at hot working temperatures. As demonstrated by the experimental results presented in Chapter 5, both deformation within the grains and sliding at the grain boundaries contribute to the creep of electrical steels at high temperatures. This chapter will thus concentrate on these findings by providing:

(1) an analysis of the interaction between dislocations and MnS precipitates during hot deformation, and

(2) an investigation of the drag effects that the particles exert on grain boundary sliding.

In addition, the applicability and sensitivity of the creep technique will be compared to those of the stress relaxation method.

8.1 INTERACTION BETWEEN DISLOCATIONS AND PRECIPITATES

In the present work, electron microscopy was employed to follow the progress of MnS precipitation in samples undergoing creep testing. The micrographs shown in Chapters 4 and 5 indicated that the plateau on the creep curve, i.e. the decrease in the creep rate, is related to the occurrence of MnS precipitation. This observation is also consistent with the precipitation kinetics described in the previous two chapters. Thus it seems reasonable to interpret this experimental phenomenon partly in terms of an interaction between dislocations and precipitates, and partly in terms of the blocking effects of the particles on grain boundary sliding. The former will be analyzed here, while the latter will be discussed in the next section.

8.1.1 GENERAL CONSIDERATIONS REGARDING DISLOCATION PARTICLE INTERACTIONS

Numerous physical models have been proposed, as reviewed in Chapter 2, for dislocation-precipitate interactions. Depending on the characteristics of such interactions, all existing models can be classified in one of the following three groups:

(1) bowing,
(2) cutting,
(3) climbing or cross slipping.

If several stable MnS precipitates are formed in materials which are being deformed, these particles will serve as additional obstacles to the motion of dislocations. As a result, the latter will bypass the former in one of the above three manners. Since the interaction between precipitates and dislocations at

high temperatures, as in the present experiments, is complex, these mechanisms must be considered and discussed one at a time.

8.1.2 IS THE BOWING MODEL APPLICABLE?

The bowing model was first proposed by Orowan[177] for the case of coarse particles. He suggested that, as a dislocation approaches a row of dispersed particles, it will bow out between them, reconnect with itself beyond, and finally leave a residual dislocation loop surrounding each particle. Detailed calculations of the Orowan stress have been made by Orowan,[177] de Wit and Koehler,[244] Chou and Eshelby,[245] Brown,[246] and de Chatel and Kovacs.[247] It was also demonstrated by Ashby[248] that if the particle is incoherent, localized plastic flow may be generated at the particle-matrix interface by the approaching dislocation. The stress necessary for this is of the order of one hundredth of the shear modulus of the matrix. Thus the Orowan process, as pointed out by Haasen,[249] truly applies only for large *coherent* particles. By contrast, the coherency of the MnS particle/matrix interface, as described in Chapter 6, is very poor. According to the above criterion, therefore, the MnS particles do not satisfy the requirements for the Orowan process and thus, dislocations cannot simply bow out between these particles in the present case.

8.1.3 CAN DISLOCATIONS CUT THE PRECIPITATES?

To answer this question, the details of the dislocation cutting mechanism need to be considered first. A dislocation moving on a slip plane containing a distribution of precipitates may cut through the particles if the applied shear stress exceeds the critical strength of the particles.[77] If this model is to apply, the particles must be very small and close to one another.[250] During cutting, sufficient energy must be applied to break favorable bonds within the particles, thus increasing their "surface" area.[249] If the precipitates are completely coherent with the matrix, the energy Σ of the interface produced is relatively small. It was estimated by Kelly and Fine[251]

to be about 0.1 J-m^{-2}. At the other extreme, if the particles are incoherent, the value of Σ will be of one order larger, i.e. about 1 J-m^{-2}.[249]

According to Haasen,[249] the stress, σ, to force an essentially straight dislocation through a distribution of precipitate particles of interspace λ and radius r is:

$$\sigma = (\frac{\Sigma}{b})(\frac{r}{\lambda})M \tag{8.1}$$

Thus, the critical size above which the particle cannot be cut by a moving dislocation can be estimated from

$$r_c = (\frac{b}{\Sigma})(\frac{\sigma_a}{M})\lambda \tag{8.2}$$

where b is the Burgers vector, σ_a is the applied stress during creep testing, and M is the mean Taylor factor. Substituting the experimental data for σ_a and λ, b = 2.48 Å as reported by Frost and Ashby,[214] Σ = 1 J-m^{-2} by Haasen[249], and M = 2.74 by Gilormini, Bacroix and Jonas[238] into this relation, the largest possible particle radius which can be sheared is estimated to be 0.8 nm. This value is even smaller than the size of the critical MnS nucleus evaluated using Eq. (7.7). The mechanism of dislocation cutting can therefore be rationally rejected under the present experimental conditions.

8.1.4 HOW DO DISLOCATIONS CLIMB OVER THE PARTICLES?

As described above, the activation energy associated with cross slip is very small in bcc metals due to their high stacking fault energies. Thus this process is expected to take place so easily under the present test conditions that it cannot serve as a barrier to the motion of dislocations. Consequently, the cross slip of screw dislocations is not considered as a possible rate controlling mechanism in the present case, and only the theories based on dislocation climb need to be treated instead.

8.1.4.1 Modified Local Climb Model

As stated earlier in this chapter, the decrease in creep rate after P_s can be partly accounted for by the interaction between dislocations and precipitates. Attempts were made in the present work to employ the existing climb models to explain such an interaction. Unfortunately, the theoretical predictions were not in satisfactory agreement with the experimental results. As an example, a local climb model is discussed below in more detail.

This model was first proposed by Brown and Ham,[252] and later modified by Shewfelt and Brown[253, 254] and Stevens and Flewitt.[25] In their investigations, it was assumed that the dislocation climbs only at the particle/matrix interface, while the dislocation segments between the particles remain in their slip plane. In order to be able to compare our experimental results with the predictions of this model, some refinements were made to their original expressions. The details of this treatment are presented in Appendix V and only the resulting strain rate equation for spherical particles is given in this section:

$$\dot{\varepsilon} = \frac{60\,\pi^4 \sigma_a^2 b^2}{M^2 \mu_{\alpha\text{-}Fe} kT \bar{r}} D_{so} exp(-\frac{Q_s}{RT}) \qquad (8.3)$$

Here, σ_a is the applied stress, M is the average Taylor factor, $\bar{r}$ represents the average radius of spherical precipitates, D_{so} and Q_s are the frequency factor and activation energy, respectively, for matrix self-diffusion, and the other parameters have their usual meanings.

The strain rate was predicted by employing the present experimental data for σ_a and $\bar{r}$, together with the other numerical values given in Tables 6.2 and 8.1 for $\mu_{\alpha\text{-}Fe}$, b, M, D_{so} and Q_s. An example of the results obtained from Eq. (8.3) is given in Figure 8.1 (represented by a dashed and dotted line), where the measured and calculated strain rates are compared for the case of electrical steel A deformed at 800 °C. It should be mentioned here that the uppermost (dashed) line in this figure was based on the general climb model, which will be

Table 8.1
Values of the Parameters Used in the Calculation of the Strain Rate by the Modified Local Climb Model

Parameter or Variable	Ref.
$b = 2.48\,Å$	[214]
$M = 2.74$	[238]
$D_{so} = 2.0\times10^{-4}\ m^2\text{-}s^{-1}$	[214]
$Q_s = 251$ kJ-mole^{-1}	[214]

described in §8.1.4.3. Since grain boundary sliding is of little importance at lower temperatures, the experimental strain rates shown in this figure (represented by a dotted line) can be regarded as being solely due to deformation within the grains. Clearly, these values decrease suddenly at about P_s and pick up slightly after a time close to P_f.

Unlike the experimental data, the strain rate predicted by the modified local climb model (the dashed and dotted line) drops continuously with time, leading to higher values than the experimental ones in the interval between P_s and P_f, and lower ones after P_f. It is worth mentioning that the same types of behavior were found at the other temperatures and for the other steels. Moreover, when still further climb models were employed, still greater divergences were observed between P_s and P_f. For simplicity, only the results calculated by the modified local climb model are presented here. Consequently, it appears that precipitation in our case exerts a particular influence on the dislocation climb process in the interval $[P_s, P_f]$. The above comparison also indicates that the local climb model is not consistent with the effects of particle coarsening. These two problems are analyzed further below.

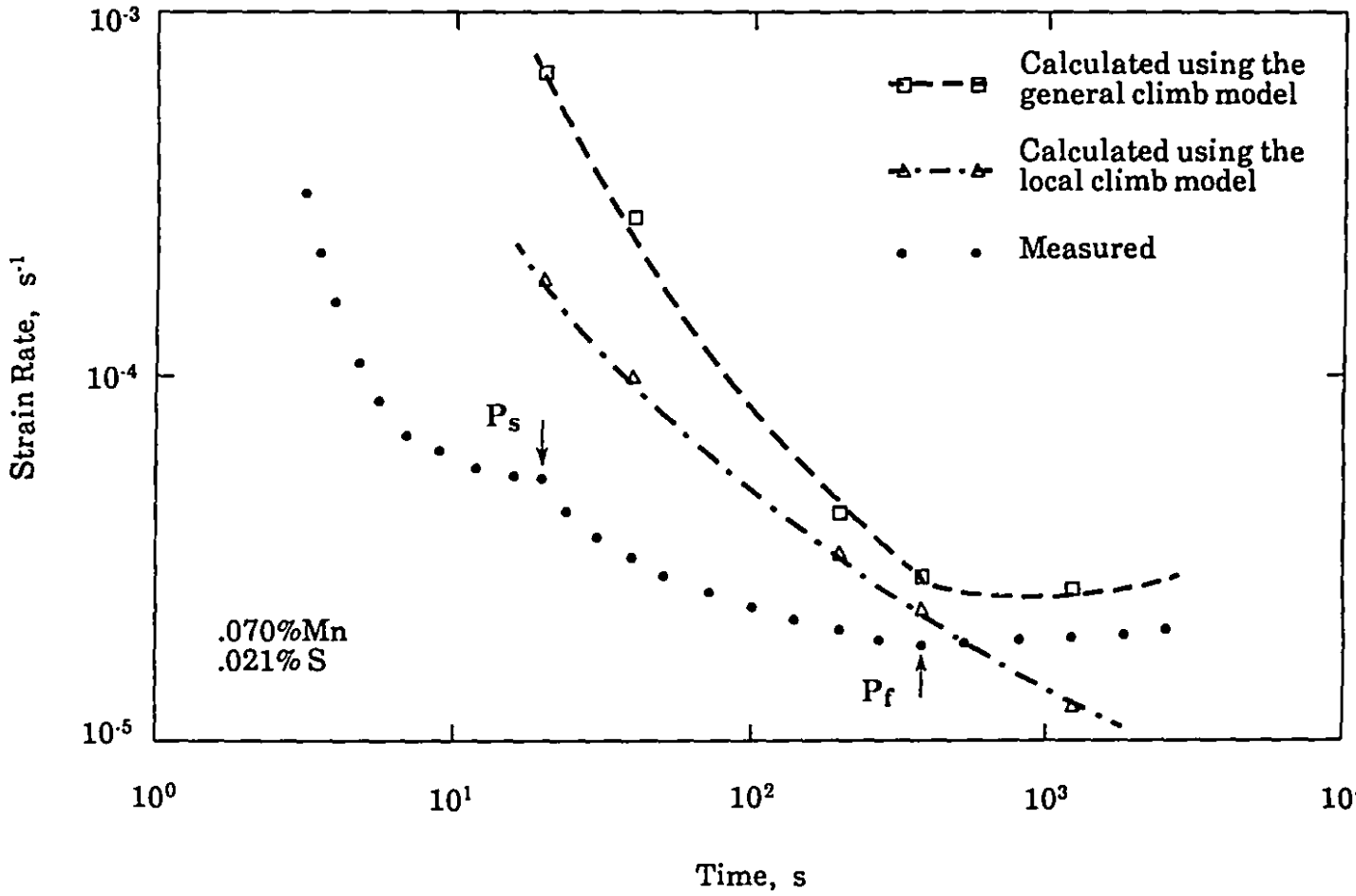

Fig. 8.1 Strain rates measured and calculated using the modified local climb model and Ansell and Weertman's general climb model for grain deformation in electrical steel A at 800 °C.

8.1.4.2 Dislocation-Particle Interactions in the Interval P_s-P_f

Almost all the existing climb models are based on the geometry of the dispersed phase (its shape, volume fraction and size distribution), but ignore its physical characteristics, such as coherency. However, in our case, the lattice mismatch between the MnS precipitates and the ferrite is known to be as large as 45%. The difference between the experimental observations and the model predictions is, therefore, understandable. Thus it is necessary to examine the influence on dislocation climb caused by such incoherency. Furthermore, the current climb models are designed for particle-containing materials in which no fresh precipitates are produced during deformation, i.e. in which the volume fraction and size distribution of the particles remain constant. By contrast, both the amount and size distribution of the MnS precipitates were changing continuously during the present creep tests. This dynamic feature must have played a great role in reducing the strain rates observed in the experiments. Since the dynamic precipitation of MnS in ferrite has not been investigated to date, dislocation-particle interactions under the present conditions will now be examined in more detail.

(a) Attractive interaction

Srolovitz et al.[256] once suggested that there is an attractive interaction between dislocations and the interface of incoherent particles. The dislocation-MnS precipitate interaction can also be influenced in this way.

Let us first consider an edge dislocation, during creep, originally traveling toward a MnS particle on an intersecting glide plane. This dislocation will end its trajectory at the incoherent particle-matrix interface. Once the dislocation reaches and moves into the interface, the change in atomic environment affects the nature of the dislocation. In contrast to its character in the matrix, where the periodicity of the lattice keeps the dislocation core small, the mismatch at the phase interface allows the dislocation core to become delocalized. This delocalization allows the core of the dislocation to spread out over the entire precipitate-matrix interface. As a result, this dislocation segment is converted into an interface dislocation, which helps to balance the lattice mismatch between the particle and the

matrix. Even when a dislocation moves onto a glide plane that does not intersect the precipitate, its trajectory may still be modified by the presence of a nearby MnS particle. Since this mobile dislocation is attracted towards the particle, the dislocation segment will lengthen and may even end up in the interface after some climb plus glide motion.

Indeed, several researchers have observed, by electron microscopy, that dislocations are pinned on the departure sides of incoherent precipitates.[257] Their observations indicate that such an attractive interaction between dislocations and incoherent particles does exist.

(b) Effects of nucleation and growth

In addition to the incoherent nature of the particles, the dynamic character of the precipitation can also modify the dislocation-particle interaction. Recently, Liu and Jonas[147] raised the possibility that the mobile dislocations can be pinned by the precipitates nucleated directly on them. By incorporating their idea into the present analysis, the following additional explanation can be given for the reduced strain rate during the course of dynamic MnS precipitation.

As described in Chapter 6, MnS precipitates prefer to nucleate on lattice defects to reduce their formation free energies. Thus, some precipitates will unavoidably nucleate on mobile dislocations during deformation. The dislocation segments involved first serve as nucleation sites, then are gradually attracted by and incorporated into the new precipitate-matrix interface, and finally are pinned by the fresh precipitates. Another possible mechanism involves the locking of the mobile dislocations as a result of the absorption of the vacancies required for particle growth. In such a case, the edge dislocations act as vacancy sources and climb towards the growing particles, around which a vacancy poor zone is created; subsequently, they are converted into interface dislocations and are pinned.

The operation of the above mechanisms is expected to lead to the pinning of the majority of the mobile dislocations by such dynamically-precipitated incoherent particles. When the pinned dislocations escape from

the particle by climb, additional energy is required to unpin them from the interface. The physical origin of this interaction is that the line tension of the dislocation lying in the interface is lower than the matrix value[179]. In this case, the problem during dislocation climb is to increase the dislocation length and also to re-create the line energy associated with the interface segment. Since only the former, but not the latter, is taken into account by current climb models, the inapplicability of these models to the present situation is not surprising. This additional line energy can be regarded as an internal stress increment, which opposes dislocation climb and thus results in a strain rate which is lower than the theoretical value in the interval between P_s and P_f. It seems likely that dislocation-particle interactions during this period are characterized by such climb events with interfacial pinning.

8.1.4.3 Dislocation-Particle Interaction after P_f

It is clearly of interest to clarify the dislocation-particle interactions that are involved in particle coarsening (competitive growth). It is important to note from Figure 8.1 that the experimental strain rate (the dotted line) is higher than that calculated by Eq. (8.3) (the dashed and dotted line) after the precipitation finish time P_f. The failure of the local climb model to apply to the stage after P_f leads to the following two possibilities:

(1) Dislocation unpinning from the precipitate interface is accomplished in the course of particle coarsening; and

(2) During this period, the creep behaviour cannot be interpreted in terms of so-called local dislocation climb. Consequently, another mechanism may influence the dislocation dynamics.

(a) Unpinning due to coarsening

As described in more detail in the previous chapter, competitive growth takes place during the coarsening stage in order to reduce the interfacial free energy. This means that the larger particles grow continuously by consuming the smaller ones, while the total volume fraction of precipitate remains

constant. Thus the dislocation-particle interaction is influenced by two additive factors. On the one hand, extra vacancies are expected to flow towards the small redissolving precipitates because of the reduction of their volumes. Such a directional flow causes the edge dislocations to be freed from the particles. Furthermore, the larger precipitates, as they are growing, are continuously becoming more and more incoherent, so that less dislocations are present at their interfaces.[78] As a result, both categories of precipitate lose their effectiveness in pinning dislocations during the coarsening stage, resulting in a distinct increase in the dislocation mobility and thus the strain rate. In addition, since the volume fraction of particles is unchanged, the interparticle spacing is enlarged, making dislocation climb easier, as discussed in the section that follows.

(b) Bypassing of coarsening particles by general climb

Because of the failure of the local climb model to describe creep during particle coarsening, another type of dislocation model, i.e. a general climb model, was considered. Unlike the local climb model, the dislocations in the general climb model are not assumed to surmount the particles only at the particle/matrix interface. Rather, it is assumed that the line tension causes the dislocations in the immediate vicinity of the particles to unravel from the particle interface by climb.[257-259] Considering the density and rate of the dislocations moving in the crystal, Ansell and Weertman[257] set up such a model, which led to the following expression for the creep rate:

$$\dot{\varepsilon} = \frac{n\sigma_a^2\lambda}{2M^2\mu_{\alpha\text{-}Fe}^2 b^2 \bar{r}} D_{so} \exp\left(\frac{2\sigma_a^2\lambda b^2}{M^2\mu_{\alpha\text{-}Fe} kT}\right) \exp\left(-\frac{Q_s}{RT}\right) \qquad (8.4)$$

Compared to Eq. (8.3), the only new parameter appearing in the above expression is λ, the dispersion spacing.

The predictions obtained from Eq. (8.4) are also presented in Figure 8.1, together with the values predicted by Eq. (8.3) and the experimental data. It can be seen that Ansell and Weertman's model always gives the highest strain rate during the whole process. In the interval between P_s and P_f, the deviation

of the predicted strain rate from the experimental one is greater than that associated with the local climb model. These values decrease significantly during this period because of the continuous increase in particle size and decrease in dispersion spacing. After about P_f, the rates predicted by this model, unlike those obtained from the local climb model, increase again, which is in accordance with the experimental observations. This agreement implies that the rate controlling mechanism during the precipitate coarsening stage could be the bypassing of the particles by the general climb of dislocations.

The mechanisms responsible for the creep caused by grain deformation are summarized in Figure 8.2. As can be seen from this figure, interfacial pinning plays an important role in preventing the motion of dislocations over MnS precipitates between P_s and P_f. Such pinning is due to both the incoherent nature and the dynamic character of MnS precipitation. After P_f, the dislocations are unpinned and bypass the coarsening particles by general climb. It is evident that, through the influence of such different dislocation mechanisms, the present type of creep experiment is capable of following precipitation kinetics provided that the precipitates appear only on the dislocations. However, some of the MnS precipitates nucleate on grain boundaries. Thus, the question arises as to why this technique maintains its effectiveness under such mixed conditions. An investigation was carried out to answer this question and is described in the next section.

8.2 BLOCKING OF GRAIN BOUNDARY SLIDING BY PRECIPITATES

A review of Gibb's investigation concerning grain boundary sliding was given in Chapter 2. As mentioned there, the general conclusion drawn from his work is that grain boundary sliding in high temperature creep is always accompanied by deformation within the grains. Excellent confirmation of his view was provided by the experimental observations presented above. In the foregoing, the mechanisms responsible for grain deformation and the effects of precipitation on such deformation have been clarified. The occurrence of grain boundary sliding and the effect of the precipitates on the sliding process is discussed next.

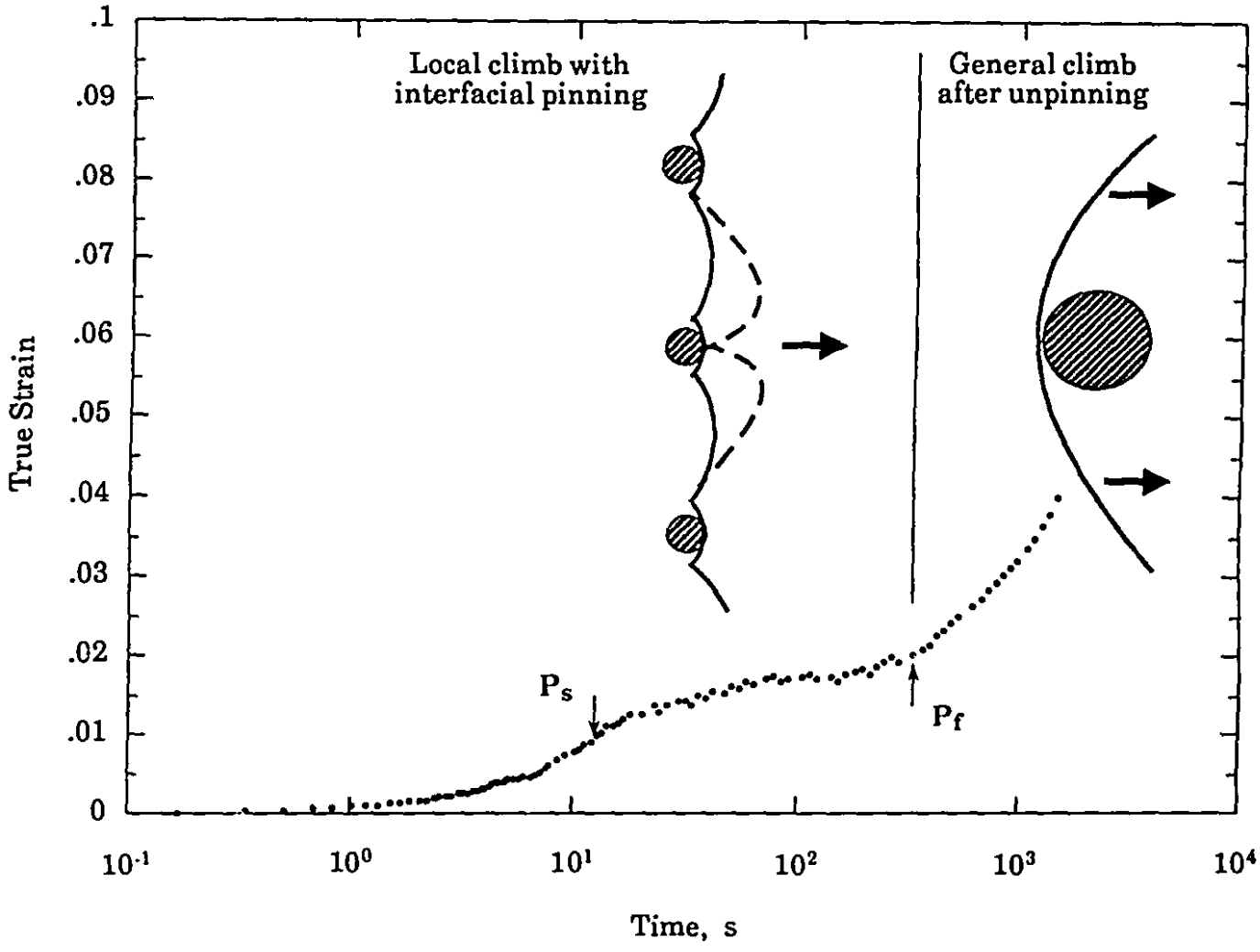

Fig. 8.2 Possible dislocation mechanisms controlling grain deformation during creep testing.

8.2.1 GENERAL STUDIES OF GRAIN BOUNDARY SLIDING

The boundary between two grains is a region of misfit. The deformation in this region differs from that in the center of grains; it is more complex.[149] Several experiments have suggested that such boundary deformation can be considered as a sliding process.[260] Boundary sliding was first regarded as a type of Newtonian viscous flow.[261, 262] Gradually, the coincident site lattice concept was used in the development of grain boundary sliding models.[263, 264] Further demonstrations indicated that grain boundary sliding is related to deformation within the grains.[265, 266] Because of the interconnection between the two deformation processes, various mechanisms have been proposed for grain boundary sliding.

For instance, many experimental results concerning sliding at high temperatures have been consistently explained in terms of diffusion controlled sliding.[169, 175, 267] The mechanism of such boundary sliding has been linked by Gifkins and Snowdon[268] and Raj and Ashby[161] to Nabarro-Herring-Coble creep occurring within the grains. In addition, some models have been presented by Kê[269] and Raj and Ashby[161] for describing grain boundary sliding with accommodation by anelastic creep. As regards the situation in which we are interested, some mechanisms for boundary sliding accompanied by dislocation motion have also been developed.[264, 270, 271] However, most of the investigations have dealt solely with particle-free grain boundaries.

There have only been very few studies concerned with the presence of precipitation. The first quantitative model regarding the influence of particles on boundary sliding was developed by Raj and Ashby in 1971[161] and since then, several refinements to the original model have been proposed.[169, 173, 272] It should be mentioned here that all the models, like the dislocation climb models, still assume that the volume fraction and size distribution of the precipitates do not change during deformation. In what follows, only Raj and Ashby's work will be examined because later researches yielded expressions similar to theirs.

8.2.2 EXAMINATION OF THE PREVIOUS WORK ON PARTICLE BLOCKING DURING BOUNDARY SLIDING

Assuming that the grain boundary has a shape that is approximately sinusoidal, with a wavelength w and amplitude h/2, Raj and Ashby[161] considered the role of the second phase particles in the boundary in impeding the sliding motion. They treated this problem with an electrostatic analogy. Their approach resulted in the following equation for the average sliding rate of a grain boundary containing an unchanging distribution of cube-shaped particles of side s and spacing λ:

$$U_{gb}^{P} = \frac{8\delta D_{gb}\omega\tau_a\lambda^2}{kTs^4} \tag{8.5}$$

Here δ is the grain boundary thickness, D_{gb} is the coefficient for boundary diffusion, ω is the atomic volume, τ_a is the applied stress, and k and T have their usual meanings.

In the same article, the above researchers[161] also presented an expression for the sliding rate of precipitate-free boundaries:

$$U_{gb} = \frac{8\delta D_{gb}\omega\tau_a}{kTh^2} \tag{8.6}$$

where h is two times the boundary amplitude. In order to examine whether Eq. (8.5) can be applied to the case of dynamic precipitation, we compared this equation with Eq. (8.6). It is evident that if the size of the particles is small enough that

$$s < \sqrt{(h\lambda)} \tag{8.7}$$

then we have

$$U_{gb}^{P} > U_{gb} \tag{8.8}$$

This result is obviously contrary to any experimental observation, even to the original expectations of the authors themselves. Indeed, it has been pointed out by them[161] and other investigators[169, 173, 272] that particles inserted in a boundary always slow down the sliding rate. Furthermore, since the interparticle spacing λ is much larger than the particle size s, Eq.(8.7) can be generally satisfied. Only for extreme situations where large second phase particles are closely spaced in the grain boundaries can Eq. (8.7) become logical and effective. Apparently, this condition cannot be met by dynamic precipitation, especially during its early stages (fine particles) and during the coarsening period (sparse distribution). Thus, an alternative model must be developed for describing the blocking effects of dynamic precipitation on grain boundary sliding.

8.2.3 AN ANALOGY FOR GRAIN BOUNDARY SLIDING

Before proposing our own model, let us first clarify the basic physical concepts that we will employ. Consider a system, as shown in Figure 8.3, made up of two blocks; the lower one, on a horizontal frictionless table, is attached to a spring, the upper one is pulled to the right with a force F_a, and, between them, there is a viscous fluid layer. Resembling the case of grain boundary sliding, the blocks represent grains, while the fluid layer between them can be imagined to be the grain boundary. Then, the force F_a is representative of the applied stress for creep deformation and the spring can taken as the elastic accommodation during sliding due to the existence of boundary steps or second phase particles in the boundary.

Once F_a is applied to the upper block, both blocks move to the right, the upper one at a higher speed. The elastic elongation of the spring obeys Hooke's law

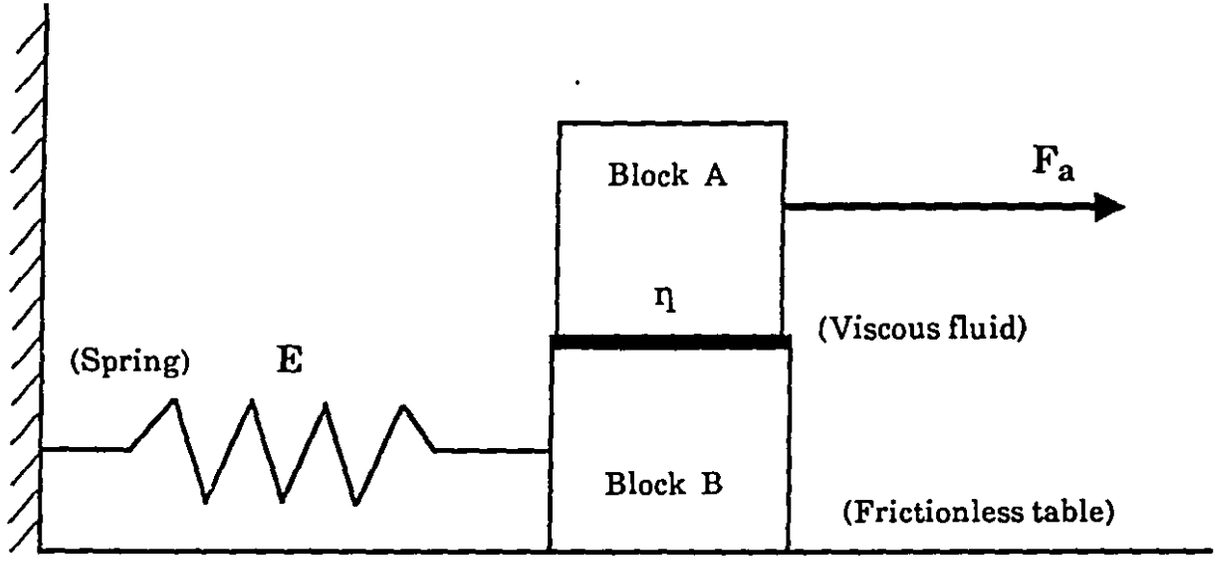

Fig. 8.3 An analogy for describing grain boundary sliding.

$$x = \frac{F_e}{E} \tag{8.9}$$

where E is the spring constant and $F_e < F_a$ is the force exerted on the lower block by the spring.

When a steady state of motion is attained, in which the lower block no longer moves, Newtonian viscous sliding between the two blocks proceeds at the steady rate

$$U_\eta = \frac{F_a}{\eta} \tag{8.10}$$

It is worthy of note that, during such steady sliding, the total free energy change of the system, dG, is only related to the work done by the applied force on the upper block; which is to say, we have

$$dG = -dW = -F_a dx_\eta \tag{8.11}$$

where dW is the work done by F_a and dx_η is the amount of sliding between the two blocks. Under these circumstances, F_a remains stable and does not depend on time. The total driving force for sliding is therefore the work done by the applied stress. This indicates that, irrespective of the specific events occurring during sliding, the whole process can be evaluated in terms of the work contributed by the applied stress. By employing this idea, the blocking effects exerted by particles on grain boundary sliding can be estimated as follows.

8.2.4 ENERGY CONSERVATION MODEL

In this subsection, the relationship between the rates of sliding of a particle-free and a precipitate-containing boundary will be quantified on the basis of the energy conservation concept. For this purpose, we first examine the work consumed in boundary sliding when particles are absent.

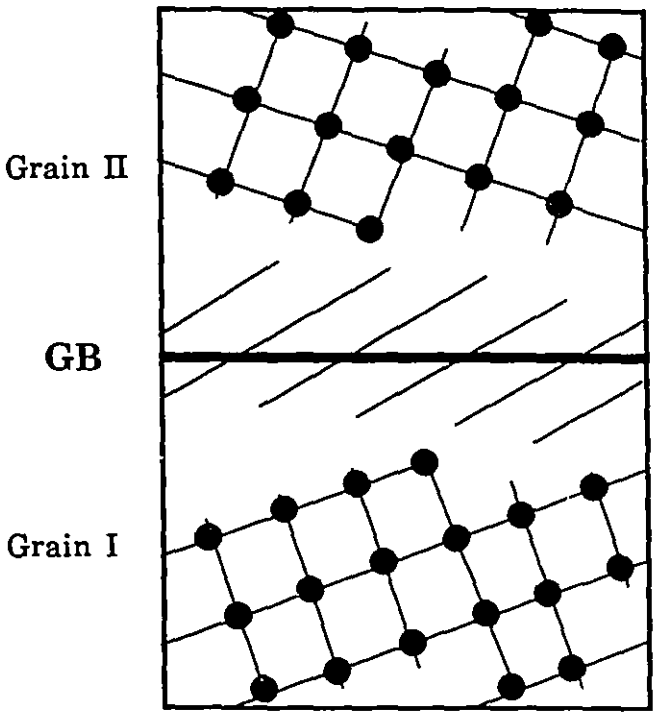

Fig. 8.4 Schematic illustration of two grains separated by their boundary.

8.2.4.1 Work Done in the Absence of Precipitates

Consider the two grains I and II separated by their boundary GB illustrated in Figure 8.4. In this figure, their positions are identified by the points representing the centers of the atoms. At first, it can be assumed that the structure of each grain far from GB is not influenced by the presence and movement of the other grain. In order to determine the structural change in the intergranular region during boundary sliding, let us treat a sector of boundary of length l and width w ($l > w$), as shown in Figure 8.5. Regardless of the mechanism responsible for the boundary sliding, it can be assumed that,

under the application of a force F_a, an array of atoms on the upper grain boundary moves to the left a distance $a_{\alpha\text{-}Fe}$ during the time interval dt, where $a_{\alpha\text{-}Fe}$ is the interatomic spacing at the boundary. At the same time, the atoms on the lower grain boundary, due to the same force F_a, are displaced the same

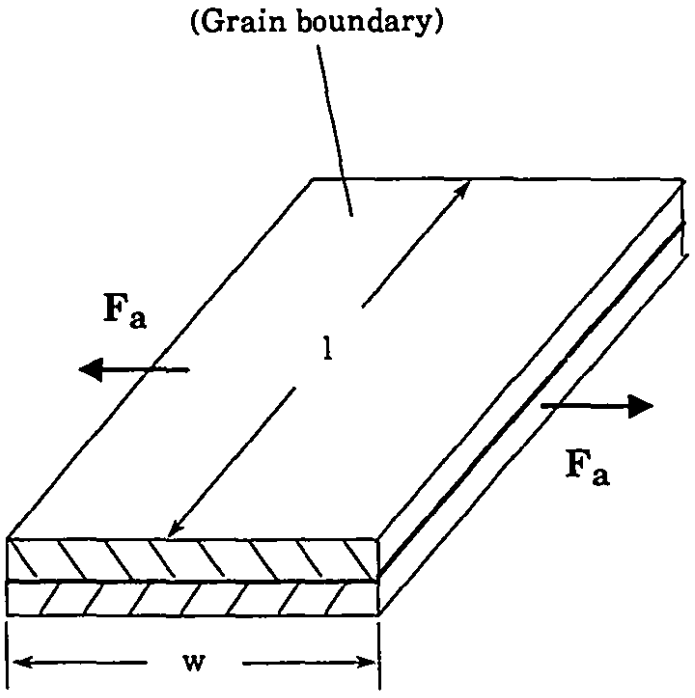

Fig. 8.5 Grain boundary sliding in the absence of precipitates.

distance $a_{\alpha\text{-}Fe}$ but in the opposite direction. As a result, the amount of sliding between the upper and lower boundaries is $2a_{\alpha\text{-}Fe}$. Since the number of atoms in the array is $l/a_{\alpha\text{-}Fe}$, we can write the following equation for the work done by F_a on the atoms during dt:

$$dW = \frac{l}{a_{\alpha\text{-}Fe}} 2\, a_{\alpha\text{-}Fe} F_a = 2\, l F_a \tag{8.12}$$

If the sliding distance during a unit interval of time is $Ka_{\alpha\text{-}Fe}$, then, according to our definition

$$W_o = \frac{l}{a_{\alpha\text{-}Fe}} K a_{\alpha\text{-}Fe} F_a = K l F_a \tag{8.13}$$

where W_0 is the work done during unit time and K is a coefficient that represents the amount of sliding.

8.2.4.2 Work Done in the Presence of Precipitates

Turning now to the case of a boundary containing second phase particles, somewhat similar forms of the work done by the applied force F_a can be obtained. Following Raj and Ashby[161] and for purposes of brevity, only cubic particles, of length s and interparticle spacing λ, are considered here.

Using the same procedure as above, we treat a (λ x w) rectangular boundary (λ > w), as depicted in Figure 8.6. The sliding rate is now changed due to the precipitates so that the boundary is displaced the relative distance ($K^P a_{\alpha\text{-}Fe}$) in unit time. Under otherwise identical conditions, the work done by the applied force on the boundary regions which do not contain the particles takes a form similar to Eq. (8.13):

$$W_o^1 = \frac{(\lambda - s)}{a_{\alpha\text{-}Fe}} K^P a_{\alpha\text{-}Fe} F_a = K^P (\lambda - s) F_a \tag{8.14}$$

Assuming that the inserted particles are impenetrable, the coherency conditions require that the atoms climbing over the particles move a distance s along the particle/boundary interface, while others are sliding a distance $a_{\alpha\text{-}Fe}$. Therefore, the work done on these atoms is

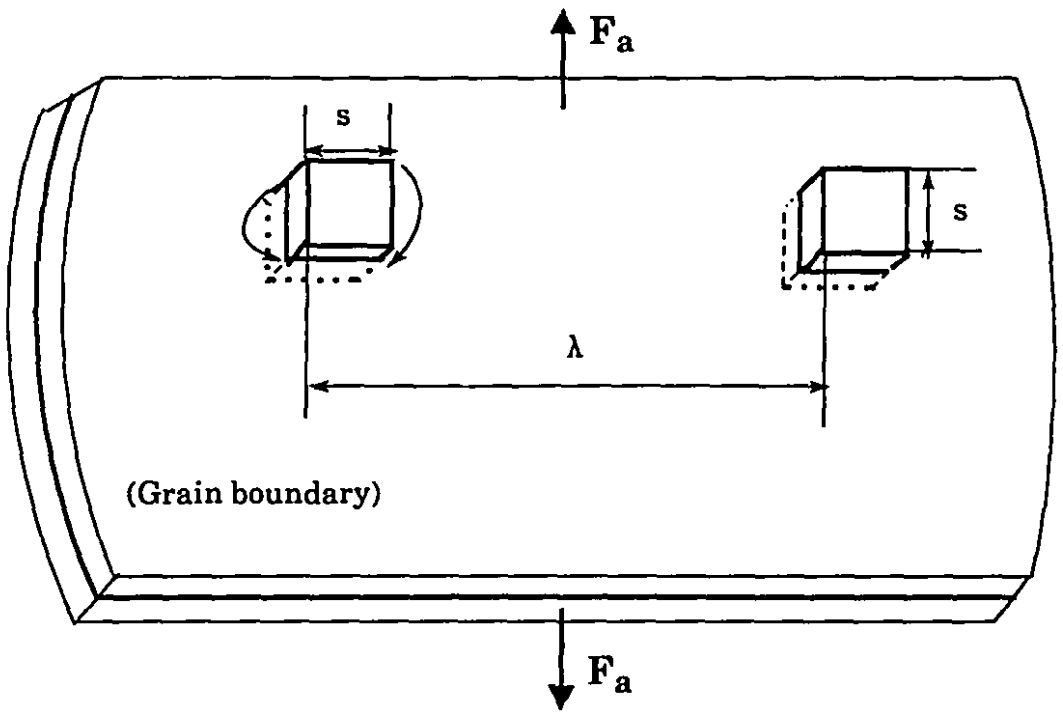

Fig. 8.6 Grain boundary sliding in the presence of precipitates.

$$W_o^2 = \frac{s}{a_{\alpha\text{-}Fe}} K^P s F_a = K^P \frac{s^2}{a_{\alpha\text{-}Fe}} F_a \qquad (8.15)$$

Here W_o^1 indicates the work associated with the atoms unaffected by the particles done in unit time, W_o^2 represents the work associated with the atoms which climb over the particles during the same period, and K^P is the sliding rate coefficient for the particle-containing boundary.

8.2.4.3 Relationship between the Rate of Sliding of a Particle-Free and of a Precipitate-Containing Boundary

We can now consider the relationship between the sliding rate of a particle-free boundary and that of a precipitate-containing boundary. If we let l equal λ in Eq. (8.13), which means that the two boundaries are of the same size, the following relation is obtained:

$$W_o = W_o^1 + W_o^2 \qquad (8.16)$$

We now substitute Eq. (8.13) into the left side and Eqs. (8.14) and (8.15) into the right side of the above equation,

$$K \lambda F_a = K^P (\lambda - s) F_a + K^P \frac{s^2}{a_{\alpha\text{-}Fe}} F_a \qquad (8.17)$$

Thus,

$$\frac{K^P}{K} = \frac{\lambda}{\lambda - s + \dfrac{s^2}{a_{\alpha\text{-}Fe}}} \qquad (8.13)$$

Accordingly, we have

$$\frac{\dot{\varepsilon}_{gb}^{P}}{\dot{\varepsilon}_{gb}} = \frac{U_{gb}^{P}}{U_{gb}} = \frac{\lambda}{\lambda - s + \dfrac{s^2}{a_{\alpha\text{-}Fe}}} \tag{8.19}$$

where $\dot{\varepsilon}_{gb}^{P}$ (U_{gb}^{P}) and $\dot{\varepsilon}_{gb}$ (U_{gb}) are the strain rates (sliding rates) associated with boundary deformation in the presence and in the absence of precipitates, respectively.

It can be seen from the above equation that when "s" is equal to zero (precipitate free), we have:

$$\dot{\varepsilon}_{gb}^{P} = \dot{\varepsilon}_{gb} \tag{8.20a}$$

or

$$U_{gb}^{P} = U_{gb} \tag{8.20b}$$

These expressions describe the experimental results obtained prior to the precipitation start time P_s (for details, see §5.2.4).

Since we always have $s > a_{\alpha\text{-}Fe}$, on the other hand, it can be seen from the denominator of the right side of Eq. (8.19) that

$$\lambda - s + \frac{s^2}{a_{\alpha\text{-}Fe}} = \lambda + s\left(\frac{s}{a_{\alpha\text{-}Fe}} - 1\right) > \lambda \tag{8.21}$$

Comparison between Eqs. (8.19) and (8.21) clearly indicates that the precipitates deposited at grain boundaries always decrease the sliding rate. Moreover, a decrease in the interparticle spacing and an increase in the particle size further amplifies this drag tendency, which trend was indeed displayed by the experimental data obtained in the interval between P_s and P_f.

Checking again the right hand side of Eq. (8.19), we can write that

$$\frac{\lambda}{\lambda - s + \frac{s^2}{a_{\alpha\text{-}Fe}}} = \frac{1}{1 + \frac{s}{\lambda}\left(\frac{s}{a_{\alpha\text{-}Fe}} - 1\right)} \qquad (8.22)$$

It is apparent that the blocking effect of precipitates on boundary sliding is weakened if the interparticle spacing is increased. This is in accordance with the experimental results observed during the coarsening stage of precipitation, in which the interparticle spacing increases due to the dissolution of the smaller particles.

Although this blocking model (Eq. (8.19)) has been shown to be logical and consistent with each stage of precipitation by the above qualitative analyses, its quantitative reliability is now considered below.

8.2.4.4 Application of the Blocking Model

The sliding rate for a precipitate-containing boundary, U_{gb}^{P}, can be estimated using Eq. (8.19) provided the sliding rate of the boundary in the absence of precipitates, U_{gb}, is known. As stated earlier, several successful models have already been developed for evaluating U_{gb} (or $\dot{\varepsilon}_{gb}$) under various experimental conditions. Thus Eq. (8.19) takes different forms for different cases, depending on the models employed for U_{gb} and $\dot{\varepsilon}_{gb}$. Since both $\dot{\varepsilon}_{gb}$ and $\dot{\varepsilon}_{gb}^{P}$ were determined experimentally in the present work (see Figure 5.38, for instance), we can simply compare the observed ratios $\dot{\varepsilon}_{gb}^{P}/\dot{\varepsilon}_{gb}$ with those calculated using Eq. (8.19).

An example is given in Figure 8.7 for electrical steel A stressed at 1000 °C. It is of interest that the experimental values and predictions are in good agreement, providing substantial evidence for the reliability of the present model. It should also be mentioned here that s in Eq. (8.19) was replaced by $s = \sqrt{2}\,\bar{r}$, where $\bar{r}$ is the measured average particle radius.

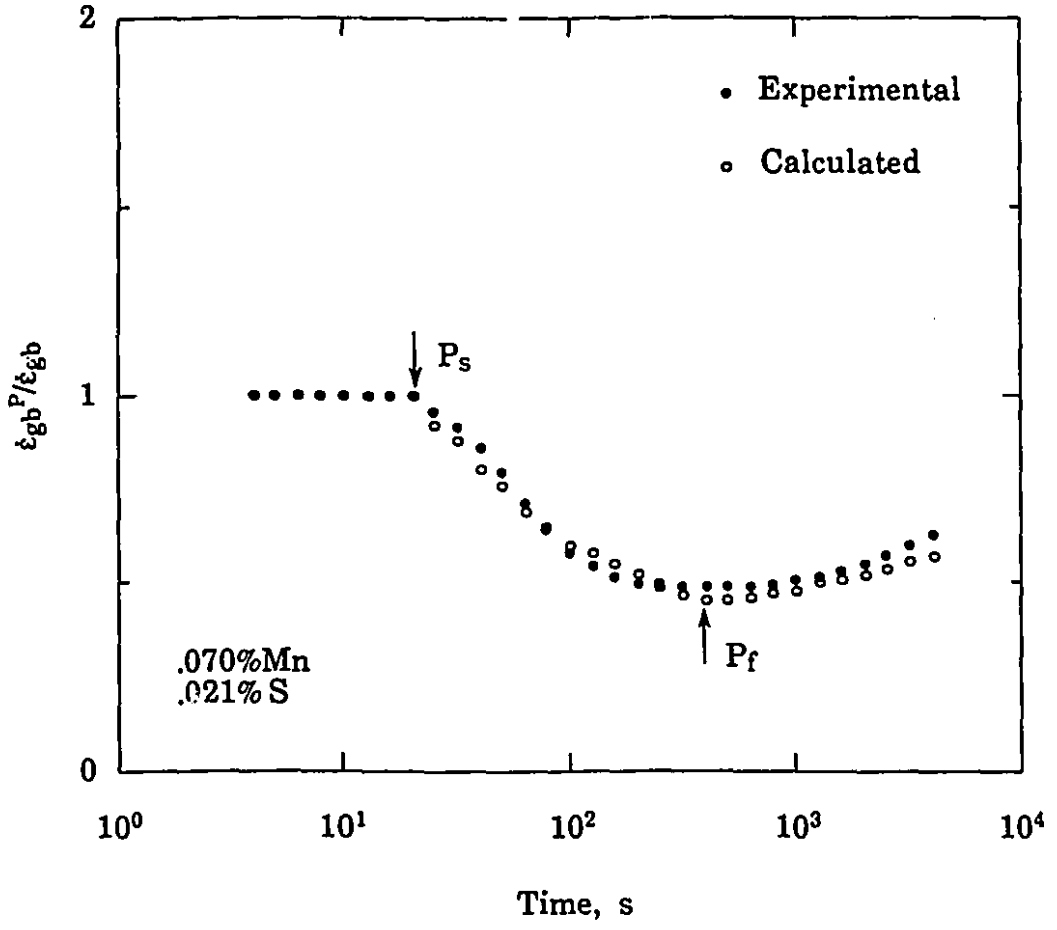

Fig. 8.7 Measured and calculated sliding ratios for 1000 °C for precipitate-containing and particle-free boundaries.

Figure 8.7 also illustrates that the strain rate attributable to boundary sliding is reduced when precipitation takes place and that this reduction is influenced by both the size and the density of the precipitated particles. The deceleration takes place during the interval from P_s to P_f. The amount of the deceleration is reduced after about P_f because of the increase in the interparticle spacing during the stage of competitive growth. The success of this model demonstrates the sensitivity of the present creep technique to

dynamic precipitation at grain boundaries. It can therefore be concluded that this method is suitable for investigating precipitation both on dislocations and at grain boundaries. In the section follows, the applicability and sensitivity of the technique are considered further and compared with that of the earlier stress relaxation technique.

8.3 APPLICABILITY AND SENSITIVITY OF THE CREEP TECHNIQUE

8.3.1 APPLICABILITY OF THE PRESENT CREEP TECHNIQUE FOR DETECTING PRECIPITATION IN FERRITE

As mentioned in Chapter 4, attempts to use the stress relaxation method to detect MnS precipitation in electrical steels have been unsuccessful to date. It is therefore relevant to explore why the creep technique is more suitable than the stress relaxation method for following precipitation in ferritic steels.

It should first be recognized that, during stress relaxation, the sum of the elastic and creep components of the strain (ε_e and ε_c, respectively) are equal to the initial elastic strain, ε_{eo}. Thus, neglecting anelastic effects,

$$\varepsilon_{eo} = \varepsilon_e + \varepsilon_c \tag{8.23}$$

Differentiating,

$$\left(\frac{1}{E^*}\right)\frac{d\sigma_a}{dt} + \dot{\varepsilon}_c = 0 \tag{8.24}$$

where σ_a is the applied stress during stress relaxation and E^* is the combined elastic modulus, defined in terms of the elastic moduli of the specimen (E) and testing machine (E°) as follows:

$$\frac{1}{E^*} = \frac{1}{E} + \frac{1}{E^{\bullet}} \tag{8.25}$$

The analysis of stress relaxation phenomena in physical terms is not simple, but a first approximation can be obtained by relating the creep rate to the effective stress σ* by a power law:[150]

$$\dot{\varepsilon}_c = B^* \sigma^{*n} \tag{8.26}$$

Substituting the above into Eq. (8.24), we get

$$\left(\frac{1}{E^*}\right)\frac{d\sigma_a}{dt} = -B^* \sigma^{*n} \tag{8.27}$$

As

$$\sigma_a = \sigma^* + \sigma_i \tag{8.28}$$

where σ_i is the internal stress of the specimen during stress relaxation, Eq. (8.27) can be transformed into:

$$\left(\frac{1}{E^*}\right)\frac{d\left(\sigma^* + \sigma_i\right)}{dt} = -B^* \sigma^{*n} \tag{8.29}$$

By assuming that the internal stress σ_i is constant during stress relaxation and integrating the above relation, the effective stress at any time t can be expressed as

$$\sigma^* = \frac{\sigma_o^*}{\left[1 + B^* E^* (n-1) \sigma_o^{*n-1} t\right]^{\frac{1}{n-1}}} \tag{8.30}$$

where σ_o^* is the initial value of the effective stress.

The quantitative estimation of σ_i and σ^* requires some input regarding the initial conditions. For this purpose, we first assume that

$$\sigma_{io} \simeq 0.5\ \sigma_{ao} \tag{8.31}$$

where σ_{io} and σ_{ao} are the initial values of the internal and applied stress, respectively. At the very beginning of stress relaxation (t=0), we therefore have

$$\sigma_o^* = \sigma_{ao} - \sigma_{io} = 0.5\ \sigma_{ao} \tag{8.32}$$

Employing the present experimental observations for σ_{ao}, the data for E° reported by Liu[77] and for E, B* and n by Frost and Ashby[214] in the above equations, the applied stresses for electrical steel A and the 0.25% Ti steel were calculated for stress relaxation after a 5% prestrain at 900°C. These are presented together with the experimental results in Figure 8.8.

After comparing the predictions for the Ti steel with the experimental curves obtained in the previous study,[147] it is evident that the assumption that the internal stress σ_i remains approximately constant as stress relaxation proceeds is consistent with the observations. For electrical steel A, however, there is a large difference between the calculated and measured values of the applied stress. Hence, the assumption that the internal stress σ_i is constant and equal to about half of σ_{ao} during stress relaxation is seen to be untenable for ferritic steels. Such steels, like most bcc metals, have higher stacking fault energies than when in the austenitic condition, so that, after straining is interrupted, more recovery is expected during the course of stress relaxation.

The effects of such recovery can be readily evaluated by making some assumptions about the kinetics of the process. For example, the recovery of internal stress can be considered to follow zero-order kinetics, so that

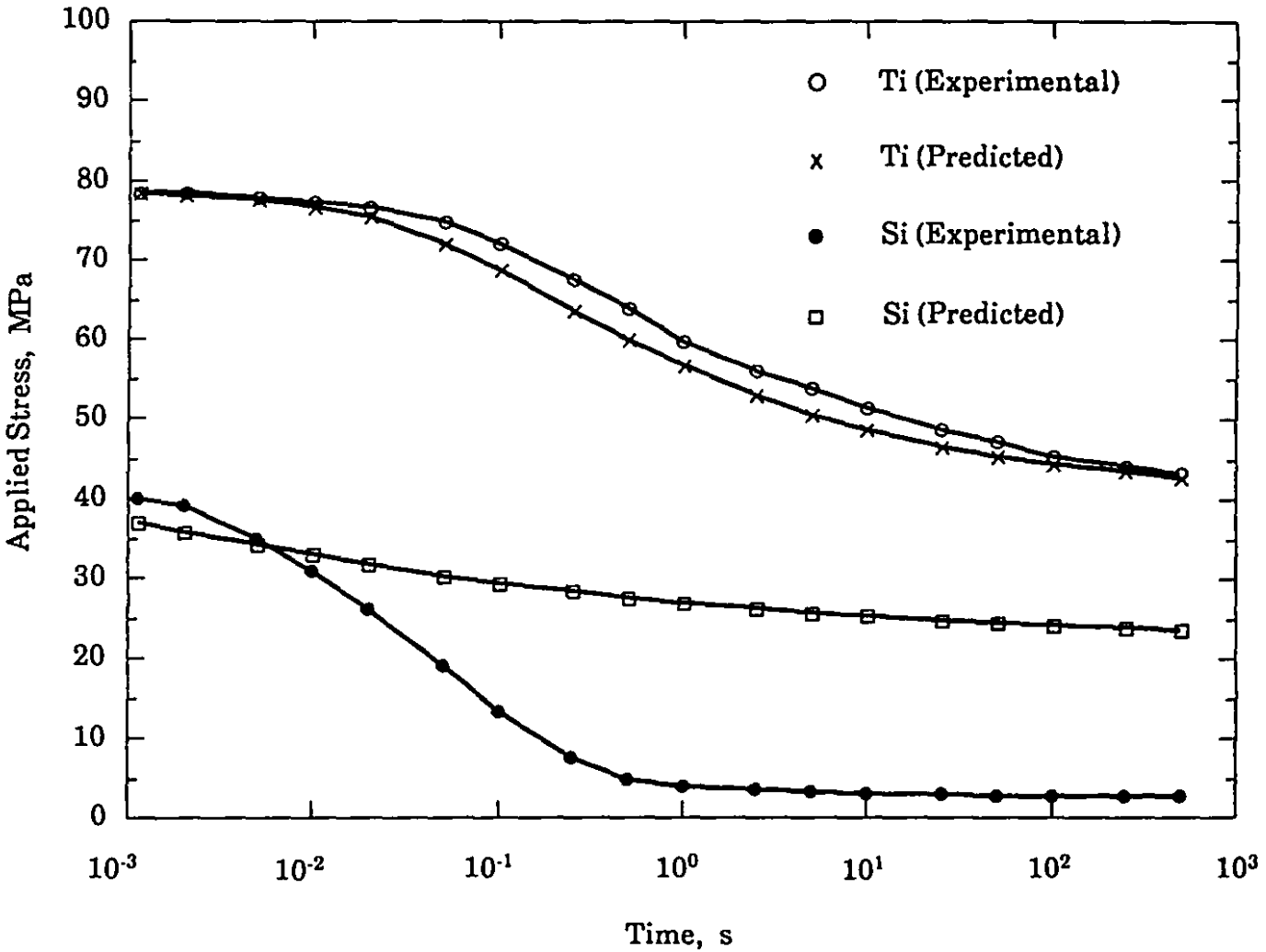

Fig. 8.8 Measured and predicted applied stresses for the relaxation of the 3 % Si and 0.25 % Ti steels after a 5 percent prestrain at 900 °C.

$$\sigma_i = \sigma_{io} - k_o t \tag{8.33}$$

Here k_0 is a zero-order rate constant, and is given by the decrement of internal stress per unit time. Alternatively, if the recovery of internal stress follows first-order kinetics, σ_i takes the form:

$$\sigma_i = \sigma_{io} exp(-k_1 t) \tag{8.34}$$

where k_1 is the first-order rate constant. The substitution of Eqs. (8.33) and (8.34) into Eq. (8.29) leads to

$$\frac{d\sigma^*}{dt} - k_o = - B^* E^* \sigma^{*n} \tag{8.35}$$

and

$$\frac{d\sigma^*}{dt} - k_1 \sigma_{io} exp(-k_1 t) = - B^* E^* \sigma^{*n} \tag{8.36}$$

respectively.

The above equations were solved by the Runge-Kutta method. The results obtained were substituted into Eq. (8.28), leading to the family of applied stress curves presented in Figure 8.9. It is evident that the predicted values match the experimental results when the recovery of internal stress is described by the first-order kinetics model (but not the zero-order model). Thus it appears that the recovery of internal stress is responsible for the rapid decrease in applied stress in the first second in electrical steels. Furthermore, the softening process develops so quickly that the internal stress almost disappears well before the initiation of MnS precipitation (15 seconds at this temperature).

Such an exponential decay of internal stress supports the view that dislocations in ferritic steels are readily annihilated during stress relaxation. Bearing in mind that the detection of precipitation by the stress relaxation

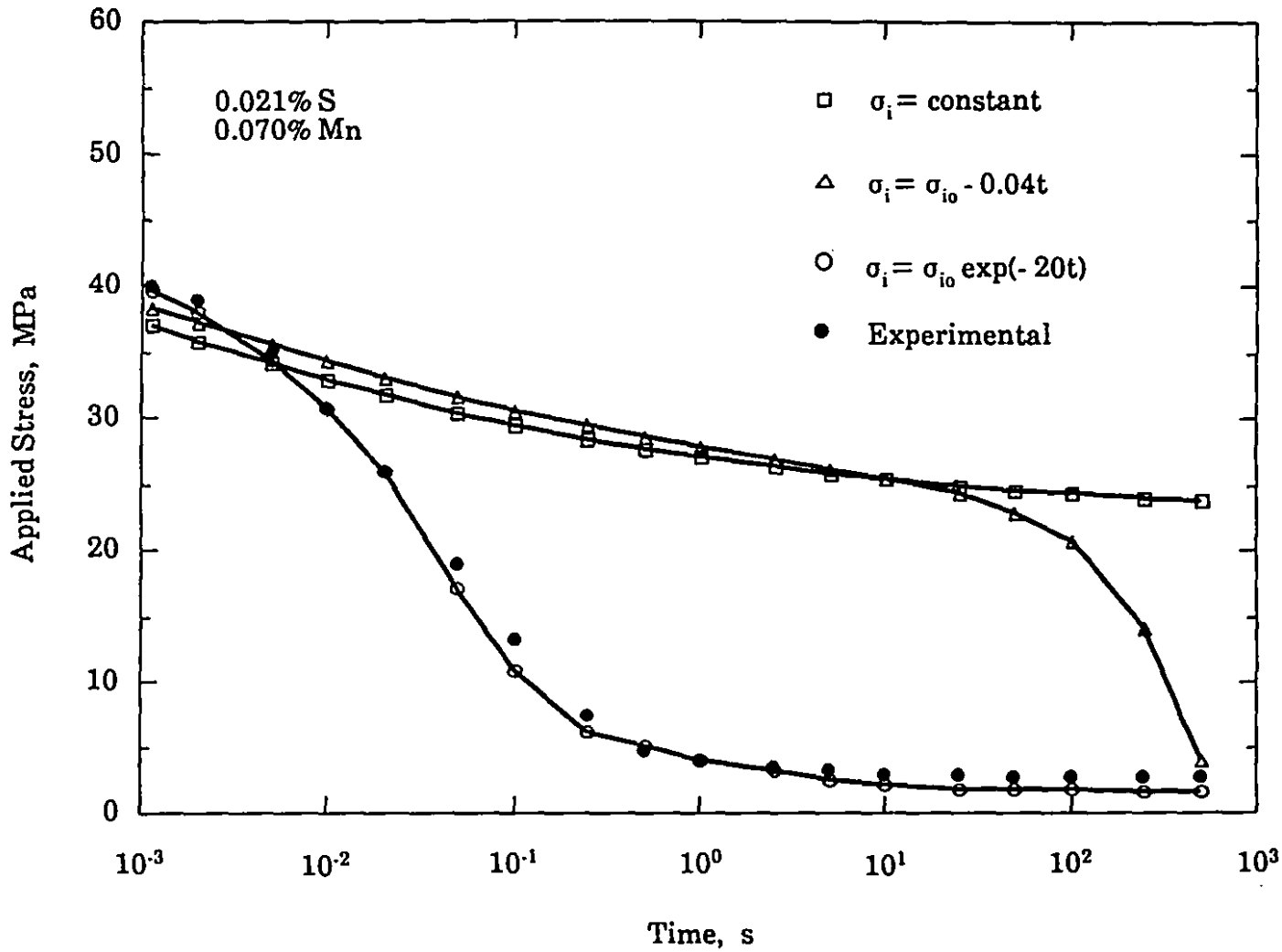

Fig. 8.9 Applied stresses measured and predicted by various models for the relaxation of electrical steel A after a 5 percent prestrain at 900 °C.

method relies on the interaction between precipitates and dislocations,[77, 147] it is clear that the rapid disappearance of dislocations in ferritic steels makes it difficult to use this method in these materials. By contrast, the present creep technique, by holding the stress constant during testing, maintains the dislocation density at a high enough level that the progress of precipitation can be monitored for as long as one hour in ferritic steels, as well as in austenitic steels at elevated temperatures.

8.3.2 COMPARISON OF THE SENSITIVITY OF THE CREEP TECHNIQUE WITH THAT OF THE STRESS RELAXATION METHOD

The PTT diagrams obtained in the present work for the 0.25% Ti steel were already compared with those determined by the stress relaxation method[147] in Figure 5.15 of Chapter 5. It is apparent from this figure that, above 950°C, there is a slight shift to the left in the P_s curve determined by the present technique. Furthermore, the stress relaxation method was not sensitive enough to detect the start and finish of precipitation at 1100°C, whereas the creep technique led to the ready definition of both the P_s and P_f times at the latter temperature. The explanation of these phenomena is the same as that presented above for why the creep method is able to handle ferritic steels. After deformation at temperatures as high as 1100°C, even austenitic steels undergo significant static recovery, during which most of the dislocations within the material are readily annihilated. This inherent shortage of dislocations seems to be a shortcoming of the stress relaxation method. By contrast, dislocations are continuously being generated and recovered during creep. As a result, the creep technique can be employed at higher temperatures than the stress relaxation method, even in austenitic steels.

CHAPTER 9

CONCLUSIONS

In the present investigation, a new mechanical technique was developed to detect precipitation start and finish times in both ferrite and austenite at hot working temperatures. With the help of this technique, PTT diagrams were determined for the first time for strain-induced MnS precipitation in electrical steels, as well as for Ti(CN) precipitation in a 0.25 % Ti steel. Using TEM and SEM, the evolution of the size distribution of the MnS precipitates was also followed. Furthermore, the progress of both grain deformation and grain boundary sliding was observed and evaluated by means of optical microscopy. The experimental results obtained in this way were analyzed in terms of the separate theories of nucleation, growth, and coarsening. Finally, the influence of MnS precipitation on the creep mechanisms operating in electrical steels was discussed, and the sensitivity of the present technique was compared with that of the stress relaxation method. From this work, the following main conclusions can be drawn:

1) During creep testing, the creep rate is sensitive to the occurrence of precipitation; thus, the slope of the creep strain-log(time) curve decreases markedly after the initiation of precipitation and increases on the completion of precipitation. Accordingly, the left and right hand ends of the plateaus on these curves can be identified as the precipitation start and finish times, respectively.

2) The PTT diagrams determined by the present technique for MnS precipitation in electrical steels are generally C-shaped, with the nose at a minimum time of about 9 seconds at 1000 °C for the 0.085% Mn-0.028% S steel, at 12 seconds and 950 °C for the 0.070% Mn-0.021% S steel and at 14 seconds and 950 °C for the 0.125% Mn-0.015% S steel. The P_s and P_f times for the 0.042% Mn-0.004% S steel are detectable solely at and below 900 °C. In addition, the P_f curves obtained here are found to be shifted to shorter times as the Mn concentration is increased.

3) Both deformation within the grains and grain boundary sliding take place during the creep of electrical steels. The latter process contributes about one-sixth to one-tenth the total strain under the current experimental conditions.

4) The following formula can be used for evaluating the chemical driving force for MnS nucleation in ferrite:

$$\Delta G_{chem} = \frac{RT}{2V_m^{MnS}} \left| ln\left(\frac{a_{Mn}^{\alpha e}}{a_{Mn}^{\alpha\infty}}\right) + ln\left(\frac{a_S^{\alpha e}}{a_S^{\alpha\infty}}\right) \right|$$

This equation shows that the driving force decreases monotonically as the temperature is increased and increases as the Mn and S concentrations are increased, agreeing well with the experimental results regarding P_s times.

5) Excess vacancies, which are continuously produced during creep testing, further enhance MnS nucleation on dislocations. In the present tests, the driving force due to the presence of the deformation vacancies is of the same magnitude as the chemical driving force.

6) Comparison between the elastic strain energy and the chemical driving force indicates that the nucleation of MnS in ferrite cannot take place in coherent form. The volume strain energy associated with the embryos is relaxed simultaneously with nucleation, through the introduction of vacancies and/or dislocations into the precipitate/matrix interface. The value of strain energy pertaining to the critical nucleus was calculated. The results reveal that the critical interface has very low coherency, so that the critical strain energy is significantly lower than the chemical driving force.

7) During hot deformation, MnS precipitates nucleate preferentially on dislocations (or dislocation substructures) and at grain boundaries. The reduction in interfacial energy is quite significant in both cases. For example, the mean value of the reduction factors is about 0.57 for nucleation on dislocations and 0.55 for nucleation at grain boundaries. It has also been demonstrated that the critical free energy, or the minimum work required to form a critical nucleus, is higher for nucleation at grain boundaries than for nucleation on dislocations. However, dislocations can provide many more sites for nucleation than grain boundaries, even though the density of the former decreases rapidly with temperature, while the density of the latter remains essentially unchanged as the temperature is varied.

8) The temperature dependence of the MnS precipitation start time can be predicted from the following two models:

$$P_s^{dis} = \frac{\Gamma}{N^{dis} D_{Mn}^{m} X_{Mn}^{\alpha o}} \exp(\Delta G_{dis}^{*}/kT)$$

for nucleation on dislocations, and

$$P_s^{gb} = \frac{\Gamma}{N^{gb} D_{Mn}^{gb} X_{Mn}^{\alpha o}} \exp(\Delta G_{gb}^{*}/kT)$$

for nucleation at grain boundaries. Comparison between the measured and predicted P_S values demonstrated that the nucleation of strain-

induced MnS precipitates on dislocations is more important at lower temperatures, while nucleation at grain boundaries becomes dominant as the temperature is increased.

9) The mean diameter of MnS particles increases with the square root of the growth time between P_s and P_f. This indicates that the growth of MnS precipitates is diffusion controlled. However, the classical rate equation for diffusion-controlled growth does not appear to be valid for such strain-induced precipitation. In this dynamic case, Mn diffusivity D_{Mn} is increased to $(X_v^{eff}/X_v^{\theta})D_{Mn}$ due to the presence of the excess vacancies generated by the deformation.

10) The following expression can be used for predicting the MnS precipitation finish time:

$$P_f = P_s + \frac{1}{K_2^m}\left[\frac{1}{4}\left(\frac{f_v}{\Theta^*}\right)^{\frac{2}{3}} - (r^*)^2\right]$$

where

$$K_2^m = 2D_o \frac{X_{Mn}^{\alpha o} - X_{Mn}^{\alpha e}}{X_{Mn}^{MnS} - X_{Mn}^{\alpha e}} exp\left(-\frac{Q_{Mn} - \eta_e \Delta H_v^f}{RT}\right)$$

$$f_v = f_m \frac{V_m^{MnS}}{V_m^{\alpha-Fe}} = f_m \frac{a_{MnS}^3}{a_{\alpha-Fe}^3}$$

$$r^* = -\frac{2\xi\gamma}{\Delta G_{chem} + \Delta G_e^* + \Delta G_{vac}}$$

11) The coarsening kinetics of MnS precipitates in electrical steels under the present conditions are controlled by both bulk and grain boundary diffusion.

12) Based on the analysis of the interaction between dislocations and MnS particles, the arrest of grain deformation during the interval [P_s, P_f] is considered to be due to the attractive and pinning effects of the precipitates on mobile dislocations. Such pinning arises from the incoherent nature and dynamic character of MnS precipitation. After P_f, the dislocations are unpinned and bypass the coarsening particles by generalized climb.

13) The precipitates nucleated at grain boundaries always reduce the boundary sliding rate. The drag effect exerted on sliding by finely-dispersed *growing* particles is stronger than by sparsely-distributed *coarsening* particles. The relationship between the sliding rate of a particle-free boundary and that of a precipitate-containing boundary can be described as

$$\frac{\dot{\varepsilon}^P_{gb}}{\dot{\varepsilon}_{gb}} = \frac{U^P_{gb}}{U_{gb}} = \frac{\lambda}{\lambda - s + \dfrac{s^2}{a_{\alpha\text{-}Fe}}}$$

14) Recovery rates during stress relaxation obey first-order kinetics in the present ferritic steels and are much higher than in the 0.25% Ti steel tested in the austenite range. The high recovery rates rapidly reduce the dislocation density to levels which are too low for the determination of P_s and P_f times by stress relaxation. By contrast, the present creep method, by maintaining the dislocation density at an appropriate level, is capable of detecting the beginning and end of precipitation in these materials. Comparison between the present technique and the stress relaxation method also shows clearly that the former is more sensitive than the latter when both are employed at high temperatures in the austenite range.

STATEMENT OF ORIGINALITY AND CONTRIBUTION TO KNOWLEDGE

The thermodynamics and kinetics of MnS precipitation were investigated during the hot deformation of electrical steels. The results obtained in this work are of industrial as well as academic interest, and include the following original contributions:

1) Creep testing was employed for the first time to determine precipitation kinetics under hot working conditions. No creep experiments have previously been performed for this purpose. As this study demonstrates, this new technique is accurate and highly sensitive to the initiation and completion of precipitation. Moreover, it is not time consuming, and is more effective in ferrite and at high temperatures than the previous stress relaxation method. Since the specimen continues to strain in the course of precipitation, industrial rolling operations are more closely simulated when this technique is used.

2) PTT diagrams for the strain-induced precipitation of MnS in ferritic steels were obtained experimentally in the present investigation. These are useful for the design of steel processing routes, but, to the author's knowledge, no other investigator has reported such diagrams to date.

3) Through the examination and comparison of the values of elastic strain energy and chemical driving force, it was concluded that the nucleation of MnS in ferrite cannot occur in coherent form. This theoretical

evaluation is simple and avoids the necessity of carrying out electron microscopy to characterize the nucleus/matrix interface.

4) Based on the analysis of the nucleation thermodynamics and kinetics, two physical models were derived for predicting the start times of MnS precipitation, one on dislocations and the other on grain boundaries. Although the model for nucleation on dislocations is similar to those proposed recently by Dutta and Sellars[118] as well as by Liu and Jonas,[120] the current analysis includes quantitative evaluations of the chemical driving force and volume strain energy, as well as of the effect of deformation vacancies, the precipitate interfacial energy and the nucleation site density. Thus it describes the physical situation more completely. In addition, this approach does not require the fitting of experimental P_s data, which is an advantage over the previous models. Furthermore, the grain boundary model developed in this study appears to be the first one applicable to precipitation taking place at grain interfaces.

5) With the aid of electron microscopy and the above two P_s models, it was demonstrated for the first time that MnS precipitates preferably on dislocations at lower temperatures but at grain boundaries at higher temperatures. This finding not only leads to good agreement with the experimental results obtained by the present technique, but also suggests a practicable way of improving steel properties. As grain boundary sliding becomes more dominant at high temperatures, the method indicates how the high temperature creep resistance of steels can be improved by introducing suitable second phase particles.

6) It was shown in a quantitative manner that the classical diffusion-controlled growth model is not suited to MnS precipitation during hot deformation. As a result, an effective diffusivity $(X_V^{eff}/X_V^{\theta})D_{Mn}$ was introduced in the present study. This new treatment can be of considerable interest for investigating the growth kinetics of strain-induced or dynamic precipitation, provided that diffusion is rate controlling.

7) A new type of model was developed to predict the finish time of MnS precipitation. The predictions of this model are in acceptable agreement with the present experimental data. Thus, this model may be of general utility for estimating P_f times for other precipitate species.

8) The coarsening of MnS particles at hot working temperatures was found to be controlled by both bulk and grain boundary diffusion. Such a finding does not seem to have been previously published.

9) The interaction between MnS precipitation and dislocations was investigated, leading to the conclusion that two mechanisms are responsible for the observed behavior: i) the interfacial pinning of mobile dislocations by dynamically-precipitated incoherent particles, which plays a key role between P_s and P_f; and ii) the generalized climb of dislocations, which is important following their unpinning after P_f. The deformation behavior occurring within grains after the initiation of precipitation was satisfactorily explained by the combination of these two mechanisms. One of the important features of this analysis is that additional energy is needed to recreate the line tension of the dislocation segment lying in the interface. This additional energy acts as an internal stress increment and reduces the creep rate.

10) In an original analysis, an energy conservation model was proposed for describing the blocking effects exerted on grain boundary sliding by dynamic precipitation. By means of this model, the relationship between the sliding rate of a particle-free boundary and that of a precipitate-containing boundary can be estimated quantitatively.

11) It was shown that recovery rates during the stress relaxation of electrical steels obey first-order kinetics. Such an investigation has not been previously carried out on ferritic steels.

REFERENCES

1. R.A. Hadfield, W.F. Barrett and W.J. Brown: *Inst. Elect. Eng.*, 1902, vol. 31, p. 674.

2. Z. Zhao: *Plastic Deformation of Metals and Rolling Theory*, Metallurgical Industry Press, Beijing, China, 1980, pp. 80-88.

3. T.B. Massalski, J.L. Murray, L.H. Bennett and H. Baker: *Binary Alloy Phase Diagrams*, vol. 2, ASM, Ohio, 1986, p. 1108.

4. K.I. Arai and K. Ohmori: *Metall. Trans. A*, 1986, vol. 17A, pp. 1295-99.

5. Y. Shimizu, Y. Ito and Y. Iida: *Metall. Trans. A*, 1986, vol. 17A, pp. 1323-34.

6. N.P. Goss: *Trans. Am. Soc. Metals*, 1935, vol. 23, p. 511.

7. K.J. Sixtus: *Physics*, 1935, vol. 6, p. 105.

8. R.M. Bozorth: *Trans. Am. Soc. Metals*, 1935, vol. 23, p. 1107.

9. J.E. May and D. Turnbull: *J. Appl. Phys.*, 1959, vol. 30, pp. 210s-12s.

10. J.R. Brown: *J. Appl Phys.*, 1958, vol. 29, p. 359.

11. H.C. Fiedler: *J. Appl. Phys.*, 1958, vol. 29, p.361.

12. H.C. Fiedler: *Metall. Trans. A*, 1977, vol. 8A, pp. 1307-11.

13. N.C. Pease, D.W. Jones, M.H.L. Wise and W.B. Hutchinson: *Met. Sci.*, 1981, vol. 15, pp. 203-09.

14. S. Mishra, C.Därmann and K. Lücke: *Acta Metall.*, 1984, vol. 32, pp. 2185-2201.

15. A.R. Büchner and H.D. Kemnitz: *Z. Metallkd.*, 1984, vol. 75, pp. 423-31.

16. Q. Lü, R. Shuai, X. Zhou and X. Zhao: *Acta Metall. Sin.*, 1981, vol. 17, pp. 58-66.

17. Y. Inokuti, C. Maeda and Y. Ito: *Trans. Iron Steel Inst. Jpn.*, 1987, vol. 27, pp. 139-44.

18. Z. He, Z. Liu, B. Zhang and W. Zhang: *Acta Metall. Sin.*, 1981, vol. 17, pp. 433-40.

19. R.L. Gershman and V.Ya. Gol'dshteyn: *Phys. Met. Metall.*, 1983, vol. 55, pp. 178-82.

20. T.H. Shen: *Metall. Trans. A*, 1986, vol. 17A, pp. 1347-51.

21. J.W. Shilling and G.L. Houze: *IEEE Trans. Magn.*, 1974, vol. 10, p. 195.

22. A. Ferro and G.P. Soardo: *J. Magn. Magn. Mater.*, 1980, vol. 19, p. 6.

23. M.F. Littman: *J. Magn. Magn. Mater.*, 1982, vol. 41, p. 1.

24. F. Assmus, K. Detert and G. Ibe: *Z. Metallkd.*, 1957, vol. 48, p. 344.

25. S. Taguchi, A. Sakakura and H. Takachima: US Patent 3 287 183, 1966.

26. S. Taguchi, T. Wada, T.Yamamoto, F. Matsumoto, A. Sakakura and K. Ueno: *Nippon Steel Tech. Rep. Overseas no. 4*, 1973.

27. K. Takashima, T. Sato and F. Matsumoto: *AIP Conf. Proc.*, 1975, vol. 29, p. 566.

28. S. Wada, S. Shimizu and S. Taguchi: *Proc. EPS Conf.*, Cardiff, 1975, p. 37.

29. I. Goto, I. Matoba, T. Imanaka, T. Gotoh and T. Kan: *EPS Conf.*, Cardiff, 1975, p. 262.

30. H. Shimanaka, I. Matoba, T. Ichida, S. Kabayashi and T. Funahashi: *EPS Conf., Cardiff*, 1975, p. 269.

31. Kawasaki Steel Corporation: Japanese Patent 118 524, 1972.

32. Kawasaki Steel Corporation: French Patent 2 213 344, 1973.

33. J.M. Jackson: US Patent 3 873 381, 1975.

34. H.E. Grenoble: *IEEE Trans. Magn.*, 1977, vol. 13, p. 1427.

35. H.C. Fiedler: *IEEE Trans. Magn.*, 1977, vol. 13, p. 1433.

36. A.J. Moses: *J. Magn. Magn. Mater.*, 1980, vol. 19, p. 36.

37. K.C. Liao: *Metall. Trans. A*, 1986, vol. 17A, pp. 1259-66.

38. S.S. Gorelik and I.A. Popova: *Phys. Met. Metall.*, 1984, vol. 58, pp. 169-73.

39. G. Abbruzzese and M. Barisoni: *J. Magn. Magn. Mater.*, 1986, vols. 54-57, pp. 1621-22.

40. S. Mishra, C. Därmann and K. Lücke: *Metall. Trans. A*, 1986, vol. 17A, pp. 1301-12.

41. E.R. Termer and V.Ya. Gold'shteyn: *Izv. Akad. Nauk. SSSR, Fiz.*, 1989, vol. 53, pp. 666-70.

42. M. Matsuo, T. Sakai and Y. Suga: *Metall. Trans. A*, 1986, vol. 17A, pp. 1313-22.

43. J.W. Schoen: *Metall. Trans. A*, 1986, vol. 17A, pp. 1335-46.

44. P. Horky and P. Pácl: *J. Magn. Magn. Mater.*, 1984, vol. 41, pp. 14-16.

45. H.A. Wriedt: *Metall. Trans. A*, 1980, vol. 11A, pp. 1731-35.

46. J. Harase, R. Shimizu and N. Takahashi: *Acta Metall.*, 1990, vol. 38, pp. 1849-56.

47. Z. He, X. Sun and R. Shuai: *Acta Metall. Sin.*, 1985, vol. 21, pp. A126-30.

48. K.C. Liao: *Metall. Trans. A*, 1986, vol. 17A, pp. 1259-66.

49. J. Harase, R. Shimizu, K, Takashima and T. Watanabe: *Trans. Iron Steel Inst. Jpn.*, 1987, vol. 27, pp. 965-73.

50. W.M. Swift: *Metall. Trans.*, 1973, vol. 4, pp. 841-45.

51. B.N. Balandin, B.K. Sokolov and V.V. Gubernatorov: *Fiz. Met. Metalloved.*, 1980, vol. 49, pp. 590-95.

52. S.V. Pashchenko, V. Ya. Gol'dshteyn, R.L. Gershman and S.G. Nitskaya: *Phys. Met. Metall.*, 1984, vol. 58, pp. 95-99.

53. W.P. Sun: *The Effects of Manganese Sulfide on Recrystallization in Silicon Steels*, Research Report, McGill University, Montreal, Canada, 1987.

54. G. Lyudkovsky and P.D. Southwick: *Metall. Trans. A*, 1986, vol. 17A, pp. 1267-75.

55. H.G. Lee, H.B. Im and Y.G. Kim: *Metall. Trans. A*, 1986, vol. 17A, pp. 1353-59.

56. B.K. Sokolov: *Fiz. Metalloved.*, 1977, vol. 43, p. 1028.

57. B.N. Balandin, B.K. Sokolov and V.V. Gubernatorov: *Fiz. Met. Metalloved.*, 1980, vol. 49, p. 590.

58. V.Ya. Gol'dshteyn, O.P. Bobkova and S.G. Nitskaya: *Fiz. Met. Metalloved.*, 1982, vol. 54, pp. 512-17.

59. G. Abbruzzese and S. Fortunati: *J. Appl. Phys.*, 1988, vol. 64, pp. 5344-46.

60. R.W.K. Honeycombe: *The Plastic Deformation of Metals*, Edward Arnold Ltd., Frome and London, 1984, pp. 180-98.

61. R. Kiessling and N. Lange: *Non-metallic Inclusions in Steel*, The Metals Society, London, 1978, Part II, pp. 97-145.

62. A. Muan and E.F. Osborn: *Phase Equilibria among Oxides in Steelmaking*, Reading, Mass., Addison-Wesley, 1965, p. 8.

63. S. Eketorp: *J. Iron Steel Inst.*, 1966, vol. 204, pp. 194-202.

64. N. G. Ainslie and A.U. Seybolt: *J. Iron Steel Inst.*, 1960, vol. 194, pp. 341-50.

65. H.C. Fiedler: *Trans. Met. Soc. AIME*, 1967, vol. 239, pp. 260-63.

66. J.R. Brown: *J. Iron Steel Inst.*, 1967, vol. 205, pp. 154-57.

67. H.A. Wriedt and H. Hu: *Metall. Trans. A*, 1976, vol. 7A, pp. 711-18.

68. G.S. Mann and L.H. Van Vlack: *Metall. Trans. B*, 1976, vol. 7B, pp. 469-75.

69. K. Iwayama and T. Haratani: *J. Magn. Magn. Mater.*, 1980, vol. 19, p. 15-17.

70. E.F. Petrova, A.I. Rogov, V.G. Borisenko, A.G. Petrenko, A.A. Kononov and L.A. Shvartsman: *Russ. Metall.*, 1976, pp. 117-22.

71. C.E. Sims and F.B. Dahle: *Trans. A.F.A.*, 1938, vol. 46, pp. 65-132.

72. R. Kiessling, S. Bergh and N. Lange: *J. Iron Steel Inst.*, 1962, vol. 200, pp. 965-67.

73. V. Radmilovic, G. Thomas, G.J. Shiflet and E.A. Starke, Jr.: *Scripta Metall.*, 1989, vol. 23, pp. 295-300.

74. L.F. Mondolfo: *Mater. Sci. Technol.*, 1989, vol. 5, pp. 118-22.

75. M. Militzer and A.N. Orlov: *Scripta Metall.*, 1989, vol. 23, pp. 1173-76.

76. L. Cheng and E.J. Mittemeijer: *Metall. Trans. A*, 1990, vol. 21A, pp. 13-26.

77. W.J. Liu: Ph.D. Thesis, McGill University, Montreal, 1987.

78. M. Djahazi: Ph.D. Thesis, McGill University, Montreal, 1989.

79. S.Q. Xiao, P.-J. Wilbrandt and P. Haasen: *Scripta Metall.*, 1989, vol. 23, pp. 295-300.

80. R.D. Naybour: *Acta Metall.*, 1965, vol. 13, p. 1197.

81. J.M. Silcock: *J. Iron Steel Inst.*, 1973, vol. 211, p. 792.

82. A.T. Davenport, R.E. Miner and R.A. Kot: *The Hot Deformation of Austenite*, J.B. Ballance ed., AIME, New York, NY, 1977, pp. 186-203.

83. G. Fitzsimons, K. Tiitto, R. Fix and A.J. DeArdo: *Metall. Trans. A*, 1984, vol. 15A, pp. 241-43.

84. I. Weiss and J.J. Jonas: *Metall. Trans. A*, 1980, vol. 11A, p. 403.

85. J.M. Silcock and W.J. Tunstall: *Philos. Mag.*, 1964, vol. 10, p. 361.

86. E. Nes: *Acta Metall.*, 1974, vol. 22, p. 81.

87. W. Kesternich: *Philos. Mag.*, 1985, vol. 52, p. 533.

88. A.R. Jones, P.R. Howell and B. Ralph: *J. Mater. Sci.*, 1976, vol. 11, p. 1593.

89. D.V. Edmonds and R.W.K. Honeycombe: *Precipitation Processes in Solids*, K.C. Russell and H.I. Aaronson, eds., AIME, 1978, p. 121.

90. D. Hamana and M. Benabdoun: *Philos. Mag. A*, 1985, vol. 52, pp. L25-28.

91. Y.P. Lin and G.C. Smith: *J. Mater. Sci.*, 1988, vol. 23, pp. 2485-94.

92. P. Czurratis, R. Kroggel and H. Löffler: *Z. Metallkd.*, 1988, vol. 79, pp. 307-12.

93. L. Chang and D. Gan: *Mater. Sci. Eng.*, 1987, vol. 95, pp. 125-36.

94. S.M. Bruemmer, L.A. Charlot, A. Bagchi and D.G. Atteridge: *Scripta Metall.*, 1989, vol. 23, pp. 1549-54.

95. C.L. Briant: *Mater. Sci. Technol.*, 1989, vol. 5, pp. 138-47.

96. A.W. James and C.M. Shepherd: *Mater. Sci. Technol.*, 1989, vol. 5, pp. 333-45.

97. N.Y. Tang, D.M.R. Taplin, G.L. Dunlop and A. Plumtree: *Creep and Fracture of Engineering Materials and Structures*, B.Wilshire and D.R.J. Owen, eds., Pineridge Press, Swansea, 1984, vol. 1, p. 235.

98. J. Zhang and Z. Cao: *Acta Metall. Sin.*, 1988, vol. 24, p. A111.

99. J.E. Harris: *J. Mater. Sci.*, 1973, vol. 7, p. 1.

100. R. Bonnet and A. Ati: *Acta Metall.*, 1989, vol. 37, p. 2153-69.

101. J.J. Irani and R.T. Weiner: *J. Iron Steel Inst.*, 1965, vol. 203, p. 913.

102. J.P. Shepherd: *Met. Sci.*, 1976, vol. 10, p. 174.

103. D.B. Rayaprolu and A. Hendry: *Mater. Sci. Technol.*, 1989, vol. 5, pp. 328-32.

104. J.-L. Strudel: *Physical Metallurgy*, R.W. Cahn and P. Haasen, eds., North-Holland, Amsterdam, 1983, pp.1411-86.

105. J.W. Martin: *Micromechanisms in Particle-Hardened Alloys*, Cambridge University Press, 1980.

106. V.A. Phillips and J.D. Livingston: *Philos. Mag.*, 1962, vol. 7, p. 969.

107. L.G. Bonar and A. Kelly: *Fifth Int. Cong. for Electron Microscopy*, Academic Press, New York, 1962, vol. 1, p. K11.

108. J.W. Matthews: *Dislocations in Solids*, F.R.N. Nabarro, ed., North-Holland, Amsterdam, 1973, vol. 2, pp. 461-545.

109. J.L. Walter, H.E. Cline and E.F. Koch: *Trans. AIME*, 1969, vol. 245, p. 2073.

110. G.C. Weatherly and R.B. Nicholson: *Philos. Mag.*, 1968, vol. 17, p. 801.

111. M. Avrami: *J. Chem. Phys.*, 1939, vol. 7, p. 1103; 1940, vol. 8, p. 212.

112. S.J. Harris and N.R. Nag :*J. Mater. Sci.*, 1975, vol. 10, p. 1137 & 1976, vol. 11, p. 1320.

113. J.W. Cahn: *Acta Metall.*, 1956, vol. 4, pp. 449-572.

114. J.W. Christian: *The Theory of Transformations in Metals and Alloys*, 2nd edition, Pergamon Press, 1975.

115. M. Volmer and H. Flood: *Z. Phys. Chem.*, 1934, vol. 170, p. 273.

116. K.C. Russell: *Advances Colloid and Interface Science*, 1980, vol. 13, pp. 205-318.

117. H.I. Aaronson and J.K. Lee: *Lectures on the Theory of Phase Transformations*, H.I. Aaronson, ed., TMS, 1986, pp. 83-115.

118. B. Dutta and C.M. Sellars: *Mater. Sci. Technol.*, 1987, vol. 3, pp. 197-206.

119. S.Q. Xiao and P. Haasen: *Scripta Metall.*, 1989, vol. 23, pp. 365-70.

120. W.J. Liu and J.J. Jonas: *Metall. Trans. A*, 1989, vol. 20A, p. 689-97.

121. I.M. Lifshitz and V.V. Slyozov: *J. Phys. Chem. Solids*, 1961, vol. 19, pp. 35-50.

122. C. Wagner: *Z. Elektrochem.*, 1961, vol. 65, p. 581.

123. R.D. Doherty: *Physical Metallurgy*, R.W. Cahn and P. Haasen, eds., North-Holland, Amsterdam, 1983, pp. 933-1030.

124. Y.-F. Han, P. Deb and M.C. Chaturvedi: *Met. Sci.*, 1982, vol. 16, pp. 555-61.

125. P.W. Voorhees: *Metall. Trans. A*, 1990, vol. 21A, pp. 27-37.

126. H.O.K. Kirchner: *Metall. Trans.*, 1971, vol. 2, pp. 2861-64.

127. I. Pontikakos and H. Jones: *Met. Sci.*, 1982, vol. 16, pp. 27-30.

128. K.C. Russell and F.H. Froes: *Scripta Metall.*, 1988, vol. 22, pp. 495-99.

129. A.J. Ardell: *Acta Metall.*, 1972, vol. 20, p. 601.

130. M. Kreye: *Z. Metallkd.*, 1970, vol. 61, p. 108.

131. G.L. Wang: Ph.D. Thesis, McGill University, Montreal, PQ, Canada, 1990.

132. M. Djahazi, X.L. Hé and J.J. Jonas: *Metall. Trans. A*, 1990, vol. 21A, in press.

133. T.M. Hoogendoorn and M.H. Spanraft: *Micro-alloying 75*, M. Korchynsky, ed., Union Carbide Corp., New York, 1977, pp. 75-85.

134. S.S. Hansen, J.B. Vander Sande, and M. Cohen: *Metall. Trans. A*, 1980, vol. 11A, pp. 387-402.

135. A. LeBon, J. Rofes-Vernis and C. Rossard: *Mem. Sci. Rev. Met.*, 1975, vol. 11A, p. 411.

136. S. Yamamoto, C. Ouchi and T. Osuka: *Thermomechanical Processing of Micro-alloyed Austenite*, P.J. Wray and A.J. DeArdo, eds., AIME, Warrendale, PA, 1982, pp. 613-39.

137. O. Popoola, M.F. Denanot, P. Moine, J.P. Villain, M. Cahoreau and J. Caisso: *Acta Metall.*, 1989, vol. 37, pp. 867-76.

138. K.A. Taylor, G.B. Olson, M. Cohen and J.B. Vander Sande: *Metall. Trans. A*, 1989, vol. 20A, pp. 2749-65.

139. U.K. Viswanathan, P.K.K. Nayar and R. Krishnan: *Metar. Sci. Technol.*, 1989, vol. 5, pp. 346-49.

140. M. Prikryl, Y. P. Lin and S.V. Subramanian: *Scripta Metall.*, 1990, vol. 24, pp. 375-380.

141. R. Simoneau, G. Begin and A.H. Marquis: *Met. Sci.*, 1978, vol. 12, pp. 381-86.

142. U.K. Viswanathan, P.K.K. Nayar and R. Krishnan: *Mater. Sci. Technol.*, 1989, vol. 5, pp. 346-49.

143. C.Y. Xie, L.C. Zhao and T.C. Lei: *Scripta Metall.*, 1989, vol. 23, pp. 2131-36.

144. I. Weiss and J.J. Jonas: *Metall. Trans. A*, 1979, vol. 10A, p. 831.

145. J.J. Jonas and I. Weiss: *Met. Sci.*, 1979, vol. 13, p. 238.

146. R.K. Amin, G. Butterworth and F.B. Pickering: *Hot Working and Forming Processing*, C.M. Sellars and G.L. Davies, eds., Sheffield, England, 1980, p. 27.

147. W.J. Liu and J.J. Jonas: *Metall. Trans. A*, 1988, vol. 19A, pp. 1403-13.

148. W.P. Sun, W.J. Liu and J.J. Jonas: *Metall. Trans. A*, 1989, vol. 20A, pp. 2707-15.

149. A.J. Kennedy: *Processes of Creep and Fatigue in Metals*, Oliver and Boyd, Edinburgh, Great Britain, 1962, pp. 147-280.

150. I. LeMay: *Principles of Mechanical Metallurgy*, Elsevier North-Holland, New York, NY, 1981, pp. 87-134 & pp. 337-58.

151. J. Weertman and J.R. Weertman: *Physical Metallurgy*, R.W. Cahn and P. Haasen, eds., North-Holland, Amsterdam, 1983, pp.1309-40.

152. P. Gondi and A. Sili: *Scripta Metall.*, 1987, vol. 21, pp. 1393-98.

153. E.N. Andrade: *Proc. Roy. Soc.*, 1910, vol. A84, p. 1.

154. E.N. Andrade: *Philos. Mag.*, 1962, vol. 7, p. 2003.

155. F.R.N. Nabarro: *Report on a Conference on the Strength of Solids*, Phys. Soc., London, 1948, p. 75.

156. C. Herring: *J. Appl. Phys.*, 1950, vol. 21, pp. 437.

157. G.J. Weng: *J. Appl. Mech. (Trans. ASME)*, 1987, vol. 54, pp. 822-27.

158. J.R. Dryden, D. Kucerovsky, D.S. Wilkinson and D.F. Watt: *Acta Metall.*, 1989, vol. 37, pp. 2007-15.

159. M. Haghi and L. Anada: *Metall. Trans. A*, 1990, vol. 21A, pp. 353-72.

160. R.O. Williams: *Acta Metall.*, 1957, vol. 5, p. 55.

161. R. Raj and M.F. Ashby: *Metall. Trans.*, 1971, vol. 2, pp. 1113-27.

162. S. Chevacharoenkul and R.F. Davis: *Acta Metall.*, 1989, vol. 37, pp. 417-27.

163. W.O. Powers and J.A. Wert: *Metall. Trans. A*, 1990, vol. 21A, pp. 145-51.

164. J. Rösler and E. Artz: *Acta Metall.*, 1990, vol. 38, pp. 671-83.

165. A.G. Evans and R.D. Rawlings: *Phys. Stat. Solidi*, 1969, vol. 34, p. 9.

166. J. Courbon, M. Ignat and F. Louchet: *Acta Metall.*, 1990, vol. 38, pp. 663-70.

167. D. Kuhlmann-Wilsdorf: *Physical Metallurgy*, R.W. Cahn, ed., North-Holland, Amsterdam, 1970, pp.787-856.

168. N.F. Mott: *Creep and Fracture of Metals at High Temperatures*, Her Majesty's Stationery Office, London, 1956, p. 21.

169. T. Mori, M. Koda R. Monzen and T. Mura: *Acta Metall.*, 1983, vol. 31, pp. 275-83.

170. K.J. Kurzydlowski and A. Garbacz: *Philos. Mag. A*, 1985, vol. 52, pp. 689-97.

171. G.B. Gibbs: *Mater. Sci. Eng.*, 1967/68, vol. 2, pp. 269-72.

172. M.F. Ashby and R.A. Verrall: *Acta Metall.*, 1973, vol. 21, pp. 149-63.

173. S. Onaka, M. Kato and T. Mori: *Metall. Trans. A*, 1986, vol. 17A, pp. 1949-53.

174. M.S. Kim, S. Hanada, S. Watanabe, and O. Izumi: *J. Mater. Sci.*, 1990, vol. 25, pp. 1590-97.

175. J.H. Schneibel and G.F. Petersen: *Acta Metall.*, 1985, vol. 33, pp. 437-42 & pp. 1255-76.

176. F.J. Humphreys: *Dislocations and Properties of Real Materials*, Proc. Conf. to Celebrate the 50th Anniversary of the Concept of the Dislocation in Crystals, The Institute of Metals, London, 1985, p. 175.

177. E. Orowan: *Symposium on Internal Stresses in Metals and Alloys, The Institute of Metals, London, 1948, p. 451.*

178. R.W. Evans and B. Wilshire: *Creep of Metals and Alloys*,The Institute of Metals, Swansea, U.K., 1985, pp. 1-36.

179. B. Wilshire and R.W. Evans: *Creep Behaviour of Crystalline Solids*, Pineridge Press, Swansea, U.K., 1985, pp. 83-135.

180. G.C. Saha, M. Blum and P. Rama Rao: *Scripta Metall.*, 1981, vol. 15, p. 657.

181. P.D. Portella: Ph.D. Thesis, University of Erlangen-Nürnberg, 1984.

182. R.A. Petkovic: Ph.D. Thesis, McGill University, Montreal, 1975.

183. M.G. Akben: Ph.D. Thesis, McGill University, Montreal, 1980.

184. M.J. Luton: Ph.D. Thesis, McGill University, Montreal, 1971.

185. J.F. Alder and V.A. Phillips: *J. Inst. Met.*, 1954-55, vol. 83, pp. 80-86.

186. M.F. Ashby and R. Ebeling: *Trans AIME*, 1966, vol. 236, p. 1396.

187. D. McLean: *J. Inst. Metals*, 1951-52, vol. 80, p. 507 & 1952-53, vol. 81, pp. 133-293.

188. A.C. Zettlemoyer: *Nucleation*, Marcel Deker, New York, 1969.

189. C.C. Dollins: *Acta Metall.*, 1970, vol. 18, p. 1209-15.

190. H.I. Aaronson and K.R. Kinsman: *Scripta Metall.*, 1970, vol. 4, pp. 101-06.

191. Des Venugopalan: *Metall. Trans.* A, 1990, vol. 21A, pp. 913-18.

192. J.H. Noggle: *Physical Chemistry*, Little, Brown & Company, Boston, 1985, pp. 302-62.

193. J.P. Morris and A.J. Williams, Jr.: *Trans. A.S.M.*, 1949, vol. 41, pp. 1425-39.

194. J.P. Morris and R.C. Buehl: *Trans. AIME*, 1950, vol. 188, pp. 317-22.

195. J.P. Morris: *J. Met.*, 1952, vol. 4, pp. 939-40.

196. C.W. Sherman and J. Chipman: *J. Met.*, 1952, vol. 4, pp. 597-602.

197. R. Hultgren, R.L. Orr, P.D. Anderson and K.K. Kelly: *Selected Values of Thermodynamic Properties of Metals and Alloys*, John Wiley, New York, 1963, p. 726.

198. L.S. Darken, R.W. Gurry and M.B. Bever: *Physical Chemistry of Metals*, McGraw-Hill Inc., New York, 1953, pp. 235-82.

199. C. Wagner: *Thermodynamics of Alloys*, Addison-Wesley, Reading, Massachusetts, 1962, p. 51.

200. C.H.P. Lupis and J.F. Elliott: *Acta Metall.*, 1966, vol. 14, pp. 529-38.

201. G.K. Sigworth and J.F. Elliott: *Met. Sci.*, 1974, vol. 8, pp. 529-38.

202. A.D. Pelton and C.W. Bale: *Metall. Trans.* A, 1986, vol. 17A, pp. 1211-15.

203. E.J. Turkdogan, S. Ignatowicz and J. Pearson: J. *Iron Steel Inst.*, 1955, vol. 180, pp. 349-54.

204. F.R.N. Nabarro: *Proc. Phys. Soc.*, 1940, vol. 52, pp. 90-104.

205. E. Kröner: *Acta Metall.*, 1954, vol. 2, pp. 302-09.

206. N.F. Mott and F.R.N. Nabarro: *Phys. Soc.*, 1940, vol. 52, pp. 86-89.

207. F. Laszlo: *J. Iron Steel Inst.*, 1950, vol. 164, pp. 5-26.

208. J.D. Eshelby: *Proc. Phys. Soc.*, 1957, vol. A241, pp. 376-96.

209. J.W. Christian: *The Theory of Transformations in Metals and Alloys*, 2nd ed., Pergamon Press, Oxford, 1975, p. 200.

210. D.M. Barnett: *Scripta Metall.*, 1971, vol. 5, pp. 261-66.

211. D.M. Barnett, J.K. Lee, H.I. Aaronson and K.C. Russell: *Scripta Metall.*, 1974, vol. 8, pp.1447-50.

212. C.J. Smithells and E.A. Brandes: *Metals Reference Book*, vol. 1, 5th ed., Butterworths, London & Boston, 1978, pp. 115-77 & pp. 186-241.

213. H.M. Ledbetter and R.P. Reed: *J. Phys. Chem. Ref. Data*, vol. 2, 1973, p. 531.

214. H.J. Frost and M.F. Ashby: *Deformation-Mechanism Maps*, Pergamon Press, Oxford, 1982, pp. 20-70.

215. H.J. Wollenberger: *Physical Metallurgy*, R.W. Cahn and P. Haasen eds., 3rd ed., North-Holland Physics Publishing, Amsterdam, 1983, pp. 1139-1221.

216. H.-E. Schaefer, K. Maier, M. Weller, D. Herlach, A. Seeger and J. Diehl: *Scripta Metall.*, 1977, vol. 11, pp. 803-09.

217. H. Matter, J. Winter and W. Triftshauser: *Appl. Phys.*, 1979, vol. 20, p.135.

218. E.W. Hart: *Acta Metall.*, 1958, vol. 6, p. 553.

219. H.A. Holl: *J. Met. Sci.*, 1967, vol. 1, p. 111.

220. K.C. Russell: *Scripta Metall.*, 1969, vol. 3, pp. 313-16.

221. R.E. Smallman: *Modern Physical Metallurgy*, 4th ed., Butterworth & Co Ltd., London, 1985, pp. 289-334.

222. G. Saada: *Physica*, 1961, vol. 27, p. 657.

223. J. Takamura: *Physical Metallurgy*, R.W. Cahn ed., North-Holland Physics Publishing, Amsterdam, 1965, pp. 681-733.

224. R. Gibala and C.A. Wert: *Diffusion in Body-Centered Cubic Metals*, ASM, Metals Park, Ohio, 1965, pp. 131-48.

225. D. Turnbull: *Impurities and Imperfections*, ASM, Cleveland, 1955, p. 121.

226. J.H. Van de Merwe: *J. Appl. Phys.*, 1963, vol. 34, pp. 117-22 & pp. 123-27.

227. L.H. Van Vlack: *J. Met.*, 1951, vol. 3, pp. 251-59.

228. J.W. Gibbs: *The Scientific Papers of J.W. Gibbs*, vol. 1, Longmans, Green and Co., New York, 1906, p. 252.

229. L. Onsager: *Phys. Rev.*, vol. 37, 1931, p. 405.

230. J.W. Cahn: *Acta Metall.*, 1957, vol. 5, pp. 169-72.

231. R. Gomez-Ramirez and G.M. Pound : *Metall. Trans.*, 1973, vol. 4, pp. 1563-70.

232. F. Larché: *Dislocations*, F.R.N. Nabarro ed., Elsevier North-Holland, New York, 1979, p. 135.

233. K.A. Taylor and S.S. Hansen: *Metall. Trans.* A, 1990, vol. 21A, pp. 1697-1708.

234. J.W. Cahn and D.W. Hoffman: *Acta Metall.*, 1974, vol. 22, p. 1205.

235. J.K. Lee and H.I. Aaronson: *Acta Metall.*, 1975, vol. 23, pp. 799-809.

236. W.C. Johnson, C. White, P. Marth, P. Ruf, S. Tuomenen, K.D. Wade, K.C. Russell and H.I. Aaronson: *Metall. Trans.* A, 1975, vol. 6A, pp. 911-19.

237. J. Weertman and J.R. Weertman: *Physical Metallurgy*, R.W. Cahn and P. Haasen, eds., North-Holland, Amsterdam, 1983, pp. 1259-1307.

238. P. Gilormini, B. Bacroix and J.J. Jonas: *Acta Metall.*, 1988, vol. 36, pp. 231-56.

239. K.R. Kinsman, J.W. Sprys and R.J. Asaro: *Acta Metall.*, 1975, vol. 23, p. 1431.

240. J.K. Lee, Y.Y. Earmme, H.I. Aaronson and K.C. Russell: *Metall. Trans. A*, 1980, vol. 11A, pp. 1837-47.

241. W.J. Liu and J.J. Jonas: *Mater. Sci. Technol.*, 1989, vol. 5, pp. 8-12.

242. J. Askill: *Handbook of Chemistry and Physics*, R.C. Weast and M.J. Astle, eds., 62nd edition, CRC Press Inc., Boca Raton, Florida, 1982, pp. F54-64.

243. J.L. Bocquet, G. Brébec and Y. Limoge: *Physical Metallurgy*, R.W. Cahn and P. Haasen, eds., North-Holland, Amsterdam, 1983, pp. 385-475.

244. G. de Wit and J.S. Koehler: *Phys. Rev.*, 1959, vol. 116, p. 1113.

245. Y.T. Chou and J.D. Eshelby: *J. Mech. Phys. Sol.*, 1962, vol. 10, p. 27.

246. L.M. Brown: *Philos. Mag.*, 1964, vol. 10, p. 441.

247. P. de Chatel and I. Kovacs: *Phys. Stat. Sol.*, 1965, vol. 10, p. 213.

248. M.F. Ashby: *Acta Metall.*, 1966, vol. 14, p. 679.

249. P. Haasen: *Physical Metallurgy*, R.W. Cahn and P. Haasen, eds., North-Holland, Amsterdam, 1983, pp. 1341-1407.

250. P.G. Shewmon: *Transformations in Metals*, McGraw-Hill, New York, 1969, pp. 286-321.

251. A. Kelly and M.E. Fine: *Acta Metall.*, 1957, vol. 5, p. 365.

252. L.M. Brown and R.K. Ham: *Strengthening Methods in Crystals*, A. Kelly and R.B. Nicholson eds., John Wiley & Sons Inc., New York, 1971, pp. 9-135.

253. R.S.W. Shewfelt and L.M. Brown: *Philos. Mag.*, 1974, vol. 30, pp. 1135-45.

254. R.S.W. Shewfelt and L.M. Brown: *Philos. Mag.*, 1977, vol. 35, pp. 945-62.

255. R.A. Stevens and P.E.J. Flewitt: *Acta Metall.*, 1981, vol. 29, pp. 867-82.

256. D.J. Srolovitz, M.J. Luton, R. Petkovic-Luton, D.M. Barnett and W.D. Nix: *Acta Metall.*, 1984, vol. 32, pp. 1079-88.

257. G.S. Ansell and J. Weertman: *Trans. AIME*, 1959, vol. 215, p. 838.

258. R. Lagneborg: *Scripta Metall.*, 973, vol. 7, p. 605.

259. E. Arzt and M.F. Ashby: *Scripta Metall.*, 1982, vol. 16, p. 1285.

260. F.N. Rhines, W.E. Bond and M.A. Kissel: *Trans. Amer. Soc. Met.*, 1956, vol. 48, p. 919.

261. N.F. Mott: *Proc. Phys. Soc.*, 1948, vol. 60, p. 391.

262. T.S. Ko: *J. Appl. Phys.*, 1949, vol. 20, p. 274.

263. S. Ranganathan: *Acta Cryst.*, 1966, vol. 21, p. 197.

264. R.S. Gates: *Acta Metall.*, 1973, vol. 21, pp. 855-64.

265. F. Weinberg: *Trans. Amer. Inst. Min. Met. Engrs.*, 1958, vol. 212, p. 808.

266. R.L. Bell and N.W.B. Thompson: *Nature*, 1962, vol. 190, p. 363.

267. B. Burton: *Acta Metall.*, 1978, vol. 26, pp. 1237-41.

268. R.C. Gifkins and K.U. Snowdon: *Trans. AIME*, 1967, vol. 239, pp. 910-15.

269. T.S. Kê: *Phys. Rev.*, 1947, vol. 71, p. 533.

270. H. Gleiter, E. Hornbogen and G. Baro: *Acta Metall.*, 1968, vol. 16, pp. 1053-67.

271. H. Kokawa, T. Watanabe and S. Karashima: *Philos. Mag. A*, 1981, vol. 44, pp. 1239-54.

272. J.S. Zhang, P.E. Li, W.X. Chen and J.Z. Jin: *Scripta Metall.*, 1989, vol. 23, pp. 547-51.

APPENDIX I

LISTING OF THE COMPUTER PROGRAM FOR MONITORING PRECIPITATION BY CREEP TESTING

```
MPC                MTS  BASIC   V01B-02D

100      DIM  A(250), B(150), K(150), W(150), H(20), X0(250), Y0(250),
         X1(250), Y1(250)
110      L$(0) = "TEST #"
120      L$(1) = "SOLUTION TEMPERATURE (°C)"
130      L$(2) = "TEST TEMPERATURE (°C)"
140      L$(3) = "STROKE RANGE (MM)"
150      L$(4) = "LOAD RANGE (KG)"
160      L$(5) = "TEST TIME (SECOND)"
170      L$(6) = "COOLING TIME (SECOND)"
180      L$(7) = "STRESS (MPA)"
190      L$(8) = "LENGTH OF SPECIMEN (MM)"
200      L$(9) = "DIAMETER OF SPECIMEN (MM)"
210      L$(10) = "LCM #"
220      PRINT "TEST (1) OR RECALL (2)"; \INPUT C
230      IF C<>2 THEN 270
240      PRINT "DIFFERENCE (3) OR NORMAL (4)"; \INPUT D
250      IF D=4 THEN 270
260      PRINT L$(10); \INPUT M$
270      PRINT L$(0); \INPUT N$
280      PRINT "DAY,MONTH,YEAR:"; \INPUT H(17), H(18), H(19)
         \PRINT
290      PRINT "C, MN, S, SI:"; \INPUT H(13), H(14), H(15), H(16) \PRINT
300      FOR I=0 TO 125 \K(I)=0 \W(I)=1 \NEXT I
310      D0=0.169 \T0=D0
320      IF C=1 THEN 370
330      GOSUB 2090
```

```
340     IF D=3 THEN GOSUB 2160
350     H(5)=INT(H(5)*D0/100)*100
360     GO TO 400
370     FOR I=1 TO 9
380     PRINT L$(I); \INPUT H(I)
390     PRINT \NEXT I
400     D=(LOG10(H(5))-LOG10(D0))/125
410     FOR I=1 TO 125
420     T1=10^(LOG10(D0)+I*D)
430     K(I)=INT((T1-T0)/D0)+K(I-1)+1
440     T0=T1 \NEXT I
450     H(5)=D0*K(I)
460     K(0)=0
470     MSW1(2)
480     GOSUB 1670
490     IF C<>1THEN 1080
500     PRINT "CHECK: STROKE CONTROL → DC ERR=0 → R/L=R →
        SPAN 1=0"
510     INPUT F$
520     REM                 DUMP CHECK
530     EDMP
540     SDMP(1, A) \IF A=0 THEN 570
550     PRINT "DUMP CARD PROBLEM"
560     STOP
570     FG1(0)
580     PRINT "TURN ON HYD=HIGH → SPAN 1 =10 → LOAD=ZERO"
590     INPUT F$
600     DACQ(0, Q1, 0, 0) \DACQ(0, S1, 2, 0)
610     PRINT Q1
620     IF ABS(Q1)<500/H(4) THEN 630 \GO TO 580
630     PRINT "GET INTO POSITION 5 MINUTES BEFORE TEST"
        \INPUT F$
640     FOR I=1 TO 500
650     I2=S0-I
660     FG1(I2)
670     GOSUB 1860
```

```
680     IF Q<-5000/H(4) THEN 710
690     NEXT I
700     PRINT "CHECK THE SAMPLE" \STOP
710     T0=0 \S0=S
720     PRINT "RETURN AS COOLING STARTS"; \INPUT F$
730     T6=0
740     GOSUB 1860
750     IF Q<-1000/H(4) THEN 760 \GO TO 770
760     IF Q>-10000/H(4) THEN 790 \GO TO 780
770     I2=I2-1 \GO TO 800
780     I2=I2+1 \GO TO 800
790     I2=I2+0 \GO TO 800
800     FG1 (I2)
810     T6=T6+0.169 \IF T6>H(6) THEN 850
820     GO TO 740
830     GOSUB 1860
840     IF Q<-H(7)*2047/H(4) THEN 860
850     I2=I2-1 \FG1(I2) \GO TO 830
860     GOSUB 1860 \S0=S
870     FOR I=0 TO 125
880     GOSUB 1860
890     IF Q<-H(7)*2047/H(4) THEN 900 \GO TO 910
900     IF Q>-H(7)*1.01*2047/H(4) THEN 930 \GO TO 920
910     I2=I2-1 \GO TO 940
920     I2=I2+1 \GO TO 940
930     I2=I2+0 \GO TO 940
940     FG1(I2)
950     T0=T0+1 \IF T0<K(I) THEN 880
960     A(I)=S \A(126+I)=Q
970     IF I<>0 THEN 980 \T0=0 \PRINT " *** TEST IS RUNNING
        *** "
980     NEXT I
990     PRINT " *** TEST HAS TERMINATED *** " \PRINT
1000    DACQ(0, S4, 2, 0)
1010    FOR I=S4 TO 0
1020    FG1(I) \NEXT I
```

```
1030    PRINT "TURN OFF THE HYD"
1040    INPUT F$
1050    FOR I=1 TO 125
1060    A(I)=A(I)-S0
1070    NEXT I
1080    W0=1
1090    REM ------------------------------------------------------------------------
1100    REM                    DATA MANAGEMENT
1110    REM ------------------------------------------------------------------------
1120    PRINT "TEST TIME" H(5)
1130    PRINT "ENTER TIME SCALE"; \INPUT X1, X8
1140    PRINT "ENTER TIME INTERVAL"; \INPUT U1
1150    PRINT "TRUE STRAIN" LOG(H(8)/(H(8)+A(125)*H(3)/2047))
1160    PRINT "ENTER LENGTH SCALE"; \INPUT Y1, Y2
1170    PRINT "ENTER LENGTH INTERVAL"; \INPUT V1
1180    X$="TIME (SECOND)" \Y$="TRUE STRAIN"
1190    J=0
1200    FOR I=1 TO 125
1210    PRINT A(I), B(I)
1220    NEXT I
1230    INPUT F$
1240    GOSUB 1780
1250    FOR I=1 TO 125
1260    X=D0*K(I) \X0(I)=X
1270    X1(I)=LOG10(X)
1280    Z=LOG(H(8)/(H(8)+(A(I)-B(I))/2047*H(3)))
1290    Y0(I)=Z \NEXT I
1300    FOR I=2 TO 124
1310    X=D0*K(I)
1320    Y=(Y0(I+1)-Y0(I-1))/(X0(I+1)-X0(I-1)) \Y1(I)=Y
1330    IF W(I)=0 THEN 1350
1340    CNTR(2) \PLOT(X,Y) \PLOT(X,Y)
1350    NEXT I \IF W0=1 THEN 1370
1360    CNTR(2) \PLOT (X1,Y1) \J0=1
1370    GOSUB 1940
1380    INPUT P$
```

```
1390    PRINT "ENTER 1ST DERIVATIVE SCALE"; \INPUT Y1, Y2, V1
1400    Y$="1ST DERIVATIVE"
1410    J=0 \GOSUB 1780
1420    FOR I=126 TO 175
1430    X=D0*K(I-125) \Y=-1.5E-3*A(I)/2047*H(4)
1440    X0(I)=X \Y1(I)=Y
1450    CNTR(2) \PLOT(X,Y) \PLOT(X,Y) \NEXT I
1460    FOR I=176 TO 224
1470    X=D0*K(I-125) \Y=-5*A(I)/I/2047/I*H(4)
1480    X0(I)=X \Y1(I)=Y
1490    CNTR(2) \PLOT(X,Y) \PLOT(X,Y) \NEXT I
1500    FOR I=225 TO 250
1510    X=D0*K(I-125) \Y=-2.5E-8*I*I*A(I)/2047*H(4)
1520    X0(I)=X \Y1(I)=Y
1530    CNTR(2) \PLOT(X,Y) \PLOT(X,Y) \NEXT I
1540    INPUT P$
1550    FOR I=1 TO 250
1560    PRINT X0(I), LOG10(X0(I)), Y0(I), Y1(I)
1570    NEXT I
1580    INPUT Q$
1590    PRINT "DO YOU WANT TO SAVE THE DATA?"; \INPUT F$
1600    IF F$="YES" THEN 1630
1610    PRINT "ARE YOU SURE?"; \INPUT G$
1620    IF G$="YES" THEN 1640
1630    GOSUB 2010
1640    STOP
1650    END
1660    REM     SUBROUTINE FOR CHECKING TEST CONDITIONS
1670    CNTR(3)
1680    PRINT "CREEP TEST FOR FOLLOWING PRECIPITATION"
        \PRINT
1690    PRINT L$(0); N$
1700    PRINT L$(10); M$
1710    PRINT "C="H(13); "MN="H(14); "S="H(15); "SI="H(16)
1720    PRINT "DAY/MONTH/YEAR:" H(17)"/"H(18)"/"H(19)
1730    PRINT
```

```
1740    FOR I=1 TO 9
1750    PRINT L$(I) "IS"; H(I)
1760    PRINT \NEXT I
1770    RETURN
1780    REM     SUBROUTINE FOR GRAPHICS
1790    CNTR(3) \CNTR(0)
1800    PHYL(100, 900, 80, 700)
1810    SCAL(J, X1, X8, Y1, Y2)
1820    AXES(X8, Y2)
1830    AXES(X1, Y1)
1840    LABL(X$, Y$, U1, V1, 0)
1850    RETURN
1860    REM     SUBROUTINE FOR CHECKING PISTON POSITION
1870    Q=0 \S=0
1880    FOR J0=1 TO 20
1890    DACQ(0, Q1, 0, 0) \DACQ(0, S1, 2, 0)
1900    Q=Q+Q1 \S=S+S1
1910    NEXT J0
1920    Q=Q/20 \S=S/20
1930    RETURN
1940    REM     SUBROUTINE ROR COMMENTS
1950    CPOS(X0, Y) \D=Y2/25
1960    CNTR(1)
1970    COMM(L$(0), X0, Y) \PRINT N$
1980    COMM(L$(1), X0,Y – D) \PRINT H(1)
1990    COMM(L$(2),X0, Y – 2*D) \PRINT H(2)
2000    RETURN
2010    REM     SUBROUTINE FOR SAVING DATA
2020    H(5)=INT(H(5)/D0+0.5) \H(6)=INT(H(6)/D0+0.5)
2030    H(7)=S0*10 \H(8)=A(0)*10
2040    FOR I=1 TO 125 \A(I)=A(I)*10 \NEXT I
2050    OPEN "DX1:" &N$ FOR OUTPUT AS FILE #1
2060    AOUT(H, 1, 0, E1)
2070    AOUT(A, 1, 1, E2)
2080    CLOSE #1 \RETURN
2090    REM     SUBROUTINE FOR RECALLING TEST DATA
```

```
2100    OPEN "DX1:" &N$ FOR INPUT AS FILE #1
2110    AINP(H, 1, 0, E1)
2120    AINP(A, 1, 1, E2)
2130    CLOSE #1
2140    FOR I=1 TO 125 \A(I)=A(I)/10 \NEXT I
2150    RETURN
2160    REM     SUBROUTINE FOR RECALLING LCM DATA
2170    OPEN "DX1:" &M$ FOR INPUT AS FILE #1
2180    AINP(H, 1, 0, E1)
2190    AINP(B, 1, 1, E2)
2200    CLOSE #1
2210    FOR I=1 TO 125 \B(I)=B(I)/10 \NEXT I
2220    RETURN
2230    FOR I=0 TO 125
2240    PRINT K(I); \NEXT I
```

APPENDIX II

LISTING OF THE COMPUTER PROGRAM FOR MEASURING FLOW STRESS

```
MFS                MTS  BASIC   V01B-02D

100      DIM X(25), T(1000), H(25), X0(140), Y0(140)
110      L$(0) = "TEST #"
120      L$(2) = "TEST TEMPERATURE (°C)"
130      L$(3) = "STROKE RANGE (MM)"
140      L$(4) = "LOAD RANGE (KG)"
150      L$(5) = "STRAIN"
160      L$(6) = "STRAIN RATE (1/SECOND)"
170      L$(7) = "LENGTH OF THE SPECIMEN (MM)"
180      L$(8) = "DIAMETER OF THE SPECIMEN (MM)"
190      PRINT "TEST (1) OR RECALL (2)"; \INPUT C
200      PRINT L$(0); \INPUT N$
210      IF C=2 THEN GOSUB 1770 \GO TO 230
220      PRINT "DAY, MONTH, YEAR"; \INPUT H(10), H(11), H(12)
         \PRINT
230      FOR I=2 TO 8
240      PRINT L$(I); \INPUT H(I)
250      PRINT \NEXT I
260      IF C=2 THEN 350
270      D0=0.0155
280      N=INT(H(7)*(1-EXP(-H(5)))*2047/H(3))
290      N9=INT(N/100) \IF N9<=1 THEN N9=N9+1
300      X0=INT(N/N9+1) \Y0=X0 \N=N9*(X0-1)
310      FOR I=1 TO N
320      T(I)=LOG((H(7)*2047/H(3)-I+1)/(H(7)*2047/H(3)-I-1))/H(6)
330      T(I)=INT(T(I)/D0)
340      NEXT I
```

```
350     GOSUB 1280
360     MSW1(2)
370     IF C<>1 THEN 920
380     PRINT "CHECK: STROKE CONTROL → DC ERR=0 → R/L=R →
        SPAN 1=0"
390     INPUT F$
400     REM                 DUMP CHECK
410     EDMP
420     SDMP(1, A) \IF A=0 THEN 450
430     PRINT "DUMP CARD PROBLEM"
440     STOP
450     FG1(0)
460     PRINT "TURN ON HYD=HIGH → SPAN 1 =10 → LOAD=ZERO"
470     INPUT F$
480     DACQ(0, Q1, 0, 0) \DACQ(0, S1, 2, 0)
490     IF ABS(Q1)<500/H(4) THEN 500 \GO TO 460
500     PRINT "GET INTO POSITION BEFORE HEATING" \INPUT F$
510     FOR I=1 TO 500
520     I2=1-I
530     FG1(I2)
540     N0=20\GOSUB 1450
550     IF Q<-5000/H(4) THEN 580
560     NEXT I
570     PRINT "CHECK THE SAMPLE" \STOP
580     T0=0
590     PRINT "INPUT HEATING TIME (SECOND)" \INPUT T9
600     PRINT "RETURN AS HEATING STARTS"; \INPUT F$
610     T6=0
620     N0=20 \GOSUB 1450
630     IF Q <-1000/H(4) THEN 640 \GO TO 650
640     IF Q>-10000/H(4) THEN 670 \GO TO 660
650     I2=I2-1\GO TO 680
660     I2=I2+1\GO TO 680
670     I2=I2+0\GO TO 680
680     FG1(I2)
690     T6=T6+0.169 \IF T6>T9 THEN 710
```

```
700     GO TO 620
710     IF F$="OVER" THEN GO TO 780
720     PRINT "MORE TIME FOR HEATING" \INPUT F$
730     IF F$<>"YES" THEN GO TO 760
740     PRINT "INPUT THE EXTRA TIME" \INPUT T9
750     GO TO 610
760     PRINT "INPUT SOAKING TIME (SECOND)" \INPUT T9
770     F$="OVER" \GO TO 610
780     N0=20 \GOSUB 1450 \S0=S
790     I3=N9-1 \I4=0
800     PRINT " *** TEST IS RUNNING *** "
810     FOR I=1 TO N
820     I3=I3+1
830     I2=I2-1 \FG1(I2)
840     NO=T(I) \GOSUB 1450
850     IF I3<>N9 THEN 880
860     I4=I4+1
870     X0(I4)=S-S0 \Y0(I4)=Q \I3=0
880     NEXT I
890     PRINT " *** TEST HAS TERMINATED *** " \PRINT
900     PRINT "TURN OFF THE HYD"
910     INPUT F$
920     REM ------------------------------------------------------------------------
930     REM                    DATA MANAGEMENT
940     REM ------------------------------------------------------------------------
950     L=H(7)+X0(I4)*H(3)/2047
960     PRINT L$(5); ":"; H(5)
970     PRINT "ENTER STRAIN SCALE"; \INPUT X1, X8
980     PRINT "ENTER STRAIN INTERVAL"; \INPUT U1
990     PRINT "STRESS (MPA)";
        -Y0(I4)/2047*H(4)*9.8*L/H(7)/H(8)/H(8)*4/PI
1000    PRINT "ENTER STRESS SCALE"; \INPUT Y1, Y2
1010    PRINT "ENTER STRESS INTERVAL"; \INPUT V1
1020    X$="TRUE STRAIN" \Y$="TRUE STRESS"
1030    J=0
1040    GOSUB 1370
```

```
1050    FOR I=1 TO I4
1060    L=H(7)+X0(I)*H(3)/2047
1070    X=LOG(H(7)/L)
1080    Y=-Y0(I)/2047*H(4)*9.8*L/H(7)/H(8)/H(8)*4/PI
1090    CNTR(2)\PLOT(X,Y)\PLOT(X,Y)
1100    NEXT I
1110    CNTR(2)
1120    GOSUB 1530
1130    INPUT P$
1140    CNTR(3)
1150    FOR I=1 TO I4
1160    L=H(7)+X0(I)*H(3)/2047
1170    PRINT LOG(H(7)/L),
        -Y0(I)/2047*H(4)*9.8*L/H(7)/H(8)/H(8)*4/PI
1180    NEXT I
1190    INPUT Q$
1200    PRINT "DO YOU WANT TO SAVE THE DATA?";\INPUT F$
1210    IF F$="YES" THEN 1250
1220    PRINT "ARE YOU SURE?";
1230    INPUT G$
1240    IF G$="YES" THEN 1260
1250    GOSUB 1600
1260    STOP
1270    END
1280    REM     SUBROUTINE FOR CHECKING TEST CONDITIONS
1290    CNTR(3)
1300    PRINT L$(0); N$
1310    PRINT "DAY/MONTH/YEAR:" H(10)"/"H(11)"/"H(12)
1320    PRINT
1330    FOR I=2 TO 8
1340    PRINT L$(I) "IS"; H(I)
1350    PRINT\NEXT I
1360    RETURN
1370    REM     SUBROUTINE FOR GRAPHICS
1380    CNTR(3)\CNTR(0)
1390    PHYL(100, 900, 80,700)
```

```
1400    SCAL(J, X1, X8, Y1, Y2)
1410    AXES(X8, Y2)
1420    AXES(X1, Y1)
1430    LABL(X$, Y$, U1, V1, 1)
1440    RETURN
1450    REM     SUBROUTINE FOR CHECKING PISTON POSITION
1460    Q=0 \S=0
1470    FOR J0=1 TO N0
1480    DACQ(0, Q1, 0, 0) \DACQ(0, S1, 2, 0)
1490    Q=Q+Q1 \S=S+S1
1500    NEXT J0
1510    Q=Q/N0 \S=S/N0
1520    RETURN
1530    REM     SUBROUTINE ROR COMMENTS
1540    CPOS(X0, Y) \D=Y2/25
1550    CNTR(1)
1560    COMM(L$(0), X0, Y) \PRINT N$
1570    COMM(L$(2), X0,Y-D) \PRINT H(2)
1580    COMM(L$(6),X0, Y-2*D) \PRINT H(6)
1590    RETURN
1600    REM     SUBROUTINE FOR SAVING DATA
1610    H(9)=I4
1620    X=24
1630    FOR I=1 TO 12
1640    X(I)=H(I) \X(I+12)=0
1650    X1=X(I)-INT(X(I)+1.0E-5)
1660    IF X1<=0 THEN 1690
1670    X(I)=X(I)^10
1680    X(I+12)=X(I+12)-1 \GO TO 1650
1690    X(I)=INT(X(I)+0.5)
1700    NEXT I
1710    FOR I=1 TO I4 \X0(I)=X0(I)*10 \Y0(I)=Y0(I)*10 \NEXT I
1720    OPEN "DX1:" &N$ FOR INPUT AS FILE #1
1730    AOUT(H, 1, 0, E1)
1740    AOUT(X0, 1, 1, E2)
1750    AOUT(Y0, 1, 2, E3)
```

```
1760    CLOSE #1 \RETURN
1770    REM     SUBROUTINE FOR RECALLING TEST DATA
1780    OPEN "DX1:" &N$ FOR INPUT AS FILE #1
1790    AINP(H, 1, 0, E1)
1800    AINP(X0, 1, 1, E2)
1810    AINP(Y0, 1, 2, E3)
1820    CLOSE #1
1830    FOR I=1 TO 12
1840    H(I)=H(I)*10^H(I+12)
1850    NEXT I
1860    I4=H(9)
1870    FOR I=1 TO H(9) \X0(I)=X0(I)/10 \Y0(I)=Y0(I)/10 \NEXT I
1880    RETURN
```

APPENDIX III

DERIVATION OF THE CHEMICAL DRIVING FORCE FOR MnS NUCLEATION IN FERRITE

For a process at constant temperature and pressure, the following substitutions can be made on condition that only pure MnS nuclei are formed:

$$G_{MnS} = X_{Mn}^{MnS}\,\bar{G}_{Mn}^{MnS} + X_{S}^{MnS}\,\bar{G}_{S}^{MnS} \tag{III.1}$$

$$G_{\alpha} = X_{Mn}^{\alpha}\,\bar{G}_{Mn}^{\alpha} + X_{S}^{\alpha}\,\bar{G}_{S}^{\alpha} + X_{Fe}^{\alpha}\,\bar{G}_{Fe}^{\alpha} \tag{III.2}$$

$$G_{\alpha o} = X_{Mn}^{\alpha o}\,\bar{G}_{Mn}^{\alpha o} + X_{S}^{\alpha o}\,\bar{G}_{S}^{\alpha o} + X_{Fe}^{\alpha o}\,\bar{G}_{Fe}^{\alpha o} \tag{III.3}$$

Here, X_i^j and $\bar{G}_i^j$ (i = Mn, S or Fe; j = MnS, α or αo) denote the mole fraction and partial molar free energies (or chemical potentials) of element i in the MnS phase, the remaining ferrite or the original matrix, respectively, while G_{MnS}, G_{α} and $G_{\alpha o}$ were already defined in §6.1.2. In addition, the following relationships are always valid:

$$X_{Mn}^{MnS} = X_{S}^{MnS} = \frac{1}{2} \tag{III.4}$$

$$X_{Mn}^{\alpha o} = f_m X_{Mn}^{MnS} + (1 - f_m) X_{Mn}^{\alpha} \tag{III.5}$$

$$X_{S}^{\alpha o} = f_m X_{S}^{MnS} + (1 - f_m) X_{S}^{\alpha} \tag{III.6}$$

The substitution of these equations into Eq. (6.3) yields

$$\Delta G_{MnS} = \frac{f_m}{2}[(\overline{G}_{Mn}^{MnS} - \overline{G}_{Mn}^{\alpha}) + (\overline{G}_{S}^{MnS} - \overline{G}_{S}^{\alpha})] + \Sigma X_i^{\alpha o}(\overline{G}_i^{\alpha} - \overline{G}_i^{\alpha o}) \qquad \text{(III.7)}$$

Apparently, the second term of the above equation takes the form of the ternary Gibbs-Duhem law and can thus be justifiably eliminated.[192] According to Aaronson *et al.*,[191] on the other hand, it can be reasonably assumed that

$$\overline{G}_i^{\alpha} = \overline{G}_i^{\alpha o} \qquad (i = Mn, S) \qquad \text{(III.8)}$$

due to the fact that the mole fraction of nuclei is very small. Furthermore, if the nuclei are in equilibrium with the ferrite after ($f_m X_{Mn}^{MnS}$) moles of Mn and ($f_m X_S^{MnS}$) moles of S are transferred from the matrix to the MnS phase, it follows that

$$\overline{G}_i^{MnS} = \overline{G}_i^{\alpha e} \qquad (i = Mn, S) \qquad \text{(III.9)}$$

where $\bar{G}_i^{\alpha e}$ indicates the partial free energy of i in the ferrite at equilibrium with the MnS precipitates. As a result, Eq. (III.7) becomes

$$\Delta G_{MnS} = \frac{f_m}{2}[(\overline{G}_{Mn}^{\alpha e} - \overline{G}_{Mn}^{\alpha o}) + (\overline{G}_{S}^{\alpha e} - \overline{G}_{S}^{\alpha o})] \qquad \text{(III.10)}$$

In consideration of the following more general statement:

$$\overline{G}_i^{j} = G_i^{\theta} + RT \ln a_i^{j} \qquad \text{(III.11)}$$

we have

$$\Delta G_{MnS} = \frac{f_m}{2} RT\left[ln\left(\frac{a_{Mn}^{\alpha e}}{a_{Mn}^{\alpha o}}\right) + ln\left(\frac{a_S^{\alpha e}}{a_S^{\alpha o}}\right)\right] \qquad \text{(III.12)}$$

In Eqs. (III.11) and (III.12), G_i^{θ} is the molar free energy of pure element i and a_i^j the activity of the element in the designated phase j.

On the basis of a unit volume of MnS nuclei in ferrite, the chemical driving force can be represented as

$$\Delta G_{chem} = \frac{RT}{2V_m^{MnS}}\left[ln\left(\frac{a_{Mn}^{\alpha e}}{a_{Mn}^{\alpha o}}\right) + ln\left(\frac{a_S^{\alpha e}}{a_S^{\alpha o}}\right)\right] \qquad (6.4)$$

where V_m^{MnS} is the molar volume of MnS precipitates.

APPENDIX IV

EVALUATION OF THE COHERENCY OF THE CRITICAL NUCLEUS/MATRIX INTERFACE

In this appendix, the coherency of the critical MnS nucleus/matrix interface is analyzed and the respective interfacial energy is estimated on the basis of the model proposed by Liu and Jonas.[241]

The model assigned a coherency loss parameter C to characterize the interface between the matrix and a nucleus, as defined by

$$C = \frac{\delta_p}{\delta} \tag{IV.1}$$

where δ is the lattice disregistry, which was assumed to be compensated by two components, one elastic δ_e and one plastic δ_p. Thus,

$$\delta_e = (1 - C)\delta \tag{IV.2}$$

By definition, the value of C varies from 0 to 1 and represents the fraction of the lattice mismatch relaxed during nucleation. In this model, the cubic dilatation ε^T of Eq. (6.13) is replaced by the following relation:

$$\varepsilon^T = \delta_e^3 + 3\delta_e^2 + 3\delta_e \tag{IV.3}$$

As a result, the strain energy can be expressed as a function of the coherency loss parameter, and thus the energy barrier opposing the formation of the critical nucleus bears a relation to this parameter. Through the analysis of these relations, it was found that the value of the parameter for the critical interface, C^*, can be determined by solving the following two simultaneous equations:

$$\frac{\partial(\Delta G_{tot})}{\partial(d)} = 0 \qquad \text{(IV.4a)}$$

$$\frac{\partial(\Delta G_{tot})}{\partial(C)} = 0 \qquad \text{(IV.4b)}$$

with the boundary conditions below

$$\Delta G_{\varepsilon}\Big|_{C=0} = \Delta G_{\varepsilon}^{o} \qquad \text{(IV.5b)}$$

and

$$\Delta G_{\varepsilon}\Big|_{C=1} = 0 \qquad \text{(IV.5b)}$$

where d denotes the diameter of spherical precipitates, ΔG_{tot} the total free energy change expressed by Eq. (6.2), and $\Delta G_{\varepsilon}^{o}$ the value calculated directly from Eq. (6.13).

The values of C^* relative to the interface between MnS and ferrite at the different test temperatures were obtained by solving the above equations numerically. The results are listed in Table IV.1. It is of interest to note from this table that the critical coherence loss parameter depends only marginally on temperature. According to the calculation, this parameter lies between 0.928 and 0.941 in the current temperature range. These relatively large C^* values indicate that the interface between ferrite and MnS nuclei is predominantly incoherent.

The critical strain energy ΔG_{ε}^* was also estimated in the same way. The results are presented in Figure IV.1 in terms of ΔG_{ε}^* versus temperature. By comparison with Figures 6.3 and 6.4, it can be seen that the strain energies associated with the interface between the critical MnS nucleus and ferrite are less than 3% of the respective coherent values and are thus about an order of magnitude smaller than the chemical driving forces. Such critical values are employed in the analysis of the nucleation kinetics of MnS precipitation in Chapter 6.

Table IV.1
Calculated critical coherency loss parameter C^*

Temperature (°C)	C^*
800	0.928 ≃ 0.93
900	0.932 ≃ 0.93
950	0.936 ≃ 0.94
1000	0.938 ≃ 0.94
1100	0.941 ≃ 0.94

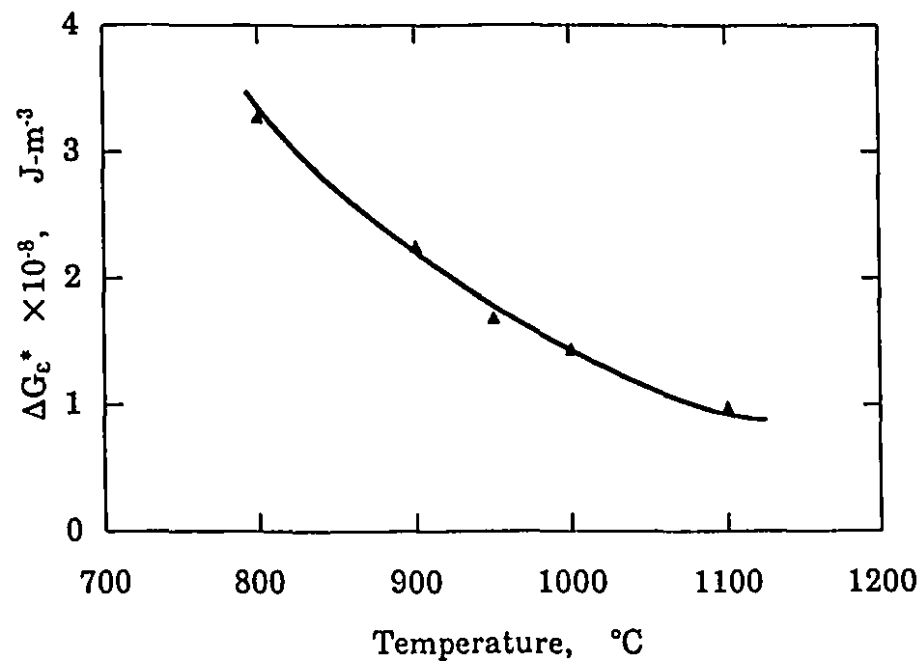

Fig. IV.1 Calculated strain energy associated with the interface between the critical MnS nucleus and ferrite.

APPENDIX V

THE BYPASSING OF PRECIPITATES BY LOCALIZED CLIMB

In order to examine whether the experimental results obtained in the present work can be interpreted in terms of the local climb model or not, the creep rate equation proposed by Brown and Ham[252] will be refined in this appendix.

Consider an edge dislocation approaching a particle of arbitrary shape and finally climbing over the obstacle. Brown and Ham proposed the following equation to describe the strain rate in the above situation based on the assumption that all the dislocations move in the same direction:[252]

$$\dot{\varepsilon} = \frac{\rho b L}{\int \frac{du}{u}} \tag{V.1}$$

Here ρ is the dislocation density, b is the Burgers vector, L is the line length of the climbing segments of the dislocations, and ∫du/u is the time taken for the dislocations to climb around the particles.

The case of spherical precipitates was investigated later by Shewfelt and Brown.[253,254] The line length of dislocation segments and the time for the dislocations to bypass the particles by local climb were given by them as

$$L = 2\theta r \tag{V.2}$$

and

$$\int_{u_i}^{u_f} \frac{du}{u} \tag{V.3}$$

Here r is the radius of the spherical particle, θ is a measure of the character of the dislocation segment, as shown in Figure V.1,[254] and u_i and u_f are the initial and final positions of the dislocation on the particle. According to the above authors, the bulk diffusion rather than the pipe diffusion of vacancies is

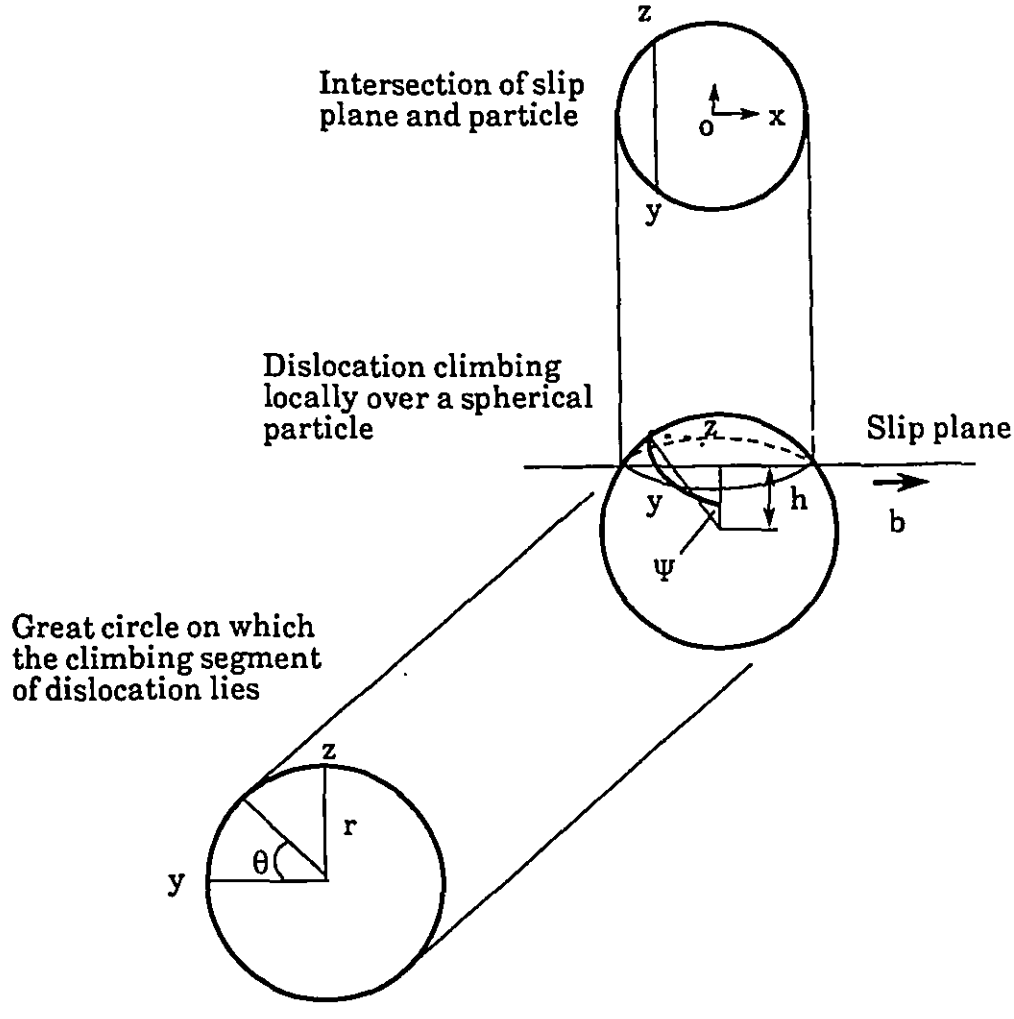

Fig. V.1 The geometry of local climb for a spherical particle.[254]

rate controlling in such a case. Assuming that the total vacancy current to the surface of the particle aids the climb of the dislocation, Eq. (V.3) can be expressed as:[254]

$$\int_{u_i}^{u_f} \frac{du}{u} = \frac{k\,T\,r}{4\,\pi\,N_v\,a_v^2\,D_v\,\mu_{\alpha\text{-}Fe}\,b^2} \int_{u_i}^{u_f} \frac{f^2(\theta, h/r)}{[(dL/du) - 2\cos(\theta/2)]}\,du \qquad \text{(V.4)}$$

where N_v is the number of vacancies per unit volume in the neighborhood of the climbing dislocations, a_v is the area associated with one vacancy in the slip plane, and D_v is the bulk diffusion coefficient of vacancies. Following these authors,

$$f(\theta, h/r) = -2\sin(\theta)\sin(\psi)\cos(\psi) - [\theta - \sin(\theta)\cos(\theta)]\,\frac{\sin(\psi)\cos^2(\psi)}{h/r} \qquad \text{(V.5a)}$$

and

$$\frac{dL}{du} = -2\,[1 - \cos(\theta)]\,\frac{\sin(\psi)}{\sin(\theta)} \qquad \text{(V.5b)}$$

Here, ψ is the angle of inclination of the particle/matrix interface when the dislocation strikes the particle half way between the mid-plane and the top of the particle, and h indicates the position of the slip plane, as noted in Figure V.1.

Using the geometrical relations shown in Figure V.1, it can be shown that

$$(\frac{h}{r})^2 = \frac{\cos^3(\theta)}{1 + \cos(\theta) - \cos^2(\theta)} \qquad \text{(V.6)}$$

and

$$\cos(\psi) = \frac{(h/r)}{\cos(\theta)} \tag{V.7}$$

Clearly, h must first be determined when substituting Eqs. (V.5a), (V.5b), (V.6) and (V.7) into Eq. (V.4) for calculation of the climb time. If the value of h is taken as r/2, θ is 48° and ψ 42 °. Then Eq. (V.4) becomes

$$\int_{u_i}^{u_f} \frac{du}{\ddot{u}} = \frac{0.035\, k\, T\, r^2}{\pi D_s \mu_{\alpha-Fe} b^3} \tag{V.8}$$

By combining Eqs. (V.1), (V.2) and (V.8), the equation for calculating the strain rate in the case of spherical precipitates is

$$\dot{\varepsilon} = \frac{15\, \pi^2 \rho\, D_s \mu_{\alpha-Fe} b^4}{k\, T\, r} \tag{V.9}$$

In this equation, the substitution of[252]

$$a_v = \frac{b^2}{\sqrt{2}} \tag{V.10}$$

and of[254]

$$D_s = N_v a_v b D_v \tag{V.11}$$

was made, where D_S is the matrix self-diffusion coefficient.

By further substituting[214]

$$D_s = D_{so} exp(-\frac{Q_s}{RT}) \tag{V.12}$$

and[151,237]

$$\rho = \left[\frac{2 \pi \sigma_a}{M b \mu_{\alpha\text{-}Fe}} \right]^2 \tag{6.30}$$

into Eq. (V.9), the final strain rate expression, based on the local climb model, can be given as

$$\dot{\varepsilon} = \frac{60 \pi^4 \sigma_a^2 b^2}{M^2 \mu_{\alpha\text{-}Fe} kT \bar{r}} D_{so} exp(- \frac{Q_s}{RT}) \tag{8.3}$$